Searching for Light Dark Matter with a Spherical Proportional Counter

Patrick Knights

Thèse de doctorat

NNT: 2021UPASP035

Searching for Light Dark Matter with a Spherical Proportional Counter

Recherche de Matière Noire Légère avec un Compteur Proportionnel Sphérique

Thèse de doctorat de
l'Université Paris-Saclay et de University of Birmingham

École doctorale n° 576, Particules, Hadrons, Énergie, Noyau, Instrumentation, Imagerie, Cosmos et Simulation, (PHENIICS)
Spécialité de doctorat: Physique des particules
Unité de recherche: Université Paris-Saclay, CEA, Département d'Electronique des Détecteurs et d'Informatique pour la Physique, 91191, Gif-sur-Yvette, France.
Particle Physics Research Group, School of Physics and Astronomy, University of Birmingham, UK.
Référent: Faculté des sciences d'Orsay

Thèse présentée et soutenue à Birmingham (Royaume-Uni), le 10 Mai 2021, par

Patrick Ryan KNIGHTS

Composition du jury:

Étienne AUGÉ Professeur, Université Paris-Saclay	Président
George FANOURAKIS Chercheur émérite, Institute of Nuclear and Particle Physics, NCSR 'Demokritos'	Rapporteur & Examinateur
Chamkaur GHAG Professeur, University College London	Rapporteur & Examinateur
Gilles GERBIER Professeur, Queen's University	Examinateur
Dinesh LOOMBA Professeur, University of New Mexico	Examinateur
Paul NEWMAN Professeur, University of Birmingham	Examinateur

Direction de la thèse:

Ioannis GIOMATARIS Docteur, Université Paris-Saclay, CEA Saclay	Directeur de thèse
Konstantinos NIKOLOPOULOS Professeur, University of Birmingham	Directeur de thèse

UNIVERSITY OF BIRMINGHAM

université PARIS-SACLAY

Searching for Light Dark Matter with a Spherical Proportional Counter

By
Patrick Ryan Knights

A thesis submitted to
the University of Birmingham
and Université Paris-Saclay
for the degree of
DOCTOR OF PHILOSOPHY

Particle Physics Research Group
School of Physics and Astronomy
College of Engineering and Physical Sciences
University of Birmingham
31 March 2021

Supervisors:
Prof. Konstantinos Nikolopoulos
University of Birmingham
Dr Ioannis Giomataris
Université Paris-Saclay, CEA Saclay

ABSTRACT

The vast majority of mass in the universe is comprised of an unknown form of matter – Dark Matter. The NEWS-G collaboration are using a novel gaseous detector, the spherical proportional counter, in a search for Dark Matter particles with masses down to sub-GeV. Having set the first exclusion limit on the spin-independent DM-nucleon cross sections for a 0.5 GeV DM particle in 2017, NEWS-G is now turning its focus to it's new detector, SNOGLOBE. The 140 cm-diameter spherical proportional counter was constructed and commissioned in France and has now been shipped to SNOLAB, Canada, for a direct DM search.

For SNOGLOBE to achieve it's physics potential, several developments are required, including the understanding of the detector, the properties of gases, background suppression techniques and the physics potential of future experiments. Developments in the spherical proportional counter read-out technology are presented, which uses high-resistivity electrodes to improve stability and energy resolution. The multi-anode sensor, ACHINOS, enables the operation of larger detectors at higher pressures. A simulation framework for the spherical proportional counter has also been developed, which is an important tool for understanding how the detector operates. Another critical component to understanding the operation of the detector when looking for low-energy nuclear recoils induced by DM interactions is the ionisation quenching factor. Measurements of this in gases are scarce, and so a method to calculate this from measurements of the W-value has been developed and applied to several gases. The suppression of radioactive backgrounds is of paramount importance for future NEWS-G spherical proportional counters, and all rare-event search experiments. A method for producing highly radiopure copper is electroforming, which has been used to apply a layer to SNOGLOBE's inner surface and suppress experimental backgrounds. The application of this technique to produce future NEWS-G detectors is discussed, along with their physics potential.

RÉSUMÉ

La collaboration NEWS-G mène des expériences qui recherchent des particules candidates pour la matière noire jusqu'à des masses en dessous du GeV avec un détecteur gazeux le compteur proportionnel sphérique. Le détecteur de nouvelle génération, SNOGLOBE, un compteur proportionnel sphérique de 140 cm de diamètre, a été construit et des plans pour des expériences futures sont en cours. Le travail présenté a permis de développer la compréhension du détecteur, les propriétés des gaz, les techniques de suppression de fond et le potentiel physique des futures expériences. La compréhension du champ électrique du détecteur est essentielle au fonctionnement du détecteur. Les calculs de la méthode des éléments finis ont été utilisés pour guider le développement des capteurs de lecture, tout comme un programme de simulation, dédié aux compteurs proportionnels sphériques, basé sur Geant4 et Garfield ++. L'utilisation d'une électrode de correction secondaire à résistivité élevée avec le capteur à anode unique a amélioré la stabilité opérationnelle et la résolution d'énergie du détecteur en ajustant le champ électrique. L'utilisation d'une électrode centrale, imprimée en 3D pour le capteur multi-anode ACHINOS et enrobée d'une couche de le carbone adamantin (DLC) a permis une percée dans la stabilité et la robustesse du détecteur. ACHINOS offre un moyen de fonctionner avec des détecteurs de plus en plus grands et à haute pression, ce qui est essentiel pour le fonctionnement du SNOGLOBE et des futures recherches sphériques proportionnelles contre les événements rares. La fraction d'énergie déposée en forme d'ionisation doit être bien comprise pour déduire l'énergie d'un noyau de recul induit par la diffusion élastique de la matière noire. Une méthode a été développée pour calculer cela à partir de mesures de précision de la valeur W dans les gaz, menées depuis plusieurs décennies. Ceux-ci fournissent des estimations expérimentales du facteur de 'quenching' d'ionisation dans plusieurs gaz. Le facteur de quenching d'ionisation dans CH_4 est d'une importance particulière pour la collaboration NEWS-G et est estimé à des énergies de recul en dessous du keV. La construction de détecteurs de matière noire impose des contraintes extrêmement rigoureuses concernant la radio-pureté des matériaux utilisés. Dans le cas de NEWS-G, le ^{222}Rn incrusté dans le cuivre du détecteur, lors de sa fabrication, conduit à une contamination de ^{210}Pb, qui est la plus grande contribution au bruit de fond expérimental. Une méthode de suppression de ce fond dans le cuivre est l'électroformage, qui a été utilisé par des expériences pour produire des composants de détecteur suite à l'amélioration significative de la radio-pureté. La technique a été rééchelonnée et une couche de cuivre très pur a été déposée à la surface interne de SNOGLOBE, réduisant le fond en dessous de 1 keV par un facteur de 2,6. Il s'agit du plus grand électroformage souterrain jamais réalisé et a démontré la faisabilité de la technique sur de grandes surfaces sphériques profondément

souterraines. L'amélioration de la radio-pureté qui peut être obtenue avec l'électroformage a motivé le développement de futurs compteurs proportionnels sphériques entièrement électro-formés directement dans un laboratoire souterrain. L'installation ECUME de SNOLAB produira un détecteur de 140 cm pour NEWS-G et entrera en service cette année. Lorsqu'il est installé dans le blindage du SNOGLOBE, le détecteur entièrement électro-formé augmentera la sensibilité matière noire de NEWS-G. Au-delà, DarkSPHERE est proposé comme successeur dans la recherche directe de matière noire NEWS-G. Le détecteur électro-formé entièrement souterrain de 3 m, installé dans un blindage de radioprotection amélioré composé principalement d'eau, aurait le potentiel d'explorer l'espace de la section efficace pour la production de la matière noir proche au plancher des neutrinos solaires, dans la gamme de masse de matière noire inférieure à 1 GeV. Le potentiel physique d'un tel détecteur pour détecter la matière noire par recul nucléaire induit a été étudié.

Dedicated to Nan and Dampi.

There is nothing like looking, if you want to find something. You certainly usually find something, if you look, but it is not always quite the something you were after.

J.R.R. Tolkien, *The Hobbit, or There and Back Again*

ACKNOWLEDGMENTS

Firstly, I gratefully acknowledge the financial support from the School of Physics and Astronomy at the University of Birmingham and from the French National Research Agency (ANR-15-CE31-0008), whose support has enabled this work to take place. I am grateful to the University fo Birmingham and CEA Saclay for hosting me over these three and a half years.

There are more people than I could possibly hope to thank for teaching, guiding and supporting me over the 26 years leading to this point – while I do not mention you all or all the ways in which I am grateful to you, my sincere thanks to you all.

I cannot begin to express my thanks to Kostas Nikolopoulos for his innumerable and tireless hours of support, guidance and patience over the past 6 years. Kostas' understanding of physics and his motivation create the perfect environment to develop as a young scientist and I count myself very fortunate to have worked with him. Kostas has been there to support me to not only become a better scientist, but also a better person, and for this I am eternally grateful.

I am extremely grateful to Ioannis Giomataris; it has been a privilege to work with you and to learn from your extensive knowledge and experience. Your scientific curiosity has been, and will continue to be, a great inspiration to me. Thank you for the many exciting discussions in the laboratory, your hospitality in welcoming me to Saclay, and for giving me the opportunity to learn from you.

I am deeply indebted to Ioannis Katsioulas for all of your support, helping me to grow scientifically and as a person (not least, culinarily!). Thank you for the kindness and hospitality you have shown me. You have always been there for me as a friend, and I will never forget that. Working with you is not only a great privilege but also a pleasure.

I also want to thank the members of the committee Étienne Augé, George Fanourakis, Chamkaur Ghag, Gilles Gerbier, Dinesh Loomba, and Paul Newman, for thier time and for the valuable feedback provided on this work and the manuscript.

I want to thank the group in Saclay for welcoming me, the great kindness you showed me and the many interesting discussions I had with you: Esther, Michel G., Xavier-Francois, Thomas, Francesca, Laura, Hector, Paco, Florian, Lukas, Fanny, Georgios, Christos, Mariam, Alain, Jean-Phillipe – I have fond memories of you all. Thank you also to the members of the Particle Physics group at the University of Birmingham for being my home during my

masters year and my Ph. D.. There are too many to name you all, but special thanks to Ioannis M., Rob, Tom, Rhys. To the other students in Birmingham, Gov, Nandish, Dan, Robbie, Joel, Jonathan, Beckie, and all the rest, my thanks for being there for a discussion or a chat, and for some great memories!

My thanks also go to the members of the NEWS-G collaboration for welcoming me and for the many enjoyable discussions in meetings and over a collaboration meeting meal. I look forward to continuing to work and spend time with you all in the future.

I would also like to thank the staff at LSM for your hospitality, and your assistance and patience to allow me to complete my work. My thanks also to the group at LPSC Grenoble for being welcoming hosts and for many stimulating discussions. Thanks especially to Jean-Francois for your friendliness and introducing me to La Ferme à Dédé(!). To the team at Boulby Underground Laboratory, my thanks for making my visits exciting and productive, and sharing in some well-earned beers (and the odd Connect4 game or pub quiz) after a day in the lab. It is a pleasure to have worked with you all.

My gratitude also goes to Eric Hoppe for his patience and kindness in answering my many questions when we were both at LSM and since, and for the exciting day trips during our stay at LSM.

A great thanks also to Andy Bartlett, for first passing on his enthusiasm for physics to me and the many hours you spent to help me achieve my goals.

The years leading up to this point would not have been the same without the friends I have been fortunate enough to have made. Many thanks to Dom for being a great friend and always being there to talk (usually over a beer...). My thanks also to Harri, Sam, Tom, and Will for your friendship and all our memories in university and since.

To Mum and Dad, thank you for always supporting me in the path I have chosen; your love and encouragement have shaped me into the person I am now. To you both, to Nan, Dampi, Nan, Granddad, Clare, Sean, Cian, Sam, Hayley and the rest of my family, thank you for your love and support.

Finally, I cannot put into words my gratitude to Sasha for her care, love and patience over the past 7 years, and all the memories made together. Without your constant encouragement and unwavering support this would not have been possible.

AUTHOR'S CONTRIBUTION

Much of the work presented was conducted within the NEWS-G collaboration, and its achievements are the product of many individual's efforts. The NEWS-G collaboration members can be found in the authors list of Ref. [1]. While emphasis is given throughout this thesis to work which I have contributed directly, work that is needed for understanding and clarity is also included. My specific contribution to each chapter will be detailed in the following paragraphs. Where the presented work has been included directly in a publication, references are given.

Chapter 2 covers material which is essential to the understanding of dark matter, and so the motivation of the later work, and is largely a literature review. Exceptions to this are the calculations of the differential event rate for different dark matter candidate masses and the event rates in the spin-independent nucleon-dark matter elastic scattering cross section versus dark matter mass figures.

The beginning of Chapter 3 describes the operation of gaseous detectors, and is compiled from many sources. I have directly contributed in much of the material presented from Section 3.3 onwards. My personal contributions include the derivation of the relationship between the gas gain and pressure in spherical proportional counters, but also the data demonstrating the background discrimination capabilities. I have directly contributed to the construction, assembly, and commissioning of SNOGLOBE at LSM.

I played an integral role in the work in Chapter 4. I performed the ANSYS finite element method calculations, that were incorporated into the simulation framework for spherical proportional counters that I helped to develop [2]. The results of the simulation were used to guide the prototyping of the single-anode and multi-anode sensors, to which I directly contributed [3, 4]. I had a major involvement in the construction and testing of many of these sensors, which have been used by NEWS-G and R2D2 collaborations [5], and in other applications of the spherical proportional counter [6].

The ionisation quenching factor calculations presented in Chapter 5 are based on measurements of the W-value by several authors. I directly contributed in the literature review and selection of data, and performed the analysis [7]. I also contributed in several campaigns to measure the ionisation quenching factor with the COMIMAC facility at LPSC Grenoble, including the construction and testing of the sensors used, and the collection and analysis of data.

The electroplating of SNOGLOBE's inner surface [1], presented in Chapter 6, was a collaborative effort encompassing not only the NEWS-G collaboration but also members from PNNL and the XMASS collaboration. The measurement of the ^{210}Pb contamination in copper was performed by the NEWS-G in collaboration with XMASS, who measured the sample with their XIA UltraLo-1800 detector. The smaller prototype sphere was constructed and tested at PNNL. For the electroplating of SNOGLOBE, I had the on-site day-to-day responsibility throughout the operation, in close contact with PNNL and LSM colleagues. I was responsible for maintaining the operation, inspecting for defects in the plating or electrolyte, and conducting the final rinsing and passivation stages for both hemispheres and the preparatory stages for the second hemisphere. The radio-assay of copper samples I provided from the plating were conducted by PNNL.

The future of spherical proportional counters for NEWS-G are discussed in Chapter 7. I am directly involved in the design and construction of ECUME. I am part of the group designing DarkSPHERE, and assisted in the shielding design and performed its physics potential estimate.

Contents

List of Figures

List of Tables

1

Introduction

It is a remarkable fact that the precise nature of over 95% of the mass-energy of the universe is unknown. Furthermore, the comparison of astrophysical observations and current understanding of how matter interacts gravitationally leads to the conclusion that around 84% of the universe's matter is composed of some form beyond that described by the Standard Model (SM) of particle physics [8]. The nature of this *Dark Matter* (DM), so called because of its apparent lack of interaction with light, has been an open question for several decades and remains one of the greatest mysteries in modern physics.

Hints of what we now know to be DM began to be observed in the universe as early as the 1930's, with the evidence building over the decades. In 1985, Goodman and Witten [9], building on the work of Drukier and Stodolsky [10], demonstrated the potential detectability of DM for a terrestrial detector, with the first experiment to place a constraint on the DM spin-independent scattering cross section doing so in 1986 in the Homestake Mine, USA [11]. The hunt for DM has sparked decades of searches, resulting in the development of novel detector technologies, great advancements in low-radioactivity materials and assaying, and

aided the development of underground laboratories, shielded from cosmic ray interference, all over the globe. Despite this, no conclusive observation of DM has been made in the laboratory, including searches at collider facilities, such as the Large Hadron Collider [12].

Direct DM searches looking for nuclear recoils induced by the elastic scattering of galactic DM have mainly focussed on the mass region above approximately 10 GeV, looking for Weakly Interacting Massive Particles (WIMPs) which arise naturally as a candidate from theories addressing other questions in physics, such as supersymmetry. This has meant that, while still having theoretical motivation, the DM-mass cross section parameter space below 10 GeV is relatively unexplored, and experiments are increasingly turning their focus to this region. The NEWS-G experiments aim to explore this region with the gaseous detector, the spherical proportional counter. The presented work contributed towards this goal.

Chapter 2 will discuss the observational evidence and motivation for particle DM as well as how it may be detected in a laboratory. Chapter 3 will discuss the operation of gaseous particle detectors. This will introduce the spherical proportional counter, its operational principles and strengths in direct DM searches. In Chapter 4 developments made to the instrumentation of the detector readout are discussed, with three main advancements; the resistive secondary correction electrode, the ACHINOS multi-anode readout and the voltage degrader. These developments improve the electric field homogeneity, stability, robustness to sparks, and increase the electric field magnitude. A dedicated simulation framework for spherical proportional counters is also presented, combining the strengths of Geant4 and Garfield++. This has been used to better understand the detector operations and also to guide the development of the detector.

In Chapter 5, the ionisation quenching factor is discussed and its implication for measuring low energy nuclear recoils, vital for DM detection. A method for calculating it from previous measurements of the average energy to produce an electron-ion pair in various gases is

presented.

Chapter 6 addresses the suppression of background contributions to the NEWS-G experiment's latest detector, SNOGLOBE, through the use of electrodeposition. The method's ability to produce highly pure copper is discussed as are its application to SNOGLOBE in an underground laboratory and the results of the procedure. Chapter 7 explores the future application of electroforming to produce full spherical cavities for detectors. Finally, these future experiments are covered.

2

Dark Matter

Only 4.9% of the energy density of the universe is made up of particles which have been observed in the laboratory [8]. The remaining energy is shared between Dark Energy and Dark Matter (DM) at 69.1% and 26%, respectively. The composition of the DM component is completely unknown save for some of its properties from astronomical observations and constraints, which imply the existence of a new fundamental particle, beyond the Standard Model (SM) of particle physics. Despite decades of searching, the precise nature of DM remains elusive, while constraints have been placed on its particle properties and abundance in the current epoch. This chapter will discuss the observations which have provided growing evidence for the presence of DM, what is known about its properties, and the efforts to observe it.

2.1 Evidence for Dark Matter

A wealth of astrophysical observations cannot be accounted for by the gravitational effect of the observed luminous matter alone. This has led to the hypothesis that significantly more mass is present in some non-luminous form - Dark Matter. All current evidence for DM is based on its gravitational effect on visible matter.

The most widely adopted model for the formation of the universe is the ΛCDM model. Λ refers to the cosmological constant associated with the acceleration of the universe's expansion driven by dark energy; CDM refers to Cold Dark Matter. The properties of DM will be presented in Section 2.2.1. The model has been successful in explaining several phenomena, which are discussed in further detail in the next section, including the abundance of light-elements in the universe, the Cosmic Microwave Background (CMB) anisotropies, and the formation large-scale structure. In defining the amount of different matter-energy components in the Universe, it is conventional to work in terms of dimensionless 'physical densities' Ωh^2, which are the products of a component's density parameter Ω and the reduced Hubble parameter h; the present-day Hubble parameter H_0 divided by 100 $\mathrm{km\,s^{-1}\,Mpc^{-1}}$. The best estimate of h is 0.677 ± 0.004 [8]. The density parameters are ratios of the observed density ρ to the critical density ρ_c which is the total density required for the universe to be flat; measurements indicate that the universe is flat, or very close to it, making the total density parameter $\Omega_{\mathrm{tot}} \approx 1$ [8].

Two parameters of interest are the physical baryon density $\Omega_b h^2$ and the physical DM density $\Omega_\chi h^2$. Current best estimates of $\Omega_b h^2$ and $\Omega_\chi h^2$ come from measurements of the CMB and Baryon Acoustic Oscillations (BAO) as 0.0224 ± 0.0001 and 0.1193 ± 0.0009, respectively [8]. Therefore, DM comprises 26% of the universe's matter-energy density and approximately 84% of the matter density.

2.1.1 Motion of galaxies in clusters

In the early 1930s, it was noted that the constituent galaxies of the Coma Cluster (Abell 1656) exhibited a wide range of apparent velocities, of order 1000 $\mathrm{km\,s^{-1}}$ [13, 14, 15]. Zwicky's then novel application of the Virial theorem to galactic clusters allowed the expected velocity dispersion to be estimated based on the visible mass; the Virial theorem relates the time-averaged kinetic energy T of a stable system of potential-bound particles to the total potential energy V in the system by

$$2\langle \mathrm{T} \rangle = -\langle \mathrm{V} \rangle \,. \tag{2.1}$$

It was found that the anticipated velocity dispersion was smaller than that measured for the Coma cluster by more than an order of magnitude [14]. Improvements in the total mass measurement of the cluster with the use of gravitational lensing (see Section 2.1.6) and in the measurement of the luminous mass have been made since, and the conclusion remains that a large fraction of non-interacting matter is required to reconcile the two [16].

2.1.2 Rotational velocities of galaxies

Under the assumption that the vast majority of a galaxy's mass is contained in the central bulge, which is then approximated as a spherical distribution of matter, the rotational velocity v_{rot} of a mass gravitationally-bound to the galaxy and situated at a radius r from its centre can be written as

$$v_{rot}(r) = \sqrt{\frac{GM(r)}{r}}\,, \tag{2.2}$$

where $M(r)$ is the mass of the galaxy contained in the radius r and G is gravitational constant. This implies that the velocity of matter in the galactic spiral arm is expected to fall as $1/\sqrt{r}$. Since around the 1940s, hints of unexpected behaviour in galactic rotation velocities

had been observed [17, 18], however, the phenomenon gained significant interest in the 1970s when Roberts et al., Bosma, Rubin et al., and others showed that the rotational velocity remains approximately constant with radius, or falls much more slowly than anticipated [19, 20, 21, 22]. Figure 2.1 shows the observed rotational curve of a spiral galaxy and that the observation may be reproduced through the addition of an extra mass component distributed as a halo, with $M_{halo}(r) \propto r$, and that this must contain the majority of mass in the galaxy. Such a distribution corresponds to a model of a gas of self-gravitating, non-interacting particles, expected for DM.

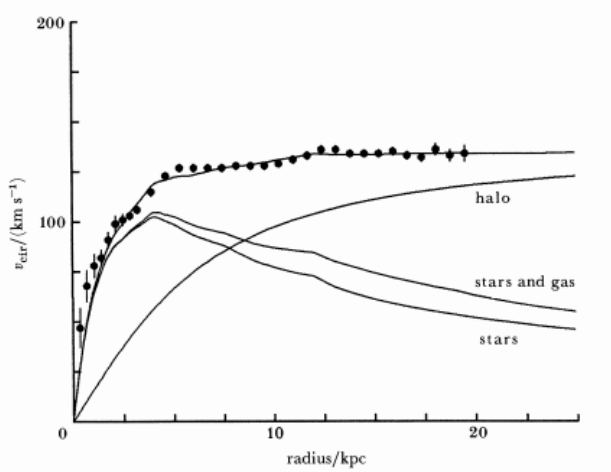

Figure 2.1: Rotation curve for the spiral galaxy NGC2403 (data points and fit). The curve can be reproduced by including a halo component to the mass of the galaxy in addition to the contribution from visible matter (stars, and stars and gasses). Figure reproduced from Ref. [23].

2.1.3 Baryon Acoustic Oscillations

Evidence for DM can also be found in the distribution of galaxies. Perturbations in the primordial plasma, generated by quantum fluctuations prior to inflation, caused over-densities. These were seeds for gravitational collapse, however, this attractive force was opposed by photon pressure. The opposing forces resulted in oscillations of the baryonic matter, analogous to sound waves; the DM, unaffected by the photon pressure, remained at the original

over-density. This effect is known as Baryonic Acoustic Oscillations (BAO). At the time of recombination, the photons decoupled from matter and freely streamed away, leaving baryonic matter in a shell around the centre of the original over-density. The fundamental frequency of the BAO corresponds to the distance the baryon-photon plasma could travel up to recombination. These over-density structures then went on to seed the formation of galaxies. Therefore, it was anticipated that there would be some characteristic distance between galaxies that would correspond to the radius of the baryonic shell, which at the time of recombination was around 150 Mpc. The correlation function $\xi(s)$ quantifies the probability of finding another galaxy at a comoving distance s from a random galaxy. The comoving distance is the proper distance between two objects at a given time divided by the universe scale factor at that time. It is, therefore, an epoch-independent measurement of the distance between two objects, assuming they move under Hubble recession. Due to the dominant role of the DM over-density, this characteristic distance would appear as a small peak in $\xi(s)$. This was observed experimentally by the Sloan Digital Sky Survey (SDSS) and 2dFGRS collaborations [24, 25], with the result of the former, shown in Fig. 2.1, clearly showing a peak at around 150 Mpc. The amplitude of the peak and overall distribution is consistent with the hypothesis that the matter density at recombination was dominated by non-baryonic DM and that this DM was non-relativistic (cold).

2.1.4 The Cosmic Microwave Background

The Cosmic Microwave Background (CMB) provides a window into the mass composition of the early universe. It was formed during 'recombination', when the universe had cooled sufficiently for electrons and atomic nuclei to bind and form neutral atoms; this transitioned the universe from being a hot, opaque plasma to being transparent to photons. The photons which decoupled from the newly-neutral matter have propagated ever since and their distribution maps the 'surface of last scattering' - the matter distribution at recombination.

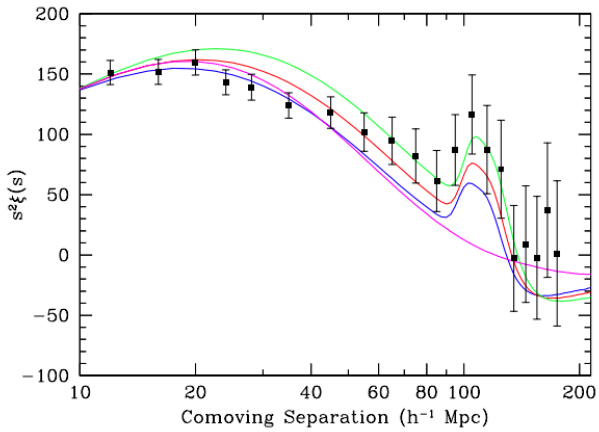

Figure 2.2: Correlation function times the comoving distance squared as a function of the comoving distance for data from the SSDS (solid squares). Overlaid are models with different matter physical densities $\Omega_m h^2$: 0.12 in green (top); 0.13 in red (middle); and 0.14 in blue (bottom with bump). The bottom, magenta line is a model with only DM and $\Omega_m h^2 = 0.105$, and so shows no BAO peak. Figure reproduced from Ref. [24].

As the universe expanded, the photons' wavelengths have increased and the CMB is now a black body radiation with a temperature of 2.7255 ± 0.0006 K [26]. The CMB is almost isotropic across the sky but contains small anisotropies. The origin of these fluctuations is the compression and rarefaction of the oscillating plasma resulting in heating and cooling, respectively. The CMB carries a 'snapshot' of these 1 part in 100,000 temperature fluctuations at reionisation. The temperature power spectrum of the CMB as a function of angular scale (multipole moment) is shown in Fig. 2.3, where the acoustic peaks are seen. The spectrum is well fit by a model of the early universe where DM dominated. The Planck results place the most stringent constraints on the parameters of the ΛCDM model, and combined with results from BOA, estimate the physical DM density of the universe to be $\Omega_\chi h^2 = 0.1193 \pm 0.0009$ [8].

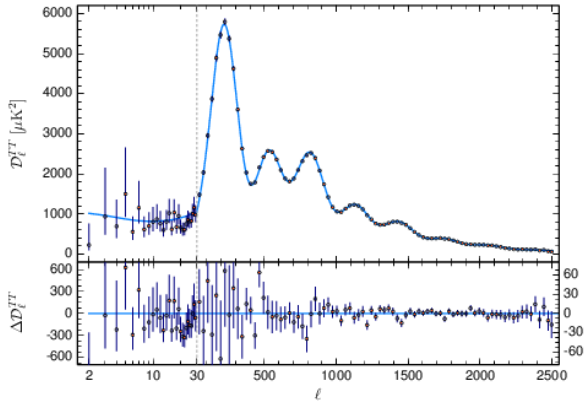

Figure 2.3: Temperature power spectrum of CMB as a function of multipole moment. The (blue) line shows the best-fit of the ΛCDM model, showing good agreement. Figure reproduced from Ref. [8].

2.1.5 Big Bang Nucleosynthesis

The production of light nuclei in the early universe was through a process known as Big Bang Nucleosynthesis (BBN). The temperature of the early universe, between around 10 seconds and 20 minutes, was sufficiently high for nuclear fusion to occur, while being low enough to allow deuterium (^{2}H) nuclei to stably form. Protons p and neutrons n could then fuse to form the light elements in the chain:

$$p + n \rightarrow {}^2\mathrm{H} + \gamma$$

$$p + {}^2\mathrm{H} \rightarrow {}^3\mathrm{He} + \gamma$$

$${}^2\mathrm{H} + {}^2\mathrm{H} \rightarrow {}^3\mathrm{He} + n$$

$${}^3\mathrm{He} + {}^2\mathrm{H} \rightarrow {}^4\mathrm{He} + p$$

$${}^3\mathrm{H} + {}^2\mathrm{H} \rightarrow {}^4\mathrm{He} + n\,.$$

Small amounts of ^{7}Li and ^{7}Be were also produced, however, heavier element production was suppressed by the lack of stable 5 and 8 nucleon isotopes. The majority of the primordial

neutrons which did not decay were combined with protons to form ^{4}He, which is at the end of the chain due to its high binding energy. BBN ceased when the universe had cooled sufficiently to prevent further fusion. However, some amount of ^{2}H was left due to incomplete chains, with the amount depending on the density of baryons at that time; a universe with higher density would have more efficient conversion of ^{2}H to ^{4}He. Models which assume that baryons made the total matter density predict a much lower quantity of ^{2}H should have survived the process than is observed in the universe. Thus, it is hypothesised that the greater fraction of the total matter density at the BBN epoch must be in the form of non-baryonic DM matter. BBN puts a constraint on the cosmological density parameter of baryonic matter $0.021 \leq \Omega_b h^2 \leq 0.024$ at the 95% confidence level (CL) [27].

2.1.6 Gravitational Lensing

The curvature of space-time induced by large astronomical objects, such as galactic clusters, is capable of inducing observable deflections in light rays passing in their vicinity. This provides a luminous-matter-independent method of measuring the total mass of a foreground object through measuring the distortion of the light from a background source. The distortion can result in an annular image, arcs or multiple images of the same source, associated with strong gravitational lensing, or may be in the weak lensing regime where more subtle distortions of multiple background sources are detectable statistically. The comparison of the mass distribution inferred from gravitational lensing measurements to that inferred from luminous matter highlights the presence of a dominant non-luminous mass component. A clear example of this is the 'Bullet cluster' (1E 0657-56), shown in Fig2.4. The bullet cluster is the remnant of the collision of two galactic clusters around 150 million years ago. The false colouring shows the hot, luminous gas, showing the name-giving 'bullet' explosion pattern from the collision. The contours (green) show the mass distribution from weak gravitational lensing which shows that the majority of the mass from the two clusters is non-luminous

and passed through the collision unimpeded. This suggests evidence that the majority of the matter in these clusters is DM and constrains the self-interaction cross section [28].

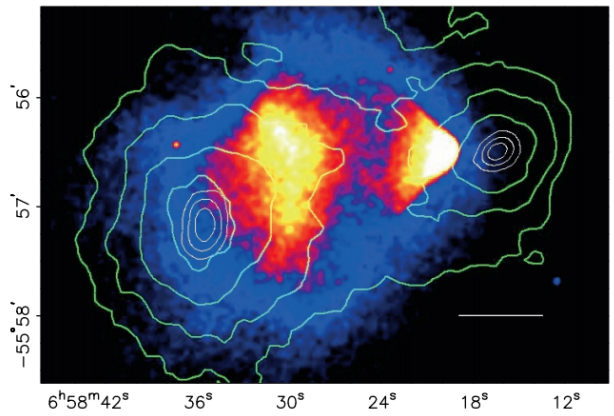

Figure 2.4: The Bullet Cluster. Coloured images from the Chandra X-ray Observatory, which map the luminous gas (the majority of baryonic matter in system) overlaid with the mass contours from weak gravitational lensing (green), showing the spatial offset between the luminous component and the majority of the mass in the clusters. Figure reproduced from Ref. [29].

2.1.7 Large Scale Structure Formation

Numerical simulations based on the ΛCDM model have generally displayed good agreement with observations of galactic clusters, super clusters and filaments which join galaxies - the largest observed structures in the universe. An example of such a filament is that connecting the binary clusters Abell 222 and 223 shown in Fig. 2.5 [30, 31].

It should be noted that there are challenges posed to the ΛCDM model, particularly on the sub-galactic scale and also the fact that more dwarf galaxies are predicted than observed. It has been posited that these galaxies may have ceased to exist for a variety of reasons, however, the model predicts many of these to have been too large to be lost in such mechanisms, known as the 'too-big-to-fail' problem. It is currently unclear if this problem is a symptom of limitations in the model or the numerical calculations. The galactic DM halo density profile

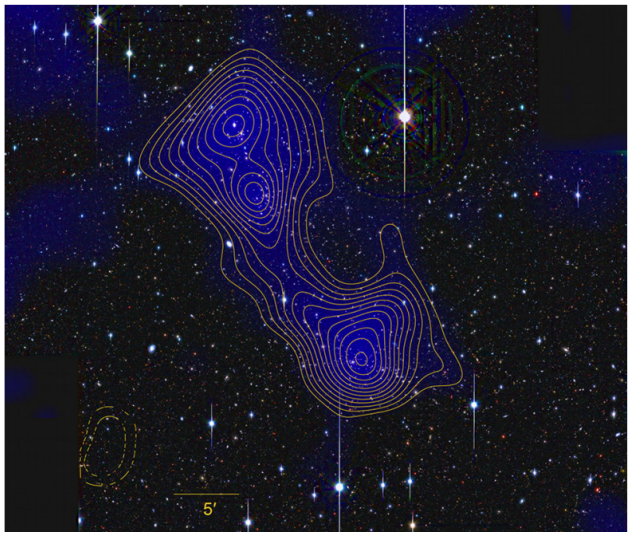

Figure 2.5: Mass density from weak lensing (blue) overlaid on a visible light image of the Abell 222 and 223 clusters. Significance contours are also shown. Figure reproduced from Ref. [31].

predicted by ΛCDM in certain galaxy types also faces challenges, as they are predicted to show a 'cusp' ($\rho \propto r^{\alpha}, \alpha \leq -1$) at low radii, whereas some observations suggest a 'core' like profile ($\alpha \sim 0$). However, the picture is not clear, with current observations of galaxies demonstrating a wide range of α from cusp- to core-like.

2.2 Particle Dark Matter

2.2.1 Properties

From the presented observations there are restrictions set on any candidate particle to be a viable, fundamental DM particle. Some are more strict than other or are model dependent, but generally a candidate must be:

- Electrically Neutral, or weakly charged [32]

- Unable to interact with photons
- Non-relativistic ('cold') at freeze-out
- Non-baryonic
- Stable on the scale of the age of the universe

The SM presents no viable candidate for this role making the DM mystery a clear case for physics beyond the SM.

2.2.2 Dark Matter Candidates

New fundamental particles are the dominant explanation for the abundance of DM. Many theoretical models introduce viable DM candidates when seeking to explain other physics phenomenon.

Standard Model Neutrinos

Neutrinos are the only SM particle that could constitute a portion of the universe's DM; neutrinos only interact via the electroweak force, are very abundant in the early universe, and are known to have a non-zero mass [33], and, thus, could behave as DM. However, neutrinos are relativistic and similar considerations for their relic abundance as presented for non-relativistic particles in Section 2.2.4 leads to a physical density parameter of

$$\Omega_\nu h^2 = \frac{\sum m_\nu}{91 \text{ eV}} \,. \tag{2.3}$$

The summed neutrino mass would need to be approximately 9 eV for neutrinos to constitute all of the DM, but measurements of the CMB have placed constraints on the summed mass

of the three neutrino generations $\sum m_\nu < 0.12$ eV, which limits their contribution to DM to around 1%. Their relativistic nature also excludes them being most of the DM due to structure formation considerations.

New fundamental particles

Much of the effort over the past decades in the direct search for DM has focussed on Weakly Interacting Massive Particles (WIMPs). They are motivated by the thermal production mechanism described in Sec 2.2.4 and by gauge hierarchy problems in the SM that implies new physics at the weak-mass scale [34]. They are particles with masses in the weak-scale, $\mathcal{O}(10\text{ GeV} - \text{TeV})$, which interact with SM particles via the weak-force. More broadly, the term WIMP is sometimes used to include DM candidates that have weak-scale interactions but not necessarily SM weak interactions, instead introducing a new fundamental force. These are also called WIMPless DM [35]. WIMPs are also an attractive candidate due to their detectability. The detection of WIMPs and WIMP-like particles will be discussed in more detail in Section 2.2.6 and after.

WIMPs are introduced by several theories that attempt to explain other SM problems, for example super-symmetric (SUSY) theories whose lightest particle, e.g. neutralinos, is a prime candidate due to its stability [36]. Another theory that provides WIMP candidates are Universal Extra Dimensions theories (UED) based on the work of Kaluza-Klein [37, 38]. Again, due to an introduced parity, the lightest particle is stable, and so a good DM candidate. Other theories also introduce viable candidates, such as little Higgs theories [39, 40].

'Hidden DM' is another possibility. In such theories, DM has no SM gauge interaction and a new fundamental force is introduced instead. While the correct relic density is achieved through freeze-out for a weak-scale DM mass and weak interactions, this is just one possible

combination, and a hidden sector allows for different choices in the annihilation cross section, and so different mass values.

As mentioned previously, the relic abundance of WIMPs is thermally produced by freeze-out. Another class of DM particles, which also benefit from the WIMP-thermal production, are superWIMPs. These particles are produced by the decay of WIMPs following their freeze-out. SuperWIMPs have much weaker interactions than the weak force, but can satisfy the current-epoch relic abundance provided they have a similar mass to the WIMPs. Again, such particles are provided by theoretic models, such as the gravitino of SUSY or lightest particles in UED. [41]

Sterile neutrinos are another example DM candidate [42]. The fact that neutrinos have mass but that only left-handed chirality neutrinos exist in the SM, and so should be massless, is a sign of new physics. The introduction of a right-handed 'sterile' neutrino, with no SM gauge interactions, enables neutrinos to aquire a mass while also presenting a potential DM candidate.

The fact that the QCD interactions are found to strictly obey CP-symmetry, which is not a requirement in the SM, is known as the CP problem. This motivated the introduction of a new symmetry and its spontaneous breaking, which results in a new particle, the axion. Axions can present viable DM candidates and, if they are DM, are constrained to be very light [43].

The direct DM searches considered from this point will focus on WIMP and WIMP-like candidates and their interactions with atomic nuclei in detectors. A more complete review of the other candidates and their detection methods can be found in the literature, e.g. Refs [34, 44]

2.2.3 Alternatives to Particle Dark Matter

Composite Astrophysical DM

Massive Astrophysical Compact Halo Objects (MACHOs) are a generic class of astronomical object which can constitute the DM in galactic halos. Examples are primordial black holes, unassociated planets, and white and brown dwarfs. MACHOS are made up of ordinary baryonic matter, but in systems where they were non-luminous. However, there is evidence against these comprising the majority of DM [45].

Modified Gravity

Several alternatives exist to the DM hypothesis, the most notable being forms and extensions of MOdified Newtonian Dynamics (MOND) [46]. MOND instead poses that the dynamics of the universe, specifically of gravity, are modified at low-accelerations, such as those experience in the spiral arms of galaxies. While these models are able to describe several phenomena, particularly on the sub-galactic scale, they do not account for all of the discussed observations. In particular, the observation of gravitational waves concurrent with electromagnetic radiation from the same source excluded large swathes of MOND models, although not all. MOND also requires there to be some 'dark matter' unobserved in the universe in order to explain observations but does not require that this matter be non-baryonic. However, MOND is not excluded and ongoing developments of the theory and experimental tests are being devised.

2.2.4 Freeze-out and Relic Abundance

The thermal freeze-out mechanism and its relation to electro-weak scale masses and cross sections is one of the motivations behind the search for WIMP DM. As has been mentioned, the early universe was a hot plasma with particles being annihilated and created from interactions in the plasma. A particle species remains in thermal equilibrium with the background plasma so long as its rate of interactions with the plasma Γ remains greater than the expansion rate of the universe. The expansion rate of the universe is given by the Hubble parameter H, which, for a flat universe such as ours, is given by the Friedmann equation,

$$H^2 = \left(\frac{\dot{a}(t)}{a(t)}\right)^2 = \frac{8\pi G}{3}\rho_{\rm c}\,, \tag{2.4}$$

where a is the scale factor (defined as 1 in the present-day) and G is the gravitational constant. When $\Gamma < H$ the species is said to have decoupled from the plasma, or have 'frozen out', and will no longer be produced by the plasma efficiently.

Initially, the temperature was high-enough that DM was produced efficiently by the plasma, $T \gg m_\chi$, and its annihilation and production were in equilibrium. The rate of annihilation is given by

$$\Gamma_\chi = \langle \sigma_{\rm ann} v \rangle \, n_{\rm eq}\,, \tag{2.5}$$

where $\sigma_{\rm ann}$ and v are the DM annihilation cross section and velocity, together averaged over the DM thermal distribution, and $n_{\rm eq}$ is the DM number density in equilibrium. For a non-relativistic species such as DM, the number density in equilibrium may be computed by integrating over the phase space distribution. It is conventional to work in terms of the yield, which is the number density divided by the entropy density, $Y = n/s$, and so, the

yield in equilibrium for a non-relativistic species is,

$$Y_{\rm eq} \propto \left(\frac{m_\chi}{T}\right)^{3/2} e^{-m_\chi/T} \,. \tag{2.6}$$

As the universe cooled to temperatures below m_χ, DM production slowed because a reducing number of particle-antiparticle collisions had sufficient energy to produce DM. Its annihilations were still occurring, so the amount of DM gradually decreased. When the expansion of the universe was greater than the annihilation rate, $\Gamma_\chi < H$, the comoving number density of DM was fixed; this is known as freeze-out. From this time, the DM density has just diluted with the expansion of the universe, i.e. inversely proportional to the scale factor a cubed. Thus, the change in the number density of DM particles with time is the sum of the dilution due to expansion and the number annihilated and produced by other particle annihilations, and can be written as a Boltzmann equation,

$$\frac{dn}{dt} = -3Hn - \langle\sigma_{\rm ann} v\rangle \left(n^2 - n^{\rm eq2}\right) \,. \tag{2.7}$$

From the Boltzmann equation, the yield at freeze-out can be computed, see e.g. Ref [47] and references therein. From this, the yield at freeze-out can be written as [48]

$$Y_0 \sim \frac{m_\chi}{T_f} \frac{1}{m_\chi M_p \langle\sigma_{\rm ann} v\rangle} \,. \tag{2.8}$$

From Eq. 2.8 it can be seen that as the thermally-averaged annihilation cross section increases, the yield at freeze-out decreases, implying that freeze-out occurred later in time.

The abundance of DM in the present-day is known as the 'relic abundance'. The energy density of dark matter ρ_χ can be written as the product of the number density n_χ and m_χ, however, it is conventional to work in terms of the yield Y, defined as n divided by the

entropy density s. Putting these together,

$$\Omega_\chi h^2 = \frac{\rho_\chi}{\rho_{\text{crit}}} h^2 = \frac{Y_0 s_0 m_\chi}{\rho_{\text{crit}}} h^2 \,, \tag{2.9}$$

$$\approx 2.8 \times 10^8 Y_0 \frac{m_\chi}{\text{GeV}} \tag{2.10}$$

where the subscript 0 indicated the present-day values. The values of s_0 (~ 2900 cm^{-3} [49]), ρ_{crit} and Ω_χ are known quantities; assuming the yield did not change since freeze-out, the yield at freeze-out can be calculated from this for a given m_χ. For 1 GeV $< m_\chi <$ 1 TeV, a freeze-out temperature of $T_f \sim m_\chi/10$ gives the observed yield. Using this in Eq. 2.8, a thermally-averaged annihilation cross section of the order 10×10^{-8} is required, which is the order of a SM annihilation cross section $\sim G_F^2 m_\chi^2$, where G_F is the Fermi constant. This surprising conclusion, coupled with well-motivated DM candidates of the correct mass proposed by Super-Symmetric theories, has driven many direct searches for Weakly-Interacting Massive Particles (WIMPs) over the last few decades. The Lee-Weinberg limit [50] puts bounds on the DM candidate mass that can interact via the weak interaction and still achieve the correct relic density; lower masses would freeze-out earlier and so be more abundant than is observed.

It should be noted that the presented mechanism of thermal production can be modified by changing the assumptions made, and other production mechanisms for DM also lead to the correct relic abundance. One example is the thermal freeze-out of a WIMP species followed by its subsequent decay to another DM species, known as Super-WIMPs. If the mass of the WIMP and Super-WIMP are similar, such models produce the correct relic abundance of DM while allowing for lower interaction cross sections.

2.2.5 Dark Matter Halo

Measurements of the rotational velocities of galaxies demonstrated the need for a halo component to the galactic mass distribution. A description of the DM halo is required in order to understand the signal expected in a direct DM search experiment. The DM halo is often approximated to be an isothermal halo distribution, such as that described in Ref. [51] or a simulation-driven model which is close to this, for example the NFW profile [52],

$$\rho(r) = \frac{\rho_{\rm crit}\delta_c}{\frac{r}{r_s}\left(1+\frac{r}{r_s}\right)^2}\,, \tag{2.11}$$

where r_s is a characteristic radius and δ_c is the over-density characteristic density of the halo; a dimensionless, galaxy specific term.

The halo is generally modelled as having isotropic velocities, referred to as the Standard Halo Model (SHM) with a truncated Maxwellian velocity probability density function [53, 54],

$$f(\boldsymbol{v}_\chi, \boldsymbol{v}_{\rm E}) = \frac{1}{k} e^{-\frac{(\boldsymbol{v}_\chi+\boldsymbol{v}_{\rm E})^2}{v_0^2}}\,, \text{ for } \mid \boldsymbol{v}_\chi \mid < v_{esc}\,, \tag{2.12}$$
$$\text{where}, k = \left(\pi v_0^2\right)^{3/2}\left(\text{erf}\left(\frac{v_{esc}}{v_0}\right) - \frac{2}{\sqrt{\pi}}\frac{v_{esc}}{v_0}\exp\left(-\frac{v_{esc}^2}{v_0^2}\right)\right)$$

where $\boldsymbol{v}_{\rm E}$ is the Earth's velocity (relative to the Galactic rest frame), $\boldsymbol{v}_\chi$ is the DM velocity, $v_{\rm esc}$ is the galactic escape velocity, v_0 is the magnitude of the most probable velocity and erf denotes the error function. The constant k normalises the velocity distribution such that $\int_0^{v_{\rm esc}} f(\boldsymbol{v}_\chi, \boldsymbol{v}_{\rm E}) {\rm d}^3\boldsymbol{v} = 1$.

For the Milky Way, $v_{\rm esc} \sim 550$ km s^{-1} [55, 56, 57], with the variation between different measurements being as much as 10%. Our solar system orbits the galactic centre and moves through the DM halo at a speed of $v_0 \approx 220$ km s^{-1} [58, 59]. The velocities usually assumed for the SHM in DM exclusion limit calculations are $v_{\rm esc} = 544$ km s^{-1}

and $v_0 = 220\,\mathrm{km\,s^{-1}}$ [60, 61]. Additionally, the local DM density ρ_χ is assumed to be $0.3\,\mathrm{GeV\,cm^{-3}}$. These nominal velocities were adopted for subsequent calculations, but it is noted that recent measurements differ from these numbers.

The velocity of the Earth relative to the DM halo **E** made of the velocity component of the solar system and the peculiar motion of the Earth around the Sun, which is time dependent on time scales relevant for direct detection experiments. While not exactly sinusoidal, $|\mathbf{E}|$ is well approximated by [54],

$$|\boldsymbol{v}_\mathrm{E}| \approx 232 + 15\sin(2\pi t_\mathrm{orb})\ \mathrm{km\,s^{-1}}\,, \tag{2.13}$$

where t_orb is the time since 2$^\mathrm{nd}$ March in years. More precise treatments of the Earth's velocity can be found, for example, in Ref. [62]. This explicit time dependence introduces an annual modulation to the DM signal, which would be visible as a change in the expected count rate in a given direction as the Earth orbits the Sun, with approximately a 3% modulation expected. Observing this modulation is one powerful method of discriminating a potential DM signal from experimental backgrounds.

The motion of the Sun relative to the DM halo also introduces a direction preference; for an Earth-borne observer, the motion of DM particle will appear as a DM 'wind', with a strongly peaked preferential direction from the Sun's galactic orbit. Directional DM detectors aim to look for this signal. It is another powerful distinguishing feature of a DM signal, as experimental backgrounds are not expected to show such a dependence.

It should be noted that, while the prescription described above is common in data analysis, recent measurements have highlighted an anisotropic component to the velocity distribution in the Milky Way resulting from the merger of a dwarf galaxy approximately 1×10^{10} years ago [63]. Extensions to the SHM have been proposed to incorporate this feature, referred to as the 'Gaia Sausage', and other substructure components, known as 'streams' [61, 64]. An

example of the modified velocity distribution is shown in Fig. 2.6.

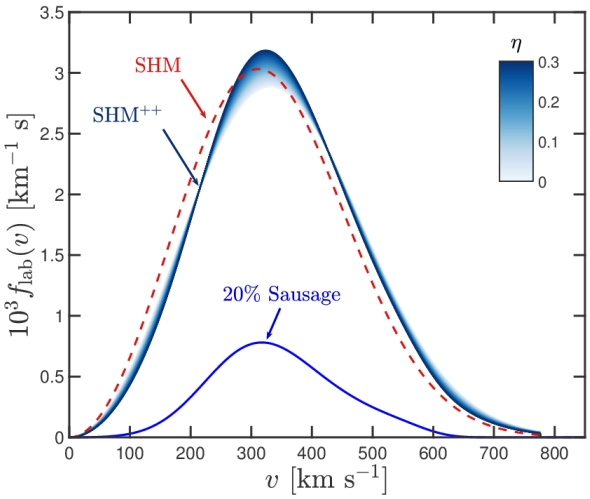

Figure 2.6: Velocity distribution from the SHM (dashed red) and from a modified model including a component with fraction η from the Gaia Sausage (shaded blue). The lower (blue) line shows the isolated Sausage component with $\eta = 0.2$. Figure reproduced from Ref. [61].

2.2.6 Interaction Rates and Cross Sections

The interaction between a cold DM particle and a nucleus is non-relativistic, but depending on the model, the interaction of a DM particle and a nucleus may be either spin-dependent or spin-independent. The DM-nucleus differential cross section can be expressed as the sum of the spin-dependent and spin-independent contributions [36, 47],

$$2m_N \frac{\mathrm{d}\sigma_{\chi N}}{\mathrm{d}|q|^2} = \frac{\mathrm{d}\sigma_{\chi N}}{\mathrm{d}E_R} = \frac{m_N}{2\mu_{\chi N}^2 v^2}\Big(\underbrace{{}_0\sigma_{\rm SI} F_{\rm SI}^2(E_R)}_{\text{Spin-independent}} + \underbrace{{}_0\sigma_{\rm SD} F_{\rm SD}^2(E_R)}_{\text{Spin-dependent}}\Big)\,, \tag{2.14}$$

where $|q|$ is the momentum transfer, ${}_0\sigma$ are the zero-momentum transfer cross section, $\mu_{\chi N} = \frac{m_N m_\chi}{m_N + m_\chi}$ is the reduced mass of the DM-nucleus system and F is the form factor which encapsulates the momentum transfer and the coherence loss.

Spin-Independent Interaction

As an example, consider the scalar interaction of a DM particle with a SM fermion, which will result in a spin-independent interaction.The interaction Lagrangian will be of the form,

$$\mathcal{L}_{\text{int}} = f_i \bar{\chi}\chi\bar{q}q\,, \tag{2.15}$$

where χ, q are the DM and quark fields and f_i is the spin-independent coupling strength to a given quark flavour [65]. To obtain the DM-nucleus interaction cross section, the individual quark coupling must be summed over, and effective coupling to protons f_p and neutrons f_n can then be calculated. The differential cross section can then be written as [65, 36, 47],

$$\frac{\mathrm{d}\sigma_{\chi N}}{\mathrm{d}E_R} = \frac{2m_N}{\pi v^2}\left[Zf_p + (A-Z)f_n\right]^2 F(E_R)^2\,, \tag{2.16}$$

where A, Z are the atomic mass and atomic number of the target. The spin-independent zero-momentum transfer cross section can be defined as

$${}_0\sigma_{SI} = \frac{4\mu_{\chi N}^2}{\pi}\left[Zf_p + (A-Z)f_n\right]^2\,. \tag{2.17}$$

While model dependent, it is generally assumed that $f_p \approx f_n$ so that ${}_0\sigma_{SI} \propto A^2$. In order to compare different experiments to each other and to theory predictions, the DM-nucleon cross section σ_{SI} is used. From Eq. 2.15, it can be shown that

$$\sigma_{SI} = \frac{4\mu_{\chi n}^2 f_n^2}{\pi}\,, \tag{2.18}$$

where $\mu_{\chi n}^2$ is the DM-nucleon reduced mass. This can be used to factorise out the target material dependence,

$${}_0\sigma_{SI} = \sigma_{SI} A^2 \frac{\mu_{\chi N}^2}{\mu_{\chi n}^2}\,. \tag{2.19}$$

The form factor $F(|q|)$ accounts for the loss of coherence when the de Broglie wavelength of the DM particle $\lambda_\chi = \hbar/q$ is no longer large compared to the size of the nucleus. If the radius of a nucleus is approximately $A^{1/3}$ fm, the form factor becomes important when

$$\frac{\hbar}{q} = \frac{\hbar}{\sqrt{2M_N E_R}} = \frac{\hbar}{\sqrt{2AM_u E_R}} < A^{1/3}\text{fm} \tag{2.20}$$

$$\implies E_R > \frac{\hbar^2}{2m_u A^{5/3}} = \frac{20}{A^{5/3}}\ \text{MeV}\,, \tag{2.21}$$

where $m_u = 0.931$ GeV is the atomic mass unit. For small-A nuclei, the form factor is generally less important than in heavier targets.

$F(|q|)$ is normalised such that $F(|q| \geq 0) \leq 1$, where equality holds for $|q| = 0$. In the case of a plane-wave scattering, this corresponds to the Fourier transform of the scattering site positions, which is approximated by the nuclear density function. For spin-independent interactions, a commonly used form is [66, 67, 54],

$$F(|q|) = \frac{3j_1(|q|r_n)}{|q|r_n} \exp\left(-\frac{|q|^2 s^2}{2}\right)\,, \tag{2.22}$$

$$\text{where } j_1(|q|r_n) = \frac{\sin|q|r_n}{(|q|r_n)^2} - \frac{\sin|q|r_n}{(|q|r_n)}\,,$$

where $j_1(x)$ is a spherical Bessel function of the first kind, r_n is the effective nuclear radius and s is the skin thickness parameter. Lewin and Smith [54] recommend values, $s = 0.9$ fm and $r_n^2 = (1.23A^{1/3} - 60\ \text{fm})^2 + \frac{7}{3}(\pi 0.52\ \text{fm})^2 - 5s^2$. The form factor for several common targets is shown in Fig. 2.7.

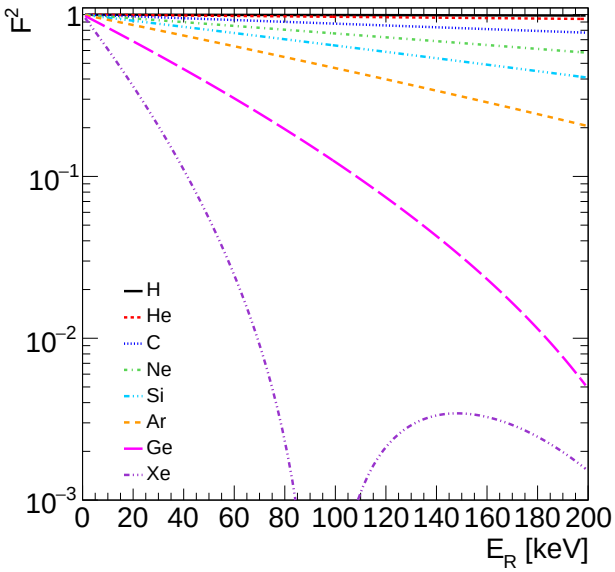

Figure 2.7: Form factor for several common target atoms as calculated with Eq. 2.22.

Spin-dependent Interaction

A spin-dependent interaction could be via an axial-vector coupling between a quark and a fermionic DM particle, with an interaction Lagarangian of the form,

$$\mathcal{L}_{\text{int}} = f_i' \bar{\chi} \gamma^\mu \gamma_5 \chi \bar{q} \gamma_\mu \gamma_5 q \,, \tag{2.23}$$

where γ_μ, γ_5 are the standard Dirac γ-matrices and f_i' is the spin-dependent coupling strength to a given quark flavour [65]. Similarly to the spin-independent case, the DM-nucleus cross section is obtained by summing over the quarks and then the nucleons. Assuming a SM weak interaction, the differential spin-dependent cross section can be written as [36],

$$\frac{\mathrm{d}\sigma_{\chi N}}{\mathrm{d}E_R} = \frac{16 m_N}{\pi v^2} G_F^2 \Lambda^2 J(J+1) F'^2(E_R) \,, \tag{2.24}$$

where J is the total angular momentum of the nucleus and Λ is defined as $\Lambda = 1/J \left(a_p \langle S_p \rangle + a_n \langle S_n \rangle\right)$, with $\langle S_p \rangle$ ($\langle S_n \rangle$) being the expectation value of the spin content

of the protons (neutrons) in the nucleus. The coefficient a_p (a_n) is a sum over quark flavour's couplings to DM and spin fractions in the proton Δ_q^p (neutron Δ_q^n),

$$a_p = \sum_{q=u,d,s} \frac{f'_q}{\sqrt{2}G_F} \Delta_q^p \,, \tag{2.25}$$

$$a_n = \sum_{q=u,d,s} \frac{f'_q}{\sqrt{2}G_F} \Delta_q^n \,. \tag{2.26}$$

The values of Δ_q^p, Δ_q^n, are determined experimentally [36].

The form factor, $F'^2(q) = S(q)/S(0)$, in the spin dependent case is often parameterised as,

$$S(q) = a_0^2 S_{00}(q) + a_0 a_1 S_{01}(q) + a_1^2 S_{11}(q) \,, \tag{2.27}$$

where $a_0 = a_p + a_n$ and $a_1 = a_p - a_n$ are the isoscalar and isovector couplings, and the individual components form factors S_{ij} are experimentally determined [36, 47, 65].

Similarly to Eq. 2.17, one may define a zero-momentum transfer DM-nucleon interaction cross section,

$$_0\sigma_{SD} = \frac{32 G_F^2 \mu_{\chi n}^2}{\pi} \Lambda^2 J(J+1) \,. \tag{2.28}$$

Instead of the A^2 dependence extracted from the nuclear matrix elements in the spin-independent case, the expectation value of the proton's or neutron's spin are found. Therefore, the spin-dependent interaction is suppressed except for in odd-neutron or odd-proton nuclei and does not benefit from the A^2 enhancement. Isotopes with either an unpaired proton, such as ^{1}H, ^{19}F or ^{127}I, or neutron, such as ^{29}Si, ^{73}Ge or ^{129}Xe, are used for probing the spin-dependent DM-nucleon cross section.

2.2.7 Event rate

Direct DM detection experiments aim to measure a signal from energy deposited by nuclear or electron recoils induced by the elastic scattering of DM particles from the galactic DM halo. For a DM particle with mass m_χ scattering off a stationary target nucleus with mass m_N, the nucleus will recoil with an energy E_R given by

$$E_R = \underbrace{\frac{1}{2} m_\chi v_\chi^2}_{E_\chi} \underbrace{\frac{4 m_\chi m_N}{(m_N + m_\chi)^2}}_{r} \frac{(1 + \cos\theta)}{2}\,, \tag{2.29}$$

where θ is the angle of recoil relative to the incoming DM particle's direction. E_χ is the DM kinetic energy, and at the most probable velocity, v_0, this is E_0. The maximum recoil energy ${}_{\max}E_R$ occurs when the collision is head on ($cos\theta = 1$) and the target and DM particle have the same mass. The term r encapsulates the kinematics of the collision and is maximal for $m_\chi = m_N$, highlighting the advantage of matching the target mass to m_χ.

The differential rate of DM events $\mathrm{d}R/\mathrm{d}E_R$ can be written as,

$$\frac{dR}{dE_R} = \frac{\rho_\chi}{m_\chi} \frac{N_A}{A} \frac{\sigma_0}{E_0 r} \frac{1}{k} \int_{v_{\min}}^{v_{\mathrm{esc}}} \frac{1}{v} f(\boldsymbol{v}, \boldsymbol{v_E}) \mathrm{d}^3\boldsymbol{v}\,, \tag{2.30}$$

where $N_A = 6.022 \times 10^{23}$ mol^{-1} is Avogadro's number. The differential rate is typically given in units of events/kg/day/keV, known as *differential rate units*, dru. For a spin-independent interaction, Fig. 2.8 shows the differential rate per unit cross section as a function of recoil energy for 0.1, 1, 10, and 100 GeV DM particles interacting in various materials. For the lowest DM masses considered, the advantage of low-mass nuclei targets is clear; while heavier targets benefit from the A^2 enhancement, the kinematic matching (r in Eq. 2.29) between the DM and nuclei results in low recoil energies that are increasingly difficult to detect. For higher mass DM candidates, the heavier nuclei have an advantage in terms of kinematic

matching and also due to the A^2 enhancement. However, the form factor partially offsets the A^2 enhancement for higher recoil energies.

In practice, an experiment will have an energy threshold which sets a minimum recoil energy that can be detected. Additionally, not all of the energy deposited by the recoil nucleus will be in a form that is observable to a given detector. For instance, in a detector that is only measuring the ionisation caused by the recoiling nucleus, only the fraction of energy dissipated that results in the formation of electron-ion pairs will be detected. This is known as a quenching factor and is discussed further in Chapter 5. The rate of events that will be observed by an experiment is then the integral of Eq. 2.30 over the experimental recoil energy window. Fig. 2.9 shows the integrated rate in the DM-nucleon cross section versus DM mass plane for 4 target atoms of interest to NEWS-G.

2.2.8 Coherent Neutrino-Nucleus Scattering

As experiments improve their sensitivity to ever lower cross sections, potential experimental backgrounds from other rare processes must be considered. One such background is Coherent Elastic Neutrino-Nucleus Scattering (CEνNS); a SM process, but only recently observed due to its low cross section [68]. The resulting nuclear recoil is indistinguishable from that produced by a DM interaction in most detectors and so the cross section below which the signal from CEνNS is expected to be larger than that from DM is known as the 'neutrino floor'. The responsible neutrinos can be from several sources, but are primarily: atmospheric, generated by cosmic rays interacting in the atmosphere; solar, produced by fusion reactions in the sun; and supernovae, a diffuse supernovae neutrino background (DSNB) from supernovea occurring through history. The energy spectrum of astrophysical neutrinos is shown in Fig. 2.10(a). Solar neutrinos are the lowest energy, being less than 18.8 MeV [69]. As the

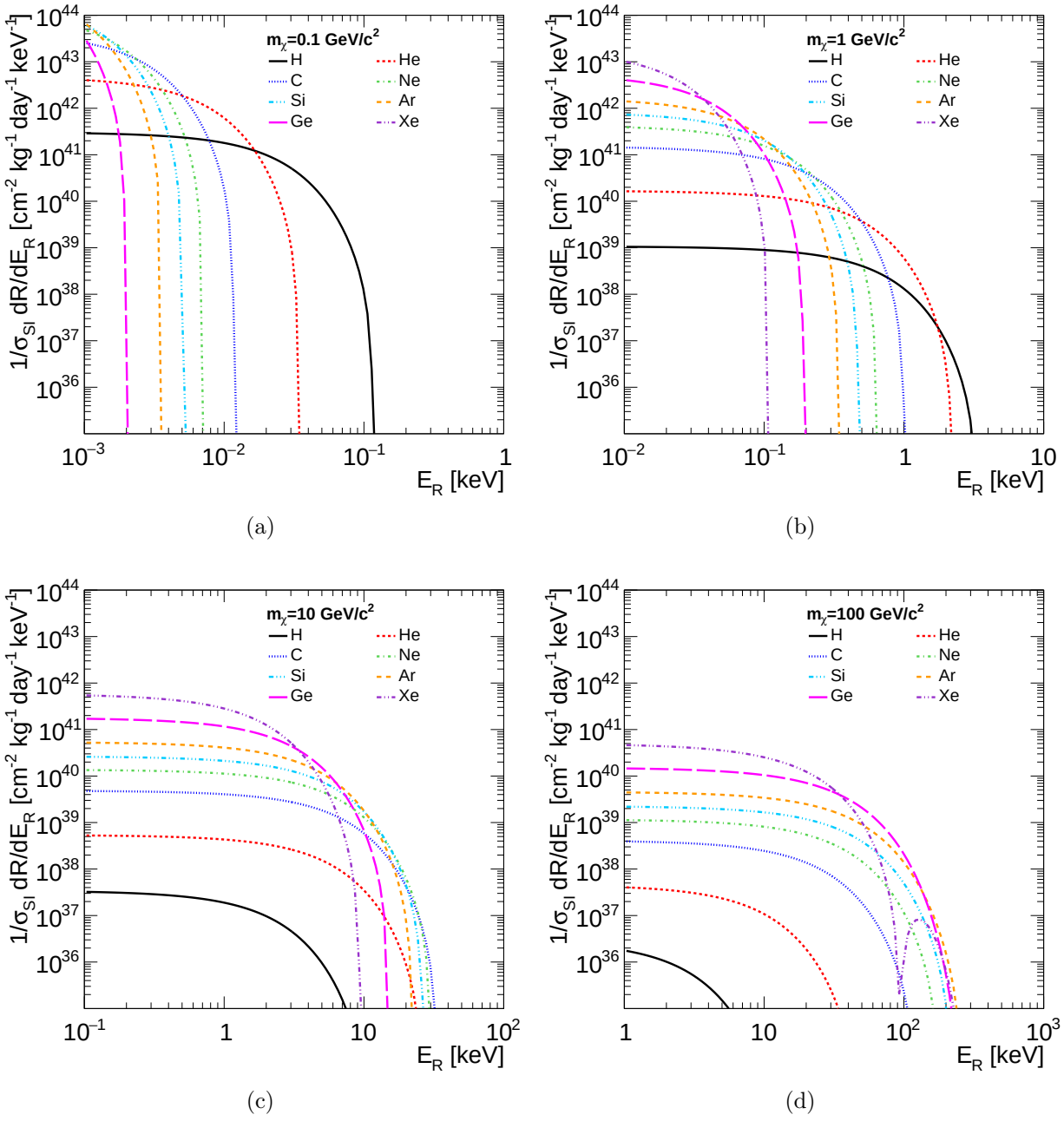

Figure 2.8: Differential rate per unit cross section for 0.1, 1, 10, and 100 GeV DM particles interacting with various target atoms. Note the x-axis range changes between plots but covers 3 decades in each case.

maximum recoil energy ${}_{\max}E_R$ is given by,

$$ {}_{\max}E_R = \frac{2E_\nu^2}{m_n + 2E_\nu}\,, \tag{2.31} $$

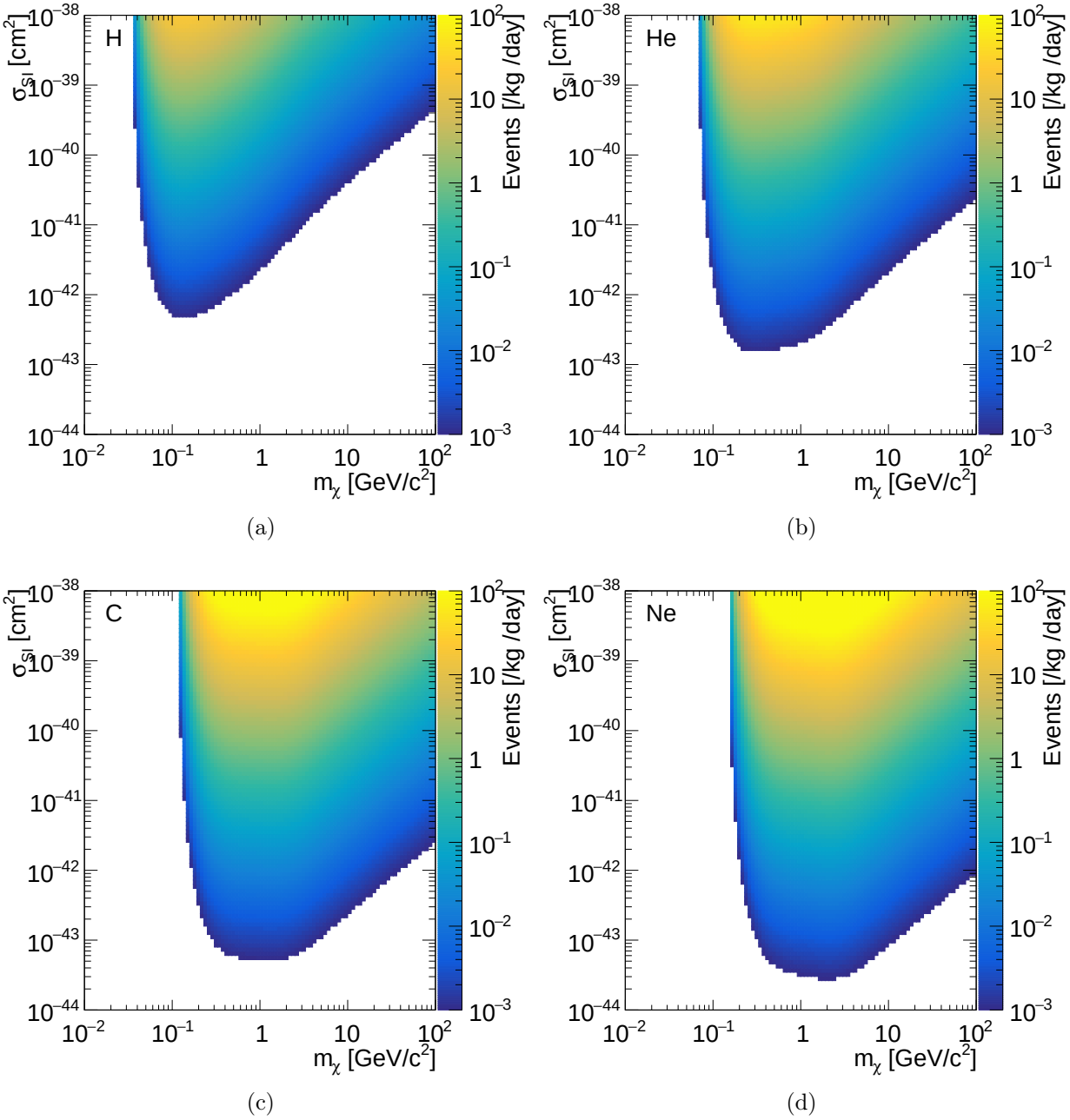

Figure 2.9: Integrated rate in the DM-nucleon cross section versus DM mass plane for (a) hydrogen, (b) helium, (c) carbon, and (d) neon targets. A recoil energy window of 14 eV to 1 keV was used.

solar neutrinos are generally of most interest to direct DM experiments, where their recoil energies can be less than $\mathcal{O}(1 - 10\,\text{keV})$.

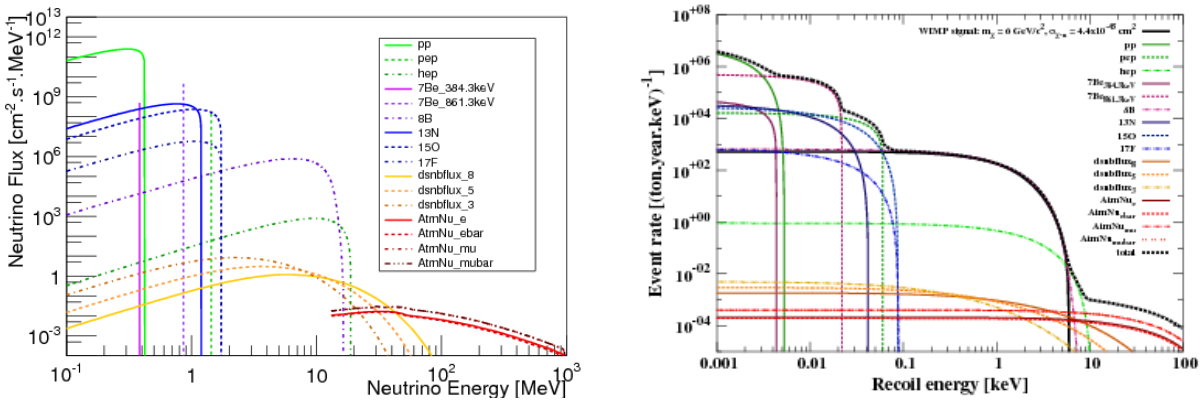

(a) (b)

Figure 2.10: (a) Neutrino flux as a function of energy for neutrinos from astrophysical sources relevant for direct DM detections. The first nine processes in the legend are solar neutrino sources; the next three are DSNB for (dsnbflux_3) ν_e, (dsnbflux_3) $\overline{\nu}_e$, and (dsnbflux_8) the other four flavours; and the final three are atmospheric neutrinos. (b) Event rate in a germanium-based detector from these neutrino sources compared to the event rate expected for a 6 GeV DM particle with $\sigma_{\mathrm{SI}} = 4.4 \times 10^{-45}$ cm^2. Figures reproduced from Ref. [70].

CEνNS is a weak neutral current process with differential cross section [71],

$$\frac{\mathrm{d}\sigma_{\nu,N}}{\mathrm{d}E_R} = \frac{G_F^2 m_N}{4\pi} Q_{\nu,N}^2 F^2(E_R) \left(1 - \frac{m_N E_R}{2E_\nu^2}\right) , \tag{2.32}$$

where $Q_{\nu,N} = A - 2Z(1 - 2\sin^2\theta_W)$ is the weak hypercharge of a target with Z protons and $A - Z$ neutrons, θ_W is the weak mixing angle and E_ν is the neutrino energy. For the astrophysical neutrino sources considered, this cross section can be used to compute the rate of events expected in a detector, with an example of this shown in Fig. 2.10(b) for a detector using germanium.

The background brought by CEνNS will need to be circumvented in order for experiments to have sensitivity to DM below the neutrino floor. The significant uncertainties in the neutrino flux make background event rate subtraction challenging [69]. For solar neutrinos, which are of most concern, one clear distinguishing feature would be the direction of the nuclear recoil; solar neutrino-induced nuclear recoils would be preferentially directed away from the Sun,

on the average. Therefore, a DM detector with directional information could distinguish solar-origin recoils from nuclear recoils from the DM wind. This method, particularly in the DM mass range below a few GeV, would provide an unambiguous method to search below the neutrino floor. However, there are other possible methods for achieving this, such as differences in annual modulation [72] or having sufficiently good energy resolution to distinguish the DM and neutrino recoil spectra [73]. The detection of a significant number of CEνNS events above the expected neutrino floor can also be a sign of new physics [74].

2.3 Landscape of Current Direct Detection Experiments

Apart from its gravitational effect, DM has not been observed. The detection of light DM or WIMPs can be done through the three methods shown in Fig. 2.11: direct detection, through interaction with a target in a laboratory; indirect detection, through its decay in the universe; production, through its production at accelerators.

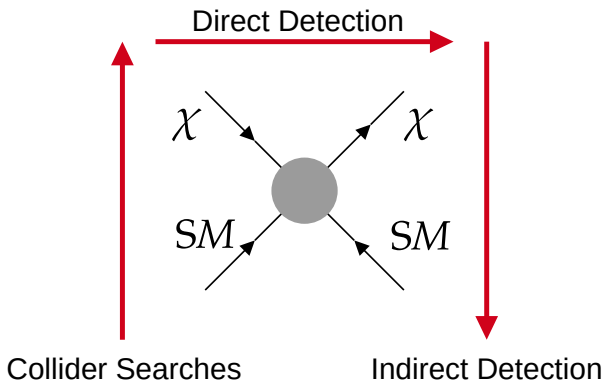

Figure 2.11: Pictorial representation of the DM detection modes.

Over the past few decades, several experiments have been dedicated to the search for DM through its elastic scattering off nuclei in target material. A recoiling nucleus in a medium transfers its energy to the medium through three processes; heating, scintillation, and ioni-

sation, with each receiving some fraction of the total energy. A detector can use one or more of the signals generated by these energy deposits to detect a nuclear recoil and to distinguish it from possible sources of background. The different technologies used are summarised in Fig. 2.12.

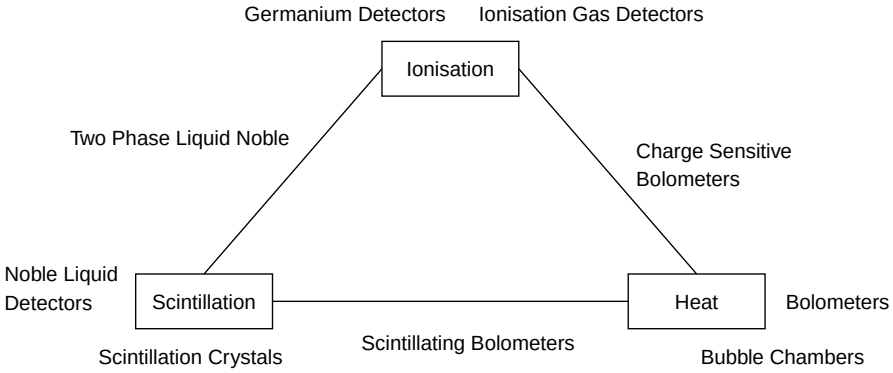

Figure 2.12: Schematic of different detection methods for elastic scattering of DM with a nucleus, and detector types that exploit them. Adapted from figure in Ref. [75].

The best constraints in the spin-independent DM-nucleon cross section as a function of DM candidate mass are shown in Fig. 2.13. The world-leading experiments in terms of

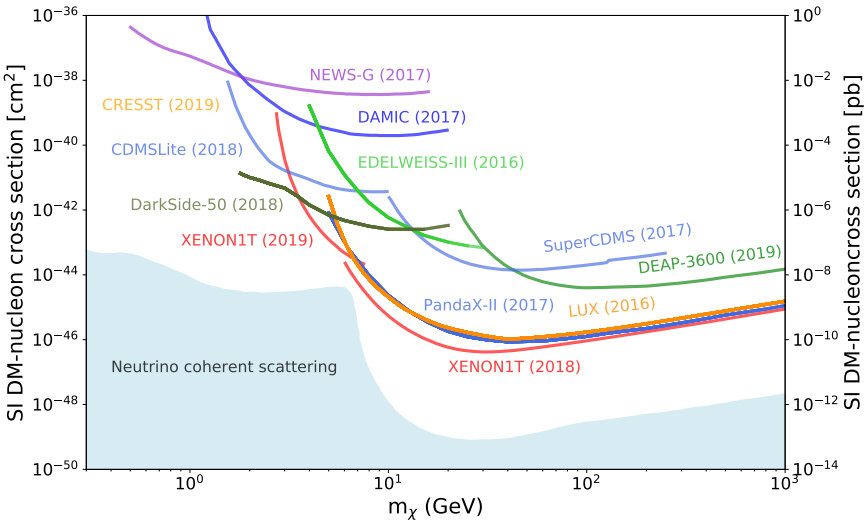

Figure 2.13: World-leading 90% CL upper limits on the spin spin-independent DM-nucleon cross section as a function of DM candidate mass. Figure reproduced from Ref. [27].

sensitivity to DM particles with mass in the range of approximately $10 - 100$ GeV utilise

multi-tonne two-phase xenon Time Projections Chambers (TPC). The detectors comprise a liquid xenon volume with a smaller gaseous xenon volume above. The interaction of a particle in the liquid produces ionisation electrons and scintillation light. The scintillation light is detected in photo-multiplier tubes (PMTs) above and below the two volumes volume, giving a prompt signal. An electric field through the detector drifts the primary electrons towards a xenon gas layer, where they are accelerated by the higher electric field, causing secondary scintillation, which generates a second signal. The comparison of these two signals allows background processes to be distinguished [76]. Three of the experiments utilising this method are XENON-1T [77], LUX [78] and PandaX-II [79]. Similar two-phase experiments are also conducted using argon, such as DarkSide-50 [80], however, xenon has the advantages that there are no natural xenon radioisotopes.The current energy thresholds and the high atomic mass of xenon and argon mean that these experiments are limited to searches above approximately 10 GeV when looking at nuclear recoils with both detection modes. However, the experiments can choose to use only the ionisation mode, allowing lower energy thresholds at the cost of background suppression capabilities in order to probe lower mass candidates, as was done by XENON1T [81].

Liquid noble-gas detectors can also be operated in single (liquid) phase, as done using xenon by XMASS [82] and with argon by DEAP-3600 [83]. These use pulse shape analysis of the detected scintillation photons to distinguish backgrounds, rather than comparison of light and ionisation signals.

The use of inorganic scintillating crystals to detect scintillation light has been explored by DAMA/NaI [84] and subsequently the DAMA/LIBRA [85], using thallium-doped sodium iodine (NaI(Tl)) scintillators installed in Laboratori Nazionali del Gran Sasso (LNGS), Italy. The results show an annual modulation, consistent with that expected for DM interactions in the crystal, over a period of approximately 20 annual cycles. Although the mass and cross section of these results have been excluded by other experiments in the case of DM-

induced nuclear recoils, they are yet to be explained. Recent results from the COSINE-100 [86] and ANAIS-112 [87] collaborations, who are also using NaI(Tl) scintillators with 1.7 years (97.7 kg years) and 1.5 years (157.6 kg years) data taking, respectively, found results compatible with both the DAMA/LIBRA result and the null hypothesis at the 68.3% CL, but both expect to obtain a more stringent coverage of the DAMA/LIBRA region within 5 years. The SABRE collaboration [88] aims to use more radiopure NaI(Tl) to investigate the DAMA/LIBRA result using detectors located in the northern and southern hemisphere laboratories to remove possible seasonal or laboratory-specific variations.

The heat produced by an interaction may be detected using a bubble chamber, as was done by PICASSO [89], COUPP [90] and PICO [91]. These detectors use small pockets of super-heated chlorofluorocarbons (C_3F_8, C_4F_{10}, etc.) or trifluoroiodomethane (CF_3I) suspended in a gel. Heat produced in an interaction causes the pocket to undergo a phase transition to a gas, releasing an acoustic shock-wave that is detected in by a piezoelectric detector. These experiments have the ability to tune sensitivity to DM by changing their operating conditions, and are particularly sensitive to spin-dependent interactions through the unpaired proton in ^{19}F.

Bolometers are sensitive to particle interactions through electric resistance variations caused by the energy deposited as heat. For DM detection applications these can be constructed from scintillating materials to also gain a second signal, such as that used by CRESST [92]. A calcium tungstate scintillation crystal is cooled to millikelvin temperatures allowing it to act as a bolometer. Again, comparison of the two signals provides background suppression. The low threshold of the bolometer and the different element nuclei available in the crystal give the detector sensitivity over a wide range of masses, down to the sub-GeV c^{-2} region.

Bolometers can also be constructed from a semi-conducting material, such as germanium or silicon, to allow the ionisation signal to be measured. CDMSlite [93], SuperCDMS [94] and

Edelweiss-III [95] use this technology, and can achieve sub-GeV c^{-2} sensitivity despite the higher mass target nuclei, due to low energy thresholds.

The final approach is to only detect the ionisation signal, which is most often done using germanium or silicon semiconductors, cooled to liquid nitrogen temperatures to reduce the electronic noise and so the energy threshold. This method is used by the CoGeNt [96], and CDEX-10 [97] experiments using germanium, and DAMIC [98, 99] employ a similar method using silicon CCDs. However, the ionisation signal may also be measured in gaseous using a TPCs such as is done by DRIFT [100] with two Multi-Wire Proportional Chambers (MWPC) and by MIMAC [101] using layers of MicroMegas. Both of these experiments are direction-sensitive through the use of TPCs and low-pressure gases. Another method to detect the ionisation signal is the spherical proportional counter, which is utilised by the NEWS-G collaboration, described in Section 3.4.

It should also be noted that many of these experiments explore other DM interaction possibilities, in particular, to explore lower-mass DM candidates. For instance, DAMIC looked for DM-electron interactions [99]. Several collaborations are exploring the potential signals induced by the inelastic DM-nucleon interaction, resulting in bremstrahlung photon emission [102], and the as-yet unobserved Migdal effect [103], both of which enhancing sensitivity to light-DM candidates. Considering these processes, XENON1T [104] and LUX [105] has set exclusion limits on light DM.

3

The Spherical Proportional Counter

This chapter will introduce the spherical proportional counter; a novel gaseous detector. First, the interactions of particles with matter are discussed to provide context to the topic of gaseous detector, which is covered after. Following the description of the general principles of gaseous detectors and how a signal is generated, we arrive at the spherical proportional counter. The detector, its operational principles, and its strengths in rare-event searches are discussed. The final sections explain how the spherical proportional counter is used by the NEWS-G collaboration in a direct search for DM, and how the detector can be used for other rare-event searches.

3.1 Particle Interactions in Matter

3.1.1 Charged Particles

A charged particle traversing a medium can interact directly with the orbital electron of atoms via inelastic Coulomb collisions. In the interaction, it may impart enough energy to the electrons to excite or ionise the atom, leaving an electron-ion pair. In the case of a charged particle heavier than an electron - referred to as a heavy charged particle - the fractional energy loss is small in each collision; however, the particle interacts simultaneously with many electrons, leading to it continually slowing down. The linear stopping power S of the particle is defined as the differential energy loss per unit length

$$S = -\frac{\mathrm{d}E}{\mathrm{d}x}\,. \tag{3.1}$$

The mean differential energy loss per unit distance, $-\langle \mathrm{d}E/\mathrm{d}x \rangle$, for a heavy charged particle Coulomb scattering on electrons is given by the Bethe formula [106],

$$-\left\langle \frac{\mathrm{d}E}{\mathrm{d}x} \right\rangle = 4\pi \frac{z^2 e^4}{m_e c^2} \frac{1}{\beta^2} N_{\mathrm{A}} \rho \frac{Z}{A} \left(\ln \left[\frac{2 m_e c^2 \beta^2 \gamma^2}{I} \right] - \beta^2 \frac{C}{Z} - \frac{\delta}{2} \right)\,, \tag{3.2}$$

where

e = electron charge,

z = charge of incoming particle in units of e,

m_e = electron mass,

c = speed of light in vacuum,

$\beta = \frac{v}{c}\,, v$ = incoming particle velocity,

N_{A} = Avogadro's Number,

ρ = Material Density,

$Z,\ A$ = Atomic number and mass of absorber material atoms,

$\gamma = \dfrac{1}{\sqrt{1-\beta^2}}$,

I = mean excitation and ionisation energy,

$\dfrac{C}{Z}$ = Shell correction, and

δ = density correction factor.

Fig. 3.1 shows the mean differential energy loss as a function of $\beta\gamma$ for several materials. For increasing velocity, the mean energy loss varies as $1/\beta^{5/3}$ until it reaches a minimum at $\beta\gamma \approx 3$. Particles with $\beta\gamma \approx 3$ are known as Minimum Ionising Particles (MIPs). Above the minimum, $-\langle \mathrm{d}E/\mathrm{d}x \rangle$ begins to increase, known as the relativistic rise. The value of I is a measured property of the material [107]. The term proportional to δ is a correction which accounts for the observation that the relativistic rise does not continue indefinitely. This is due to the dielectric polarisation of the surrounding atoms, known as the density effect, and becomes important for high energy relativistic particles [108]. The term C/Z is known as the shell correction, and corrects for when the velocity of incoming particle is of the same order or less than the atomic electron orbital velocity [109]. This becomes increasingly important for decreasing particle energy. Other corrections can also be applied to improve the accuracy of the model [110].

While Eq. 3.2 describes the mean stopping power, the process is random, and so there is a distribution of energy loss, known as straggling. For moderately thick materials, the energy loss distribution can be described by a Landau-Vavilov distribution [111, 112], meaning the most probable energy loss is below the average. An initially monoenergetic beam of particles having passed through some thickness of material will have a distribution of energies, and

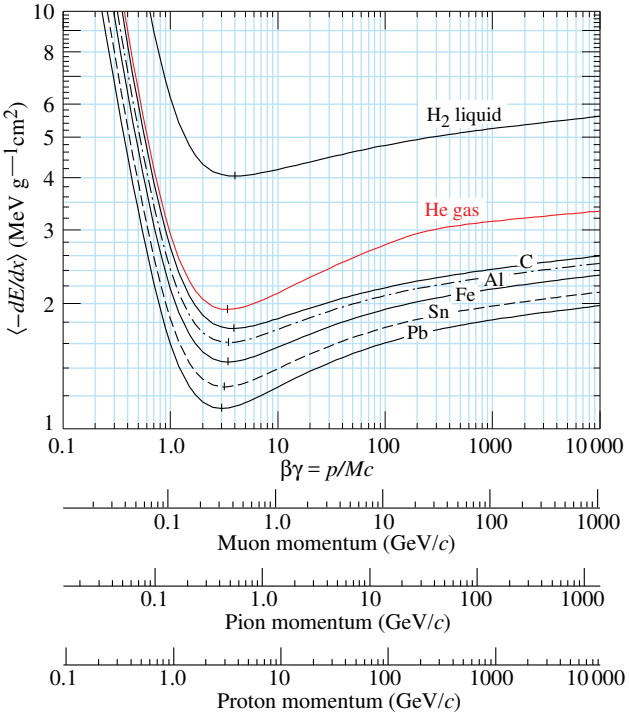

Figure 3.1: Mean differential energy loss in liquid hydrogen, helium gas and solid carbon, aluminium, iron, tin and lead. Figure reproduced from Ref. [27].

this *energy straggling* is a function of the depth in the medium.

Charged particles may also lose energy by elastic scattering interactions with the nuclei of the material, resulting in deflections of the incident particle. Other energy loss mechanisms become important for lighter charged particles or increasing kinetic energy, such as *brehmstrahlung*, transition radiation and Cherenkov radiation, however, these are not discussed further here [27].

In the case that the atom is ionised by the passage of the charged particle, the ejected electrons can have significant kinetic energy ($\mathcal{O}$(keV)), and are capable of inducing further ionisation. These δ rays can have a maximum energy of $T_{\max}$ given by the maximum energy transfer in a collision,

$$T_{\max} = \frac{2m_e\beta\gamma}{1 + 2\gamma\frac{m_e}{M} + \left(\frac{m_e}{M}\right)^2}\,, \tag{3.3}$$

where M is the incoming particle mass. For a given energy transfer T the distribution of

these electrons is given by

$$\frac{\mathrm{d}^2N}{\mathrm{d}T\mathrm{d}x} = 2\pi\frac{z^2e^4}{m_ec^2}N_A\rho\frac{Z}{A}\frac{1}{\beta^2}\frac{f(T)}{T^2}\,, \tag{3.4}$$

for the case where $I \ll T$. The factor $f(T)$ is spin dependent, but is approximately unity when $T \ll T_{\max}$. The angle θ at which the δ electrons are emitted is given by

$$\cos\theta = \frac{T_e}{p_e}\frac{p_{\max}}{T_{\max}}\,, \tag{3.5}$$

where T_e and p_e are the electron energy and momentum respectively, and $p_{\max}$ is the momentum of an electron with energy $T_{\max}$.

3.1.2 Electrons

The interactions of electrons in a medium differ from those of heavier charged particles in several ways. Electrons Coulomb scattering off of atomic electrons are able to transfer a greater fraction of energy per collision than heavier ions. The incident electrons may also interact with the atomic nucleus and be scattered through large angles. These effects result in large deflections in the electron's trajectory. Electrons may also lose energy through *bremsstrahlung* at lower kinetic energies than heavier particles, radiating photons while being deflected.

The mean stopping power for electrons for excitation and ionisation of atoms in the medium is given by [113]

$$-\left\langle\frac{\mathrm{d}E}{\mathrm{d}x}\right\rangle = 2\pi\frac{e^4}{m_ec^2}\frac{1}{\beta^2}N_{\mathrm{A}}\rho\frac{Z}{A} \tag{3.6}$$

$$\times\left(\ln\left[\frac{m_ec^2\beta^2\gamma^2E}{2I^2}\right] + (1-\beta^2) - \frac{2\gamma-1}{\gamma^2}\ln(2) + \frac{1}{8}\left(\frac{\gamma-1}{\gamma}\right)^2 - \delta\right)\,, \tag{3.7}$$

where E is the kinetic energy of the electron $E = m_e c^2(\gamma - 1)$. The form of $-\langle \mathrm{d}E/\mathrm{d}x \rangle$ for positrons is different because they undergo Bhabha scattering, which includes both s- and t-channel interactions, whereas electrons undergo Møller scattering, which is t- and u-channel scattering.

The ratio of the mean energy lost though radiative processes $-\langle \mathrm{d}E/\mathrm{d}x \rangle_{\mathrm{rad}}$, such as bremstrahlung, to the collisional losses is approximately [114]

$$\left\langle \frac{\mathrm{d}E}{\mathrm{d}x} \right\rangle_{rad} / \left\langle \frac{\mathrm{d}E}{\mathrm{d}x} \right\rangle = \frac{ZE}{1600 m_e c^2} \,. \tag{3.8}$$

3.1.3 Photons

For photon energies typically detected in gaseous detectors, only three of the photon's possible interaction modes are of significant importance; Compton scattering, photoelectric absorption and pair production. Other interactions, such as photonuclear interactions, can also occur but are generally not of interest in proportional counters, so are not discussed further. The total photon-atom interaction cross section for carbon and lead is shown in Fig. 3.2, including the contributions from the various interaction modes.

The linear attenuation coefficient μ is defined as the probability per unit length that a photon is removed from a beam, combining all the above effects. A beam of photons with initial intensity $\mathcal{I}_0$ has an intensity $\mathcal{I}(x)$ after traversing a thickness $\mathrm{d}x$ of material, given by

$$\mathcal{I}(x) = \mathcal{I}_0 \exp\left(- \int \mu(x) \mathrm{d}x \right) \,. \tag{3.9}$$

The reciprocal of μ is the mean-free-path λ. Conventionally, the mass attenuation coefficient

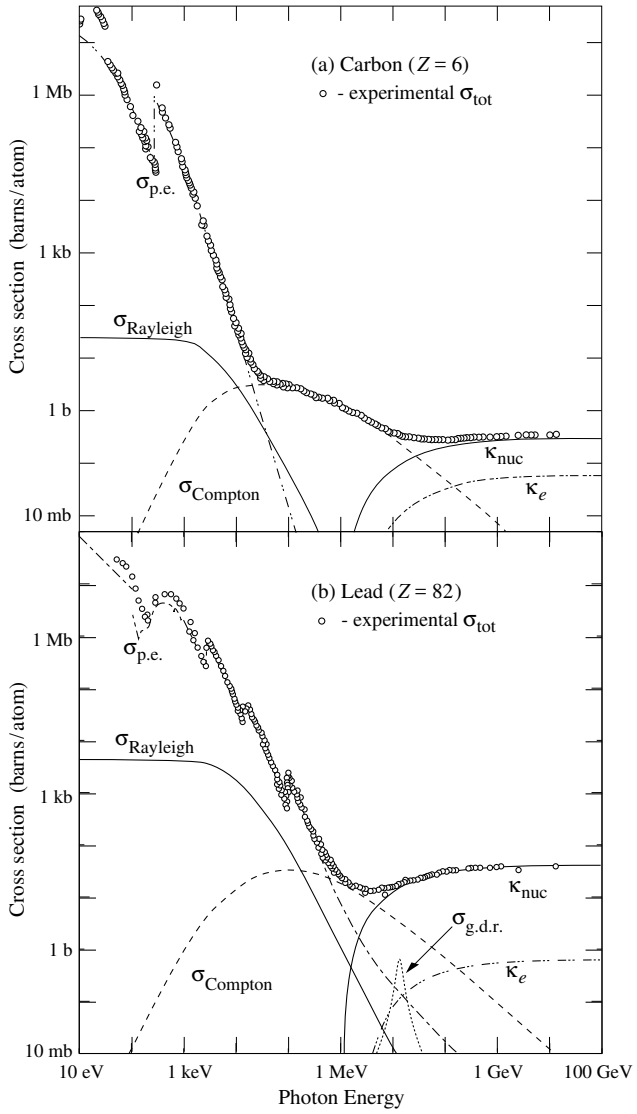

Figure 3.2: Photon interaction cross sections in carbon and lead as a function of energy. The open circles show the total cross section while the other processes are labelled: $\sigma_{\text{p.e.}}$ photoabsorption; σ_{Rayleigh} Coherent (Rayleigh) scattering; σ_{Compton} Incoherent (Compton) scattering; κ_{nuc} Pair production in nuclear field; κ_e Pair production in electron field; and $\sigma_{g.d.r}$ Photonuclear interactions. Figure reproduced from Ref. [27].

is defined μ_ρ which is the ratio of μ and the density of the medium ρ:

$$\mu_\rho = \frac{\mu}{\rho}\,. \tag{3.10}$$

The mass attenuation coefficient is related to the total photon interaction cross section per

atom σ_{tot} by

$$\mu_\rho = \sigma_{\text{tot}} \frac{N_A}{m_r}\,, \tag{3.11}$$

where m_r is the atomic mass of the target atom in grams per mole. μ_ρ is independent of the medium's physical state, and for a compound or mixture is the sum of individual component's μ_ρ weighted by their relative masses in the mixture.

Photoelectric absorption

A photon interacting with an atom can undergo photoelectric absorption, which is the dominant interaction at low energy. In this process, which is shown in Fig. 3.3, the photon loses its entire energy E_γ to the atom, causing an electron to be ejected with kinetic energy E_e given by

$$E_e = E_\gamma - E_b, \tag{3.12}$$

where E_b is the electron binding energy. The atom is then left ionised and either absorbs a free electron from the medium to be neutralised or electrons from weaker-bound shells will occupy the vacancy, causing the emission of either a characteristic X ray or Auger electrons. It is possible that the X ray can escape the medium, resulting in a total energy less than E_γ being deposited in the medium. This can result in an *escape peak* being observed in a particle detector - a second peak in the measured energy spectrum at a characteristic energy below the full energy peak.

The photoelectric absorption cross section $\sigma_{\text{p.e}}$ is strongly dependent on the atomic number Z of the target atom, as can be seen in Fig. 3.2, and increases with decreasing energy;

$$\sigma_{\text{p.e.}} \propto \frac{Z^n}{E_\gamma^{3.5}}\,, \tag{3.13}$$

where n is between 4 and 5, varying with energy [115]. The sharp discontinuities visible

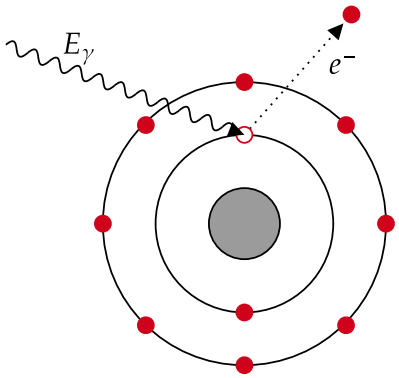

Figure 3.3: Sketch of photoelectric absorption.

in $\sigma_{\text{p.e}}$ arise when the photon energy reaches the binding energy of an electron shell; above this point, known as an absorption edge, the photon has sufficient energy to undergo the photoelectric interaction where an electron in that shell is ejected. The highest energy absorption edge will be that corresponding K shell electron binding energy.

Compton Scattering

A photon can interact with an electron in the medium, scattering through an angle θ and transferring a portion of its energy to the electron as depicted in Fig. 3.4. The energy given to the electron is

$$E_e = E_\gamma \left(1 - \frac{1}{1 + \frac{E_\gamma}{m_e c^2}(1 - \cos\theta)} \right) , \tag{3.14}$$

where $m_e z$ is the mass of the electron. As this interaction occurs with the electrons, the cross section is proportional to Z. The Klein-Nishina formula predicts the angular distribution for the scattering, which tends to forward scattering as photon energy is increased [116, 117].

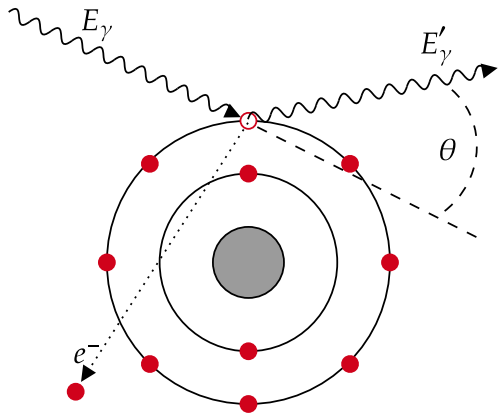

Figure 3.4: Sketch of a Compton scatting interaction, showing the photon scattered through an angle θ, ejecting an electron from the atom.

Pair Production

A photon with energy twice the mass of an electron ($2m_e = 1.022$ MeV) may undergo pair production. The photon converts into an electron and a positron, which share the remaining energy of the photon after subtracting the mass of the particles. This process must occur in the vicinity of an atomic nucleus or an electron in order to conserve momentum; the latter having a higher threshold energy and the name 'Triplet production' due to the additional electron which is ejected. Typically, the positron rapidly loses its kinetic energy and annihilates with an electron in the medium. The two 511 keV photons produced may then go on to interact or escape the medium. The process is shown in Fig. 3.5.

3.1.4 Neutrons

Neutrons have no electrical charge, so are unable to interact electromagnetically. However, they may interact with the atomic nucleus in a variety of ways depending on their energy. Neutrons will scatter in a medium multiple times and, unless they are absorbed, they will eventually reach thermal kinetic energies of approximately 25 meV.

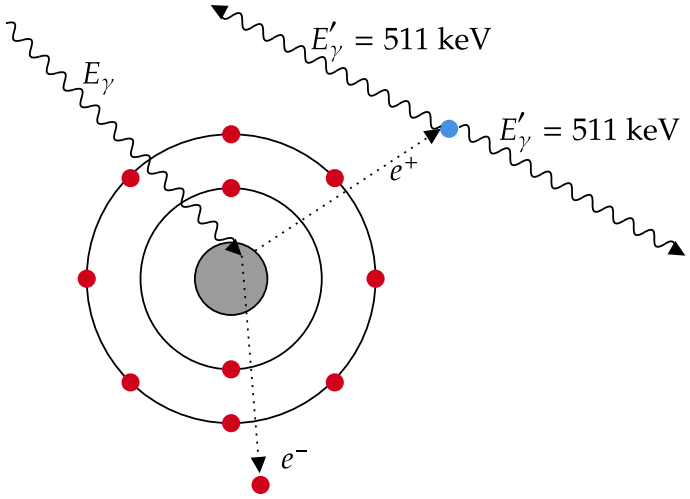

Figure 3.5: Sketch of pair production in the vicinity of an atomic nucleus, followed by the subsequent annihilation of the produced positron.

Neutrons with energies of around 1 MeV and greater are known as fast neutrons. An example source of fast neutrons is the spontaneous fission of a nucleus, such as californium-252. Fast neutrons interacting with a nucleus may undergo reactions such as (n, α) and (n, p), and usually result in neutron-deficient nuclei that decay via beta plus decay or electron capture. Fast neutrons of sufficiently high energy can undergo inelastic scattering, exciting the nucleus and resulting in the emission of gamma rays when it deexcites. The neutron can lose a significant fraction of its energy in this interaction. Neutrons can also lose a significant, although smaller, fraction of their energy by elastically scattering on a nucleus, which it may do many times gradually reducing its kinetic energy in a process known as moderation. Similarly to Eq. 2.29, the greatest energy transfers occur when the nucleus' mass is similar to that of the neutron. For instance, the neutron may lose all of its kinetic energy in a single collision with a hydrogen nucleus. Thus, the lightest nuclei are best suited for moderators. In both elastic and inelastic scattering, the recoil nucleus may go on to deposit its kinetic energy in the material.

As the neutron kinetic energy is reduced by moderation, some nuclear interactions become energetically prohibited until eventually only interactions with a positive Q-value (exothermic reactions) may take place. These are neutron capture processes, and the most probable is

generally radiative capture (n,γ), although, others are possible. The cross section for neutron capture is proportional to the inverse of the neutron velocity, however, peaks in the cross section are observed at certain neutron energies when the sum of the neutron binding energy and its kinetic energy equal to the energy of an excited state in the nucleus.

3.2 Gaseous Detectors

3.2.1 Gas Ionisation

Particles interacting with the gas in a detector can produce electron ion pairs through the interactions described previously. These processes can be grouped into *direct* and *indirect* processes. The interacting particle may directly ionise the gas through interactions with the gas molecules. In this case, the mean-free-path of the initial particle λ is equal to $1/(n_e\sigma)$, where n_e is the electron number density and σ is the interaction cross section. As the interactions in a path length L are random and independent, and have mean number L/λ, the simplest model for the primary number of generated electron-ion pairs N_p would be a Poisson distribution,

$$P(L/\lambda \,|\, N_p) = \frac{(L/\lambda)^{N_p}}{N_p!}\mathrm{e}^{-L/\lambda}\,. \tag{3.15}$$

Electron-ion pairs may also be produced by the interacting particle indirectly, referred to as secondary ionisation. One method of this is additional ionisation induced by δ-electrons. Another method is the excitation of atoms in the gas. The excited atom may deexcite, emitting photons that can cause ionisation, or it can interact with another atom in the gas and cause further ionisation. An example of the latter case is the Penning effect [118], where

an excited atom in the gas A^* interacts with a second atom B, leaving the latter ionised,

$$A^* + B \rightarrow A + B^+ + e^- . \tag{3.16}$$

This process can only occur when the excited energy of A^* is greater than the ionisation energy of B. Penning ionisation can also occur if the excited atom interacts with a second excited atom and its ionisation is less than twice the excitation energy. This is the case with noble gases [119], and the process is represented by,

$$A^* + A^* \rightarrow A + A^+ + e^- . \tag{3.17}$$

An alternative process is associative ionisation, where an ionic dimer is formed instead,

$$A^* + A^* \rightarrow A_2^+ + e^- , \tag{3.18}$$

$$A^* + A \rightarrow A_2^* \rightarrow A_2^+ + e^- . \tag{3.19}$$

The total number of electron-ion pair produced N_T is sum of those produced directly and indirectly.

There are also energy loss mechanisms that do not lead to ionisation in the detector, such as the excitation of vibrational or rotational degrees of freedom of a molecule. The portion of energy deposited by the interacting particle that goes into these processes is not seen by a detector looking only at ionisation. The average energy required to produce an electron-ion pair is quantified by the W-value W which is related to the average total number of electron-ion pairs $\overline{N_T}$ by

$$W = \frac{\Delta E}{\overline{N_T}} , \tag{3.20}$$

where ΔE is the energy deposited by the interacting particle. Values of W are shown for various gases in Table 3.1.

Table 3.1: First ionisation energy [120] and W for α particles ($E \sim 5-6$ MeV) and electrons ($E \sim \mathcal{O}(100$ keV) [109] in various gases. The total number N_T and number of primary electron-ion pairs N_P produced per centimetre for a MIP traversing the gas at 1 atmosphere pressure are also shown. Compiled from data in Ref. [107].

Gas	First Ionisation Energy [eV]	W[eV]		N_p [cm^{-1}]	N_T [cm^{-1}]
		α	e		
H_2	15.4	36.4	36.5	5.2	9.2
N_2	15.6	36.4	34.8	∼10	56
Ar	15.8	26.3	26.4	29.4	94
CH_4	12.6	29.1	27.3	∼34	91
CO_2	13.8	34.2	33.0	16	56
C_4H_10	10.5	26.0	23.4	∼46	195

It should be noted that W depends on the interacting particle species and its kinetic energy, as well as the gas, which will be discussed further in Chapter 5.

3.2.2 Fluctuations in Primary Ionisation

In the simplest case where the formation of each primary electron-ion pair is considered a Poisson process, as in Eq. 3.15, the variance on the number of electron-ion pairs is,

$$\sigma_N^2 = N\,. \tag{3.21}$$

However, the fluctuation in N is experimentally observed to be less than this. Fano introduced an empirical factor to account for this [113];

$$\sigma_N^2 = FN\,. \tag{3.22}$$

In the case that the Fano factor F is unity, then the variance of Poisson statistics is recovered.

3.2.3 Drift of Electrons and Ions

For a particle of mass m and charge q moving in an electric and magnetic fields, $\boldsymbol{E}$ and $\boldsymbol{B}$, with velocity $\boldsymbol{v}$, the equation of motion is given by the Lorentz force,

$$m\frac{\mathrm{d}\boldsymbol{v}}{\mathrm{d}t} = q\boldsymbol{E} + q(\boldsymbol{v}\times\boldsymbol{B}) - k\boldsymbol{v}\,. \tag{3.23}$$

The magnetic field is neglected in what follows, but a more complete treatment may be found in several sources, e.g. Ref. [119]. The last term in Eq. 3.23 describes the collisions of the charged particle with the gas as a frictional force, where the quantity $m/k = \tau$ has dimensions of time. This model of a frictional force holds if we consider times much greater than the average time between collision, so that the solution is a steady state; $\mathrm{d}\boldsymbol{v}/\mathrm{d}t = 0$. In this case,

$$\boldsymbol{v} = \frac{q}{m}\tau\boldsymbol{E} = \mu\boldsymbol{E}\,, \tag{3.24}$$

where

$$\mu = \frac{q}{m}\tau\,, \tag{3.25}$$

is defined as the mobility. The characteristic time τ is the mean time between collisions. It should be noted that the drift velocity varies with the ratio E/P, known as the reduced electric field, where P is the gas pressure. This means that μ scales with pressure, i.e. $\mu(P) = \mu(P_0)P_0/P$.

Electrons

The low mass of electrons m_e relative to the gas molecules means that they scatter isotropically at each collision. Between collisions, the electron will drift under the influence of the electric field and acquire a velocity $\boldsymbol{v}$ in addition to its instantaneous and randomly

directed velocity it had after scattering $\boldsymbol{v}_c$. At the next interaction, the electrons will again isotropically scatter loosing all preferential direction given by the last scattering, as well as the additional energy gained between the last two collisions, on average. Therefore, the mean additional velocity it gains between collisions is observed as the drift velocity of the electrons. Fig. 3.6 shows the electron drift velocity in various gases. In very low magnitude electric fields, the drift velocity can be calculated using Eq. 3.24 with a constant μ. However, at reduced-electric fields generally used in particle detectors, more complex behaviour is observed in $\boldsymbol{v}$, where it can be seen to plateau, or even fall, as the reduced electric field is increased. This is due to the underlying microscopic behaviour of the electron interactions, such as the minimum in the scattering cross section known as the Ramsauer minimum [119, 115].

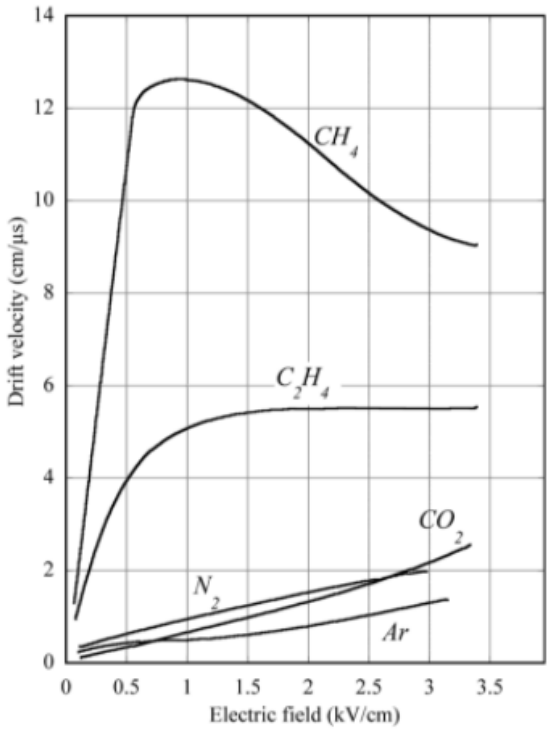

Figure 3.6: Electron drift velocity as a function of electric field magnitude in pure gases at $20°C$ and 1 atm. Figure reproduced from Ref. [121].

The drift velocity can be heuristically related to the underlying microscopic processes. The

mean time between collision may be written as a collision rate R_e per electron, which is the product of the number density of gas molecules n, the interaction cross section σ and the electron's velocity v_c;

$$R_e = \frac{1}{\tau} = n\sigma v_c \,. \tag{3.26}$$

In practise, the gas pressure p is a more convenient variable than the number density, and they are related by the ideal gas law

$$p = nk_BT \,, \tag{3.27}$$

with k_B and T being the Boltzmann constant and temperature, respectively.

The velocity v_c can be found by considering the total kinetic energy of the electron, which will have a contribution from the acceleration in the electric field between collisions ε_E and a contribution from the thermal energy $\frac{3}{2}k_BT$. The latter comes from the application of equipartition theorem to the electron, which has three degrees of freedom. For reference, for $T = 273.15$ K, $\frac{3}{2}k_BT \approx 0.035$ eV. The velocity can then be related to the two energy contributions by

$$\frac{1}{2}m_e v_c^2 = \varepsilon_E + \frac{3}{2}k_BT \,. \tag{3.28}$$

In order to compute ε_E, consider the number of collisions ξ for the electron drifting over a distance d; $\xi = d/(v\tau)$. Considering that the electron loses an average fractional energy f at each collision, the total energy loss over d is ξf. In the same distance, the electron has gained an energy eEd from the electric field E, assuming E does not significantly change over d. Therefore, the net energy gained by the electron is given by

$$\varepsilon_E = \frac{eEd}{\xi f} \,. \tag{3.29}$$

In typical detector operating conditions, drifting electrons generally have $\varepsilon_E \gg \frac{3}{2}k_BT$, so

Eqs. 3.26, 3.28 and 3.29 can be combined with Eq. 3.24 to write the drift velocity as

$$v^2 = \frac{eE}{m_e n \sigma}\sqrt{\frac{f}{2}}\,. \tag{3.30}$$

Both σ and λ are functions of the energy of the drifting electron and so the magnitude of the electric field.

In gas mixtures with i components, each with number densities n_i, the cross section and fractional energy loss per collision can be calculated as

$$\sigma = \frac{1}{n}\sum n_i \sigma_i \tag{3.31}$$

$$f\sigma = \frac{1}{n}\sum n_i \sigma_i f_i\,, \tag{3.32}$$

where the total number density is the sum over all components $n = \sum n_i$.

3.2.4 Ions

For ions drifting in a gas, the energy lost at each collision is much greater than in the case of electrons and their direction is not randomised. Following a collision, the velocity of the ion will have a randomised components $\boldsymbol{v}_r$ and a component in the drift direction $\boldsymbol{v}_d$. Up until the next collision, an average time of τ later, the ion of mass m_i will gain an additional velocity $\boldsymbol{v}_f = q\boldsymbol{E}\tau/m_i$ from its acceleration in the electric field. The drift velocity $\boldsymbol{v}$ is the sum of $\boldsymbol{v}_f$ and $\boldsymbol{v}_d$. As $\boldsymbol{v}_d$ is the velocity remaining in the drift direction after a collision, it will be proportional to $\boldsymbol{v}_f$ with constant of proportionality g related to the fractional momentum

loss in the collision. Thus,

$$\begin{aligned} \boldsymbol{v} &= \boldsymbol{v}_f(1+g) = \boldsymbol{v}_f g' \\ &= \frac{q\boldsymbol{E}\tau}{m_i} g' \,. \end{aligned} \tag{3.33}$$

As the ion and gas molecule have similar mass, the velocity in Eq, 3.26 becomes the relative velocity between the ion and gas molecule v_{rel}. In typical pressures and electric fields, the thermal energy dominates for the ions, so v_{rel} can be written as the average difference of the random ion v_i and gas molecule v_g velocities,

$$v_{\text{rel}}^2 = v_i^2 + v_g^2 \tag{3.34}$$

$$= 3k_B T \left(\frac{1}{m_i} + \frac{1}{m_g} \right) , \tag{3.35}$$

where equipartition theorem has been applied to get Eq. 3.35 and m_g is the mass of the gas molecule. The factor $\left(\frac{1}{m_i} + \frac{1}{m_g}\right)$ is the reduced mass of the ion-gas molecule system. Combining Eq. 3.26, Eq. 3.33, and Eq. 3.35, the ion drift velocity can be written as,

$$v = g' \left(\frac{1}{m_i} + \frac{1}{m_g} \right)^{1/2} \left(\frac{1}{3k_B T} \right)^{1/2} \frac{qE}{N\sigma} \,. \tag{3.36}$$

Unlike in the electron case, the drift velocity is proportional to E, meaning the mobility is independent of E. In practise, μ is found to be a constant over a wide range of operating pressures and electric fields, as shown in Fig. 3.7. Table 3.2 has the mobility for various ions in common gases.

In a gas composed of components i with individual number densities n_i, the drift velocity of

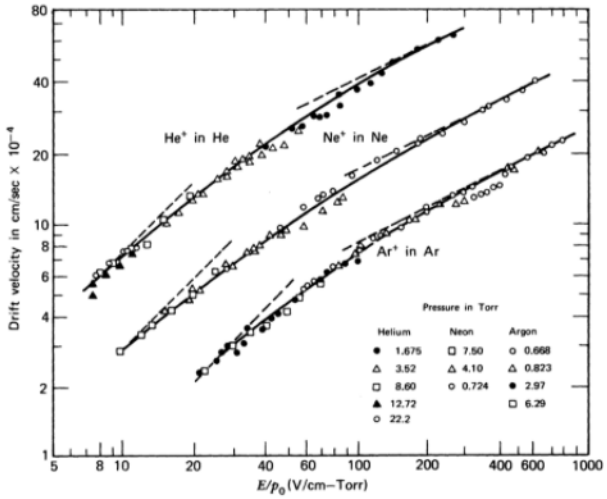

Figure 3.7: Drift velocity as a function of reduced electric field for several ions in their own gas. Figure reproduced from Ref. [121].

Table 3.2: Measured ion mobility for several ions in different gases. Compiled from data in Ref. [119].

Gas	Ion	Mobility $[\mathrm{cm^2\,V^{-1}\,s^{-1}}]$
He	He^+	10.40
Ne	Ne^+	4.14
Ar	Ar^+	1.53
Ar	$[CH_4]^+$	1.87
Ar	$[C_4H_{10}]^+$	1.56
CH_4	$[CH_4]^+$	2.26
C_4H_{10}	$[C_4H_{10}]^+$	0.61

one ion species can be determined using Blanc's law:

$$\frac{1}{v} = \frac{1}{n}\sum \frac{n_i}{v_i}\,, \tag{3.37}$$

where v_i is the drift velocity of the ion in pure gas i with number density n.

3.2.5 Diffusion of Electrons and Ions

In the absence of an electric field, electrons and ions generated by ionisation will collide with gas molecules and quickly lose their energy. As each particle has three degrees of freedom, by equipartition theorem, their average energy will be $\frac{3}{2}k_BT$. They will assume a thermal energy distribution given by the Maxwell-Boltzmann distribution,

$$f(E) = \frac{2}{\sqrt{\pi}\sqrt{E}}\left(\frac{1}{k_BT}\right)^{3/2}\exp\left(-\frac{E}{k_BT}\right), \tag{3.38}$$

where E is the energy of the particle. After some time t, the distribution of the charges in one dimension x will be given by,

$$\frac{\mathrm{d}N}{\mathrm{d}x} = \left(\frac{N_0}{\sqrt{4\pi Dt}}\right)\exp\left(\frac{-x^2}{4Dt}\right), \tag{3.39}$$

where D is the diffusion coefficient. In one dimension, the standard deviation of the particles from the centre is

$$\sigma_x = \sqrt{2Dt}\,. \tag{3.40}$$

When the energy of the diffusing particles is dominated by thermal energy $\frac{3}{2}k_BT$, the diffusion is related to the mobility through the Nernst-Townsend formula,

$$\frac{D}{\mu} = \frac{k_BT}{q}, \tag{3.41}$$

where q is the particles charge. Substituting Eq. 3.41 into Eq. 3.42, the standard deviation of particles drifting a distance x can be related to the electric field magnitude E,

$$\sigma_x = \sqrt{\frac{2Dx}{\mu E}} = \sqrt{\frac{2xk_BT}{\mu qE}}\,. \tag{3.42}$$

In practise, the diffusion along the drift direction - the longitudinal diffusion - is different from that perpendicular to the drift - the transverse diffusion [119]. In the case of ions in high electric fields, their similar mass to the gas molecules means they do not scatter isotropically, and so retain some component of velocity in the drift direction. This causes the longitudinal diffusion to be higher than the transverse. In the case of electrons, it has been shown that their energy is higher at the leading edge of the diffusion cloud, which results in a change in μ over the cloud. The net result is a reduction in the longitudinal diffusion.

3.2.6 Electron Loss Mechanisms

It is important that the generated electrons remain free for long enough to generate a measurable signal. One method that these electrons may be removed is when they combine with a positive ion to form a neutral molecule may, known as electron recombination. The rate of electron recombination R_{rc} depends on the local number density of electrons n_e and ions n_+ and is related by the recombination coefficient α_{rc};

$$R_{\mathrm{rc}} = \frac{\mathrm{d}n_e}{\mathrm{d}t} = \frac{\mathrm{d}n_+}{\mathrm{d}t} = -\alpha_{\mathrm{rc}} n_e n_+ \,. \tag{3.43}$$

Columnar recombination occurs along the ionisation trail left by a charged particle traversing the gas, and so is dependent on the density of the initial ionisation. For instance, this is more prolific in the case of alpha particles, which are more densely ionising compared to electrons. Volume recombination on the other hand occurs due to high numbers of free electrons and ions throughout the gas volume due to a high rate of charged particles interacting in the gas.

Electrons may also be lost through attachment to molecules in the gas forming negative ions. Electronegative molecules, such as halogen-containing molecules and oxygen, are primarily responsible for this process. The rate electrons collisions with electronegative molecules is

given by the product of the contamination fraction of electronegative gas κ and the total interaction rate R_e, given by Eq. 3.26. If the probability of such an interaction resulting in electron attachment is h, then for electrons with drift velocity v, the probability of electron attachment per unit length is,

$$\eta = \frac{v}{h\kappa R_e} \,. \tag{3.44}$$

It should be noted that h is a function of the electron energy, and so electric field magnitude, and so η is a function of the electric field through h, v and R. If there are initially n_0 electrons at a point x_1, then after a distance $x_2 - x_1$ there will be n electrons remaining, given by

$$n = n_0 \exp\left(-\int_{x_1}^{x_2} \eta(x)\mathrm{d}x\right) \,. \tag{3.45}$$

It is therefore critical to control contamination the of oxygen and water in the gas to prevent significant loss of signal. Fig. 3.8 shows the attachment coefficient for various contamination of O_2 in gas as calculated using Magboltz [122, 123].

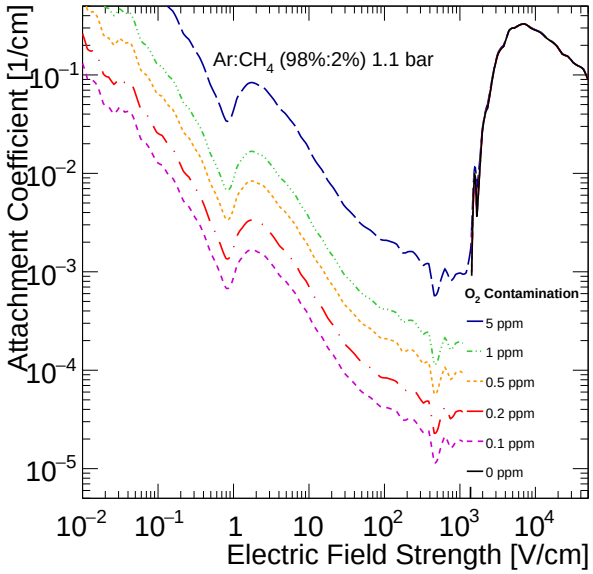

Figure 3.8: Attachment coefficient as a function of electric field strength in 1.1 bar Ar:CH_4 gas for various amounts of contamination with O_2 as calculated using Magboltz.

3.2.7 Charge Multiplication

In sufficiently high electric fields, the energy gained by an electron between collisions can be sufficient to induce further ionisation. The first Townsend coefficient α represents the number of electron ion pairs generated per unit length. Starting with one free electron, after a distance α^{-1}, statistically, an electron ion pair will have been produced; two electrons are then drifting. After another α^{-1}, each electron has produced an electron ion pair, and this process continues with each new electron generation. Due to the $\mathcal{O}(10^3)$ higher drift velocity of the electrons, the electrons quickly move away from the ions leaving an 'avalanche' of electrons proceeding at the front with the slower ions forming a tail. The Townsend avalanche continues over a distance $\mathrm{d}x$, leading to an increase in the number of electrons n of

$$\mathrm{d}n = n\alpha(x)\mathrm{d}x. \tag{3.46}$$

The avalanche multiplication factor, or gain, M is defined as the ratio n/n_0, where n_0 is the number of initial electrons. M is calculated by integrating Eq. 3.47 over the avalanche distance between x_1 and x_2,

$$\begin{aligned} n &= n_0 \exp\left(\int_{x_1}^{x_2} \alpha(x)\mathrm{d}x\right) \\ M &= \exp\left(\int_{x_1}^{x_2} \alpha(x)\mathrm{d}x\right). \end{aligned} \tag{3.47}$$

α is a function of both the gas pressure and electric field, and at fixed reduced electric field scales proportionally to the change in pressure, and is shown in Fig. 3.9. An analytical form for α would allow the calculation of the gain in a given gas. Several parameterisations for α

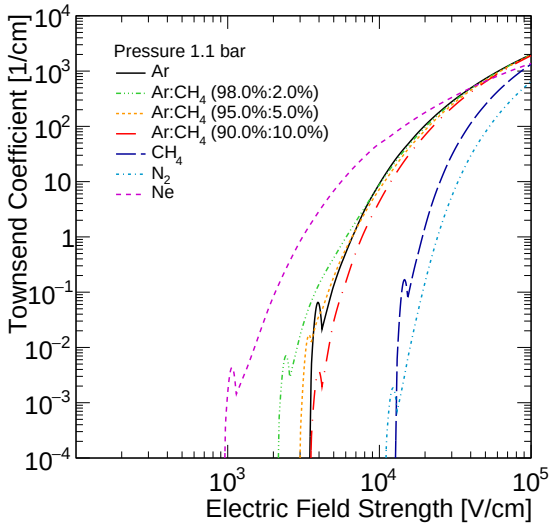

Figure 3.9: First Townsend coefficient computed using Magboltz in pure neon, nitrogen, argon, pure methane and several common mixtures of the argon and methane.

exist [124], however, a common one is [125, 126, 127, 128],

$$\alpha = pA \exp\left(-B\frac{p}{E}\right) , \tag{3.48}$$

where A, B are constants related to the mean free path of the electron, the electron's instantaneous velocity and drift velocity, and to the average energy gained by the electron in the field, respectively [128]. Values for these constants can be found in Table 3.3 for several gases.

The gain cannot be increased indefinitely because of secondary processes which are detailed in Section 3.2.8. This physical limit on the gain is found to be approximately $M < 10^8$ or $\int_{x_1}^{x_2} \alpha(x)\mathrm{d}x < 20$, known as the Raether limit.

While Eq. 3.47 defines the mean gain, the avalanche process is subject to statistical fluctuations resulting in deviations from this. Under the assumption that the probability for an electron to ionise is independent of its history, the probability for the avalanche of a single

Table 3.3: Values of A, and B for Eq. 3.48 in several gases. σ_r is the relative standard deviation of the experimental data from the parameterisation over the ranges specified. From compilation in Ref. [128]

Gas	E/P range [V cm^{-1} mbar^{-1}]	α/P range [cm^{-1} mbar^{-1}]	A [cm^{-1} mbar^{-1}]	B [V cm^{-1} mbar^{-1}]	σ_r [%]
Ar	≤ 40	≤ 0.5	2.011	54.7	2.5
	40-140	0.5-2.9	6.055	101.3	4.9
N_2	≤ 110	≤ 0.8	4.482	196.5	1.8
	110-700	0.76-7.1	10.777	290.0	3.2
CH_4	≤ 25	≤ 0.01	26.315	193.5	6.0
	25-150	0.01-2.5	7.866	173.8	1.0
C_4H_{10}	≤ 100	≤ 1	19.579	300.1	1.0
Ar:CH_4 (98%:2%)	20-50	0.4-1.7	4.458	50.9	6.0
Ar:CH_4 (90%:10%)	26-50	0.6-1.5	4.551	55.8	4.0

electron to produce n electrons, $P(n)$, is given by the Furry distribution [119],

$$P(n) = \frac{1}{M} \exp\left(-\frac{n}{M}\right) . \tag{3.49}$$

For high values of M and high reduced electric fields, $P(n)$ is better described by the Polya distribution,

$$P(n) = \frac{1}{M} \frac{(1+\theta)^{1+\theta}}{\Gamma(1+\theta)} \left(\frac{n}{M}\right)^{\theta} \exp\left(-(1+\theta)\frac{n}{M}\right) , \tag{3.50}$$

which has variance

$$\sigma^2 = \frac{M^2}{1+\theta} . \tag{3.51}$$

Γ is the gamma function, $\Gamma(y) = \int_0^\infty x^{y-1} \exp(-x) \mathrm{d}x$. The parameter θ defines the shape of the distribution, where the Furry distribution is recovered when $\theta = 0$. As θ is increased, the distribution tends to a Normal distribution. The Polya distribution is shown for various values of n in Fig. 3.10. If the avalanches of individual electrons are considered independent, then for n_0 electrons undergoing avalanches $P(n)$ is given by the convolution of n_0 Polya

distributions,

$$P(n|n_0) = \frac{1}{M}\left(\frac{(1+\theta)^{1+\theta}}{\Gamma(1+\theta)}\right)^{n_0}\left(\frac{n}{M}\right)^{n_0(\theta+1)-1}\exp\left(-(1+\theta)\frac{n}{M}\right) \times \prod_{i=1}^{n_0-1}\frac{\Gamma(i+i\theta)\Gamma(1+\theta)}{\Gamma((i+i\theta)\cdot(1+\theta))}\,. \tag{3.52}$$

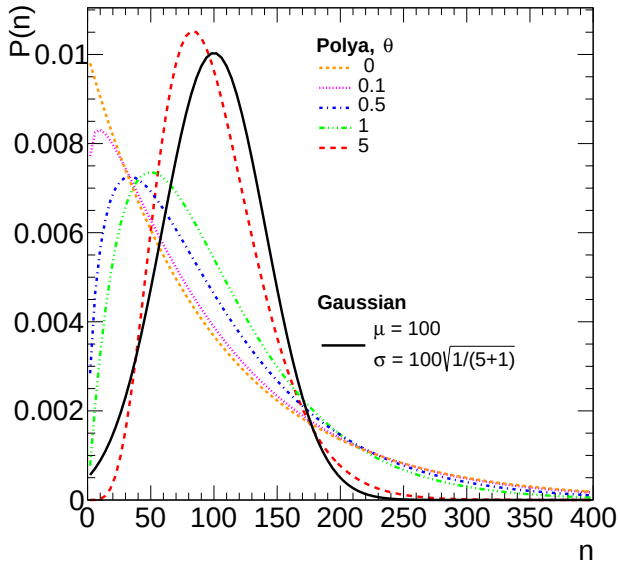

Figure 3.10: Polya distribution for various values of n for $M = 100$. A Gaussian distribution with mean $\mu = 100$ and standard deviation σ given by Eqn. 3.51 is included for comparison to the $\theta = 5$ Polya distribution.

3.2.8 Modes of Gaseous Detector Operation

A gaseous detector can be operated in one or more of several modes depending on the applied voltage at the collection electrode. These are summarised in Fig. 3.11 which shows the charge collected as a function of the applied voltage for two interactions in the gas depositing different amounts of initial energy ($E_1 > E_2$). For the lowest voltages, the electric field is insufficient to drift all of the initial charges before they are lost by recombination. As such, the collected charge is less than the initial number of electron ion pairs generated. As the

voltage is increased, the charge collection become more efficient, overcoming recombination, until the total initial charge is collected. This region of ion saturation is the operational condition of an ionisation chamber.

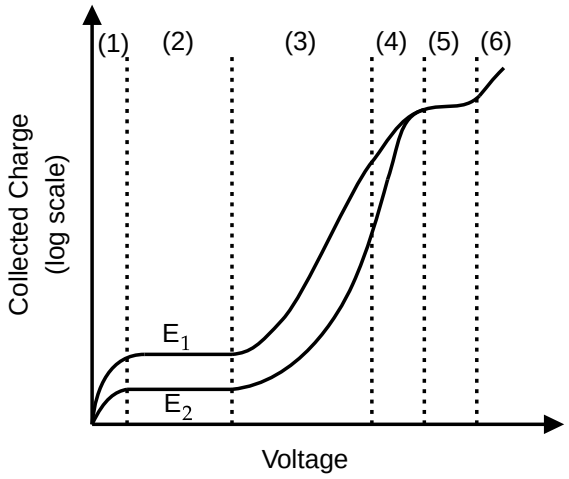

Figure 3.11: Modes of detector operation for gaseous detectors. The collected charge is plotted as a function of voltage for two different energies deposited in the gas ($E_1 > E_2$). The labels regions are: (1) recombination before total charge collection; (2) ionisation mode; (3) proportional mode; (4) region of limited proportionality; (4) Geiger-Müller mode; (5) discharge region.

Increasing the voltage further, the electric field becomes sufficiently large for avalanche multiplication to occur, resulting in an increase in the collected charge to increase. Over a range of voltages, the multiplication remains linear and the recorded charge will be proportional to the initial number of electron ion pairs. This is the region in which the proportional counters operate. Non-linear effects can affect this operational mode. Two effects mainly contribute to this loss of linearity: accumulation of positive ions near the anode and secondary avalanches caused by photoemission in the avalanches and by neutralising ions at the cathode. While the electrons generated in the avalanche are quickly collected at the anode, the $\mathcal{O}(10^{-3})$) slower drift velocity of the ions means they can take from milliseconds to seconds to reach the cathode. In high avalanche gains, the positive ions in the vicinity of the anode can reduce the magnitude of the electric field around the anode, reducing the avalanche gain of

a subsequent avalanche. This is known as the *space-charge effect* and becomes an increasing problem as the voltage is increased.

The second process originates from the fact that ionised and excited atoms are formed during the avalanche. For noble gas atoms, the return to the ground state is possible only through photon emission. If these photons have an energy above the ionisation energy of another gas component or the cathode material they can cause the extraction of more electrons. If these photons interact and cause the liberation of an electron at a distance further from the anode than the start of the avalanche then a second, independent avalanche will be generated by this electron. Additionally, the ions generated by the avalanche will drift toward the cathode. Upon reaching it they will be neutralised by extracting an electron from the cathode. In order to balance the energy, this also results in either the emission of a photon or the secondary emission of an electron from the cathode; both having the potential to generate a second, independent avalanche. As the voltage, and so gain, is increased, there comes a point where these processes can result in the continuous discharge of the detector, resulting in a limit to the operational gain of a proportional counter.

However, in polyatomic molecules the behaviour is different. The additional rotational and vibrational degrees of freedom introduced allow for non-radiative excited states. The dissipation of this energy is done through either elastic collisions or dissociation. Thus, the interaction of a photon from the avalanche with such a gas molecule reduces the probability of secondary electron emission. Similarly, an ionised polyatomic molecule being neutralised at the cathode is more likely to recombine with other ionised molecules to form more complicated molecules or even polymerise, than to undergo secondary emission. This property is possessed by most hydrocarbons, alcohol vapours and many organic compounds.

There is an efficient charge exchange in collisions of gaseous molecule that results in only the ion species with the lowest ionisation energy remaining. Noble gases typically have a higher

ionisation energy than polyatomic molecules, and so, in a gas mixture containing both gases, noble gas ions are quickly neutralised by transferring their charge to the polyatomic molecule. Thus, the introduction of a small amount of *quencher* gas is typical for proportional counters in order to suppress secondary avalanches.

As the voltage is increased further, the non-linear effects begin to prevail and result in a region of limited proportionality. At still higher voltages, these processes become completely dominant. The photoemission propagates avalanches which cease only when enough positive ions have been generated to reduce the electric field below the threshold for subsequent avalanches. At this point the signal generated is no longer proportional to the initial ionisation but is instead a constant due to its self-limiting nature. This is the mode in which Geiger-Müller detectors operate. At voltages beyond this, there is a complete breakdown of the gas which cause sparks.

3.2.9 Signal Formation

The movement of charges in the detector induces a current in the electrode which may then be read out. Fig 3.12 shows a particle of electric charge q moving in the vicinity of a set of electrodes, each at voltage V_i, the charge induced on each will be $Q_i(t)$, dependent on the particle's velocity $\boldsymbol{v} = \mathrm{d}\boldsymbol{r}/\mathrm{d}t$. The instantaneous current I induced on electrode i may be calculated using the Shockley-Ramo theorem,

$$I_i = -q\frac{{}_w\boldsymbol{E}_i \cdot \boldsymbol{v}}{{}_wV_i}\,, \tag{3.53}$$

where ${}_w\boldsymbol{E}_i$, known as the weighting field, is the electric field at the position of the charge in the case that electrode i is at a voltage ${}_wV_i$ and all other electrodes are grounded and the charge is not present.

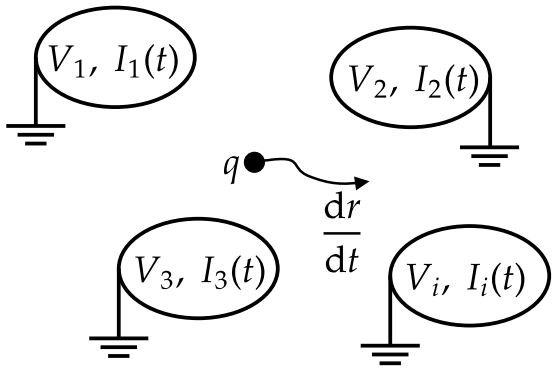

Figure 3.12: A charge q moving in the vicinity of a set of electrodes and inducing a current I_i on each of them that may be computed using Shockley-Ramo theorem.

3.3 The Spherical Proportional Counter

The spherical proportional counter [129, 130] is a gaseous detector comprising a grounded, metallic, spherical shell that acts as a cathode and a high-voltage central anode structure, as shown in Fig 3.13. The anode radius is chosen to be $\mathcal{O}(\mathrm{mm})$ to give a high electric field at its surface, and so provide gain. Particles interacting in the gas may cause ionisation either directly, through recoils induced by collisions with nuclei or electrons, or through secondary reaction products. Electrons generated by ionisation drift under the influence of the electric field toward the anode. Within approximately 1 mm of the anode the electric field is large enough that the electrons have sufficient energy to induce further ionisation, causing a Townsend avalanche. While the electrons produced by the avalanche almost immediately reach the anode, the ions may take seconds to drift to the cathode, generating a measurable current in the anode.

Approximating the detector as two concentric spheres, the anode and cathode, with radii r_a and r_c, respectively, the electric field is purely radial $\hat{\boldsymbol{r}}$. In this case, the electric field $\boldsymbol{E}(\boldsymbol{r})$

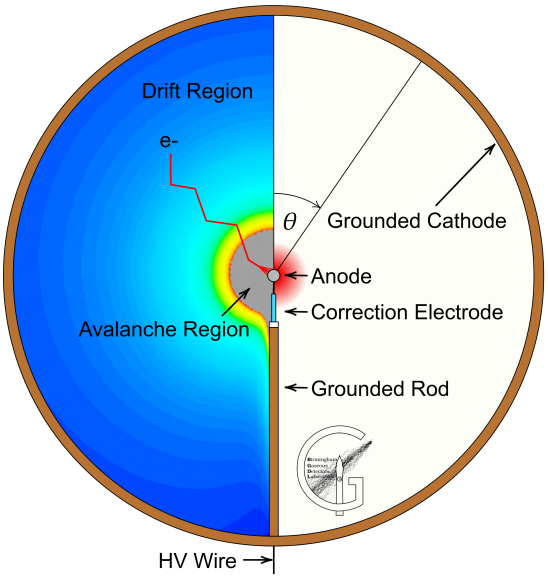

Figure 3.13: A schematic of the spherical proportional counter and the generation of an avalanche from a primary electron. Figure reproduced from Ref. [3].

may be calculated through the use of Gauss' law,

$$\oiint_S \boldsymbol{E} \cdot \mathrm{d}\boldsymbol{S} = \frac{Q}{\varepsilon}\,, \tag{3.54}$$

where ε is the permittivity of the material between the spheres and Q is the charge enclosed within the surface S. Performing the integration for a spherical surface and rearranging,

$$\boldsymbol{E}(r) = \frac{Q}{4\pi\varepsilon}\frac{\hat{\boldsymbol{r}}}{r^2}\,. \tag{3.55}$$

Using the relation

$$\boldsymbol{E} = -\nabla V \tag{3.56}$$

and the boundary conditions that the anode is at voltage V_0 ($V(r_a) = V_0$) and the cathode is grounded, $V(r_c) = 0$ V, the potential difference between the anode and cathode may be

written as,

$$V(r_a) - V(r_b) = V_0 = -\int_{r_c}^{r_a} \boldsymbol{E}(r) \cdot \mathrm{d}\boldsymbol{r}$$
$$V_0 = \frac{Q}{4\pi\varepsilon}\frac{1}{r}\bigg|_{r_a}^{r_c}$$
$$= \frac{Q}{4\pi\varepsilon}\frac{r_c - r_a}{r_a r_c}\,. \tag{3.57}$$

Substituting Eq. 3.57 into Eq. 3.55,

$$\boldsymbol{E}(r) = \frac{V_0}{r^2}\frac{r_a r_c}{r_c - r_a}\hat{\boldsymbol{r}}\,. \tag{3.58}$$

For a spherical proportional counter that has $r_c = 15$ cm, $r_a = 1$ mm and $V_0 = 2000$ V, the electric field magnitude at a radius of 1.1 mm (1 cm) is 1.7 kV cm^{-1} (20.1 V cm^{-1}).

As it is usually the case that $r_c \gg r_a$, a useful approximation of the field is given by the Taylor expansion of $\boldsymbol{E}(r)$ at $r_a/r_c = 0$,

$$\boldsymbol{E}(r) \approx \frac{V_0}{r^2} r_a \hat{\boldsymbol{r}}\,, \tag{3.59}$$

which is independent of r_c.

3.3.1 Gas Gain

The parameterisation of the first Townsend coefficient given by Eq. 3.48 has previously [131] been used to write an analytical expression for the gas gain in a MicroMegas detector [132]. Using Eq. 3.58, the first Townsend coefficient and gas gain in a spherical proportional counter

can be written as

$$\alpha(r) = AP \exp\left(-BP\frac{r^2}{V}\frac{r_c - r_a}{r_a r_c}\right), \tag{3.60}$$

$$M = \exp\int_{r_x}^{r_a} \alpha \mathrm{d}r\,, \tag{3.61}$$

where r_x is the radius at which the electron undergoing amplification was produced. Defining $\Delta_r = \frac{r_a r_c}{r_c - r_a}$ and performing the integral, the gain can be written as

$$\ln M = \frac{AP\sqrt{\pi}}{2\sqrt{\frac{BP}{V\Delta_r}}}\left\{\mathrm{erf}\left(\sqrt{\frac{BP}{V\Delta_r}}r_x\right) - \mathrm{erf}\left(\sqrt{\frac{BP}{V\Delta_r}}r_a\right)\right\}, \tag{3.62}$$

where erf is the error function, $\mathrm{erf}(x) = \frac{2}{\sqrt{\pi}}\int_0^x \exp\left(-z^2\right)\mathrm{d}z$.

3.3.2 Signal Formation

Current Induced in Anode

The ions produced in the avalanche will drift towards the cathode, inducing a current in the anode. As their mobility is well approximated by a constant over a wide range of electric field magnitudes, the velocity of the drifting ions can be approximated by Eq. 3.24. Rearranging Eq. 3.24 and substituting in Eq. 3.58, the mobility can be written as

$$\mu = \frac{r^2}{V}\left(\frac{r_a r_c}{r_c - r_a}\right)^{-1} v\,, \tag{3.63}$$

where the ion's instantaneous velocity v is radial $v = \mathrm{d}r/\mathrm{d}t$. Defining $\delta = \mu V r_a r_c (r_c - r_a)$ and rearranging,

$$\delta \mathrm{d}t = r^2 \mathrm{d}r\,. \tag{3.64}$$

Assuming that all ions in the avalanche are produced at $t = 0$ and at the anode surface r_a, the current induced as a function of time can be calculated. In a time t the ions have drifted to a radius r, so integrating Eq. 3.64,

$$\begin{aligned} \int_0^t \delta \mathrm{d}t &= \int_{r_a}^r r^2 \mathrm{d}r \\ t &= \frac{(r^3 - r_a^3)}{3\delta} \,. \end{aligned} \tag{3.65}$$

When $r = r_c$, t is the total drift time of the ion. For a spherical proportional counter that has $r_c = 15$ cm, $r_a = 1$ mm and $V_0 = 2000$ V, and using an ion mobility of 1.53 $\mathrm{cm^2\,V^{-1}\,s^{-1}}$ (corresponding to Ar^+ in Ar, Table 3.2), the total ion drift time is 3.6 s.

By rearranging Eq. 3.65, the ion's radius as a function of time can be computed,

$$r = \left(3\delta t + r_a^3\right)^{\frac{1}{3}} \,. \tag{3.66}$$

Applying Shockley-Ramo theorem (Eq. 3.53), and substituting in Eq. 3.58,

$$I = -\frac{q}{V_0} v(t) \frac{V_0}{r^2} \frac{r_a r_c}{r_c - r_a} \,, \tag{3.67}$$

where q is the charge of all the ions. Using Eq. 3.24 to substitute for the ion instantaneous velocity $v(t)$ and simplifying,

$$\begin{aligned} I &= -qE(r)\mu \frac{1}{r^2} \frac{r_a r_c}{r_c - r_a} \\ &= -qV_0\mu \frac{1}{r^4} \left(\frac{r_a r_c}{r_c - r_a}\right)^2 \\ &= -q\alpha\delta \frac{1}{r^4} \frac{r_a r_c}{r_c - r_a} \,. \end{aligned} \tag{3.68}$$

Combining this result with Eq. 3.66,

$$I(t) = -q\alpha\delta \frac{1}{(3\delta t + r_a^3)^{\frac{4}{3}}} \frac{r_a r_c}{r_c - r_a} \,. \tag{3.69}$$

Read-out Electronics

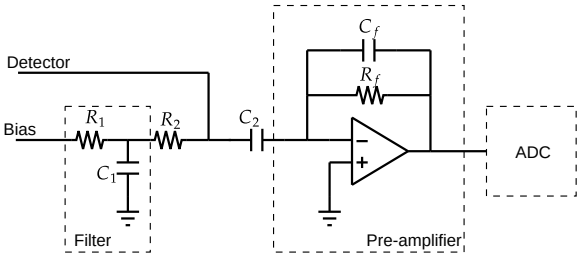

Figure 3.14: Simplified schematic of the readout electronics used with the spherical proportional counter.

In order to calculate the signal that would be measured from the induced current in Eq. 3.69, knowledge of the read-out electronics is required. The simplified read-out electronics for a typical spherical proportional counter are shown schematically in Fig. 3.14. A Direct Current (DC) bias voltage is applied to the detector by a power supply, typically the ISEG NHR 22 60r, chosen for its low ripple noise of 3 mV [133]. This is applied through a low-pass filter with cut-off frequency $\omega_0 = 1/(R_1 C_1)$, which is defined at the frequency at which the input is attenuated by 3 dB. The voltage is supplied to the detector through the bias resistance resistance R_2. The signal coming from the detector is decoupled from the bias voltage by C_2 and passed through the preamplifier. Generally, a charge-sensitive pre-amplifier is used, which, while practically more complex, is functionally similar to the operational amplifier integrator circuit shown in the dashed box in Fig. 3.14. A more complete, albeit still simplified, pre-amplifier design may be found in Ref [134]. The preamplifier integrates the current

from the detector and gives a voltage output,

$$V'_{\text{out}}(t) = -\frac{1}{C_f}\int I(t)\mathrm{d}t + \text{const.}\,. \tag{3.70}$$

This integration time is typically $\mathcal{O}(1-100$ ns). Integrating from the start of the avalanche to the time when the ions reach the cathode, the total output voltage is $V'_{out} = \frac{q}{C_f}$. Additionally, the preamplifier has some gain which is applied to the signal. The resistor R_f provides a DC feedback across the operational amplifier and discharges C_f with a time constant $\tau = R_f C_F$. This is significantly greater than the rising time, which can then be neglected, and so the preamplifier response can be parameterised by

$$R = A\exp\left(-\frac{t-t_0}{\tau}\right)\,, \tag{3.71}$$

where A represents the gain of the preamplifier in volts per unit charge. Values for τ, preamplifier gain and noise for typical preamplifier used with the spherical proportional counter are shown in Table 3.4.

The voltage output from the preamplifier is then passed to an Analogue-to-Digital Converter (ADC) which provides a digital signal to the acquisition software based on the amplitude of the voltage. Two ADCs used with the spherical proportional counter are the "CALI" and the Redpitaya STEMlab 125-14. The "CALI" digitiser was manufactured by CEA Saclay [135], with a dynamic range of ± 1.25 V over a 16 bit resolution and maximum sampling frequency of 5 MHz. The Redpitaya [136] has a dynamic range of ± 1 V over 14 bit and a sampling frequency of 40 MHz.

Table 3.4: Comparison of preamplifiers typically used with the spherical proportional counter.

Preamplifier	Gain [V pC^{-1}]	τ [µs]	Noise [electrons]	
			$C_{\text{det}} = 0$	$C_{\text{det}} = 100$ pF
CREMAT CR-110-R2 [134]	1.4	140	200	-
ORTEC/AMTEK 142AH [137]	1.01	500	490	1000
Canberra 2006 [138]	0.3 or 1.5	50	< 350	< 460

Signal Induced

The signal induced S from $t = 0$ to t is given by the convolution of the current induced and the preamplifier response,

$$S(t) = \int_0^t R(t-x)I(x)\mathrm{d}x \tag{3.72}$$

$$= -q\alpha\delta A\frac{r_a r_c}{r_c - r_a}\int_0^t \exp\left(-\frac{t-x}{\tau}\right)\left(3\delta x + r_a^3\right)^{-\frac{4}{3}}\mathrm{d}x\,. \tag{3.73}$$

A Monte Carlo integration of this for a single ion signal ($q = +1e$) is shown in Fig. 3.15. The drop in amplitude observed when a finite τ is used compared to an infinite τ is known as ballistic deficit.

It has previously been shown [140] that Eq. 3.73 can be approximated by a sum of two exponentials;

$$S(t) = -k\left(e^{-t/\tau_f} - e^{-t\left(1/\tau_f - 1/\tau_r\right)}\right)\,, \tag{3.74}$$

where k is a scaling constant and τ_f, τ_r are effective falling and rising time constants of the signal, respectively. This parameterisation has been fit to the signal in Fig. 3.15 for comparison.

In the case of an interaction in the detector generating N electrons, diffusion will cause a spread in their spread in arrival time to the anode. The diffusion of the charges is given by

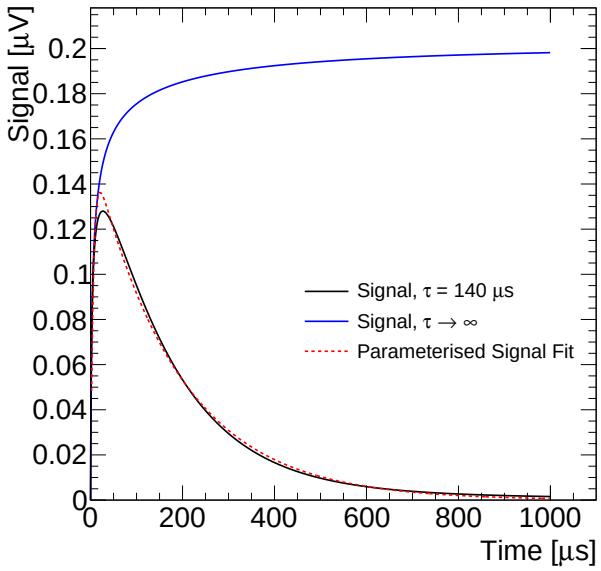

Figure 3.15: Signal generated by a charge of $q = +1e$ in a ⌀30 cm spherical proportional counter with a ⌀2 mm anode at 2000 V. An ion mobility of 1.535 $\mathrm{cm^2\,V^{-1}\,s^{-1}}$ (corresponding to Ar^+ in Ar [139]) was used along with the preamplifier time constant τ and gain for the CREMAT CR-110-R2. The parameterisation of the signal given by Eq. 3.74 was fit to the signal, yielding $k = 0.161$ µV, $\tau_f = 180.2$ µs and $\tau_r = 5.1$ µs. The signal in the case of $\tau \to \infty$ is given for comparison.

Eq. 3.39, and so the total signal will be the sum over the N electrons for a convolution of Eq. 3.73 with Eq.3.39.

An example digitised output pulse, recorded with a "CALI" digitiser at a rate of 1 MHz operated with a CREMAT CR-110-R2 preamplifier, is shown in figure 3.16. A preamplifier output of 1 Analogue-to-Digital Units (ADU), corresponds to a charge of approximately 0.027 fC at the preamplifier input.

Key signal pulse parameters which are used in analysis are: the base line, defined as the ADU value of the pre-trigger of the pulse; the amplitude, defined as the peak amplitude of the pulse above the baseline; the rise time, defined as the time between 10% and 90% amplitude on the rising edge of the pulse; and the integral, defined as the integral under the pulse, with the base line subtracted.

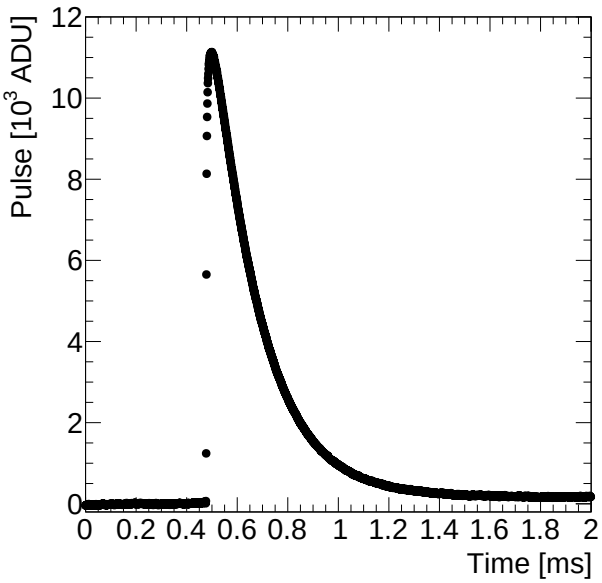

Figure 3.16: Digitised output pulse recorded in a 2 ms window, with the pulse peak positioned at 25% of the window width.

3.3.3 Advantages in Rare Event Searches

The spherical geometry of the detector offers several advantages compared to other gaseous detectors, especially for large-volume, and so large active mass, detectors. Compared to cylindrical and parallel plate detectors of the same size, a spherical detector has the lowest capacitance and so the lowest electronic noise. From Eq. 3.57 and the definition of capacitance $Q = CV$, the capacitance C of the detector is,

$$C = 4\pi\varepsilon \frac{r_a r_c}{r_c - r_a} \,. \tag{3.75}$$

Considering the same example spherical proportional counter as in Section 3.3, the capacitance is less than 1 pF. By again performing a Taylor expansion with the condition that $r_c \gg r_a$, the capacitance is approximated by,

$$C \approx 4\pi\varepsilon r_a \,, \tag{3.76}$$

which is independent of r_c, meaning large detector can be constructed with no commensurate increase in capacitance. Thus, the detector has low electronic noise, allowing it to operate with a single electron level threshold [141, 142].

One of the main sources of background in rare event searches is nuclear disintegration in the material of the detector. A sphere naturally has the smallest surface area to volume ratio for any geometry, suppressing this contribution. Additionally, the relatively simple design reduces the number of materials in contact with the gas; the cathode and rod supporting the anode being the main mass components, which can be made from high-purity copper. The use of electrodeposition to suppress this background contribution, along with the future prospects for using electroforming for spherical proportional counters is addressed in Chapter 6.

The detector can be operated with a variety of different gases, which brings two main benefits. Firstly, this allows a larger range of candidate DM masses to be explored by changing the mass of the target gas. In particular, light nuclei, such as hydrogen, helium and neon, can be used to kinematically match light DM candidates. Gases with odd-nuclei isotopes like hydrogen and carbon, which has approximately a 1% natural abundance of ^{13}C, can provide sensitivity to spin-dependent interactions. Secondly, the ability to vary gas composition, pressure and anode voltage to change the avalanche multiplication gain can provide an additional handle in assessing background contributions.

In its simplest form the detector can operate with a single-channel readout, greatly simplifying readout electronics while still having background rejection capability. However, a multi-anode sensor system has been designed and is currently being developed [143, 4] that would potentially provide information about the direction of the incoming particle. This will be discussed further in Section 4.3.

Despite only using one channel in its simplest form, background rejection may be achieved in

the spherical proportional counter through the use of pulse-shape analysis. The radial electric field falls as $1/r^2$. Primary electrons generated at larger radii are expected to undergo more diffusion as they drift to the anode ($\sigma_d(r) \sim (r/r_c)^3$ [144]) and so will arrive at the anode over a longer period of time. This translates to larger pulse rise time. This allows events occurring near the inner surface of the detector to be discriminated. Similarly, track like events may be distinguished from point-like events, which are expected for DM-induced nuclear recoils, based on the characteristics of the generated pulse. As example, Fig. 3.17 shows the pulse

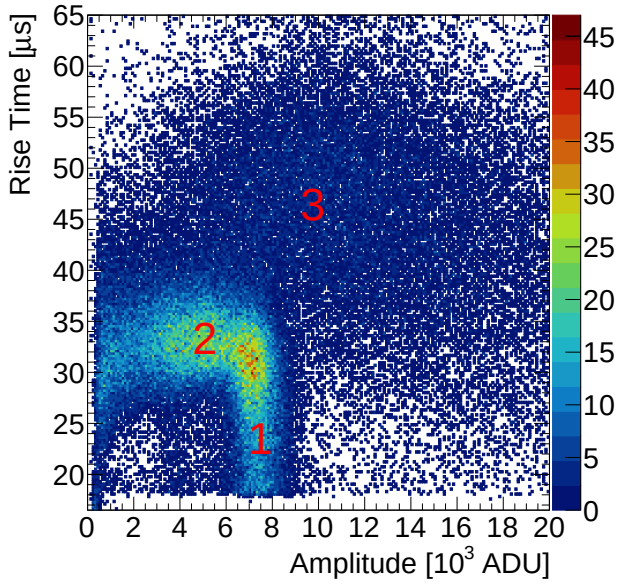

Figure 3.17: Pulse amplitude versus rise time for signals recorded by a 15 cm diameter spherical proportional counter filled with He:Ar:CH_4 (51.7%:46%:2.3%) at 1.3 bar and the 3 mm diameter anode at 2400 V. The labelled population correspond to: (1) 5.9 keV X ray interactions in the gas volume, (2) interactions of the X ray near the cathode surface and (3) cosmic muons. The escape peak is also visible at approximately 4000 ADU.

amplitude versus rise time for signals recorded by a 15 cm diameter spherical proportional counter filled with He:Ar:CH_4 (51.7%:46%:2.3%) at 1.3 bar and the 3 mm diameter anode at 2400 V. An ^{55}Fe source was placed inside the detector, which decays via electron capture to ^{55}Mn, emitting a 5.9 keV X ray [145]. These photons are most likely to interact by photoelectric absorption and have a mean free path of 7.2 cmin this gas [146]. Thus, they will interact at a variety of radii with approximately 98% having interacted in the first 15 cm.

The population labelled (1) are these photons - they have approximately the same amplitude because the vast majority of the generated electrons are collected, however, have a range of rise times because of the radius at which they interacted; a larger rise time indicates a photon that interacted at a larger radius. Population (2) shows those photons that interacted near the cathode surface, which have resulted in some of the electrons colliding with the cathode and being lost.These electrons travel a significantly shorted distance than the photons, and so also interact near the cathode. Therefore, rise time discrimination can be used to select against interactions occurring near the cathode, which is the dominant source of background for current generation rare event searches with spherical proportional counters. Population (3) are cosmic muons. As these are minimum ionising particles, they will leave a track of ionisation in the detector, which results in a large deviation in electron arrival times to the anode, and so, a significantly larger rise time than point-like events near the cathode. This allows track-like energy deposits to also be selected against using rise time selections.

3.4 NEWS-G

The New Experiments With Spheres - Gas (NEWS-G) collaboration utilises the spherical proportional counter to probe the $0.1 - 10$ GeV DM mass range [141, 142, 147, 144]. The NEWS-G Collaboration operates SEDINE, a 60 cm diameter detector made from Aurubis NOSV copper, shown in Fig. 3.18(a). The detector is installed in the Laboratoire Souterrain de Modane inside a shield comprising 8 cm cooper, 15 cm lead and 30 cm polyethylene, as shown in Fig. 3.18(b).

The detector was operated in sealed mode with the Ne:CH_4 (99.3% : 0.7%) gas mixture at 3.1 bar pressure for 42.7 days, with a total exposure of 9.7 kg days. The Region Of Interest (ROI) was optimised for 8 candidate DM masses from 0.5 GeV to 16 GeV using a Boosted Decision Tree. Using standard DM halo assumptions, and considering all events in the ROI of

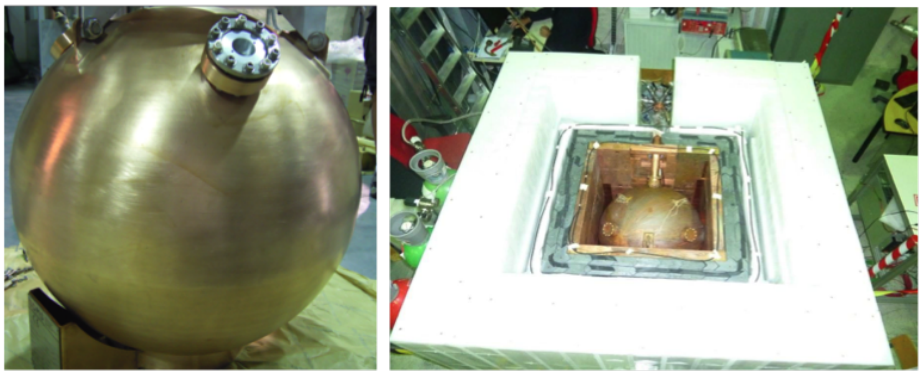

(a) (b)

Figure 3.18: (a) ⌀60 cm spherical proportional counter, SEDINE, and (b) shielding of 8 cm copper, 15 cm lead and 30 cm polyethylene. Figures reproduced from Ref. [144] and Ref. [135], respectively.

each candidate mass as signal, the results shown in Figure 3.19 were obtained with Poisson statistics. A spin-independent DM-nucleon scattering cross section of 4.4×10^{-37} cm^2 is excluded at 90% confidence level (CL) for DM mass of 0.5 GeV [144] - the strongest constraint on that mass of DM candidate at the time.

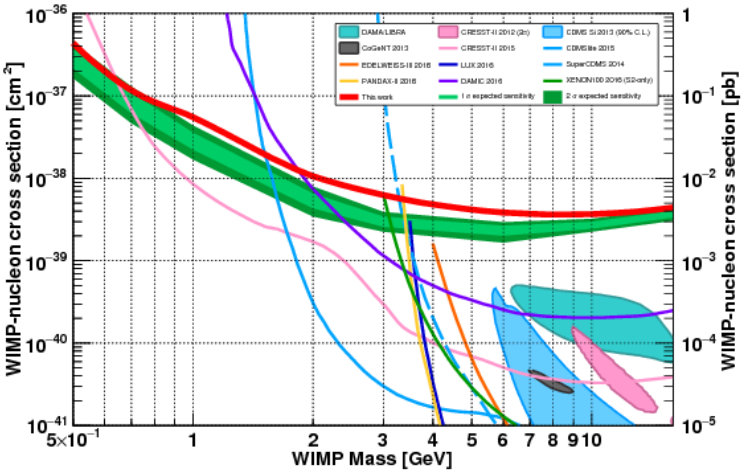

Figure 3.19: Spin-independent DM-nucleon interaction cross section as a function of DM mass, showing the result from SEDINE exclusion limit (solid red). Figure reproduced from Ref. [144].

The next stage of the direct DM search by NEWS-G is a ⌀140 cm spherical proportional

counter, SNOGLOBE, shown in Fig. 3.20(a). The detector is made out of higher purity 4N (99.99% pure) oxygen free copper (OFCu) and housed in a compact shielding, shown in Fig. 3.20(b). Following a commissioning phase in Laboratoire Souterrain de Modane (LSM), the detector was installed in SNOLAB, Canada. SNOLAB offers a 6000 m water equivalent overburden, and a cosmic muon flux of approximately 0.25 $m^{-2}\,day^{-1}$, as well as being a Class2000 clean room. The increase in detector volume, use of compact shielding and use of light-nuclei gas targets are expected to increase the detector's sensitivity to light DM candidates, as shown in Fig. 3.21. The suppression of background contributions from the copper sphere though the use of ultra-pure copper electroplating [1] is the subject of Chapter 6, and future spherical proportional counters utilising this technology are discussed in Chapter 7.

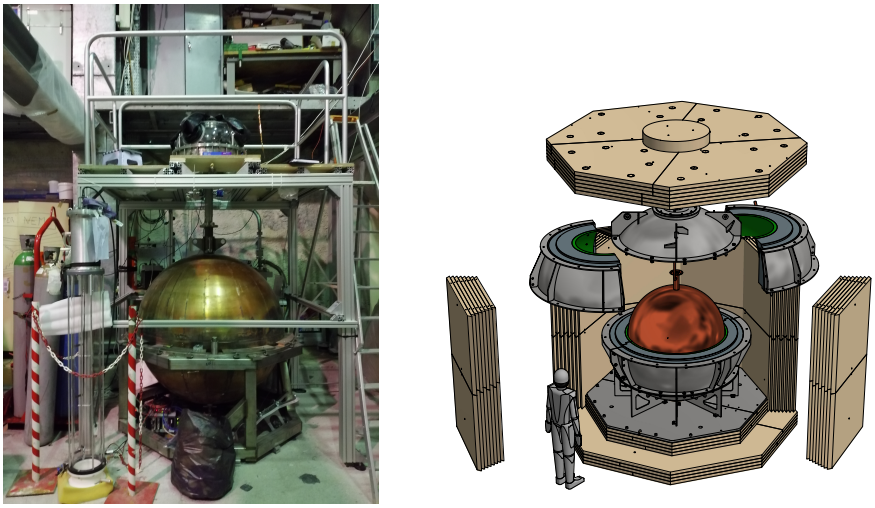

(a) (b)

Figure 3.20: (a) ⌀140 cm spherical proportional counter, SNOGLOBE, during the commissioning phase in LSM and (b) its shielding of 3 cm archaeological lead, 22 cm low radioactivity lead and 40 cm high-density polyethylene (HDPE), reproduced from Ref. [1].

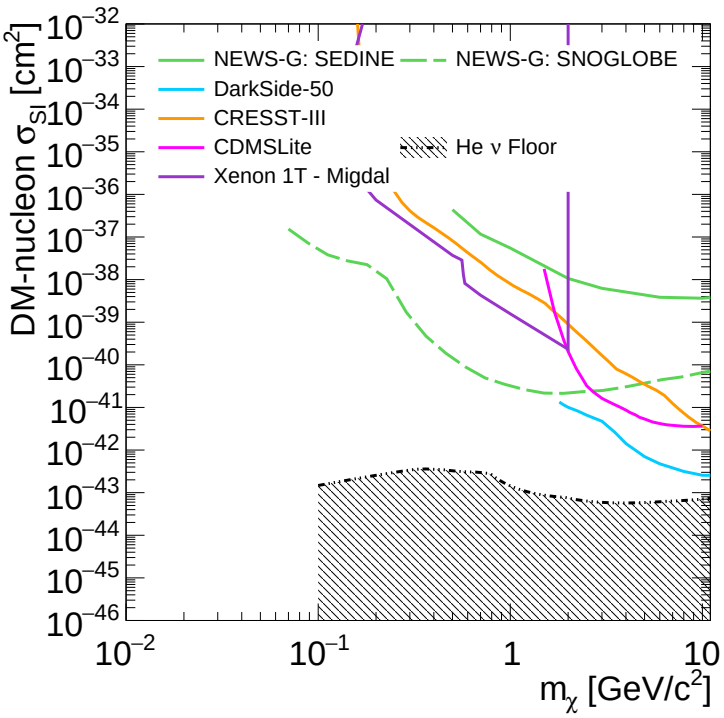

Figure 3.21: Projected 90% CL upper limit on the spin-independent DM-nucleon interaction cross section as a function of DM mass projected for SNOGLOBE. The neutrino floor is shown for helium [74]. Experimental exclusion limit measurements for SEDINE [144], and other direct DM experiments, DarkSide-50 [148], CRESST-III [149], CDMSlite [93] and Xenon-1T [104], are given for comparison.

3.5 Other Applications of the Spherical Proportional Counter

A number of other applications make use of the advantages of the spherical proportional counter, including supernovae detection [150] and neutrino coherent scattering measurements [130]. Two further uses are detailed below.

3.5.1 Neutron Spectroscopy

Neutron measurements are important for industrial application, but also for assessing experimental backgrounds for rare-event searches in underground laboratories. Current technolo-

gies for neutron spectroscopy have several limitations, such using expensive gases, toxic gases, or having poor γ-neutron discrimination capabilities [151]. An alternative is a nitrogen-based detector, which takes advantage of the exothermic and endothermic reactions, ^{14}N(n, p)^{14}C and ^{14}N(n, α)^{11}B, respectively. While the exothermic reaction provides sensitivity to thermal neutrons, the endothermic reaction is sensitive to fast neutrons directly, without need of moderation. The latter enables fast neutron spectroscopy.

A nitrogen-filled spherical proportional counter could be used as a neutron detector. Initial measurements were made challenging by the 'wall effect', induced by the reaction products having a stopping range longer than the size of the detector and so not depositing all of their energy in the gas [152]. This is determined by the detector operating pressure, which was previously limited the high-voltages required to operate a nitrogen detector in proportional mode. Developments in detector read-out instrumentation, discussed in the next chapter, have opened the possibility of higher-pressure operation. Studies are ongoing to use these with a nitrogen-based detector [6], with measurements taking place at the University of Birmingham and Boulby Underground Laboratory, UK [153]. An initial calibration was made with a triple-α source, containing ^{239}Pu, ^{241}Am, and ^{244}Cm, which mainly emit α particles with energies 5.2 MeV, 5.5 MeV and 5.8 MeV, respectively. The measurement was performed with a spherical proportional counter at the University of Birmingham, shown in Fig. 3.22(a), with the results of the calibration, using 1 bar of N_2, shown in Fig. 3.22(b). Measurements are ongoing to operate at pressures of up to 2 bar and to collect data using a neutron source.

3.5.2 Neutrinoless Double Beta Decay Searches

Another application of the spherical proportional counter is the search for neutrinoless double beta decay ($0\nu\beta\beta$) that is being conducted by the R2D2 collaboration [154, 155], which

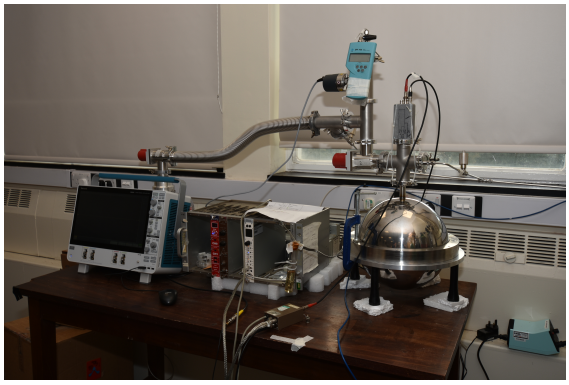

(a)

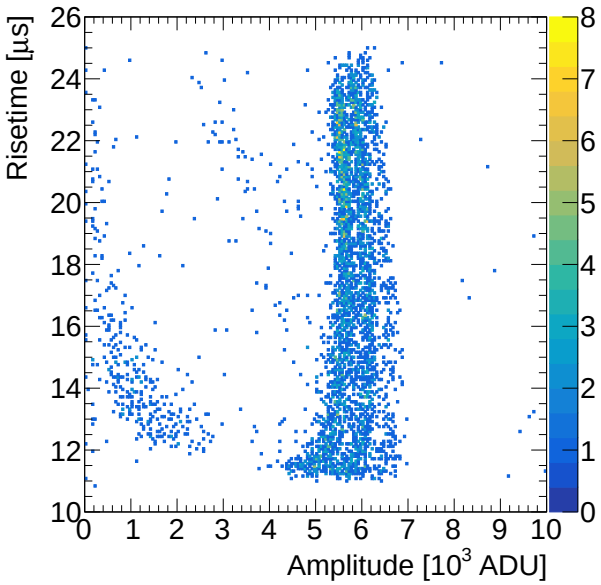

(b)

Figure 3.22: (a) A ⌀30 cm spherical proportional counter at the University of Birmingham Gaseous Detector Laboratory. Photograph taken by Rhys Owen. (b) Pulse amplitude versus risetime for alpha particles from a triple-α source inside a detector operated with 1 bar N_2.

intends to use high-pressure xenon gas to look for $0\nu\beta\beta$ from ^{136}Xe decays. The experimental signature of $0\nu\beta\beta$ is a peak in the energy spectrum of the two electrons from the decay located at the reaction Q-value. To discern such a peak from the continuous energy spectrum from ordinary double beta decay, where a portion of energy is carried away by the two neutrinos, an energy resolution goal of 1% Full-Width-at-Half-Maximum (FWHM) at the reaction Q-value of 2.458 MeV has been set. Research is ongoing into developing the necessary capabilities of the detector for this application, where first steps have been made in studying the energy resolution [5].

4

Read-out Sensors

This chapter details the developments to the spherical proportional counter read-out instrumentation. This comes in two forms; the simpler single-anode sensor and the multi-anode sensor, ACHINOS. Additionally, an electrode designed to improve the electric field homogeneity in both cases is presented. These developments were assisted by finite element calculations and also by a dedicated simulation framework for spherical proportional counters, which is also discussed. This work is presented in detail in Ref. [3, 4], of which I am a main author and heavily contributed to the preparation of the manuscript. As a result, texts and figures from Ref. [3, 4] are included here. The discussed simulation framework is presented in detail in Ref. [2].

4.1 Detector Simulation

4.1.1 Finite Element Method Calculations

FEM is a numerical method used to solve partial differential equations over some space. This allows problems such as, heat transfer, fluid flow and electrostatics, for example, over complicated geometries to be solved. In the case of an electrostatic analysis, the electric potential across the volume of the detector is the quantity of interest. From Maxwell's equations in differential form, the electric displacement field $\boldsymbol{D}$ is related to the charge density ρ by,

$$\nabla \cdot \boldsymbol{D} = \rho \,, \tag{4.1}$$

where $\boldsymbol{D}$ is related to the electric field by the permittivity ε, $\boldsymbol{D} = \varepsilon \boldsymbol{E}$. Using Eq. 4.2 with Eq. 3.56, the governing equation for the electric potential V can be written as,

$$-\nabla \cdot (\varepsilon \nabla V) = \rho \,. \tag{4.2}$$

For this work, ANSYS Mechanical APDL FEM software was used. This software provides a means of creating a geometry, including the material properties, meshing the volume with the selected predefined or user-defined element type, solving the problem and presenting the results. In order to be directly compatible with Garfield++, which is used in the simulation framework discussed in the next section, the `PLANE121` and `PLANE123` elements were selected for 2D and 3D models, respectively. `PLANE121` was used with triangular-shaped elements, using six nodes, and with the 'axisymmetric' option on, meaning the calculated solution assumes symmetry about one axis parallel to the grounded rod. This element was used when modelling the single anode sensors. The `PLANE123` element, with 10 nodes, was used

when modelling the multi-anode sensor, where the axial symmetry is broken.

4.1.2 Simulation framework

Various different software packages exist for simulating a detector. Geant4 [156, 157] provides a toolkit for simulating the passage of particles through matter. Garfield++ [158, 159] provides a toolkit for simulating gaseous detectors, including interfaces to Magboltz [122, 123] for the modelling of electron transport parameters and other properties of gases and HEED [160] which simulates particle interactions. Garfield++ can be provided with an electric field map of the detector, which can either be analytical or calculated using FEM. It has previously been shown [161] that these various toolkits can be combined, and this has been used to construct a predictive framework for the simulation of spherical proportional counters [2, 162].

The simulation framework is based in Geant4 and interfaces with Garfield++. Geant4 handles the detector material simulation, as well as generating, tracking and interacting initial particles. Electrons with an energy below 2 keV are passed to Geant4 via a custom physics model where HEED calculates any subsequent ionisation. At this point, Magboltz-generated electron transport parameters are used to drift electrons towards the anode and simulate their diffusion in the electron field, using the Garfield++ drift line model. The Magboltz gas properties are also used to compute the avalanche multiplication. For this, a custom Monte Carlo model combining the Townsend α and attachment η coefficients, was used to compute the average avalanche gain G as

$$\bar{G} = \exp\left\{\int \left[\alpha(\mathbf{r}) - \eta(\mathbf{r})\right] \mathrm{d}\mathbf{r}\right\} , \tag{4.3}$$

where the integral is evaluated over the path of the electron. Fluctuations to the average

gain are then applied from a Polya distribution. In order to compute the parameters of the Monte Carlo model, Garfield++'s microscopic drift line model was used, which follows the multiplication of each electron at individual atom collisions. The avalanche multiplication of each electron is used to generate a single multiply-charged 'electron' and 'ion', with charges $-e(G+1)$ and eG, respectively. This reduces the computation cost of drifting each individual avalanche charge without appreciable loss to signal information. These multiply-charged electrons and ions are then passed to a custom Geant4 end of event action which uses Garfield++ to drift the charges and compute the current induced on the anode using the Shockley-Ramo theorem. The effect of the electronics chain, including timing digitisation and preamplifier shaping, are then applied to the signal. The simulation framework provides a means of studying detector response which facilitates sensor development, event reconstruction. The framework has been used to understand and interpret experimental results [4, 5].

4.2 Single Anode Read-Out System

4.2.1 Distortion to electric field in realistic case

For the ideal case of a floating anode, the electric field in the spherical proportional counter is given by Eq. 3.58. However, in practise the anode is connected to the external electronics by a high-voltage wire, typically a ⌀150 µm copper wire insulated by a 200 µm thick insulating layer. This wire distorts the electric field in the volume, resulting in an inhomogeneous response for interactions occurring at different locations in the detector. This can impact both the background suppression and fiducialisation capability, as well as the energy resolution of the detector. Fig. 4.1(a) shows an FEM calculation of the electric field in the ideal case, while Fig. 4.1(b) shows the distortion to the field after the wire is included.

4.2.2 Electric field configuration

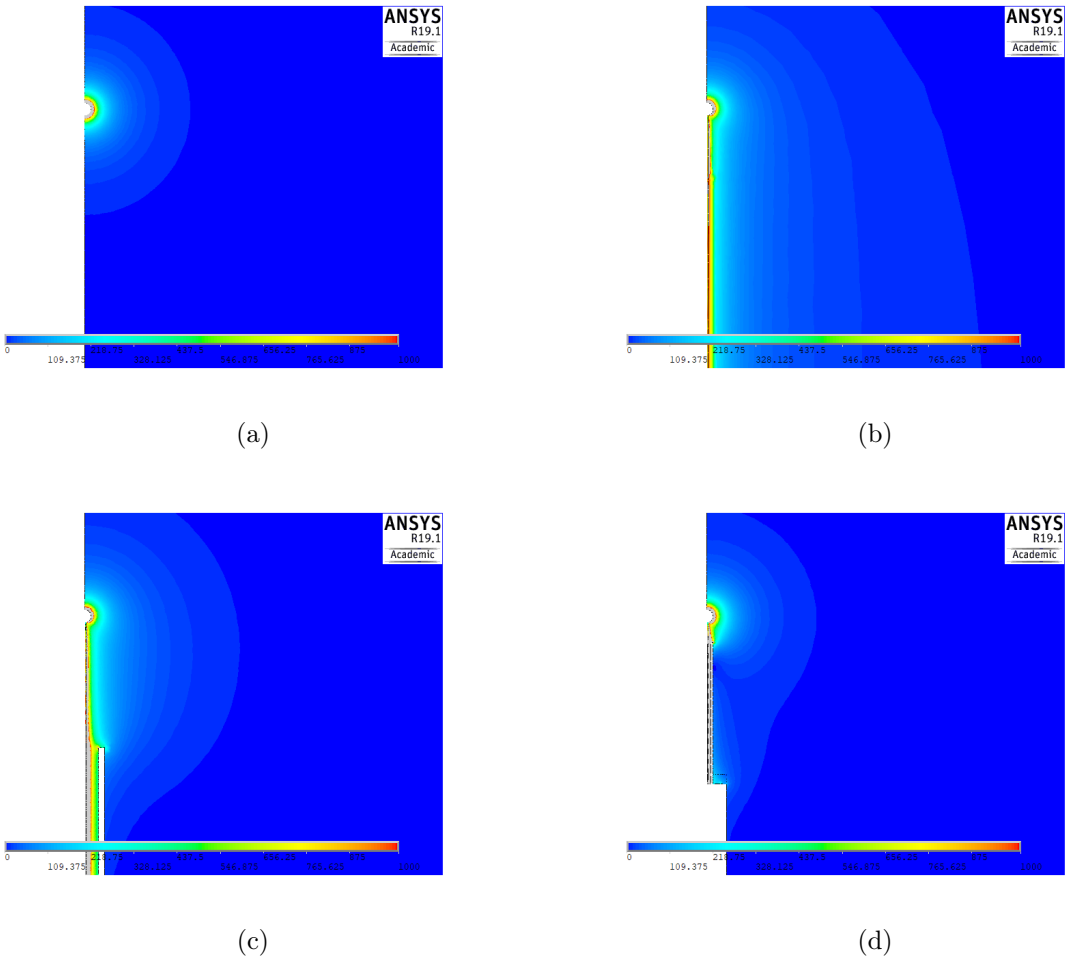

Figure 4.1: Electric field equipotential lines calculated using FEM software for a 15 cm radius spherical proportional counter with a 1 mm radius anode at 2000 V (a) for the ideal case comprising just the anode at high voltage, (b) including the anode wire to supply the high voltage, (c) including the grounded metallic rod surrounding the anode wire, and (d) including a second correction electrode placed 3 mm from the anode and set to 250 V. field due to the wire causes asymmetries in the detector response for primary electrons arriving from different regions of the detector. The grounded rod and the second electrode work to reproduce more closely the field configuration of the ideal case.

The inhomogeneous electric field in the avalanche region results in gain variations for electrons arriving to different regions of the anode, significantly increasing the energy resolution. An inhomogeneous electric field at larger radii causes zenith angle-dependent rise time varia-

tions, reducing the ability to distinguish interactions occurring near the cathode or track-like events. In order to support the anode, a 4 mm (6 mm) internal (external) diameter grounded support rod is used, with the resulting electric field shown in Fig. 4.1(c). This acts as a correction electrode, to shield the volume from the influence of the wire [129]. In the absence of the rod, a large fraction of electrons generated in the case would be collected on the wire.

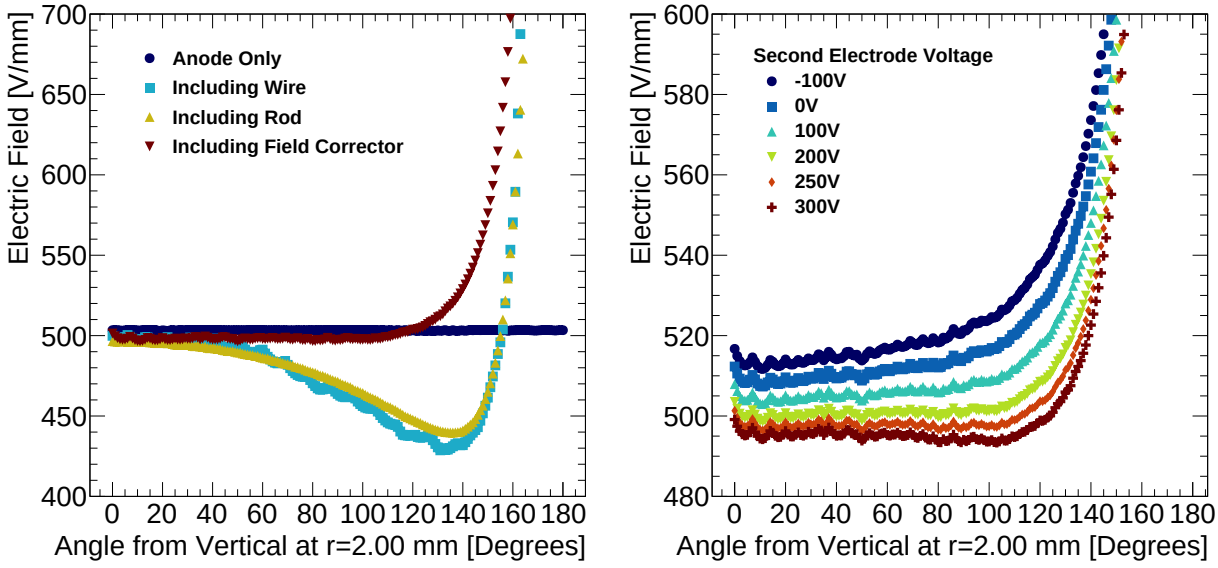

(a) (b)

Figure 4.2: FEM calculation of the electric field as a function of the zenith angle calculated at a radius of 2 mm in an spherical proportional counter of radius 15 cm with a 1 mm radius anode set at 2000 V. (a) The comparison of the electric field for the case of a grounded rod surrounding the wire to the anode and the case where a second electrode consisting of 20 mm of glass at 250 V located 3 mm from the anode is included. the latter showing a more uniform electric field, which translates to a better energy resolution and more uniform detector response for primary electrons generated in different regions of the gas volume. (b) The electric field for a second electrode consisting of 20 mm of glass located 3 mm from the anode for various applied voltages on the second correction electrode. A voltage of approximately 250 V provides the most homogeneous field for this geometry.

In order to restore the homogeneity of the electric field near the anode, a second correction electrode can be introduced a few millimetres from the anode surface. The electric field configuration for the ideal geometry, the addition of the wire and the addition of the grounded rod were studies using FEM and are presented in Fig. 4.1. A second correction electrode

comprising a ⌀1 mm to 2 mm cylinder was added to the anode support structure, placed a few millimetres from the anode and the effect on the electric field is shown in Fig. 4.1(d). The introduction of the second correction electrode provides higher electric field homogeneity and, thus, a more uniform response for large zenith angles, as demonstrated in Fig. 4.2(a). The electric field around the anode can be fine-tuned by varying the voltage on the surface of the second correction electrode. This is particularly important for the hemisphere containing the grounded rod where the distortion to the electric field is greatest. Fig. 4.2(b) shows the electric field near the anode as a function of azimuth for several voltages applied to the second correction electrode, which shows that for this configuration a voltage of approximately 250 V provides the most homogeneous field as a function of azimuth.

FEM Study of Second Correction Electrode Geometry

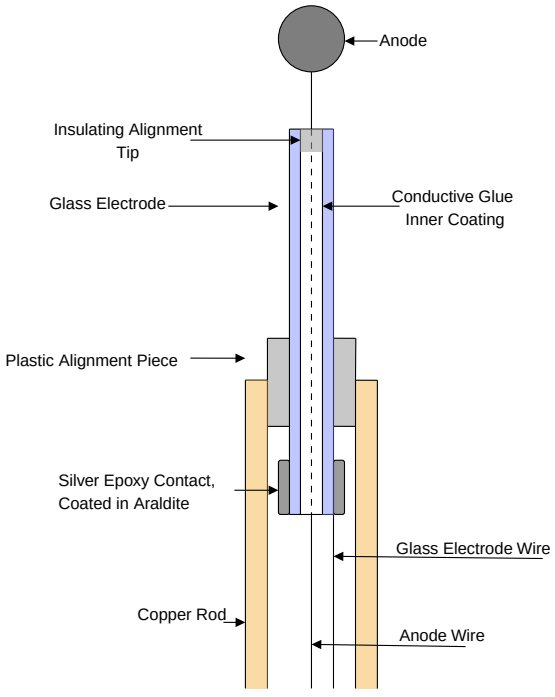

Figure 4.3: Schematic of the sensor support structure with a second correction electrode.

The anode support structure with a second correction electrode is shown in Fig. 4.3. The

distance between the anode and second correction electrode d, the length of the second correction electrode l and the voltage applied to it V_2 were highlighted as parameters which could be tuned to shape the electric field near the anode. In order to study this, a model with using ⌀15 cm sphere with a ⌀2 mm anode at 2000 V was implemented in ANSYS, unless otherwise stated. As starting parameters, l, V_2 and d were set at 5 mm, 200 V, and 4 mm, respectively.

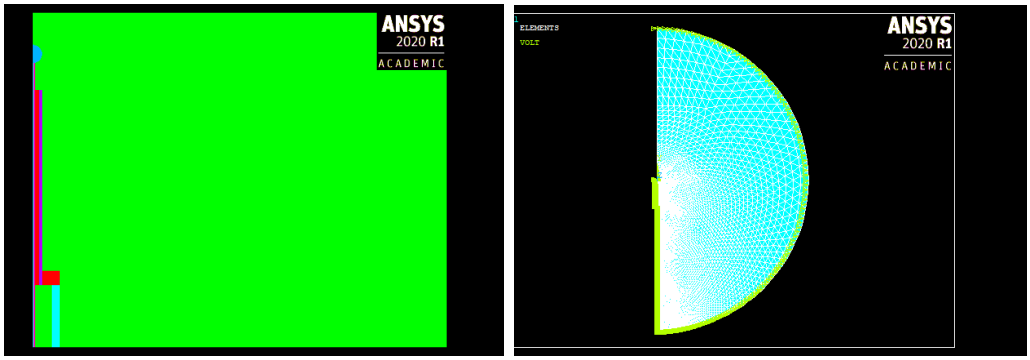

(a) (b)

Figure 4.4: Example ANSYS model:(a) close-up of the module in ANSYS and (b) the produced mesh.

An example of the model and produced mesh in ANSYS is shown in Fig. 4.4. Fig. 4.5(a) shows the electric field magnitude at a radius of 2 mm for various second correction electrode voltages while l and d were fixed. It can be seen that for this configuration a voltage of approximately -50 V provides the most homogeneous electric field in azimuthal angle. For fixed V_2 and l, Fig. 4.5(c) shows the effect on the electric field magnitude when d is varied. To show the effect of changing the anode radius, in Fig. 4.5(d) it has been changed to 1.5 mm, and the field evaluated at 2.5 mm to maintain the 1 mm distance from the anode. The value of d that yields the most homogeneous field in both cases is approximately 3.5 V. In Fig. 4.5(b) the value of l was varied, showing just a shift in absolute electric field magnitude, but no perceptible change in homogeneity. With this information, comparing Fig. 4.5(b) and 4.2(b) indicates that the difference in the value of V_2 which gives the most homogeneous electric field is primarily due to the change in d.

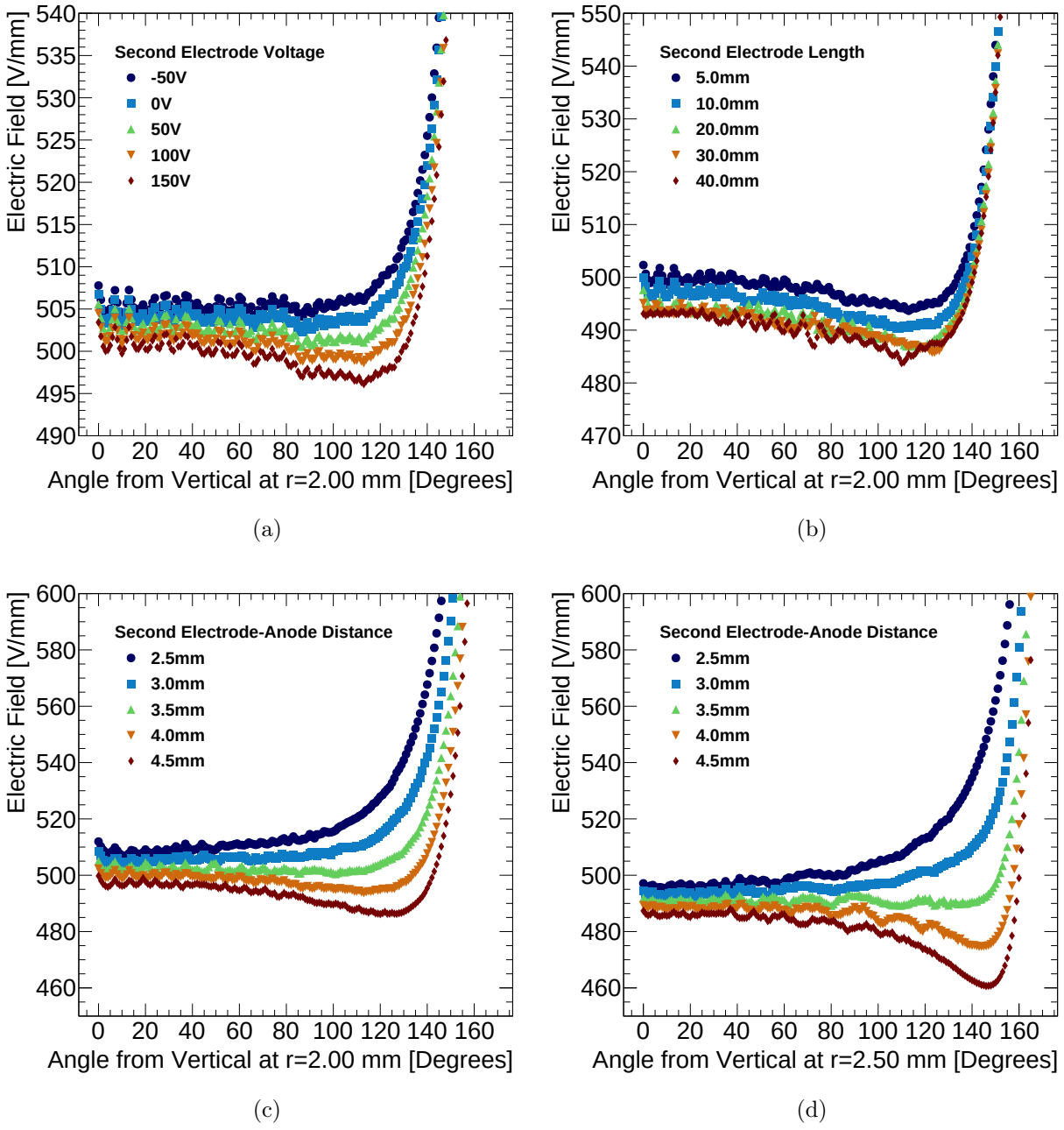

Figure 4.5: Electric field magnitude at 2 mm radius calculated using FEM software for a 15 cm radius spherical proportional counter with a ⌀2 mm anode at 2000 V (a), (c) and (b) for varying V_2, d and l, respectively while the other parameters are fixed at $V_2 = 200$ V, $d = 4$ mm and $l = 5$ mm. (d) shows the electric field magnitude at 2.5 mm in the case of a ⌀3 mm anode for various values of d, keeping all other parameters the same as (c).

Capacitance

From Eq. 3.75, the capacitance of a detector with a 15 cm radius and a 1 mm radius anode is 0.11 pF. However, the introduction of the wire, grounded rod, and second correction electrode alter the capacitance from this ideal value. Using the `CMATRIX` command in ANSYS, for a module with a 20 mm of second correction electrode located 3 mm from the anode, along with the grounded rod and wire, the capacitance was calculated to be 4.5 pF between the anode combined with the wire and all other components. The main component of this is the capacitance between the anode plus wire and the rod, which accounts for 2.8 pF, and is mainly due to the wire inside the rod. This can be seen by considering the capacitance per unit length L of a wire of radius r_1 inside a cylindrical conductor of radius r_2 (i.e. a coaxial cable) is given by

$$C_{\text{wire}} = \frac{2\pi\varepsilon_0 L}{\ln\left(\frac{r_2}{r_1}\right)}\,. \tag{4.4}$$

For a length of 12.5 cm this corresponds to a capacitance of 2.6 pF, and so accounts for most of the 2.8 pF. Therefore, the capacitance of the realistic detector will scale approximately proportional to the cathode radius.

4.2.3 The resistive correction electrode

The correction electrode provides a simple but effective solution to the inhomogeneity of the electric field. However, to obtain the greatest control over the electric field it must be positioned only a few millimetres from the surface of the anode, supported by the grounded rod. The close proximity and difference in voltage of the second correction electrode and anode increases the probability of a discharge.

Following initial conceptual designs using FEM software, several prototypes were constructed.

Testing of these prototypes has demonstrated that it is impractical to implement such a correction electrode using metallic or any conductive materials due to the increased sparking rate and intensity. A solution explored was the coating of the conductive material in an insulating layer, usually consisting of a layer of glue, Araldite®, or PLO plastic. However, the introduction of insulating materials close to the anode induces charging-up of the electrode and results in time-dependent gain variations, with time constants depending on geometry and operational conditions.

An alternative was found in the use of resistive materials as electrodes, which has been shown to reduce the spark rate and intensity in many detector designs, especially small gap micro-pattern detectors [163, 164, 165]. Furthermore, using resistive materials for electrodes is an effective technique to achieve higher gain operation and increased operational stability. The resistivity in these materials, is high enough to quench sparks and allow normal detector operation in the occasion of a spark, while it is adequately low to prevent charging-up and, thus, time-dependent gain variations.

A series of resistive materials has been tested. Following the experience of resistive bulk Micromegas, initial tests involved polymer paste with resistivity in the $10^3 - 10^6\ \Omega\,\mathrm{cm}$ range. The construction of cylindrical electrodes at high precision when using paste was found to be challenging, while the obtained resistivity was inadequate for the desired effects.

Glass as a resistive material has been used to construct electrodes for various detectors including large surface Resistive Plate Chambers [166, 167, 168, 169]. The glass electrode we used was in the form of a cylindrical tube with an 1.85(1.2) mm external (internal) diameter. The glass type was lime-soda glass, a common material used in a large number of applications.

Resistivity of the glass electrode

The volume resistivity, ρ, of the glass tube was measured based on a method described in Ref. [170]. The measurement method is presented in Fig. 4.6. The glass tube was sealed at one end with an insulating glue (Araldite) and heated to 200°C for a day to remove humidity from the surface. The tube was left to return to room temperature and was filled with an electrolyte of a salt water solution to a level L, shown in Fig. 4.6. It was then immersed up to this level in a container filled with the same electrolyte. The electric circuit is closed and a voltage applied using two copper wires, one immersed into the container and one in the tube. Electrons must cross the volume of glass to be collected by the electrode inside the

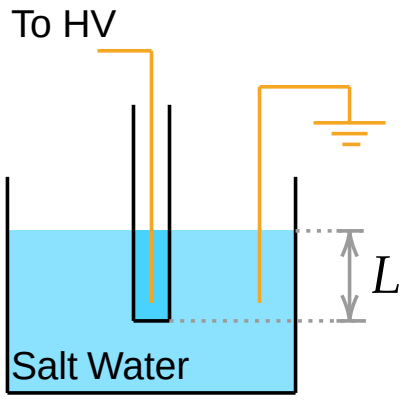

Figure 4.6: Setup of resistivity measurement. The glass tube is filled with and immersed in the solution to depth L. A voltage is applied across the glass allowing measurement of the current through its volume.

tube and measured. The current I was measured as a function of the applied voltage V, up to 1 kV. A linear response is observed, as shown in Fig. 4.7. The resistivity of the glass tube is calculated from the average of measurements using,

$$\rho = \frac{2\pi LR}{\ln\left(\frac{b}{a}\right)}, \tag{4.5}$$

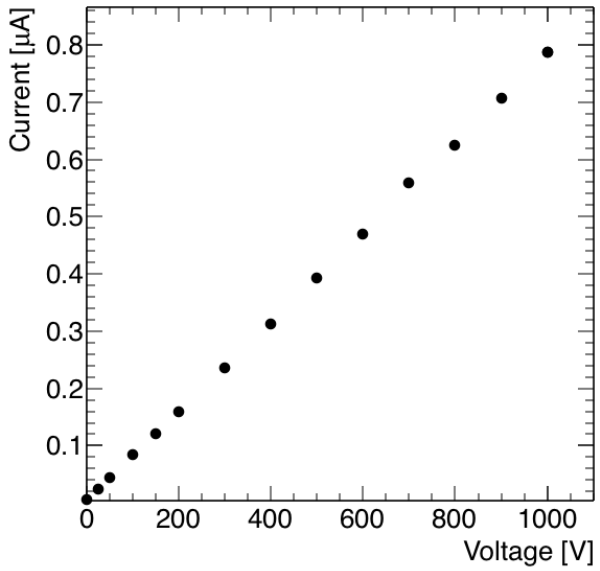

Figure 4.7: Current measured flowing through the glass versus applied voltage. From an average of these measurements, the resistivity of the glass tube was calculated as $\rho = (5.1 \pm 1.4)10^{10}\ \Omega\,\mathrm{cm}$.

where $R = V/I$ is the resistance between the outer and inner surface of the tube, $L = 2.2$ cm, $a = 0.12$ cm ($b = 0.185$ cm) is the internal (external) diameter of the tube. The resistivity obtained is $\rho = (5.1 \pm 1.4)10^{10}\ \Omega\,\mathrm{cm}$. The uncertainty on the measured resistivity arises mainly from the limited accuracy of the electric current measurement in the voltage range between 0 V and 150 V.

4.2.4 Development and performance of the resistive glass electrode prototypes

The rod with the glass electrode structure is presented in Fig. 4.8(b) and Fig. 4.8(a). The internal surface of the glass tube is covered with a layer of conductive glue and electric potential can be applied through a thin wire. This conductive layer facilitates the application of the electric potential on the glass electrode and shields from the influence of the wire's electric field. The external part of the layer is covered with insulating glue, with a resistivity

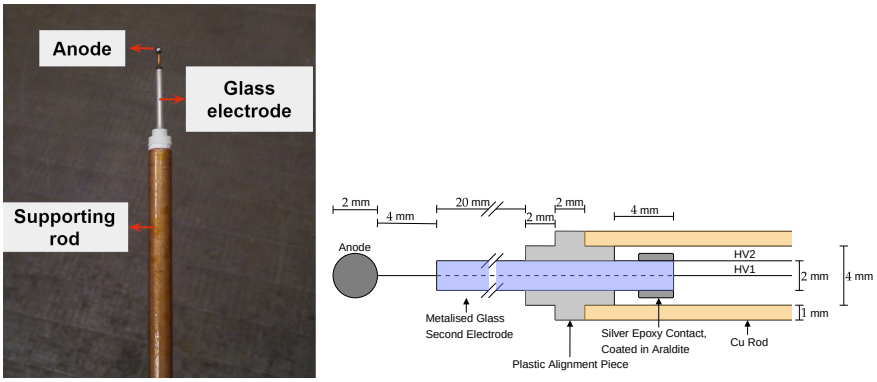

(a) (b)

Figure 4.8: Sensor support structure with a cylindrical glass correction electrode, (a) photograph and 4.8(b) schematic.

greater than $10^{14}\ \Omega\,\mathrm{cm}$, to avoid sparks between the conductive layer and the rod. The wire of the anode passes through the glass tube and is aligned by a short insulating tip. The bottom part of the glass tube with the conductive layer and the insulating cover is placed in an insulating support base, made of PLO, constructed with high precision using 3D-printing. Finally, the support base is inserted into the rod.

The constructed module is presented in Fig. 4.8(a). It incorporates 2 mm diameter anode made of stainless steel. The anode is connected to the high voltage power supply with a thin wire, 150 µm in diameter, surrounded by a 200 µm thick insulating material. The glass tube has a length of 20 mm and the distance between the ending edge of the tube and the surface of the anode is 3 mm. The module is at the centre of a spherical, stainless steel vessel of 15 cm radius and is supported by a copper rod with a 4 mm (6 mm) inner (outer) diameter. The connection interface between the rod and the detector's spherical vessel ensures that both be grounded. The spherical vessel is 3 mm thick and is built to sustain pressure up to 10 bar.

The module was tested for sparking in an argon atmosphere. This test involved enclosing the module in a transparent container that is flushed with argon, applying a high voltage to the anodes, and observing the path of any discharges, as shown in Fig. 4.9(b).The secondary

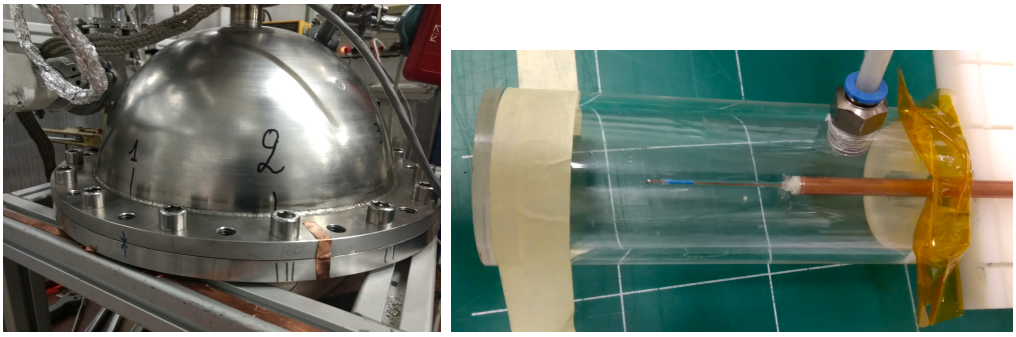

(a) (b)

Figure 4.9: (a) ⌀30 cm stainless steel spherical proportional counter used for tests in CEA Saclay. (b) the chamber used for testing modules for sparks.

electrode was grounded and the anode voltage gradually increased to 7000 V, without any sparks being observed.

In the following, tests of the performance of the ⌀30 cm spherical proportional counter, shown in Fig. 4.9(a), are presented. The counter was prepared by initially evacuating the spherical shell using a turbomolecular pump, to a pressure of 5.37×10^{-5} mbar L.

Voltage application on the glass electrode

A test was carried out to study the response of the module to a change in the voltage of the second correction electrode. The detector was filled with a gas of He:Ar:CH_4 (87%:10%:3%) at a pressure of 1 bar, with the anode voltage set to 1640 V. The high voltage applied on the glass electrode was varied to check that it is properly applied on the electrode surface. The voltage variations resulted in simultaneous gas gain variations. An example is displayed in Fig. 4.10 which shows the measured pulse amplitude as a function of time. Initially, the second correction electrode voltage was 100V, but was changed to 200 V after 8000 s, where the detector responded immediately with a gain drop. The detector operated without a visible time dependence to the gain after this change, indicating the voltage application was immediate.

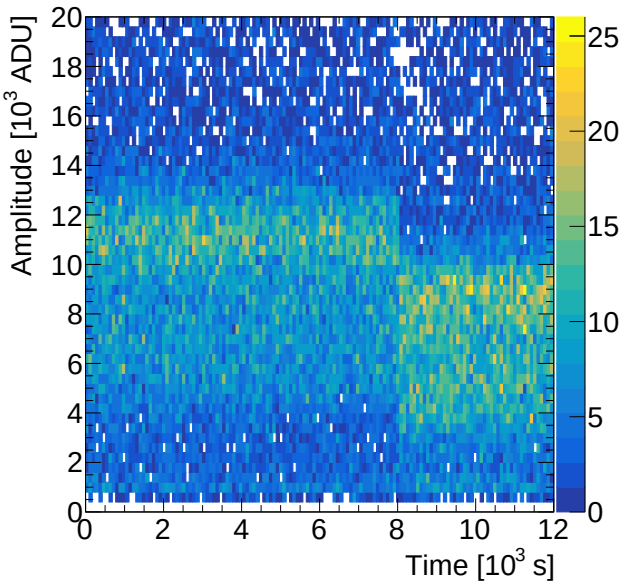

Figure 4.10: Amplitude versus time in a module with a second correction electrode. Initially, the second correction electrode voltage was at 100 V but was increased to 200 V at 8000 s.

Homogeneous response

To experimentally test the homogeneity of electric field achieved by the module, an ^{55}Fe source was placed inside the detector. The location of this collimated source could be changed during detector operation. ^{55}Fe decays through electron capture to ^{55}Mn emitting 5.9 keV X rays.

The detector was filled with 1 bar of He:Ar:CH_4 (92%:5%:3%) with the anode and second correction electrode voltages set at 1450 V and 200 V, respectively. Data were collected with the source located at 90° and 180° to the grounded rod and their amplitude distribution is shown in Fig. 4.11. At 180° any distortions to the electric field caused by the wire and grounded rod should be minimised. However, at 90° the X rays interact in a detector region potentially influenced by electric field distortions [147]. Such distortions could result in primary electrons arriving at the anode closer to the wire, leading to a worse energy resolution due to spatial gain variations. However, Fig. 4.11 demonstrate similar response

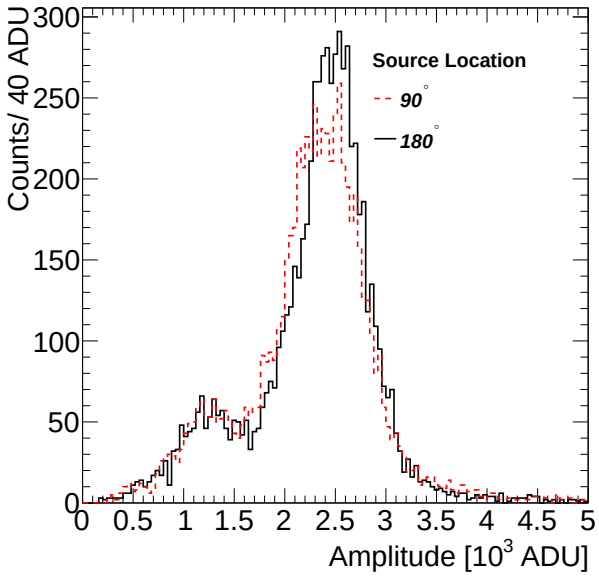

Figure 4.11: The overlaid amplitude distributions for the recorded pulses, for 5.9 keV X rays from an ^{55}Fe source located inside the detector placed at a zenith angle of 90° (red) and 180° (black), relative to the grounded rod.

in both cases. Thus, electric field distortions are corrected for by the second correction electrode.

Operational stability

The main goal was to be able to operate the detector in a gas pressure up to 2 bar and to avoid sparks when voltages over 2000 V were applied. To test the detector stability of operation, a gas of 2 bar of He:Ar:CH_4 (87%:10%:3%) was introduced into the detector through an Oxysorb® filter to remove oxygen and water traces from the gas. A voltage of 2350 V was applied to the anode with 0 V applied on the second correction electrode. The 6.4 keV X ray fluorescence of the ^{55}Fe K-line, induced by cosmic muons, was used to monitor the change in gain over time. Data were collected for 12 days and the pulse height recorded versus time is shown in Fig. 4.26. A gradual decrease of the pulse height is observed which is caused by the introduction of contaminants due to the imperfect vacuum tightness

of the detector. However, the detector was stable throughout the entire period, with no spark-induced gain variations.

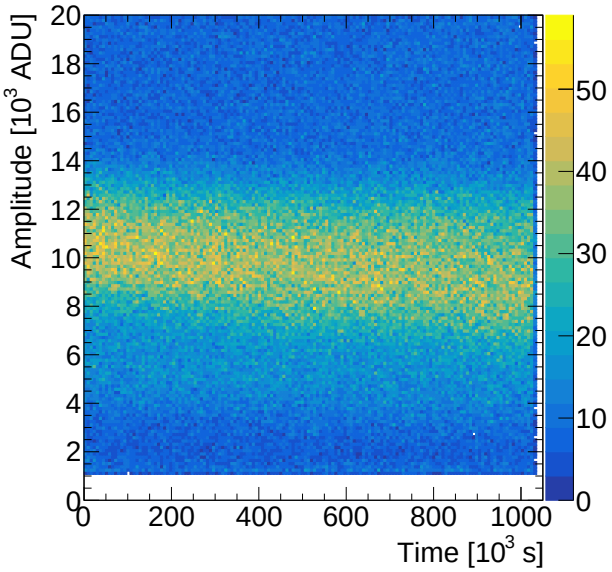

Figure 4.12: Pulse height as a function of time recorded using a module with a second correction electrode at 0 V, with an anode voltage of 2350 V in a detector filled with 2 bar of He:Ar:CH_4 (87%:10%:3%). The decrease in pulse height over time is due to contaminants, such as oxygen, leaking into the detector. Detector operation is stable and no discharges are observed.

4.2.5 Conclusions

The presented read-out module for the spherical proportional counter, incorporating the second correction electrode, has addressed two challenges in the detector operation. Firstly, the tuning of the electric field near the anode has reduced distortions to the electric field induced by the necessary supporting structures and wire, and so improved the energy resolution of the detector. Secondly, the use of high-resistivity materials has reduced the probability of sparking and so improved the detector's operational stability. The second point is of critical importance to the direct DM search, as the detector needs to be able to operate stably over long periods of time during physics data collection stages. This design of module has

been used by the NEWS-G collaboration in SEDINE and SNOGLOBE. These advancements are also of great interest to other applications of the detector and are generally adopted in spherical proportional counters. In particular, $0\nu\beta\beta$ searches with the detector, proposed by the R2D2 collaboration [155], have set a goal of achieving 1% FWHM energy resolution at 2.458 MeV. Initial tests in 1 bar of Ar:CH_4 (98%:2%) have yielded an energy resolution (FWHM) of 1.2% at 5.3 MeV [5]. Further optimisation of the module used for these measurements, following the methods discussed above, are envisaged to improve this result further.

4.3 Multi-Anode Read-Out System

For large detectors, or detectors operating in high pressure, the small ratio of electric field strength to gas pressure (E/P) increases the probability of electron attachment and recombination. For a fixed P in the single anode configuration, increasing E/P can be achieved by either increasing the anode voltage or the anode size, both of these options lead to an increased discharge probability. From Eq. 3.58, for a ⌀1 mm anode at 2000 V inside a ⌀15 cm spherical proportional counter, the electric field magnitude at $r = 15$ cm is 0.9 $\mathrm{V\,cm^{-1}}$. If the same module was installed inside a ⌀65 cm detector, the electric field magnitude at the cathode is $E = 0.05$ $\mathrm{V\,cm^{-1}}$. In order to achieve the same electric field at the cathode surface and anode surface would require a ⌀4.3 mm anode at 8700 V. The coupled avalanche and drift fields limit the practical electric fields which can be achieved with the module.

ACHINOS, a sensor structure composed of several anodes at a radius r_s from the centre, shown in Fig 4.13, has been proposed to overcome this challenge [143]. The anodes are maintained in position by means of a central support structure. This structure needs to be constructed using resistive materials for the same reasons as outlined in Section. 4.2.3. The gain and drift fields are decoupled with ACHINOS. The avalanche gain is determined by the

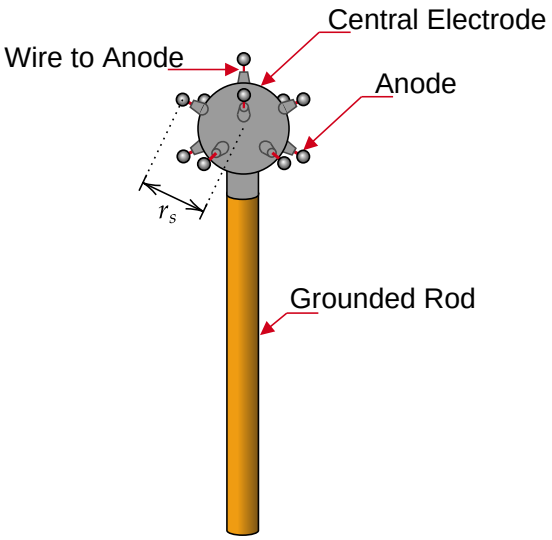

Figure 4.13: Schematic of the multi-anode read-out structure, ACHINOS.

anode radius r_a and voltage V, while the electric field at large radii is the collective electric field of all the anodes, determined by V, r_c, and the number of anodes.

4.3.1 Anode Positions

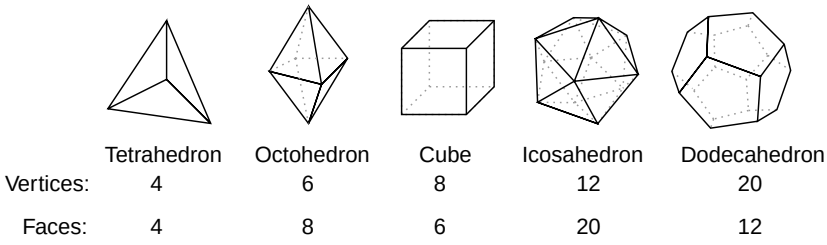

Figure 4.14: The five platonic solids.

In order to keep the electric field at the surface of each anode the same, the distance between each anode and its nearest neighbours should be the same. This can be realised by placing the anodes at the vertices of one of the five Platonic solid, shown in Fig. 4.14. The ACHINOS modules presented are primarily based on the icosahedron, which has origin-centred cartesian

vertex locations

$$\begin{aligned}(x, y, z) =& (0, \pm 1, \pm\phi)\,,\\ & (\pm 1, \pm\phi, 0)\,,\\ & (\pm\phi, 0, \pm 1)\,,\end{aligned}$$

where ϕ is the golden ratio, $\phi = \frac{1+\sqrt{5}}{2}$. In practice, the grounded rod which supports the module occupies one of the vertices of the icosahedron meaning that the ACHINOS has 11 anodes.

While keeping the anodes equally spaced from their nearest neighbours ensures the same electric field magnitude at each, if a different voltage can be applied to each anode then this is not a strict constraint. Differences in field magnitude due to some anodes being closer to neighbours than others could be compensated for by an appropriate change in voltage. This allows shapes with more vertices to be used. One such shape which was studied is the truncated-icosahedron, which has 60 vertices. This will be discussed further in Section 4.3.5.

4.3.2 ACHINOS with "resistive glue" coating

The ACHINOS central electrode is manufactured with a resistive material in order to reduce sparking rate and intensity. Initial designs of ACHINOS utilised a spherical Bakelite central electrode that was machined in order to support the anodes [143]. In an effort to construction, the use of 3D printed central structures were explored. 3D printing provides a convenient means to produce a high-precision structure, however, currently 3D printing with insulators and conductors is more widely available. Thus, an appropriate coating needs to be applied to the insulator. Initially, Araldite adhesive mixed with copper powder was explored, with main benefits being the relatively low radioactivity of Araldite 2011 [171] and the possibility

Figure 4.15: ACHINOS using an Araldite-copper layer on the 3-D-printed structure to form the central electrode.

to control the resistivity of the coating by changing the relative amounts of Araldite and copper. It was found that mixtures containing 20% to 50% w/w copper powder provided the desired detector stability. An example is shown in figure 4.15. Despite promising results, the coating layer was found to be susceptible to damage from discharges. Specifically, a single discharge could destroy the central electrode coating, by creating a conductive path through the layer to the grounded rod. This behaviour was also observed repeatedly when the module was installed in a spark-test chamber, similar to that presented in Fig. 4.9(b).

4.3.3 ACHINOS using DLC coating

DLC is a form of amorphous carbon containing both the diamond and the graphite crystalline phase. Thanks to its excellent surface resistivity, in addition to structural, chemical and thermal stability, DLC coating [172] offers a novel method for producing high quality resistive materials for gaseous detectors [173, 174].

The central structure was constructed using 3D printing with different substrates, including resin, nylon, and glass, as shown in figure 4.16(a). DLC was deposited using magnetron sputtering. Several batches of DLC-coated structures were produced, with a range of coating

thickness between 360 nm and 720 nm. The measured resistance between two anti-diametric points on the surface, ranged from 0.3 to 10 GΩ. The DLC-coated resin 3D printed structure was mounted on a copper rod and electrically connected to it using a conductive Araldite copper mixture, as shown in Fig. 4.16(b).

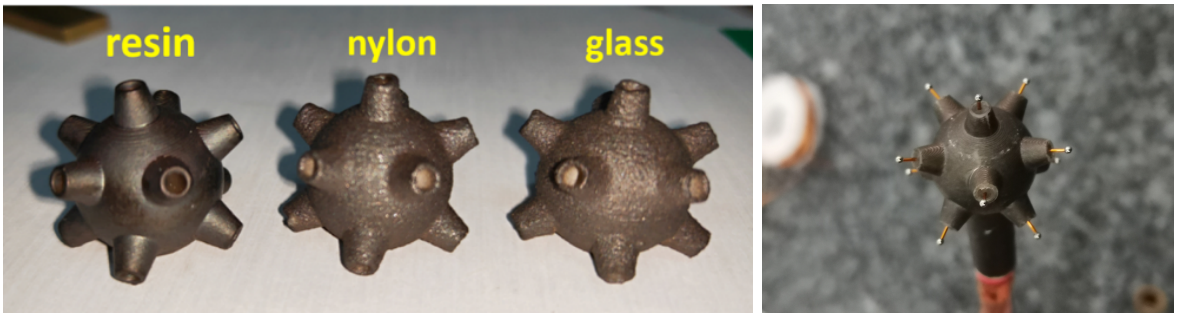

(a) (b)

Figure 4.16: (a) Three different support materials (resin, nylon, glass) covered with a DLC layer. Figure reproduced from Ref. [4]. (b) An 11-anode ACHINOS constructed using a DLC-coated support structure.

4.3.4 Experimental performance of DLC ACHINOS

The ACHINOS structure with 11-anodes, each 1 mm in diameter, shown in figure 4.16(b) was installed in a 30 cm diameter spherical proportional counter that operated in sealed mode, shown in Fig. 4.9(a). An ^{55}Fe source was installed inside the detector, the position of which could be adjusted without opening the detector. The experimental set-up is shown in figure 4.17. The central electrode was, typically, grounded through the rod, but alternative configurations were also tested. Signals are read out by a CREMAT CR-110-R2 charge sensitive preamplifier. The preamplifier output is passed to a "CALI" digitiser.

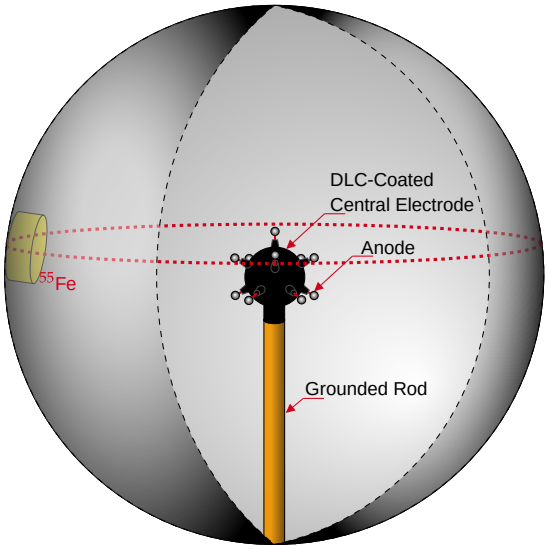

Figure 4.17: Schematic of the experimental set-up, with the position of the ^{55}Fe source relative to the ACHINOS.

Gain

The detector was filled with 500 mbar of Ar : CH4 (98% : 2%) and data were collected for a range of anode voltages at various pressures, and the amplitude of the 5.9 keV peak was recorded. These measurements, performed with the central electrode electrically floating, are presented in Fig. 4.18, where the detector is shown to operate in proportional mode over a wide pressure range. Furthermore, it is demonstrated that large gas gains (avalanche electron multiplication factor) of up to 10^4 can be achieved with this detector configuration.

Anode response uniformity

To check the uniformity of the sensor response, data were taken with the ^{55}Fe source at various longitudinal positions, while at a fixed latitude of approximately 12° below the equator, as shown schematically in figure 4.17. The detector was operated with 1000 mbar of Ar : CH4 (98% : 2%) and an anode voltage of 2200 V. The amplitude and local energy

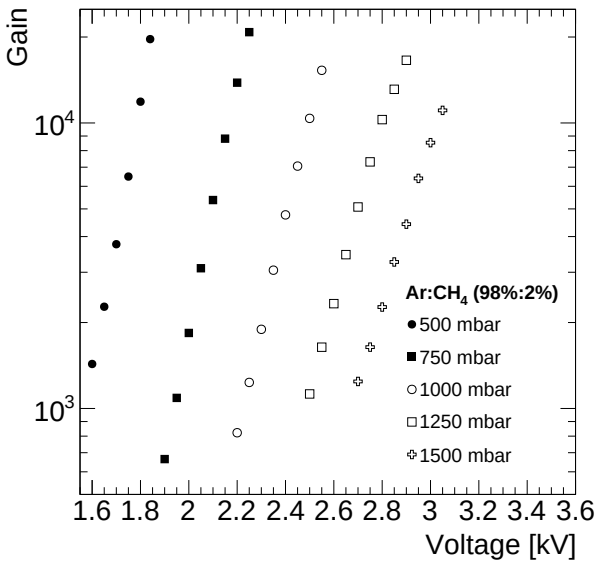

Figure 4.18: Measured amplitude versus the voltage applied to the anode for several pressures of Ar : CH4 (98% : 2%) in a spherical proportional counter using an ACHINOS.

resolution were estimated using the 5.9 keV peak and an example spectrum is shown in figure 4.19. A gaussian fit of this yielded an amplitude of (11090 ± 10) ADU, corresponding to a gas gain of 8.3×10^3, and a local energy resolution σ of $(7.4 \pm 0.1)\%$. The same procedure was repeated for the other measurements, with the results shown in figure 4.20(a) for the amplitude and figure 4.20(b) for the local energy resolution, which varies between 7.1% and 9.2%.

The maximum (minimum) amplitude at approximately 320° (210°) corresponds to a gas gain of 8.8×10^3 (5.7×10^3). To understand the origin of the amplitude modulation as a function of the azimuthal angle observed in Fig. 4.20(a) the dedicated simulation framework described in Sec. 4.1.2 was used. In the simulation, 50000 5.9 keV photons were generated near the cathode surface and directed within a 45° cone towards the detector centre. A similar analysis to those applied to the data was implemented. The open circles in Fig. 4.20(a) correspond to the simulation results which reproduce the modulation observed in the data.

To understand the origin of the effect, the 11-anodes of the ACHINOS were split in two

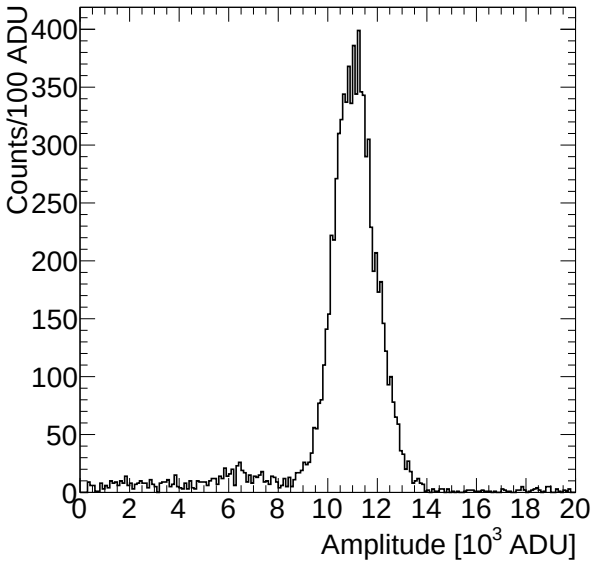

Figure 4.19: Energy spectrum from an ^{55}Fe source measured using a spherical proportional counter filled with 1000 mbar of Ar : CH4 (98% : 2%) and using an ACHINOS. The primary peak has an energy resolution (σ) of (7.4 ± 0.1)%. The second peak, to the left of the main one, is the argon escape peak.

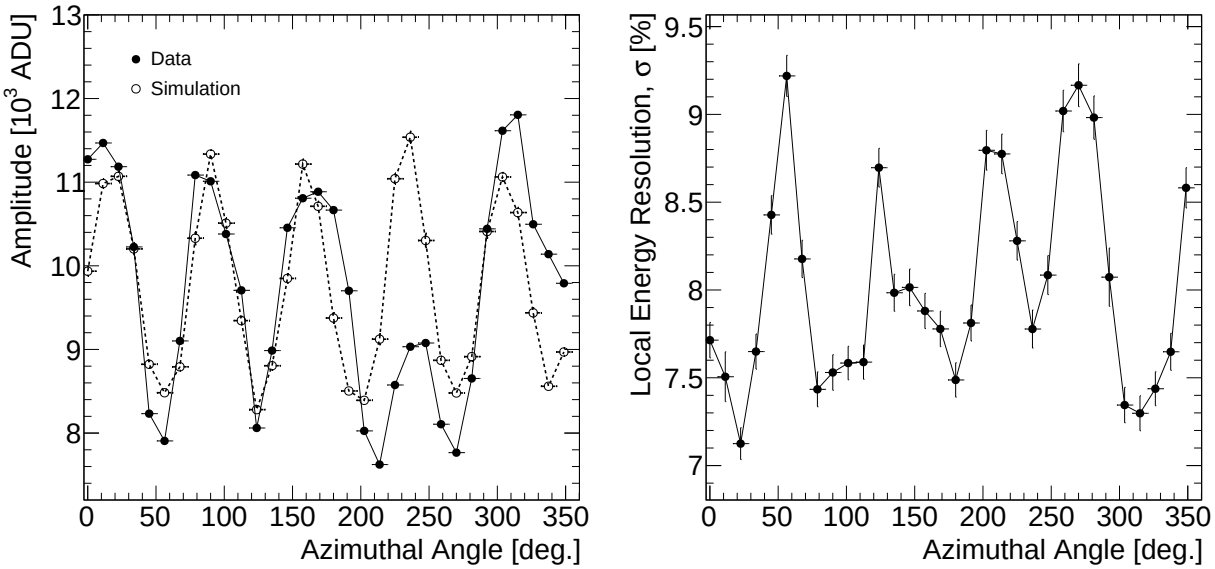

(a) (b)

Figure 4.20: Measured and simulated amplitude (a) and measured local energy resolution σ (b) of the 5.9 keV X-ray in a spherical proportional counter with an ACHINOS as a function of azimuthal angle. The detector was operated filled with 1000 mbar of Ar : CH4 (98% : 2%).

groups. The first group comprises the five co-planar anodes near the support rod, while the second group comprises the five co-planar anodes far from the support rod and the anode furthest away from the support rod. These two groups will be referred to as "Near Anodes" and "Far Anodes" respectively. In figure 4.21(a) the amplitudes recorded by reading out each set separately is presented. It is observed that the amplitudes are modulating in antiphase. The modulation in the data can then be explained as follows; as the source is moved around the sphere, the produced primary electrons are drifting towards different anodes, alternating between the Near and the Far anodes.

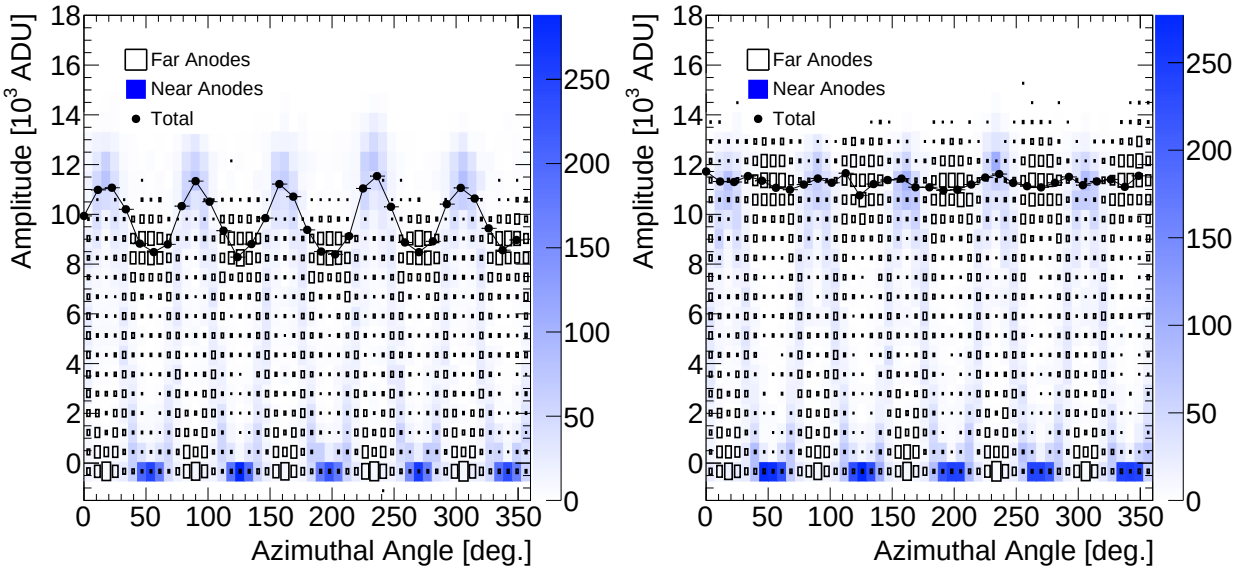

(a) (b)

Figure 4.21: (a) Simulated amplitude recorded by the Near and Far anodes as a function of azimuthal angle. The difference in relative maximum amplitude between the two is due to a higher electric field magnitude for the Near anodes, which is caused by their proximity to the rod. (b) The amplitude recorded by the Near and Far anodes in the case where 30 V more is applied to the Far anodes.

The relative difference in maximum amplitude between the Near and Far anodes is due to the gain difference between the two sides. The Near anodes exhibit an increased electric field due to the proximity to the grounded support rod, which results in deviations from the spherical symmetry. This effect can be readily corrected for by separately adjusting

the applied voltage to the Near and Far anodes. In Fig. 4.21(b) the simulation is repeated with the voltage applied to the Far anodes increased by 30 V. In this case the azimuthal dependence of the amplitude is minimised, and could be eliminated by further tuning of the Far anode's voltage.

A potential source of additional response non-uniformity may arise from construction differences of the individual anodes. This effect is not included in the simulation, however, it can be estimated from the experimental data. The difference in amplitude within the two sets of co-planar anodes are typically within 10%. This is shown in Fig. 4.20(a), where a single outlier is also observed in each of the sets. These differences are attributed to variations in the anode radii, the smoothness of the anode surface, and the distance to the central electrode. These non-uniformities can be corrected for either with an anode-by-anode calibration, when each anode is read-out individually, or by applying a different voltage to each anode in order to achieve the same gain.

Near-Far Voltage Correction

It was hypothesised that for a given ACHINOS geometry, the ratio of the Near and Far anode voltages would be constant, regardless of absolute voltage applied to the anodes. In order to study this, ANSYS was used to produce electric field maps for various ratios of Near to Far anode voltages, for three ACHINOS with different absolute anode voltages of 1500 V, 2250 V, and 3000 V. The ACHINOS model used anodes with ⌀1.7 mm anodes at r_s = 13.5 mm inside a ⌀15 cm detector. The field maps produced were used in the simulation framework to repeat the experiment described in the previous section and 20000 5.9 keV photons were generated in each case, with the results shown in Fig. 4.22. The amplitude as a function of azimuthal angle again shows a sinusoidal-like behaviour. The distribution was fit with a function of the form $y = A\sin(bx + \phi) + c$ and the amplitude

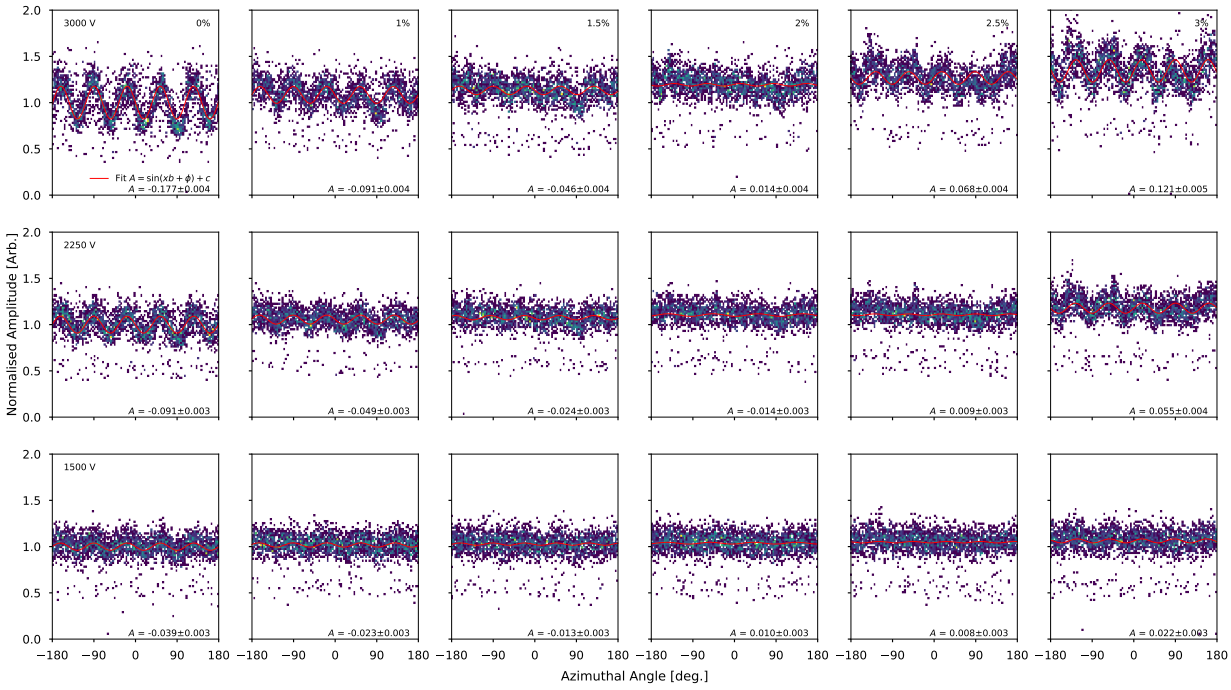

Figure 4.22: Simulated amplitude recorded by an ACHINOS for 5.9 keV photons were generated near the cathode surface and directed within a 45° cone towards the detector centre. Rows correspond to different voltages applied to the Near anodes; columns correspond to successively higher voltages on the Far anode. The distributions were fit with a sinusoidal function, and the amplitude A is shown for each.

A of the function, shown in each panel of Fig. 4.22, was used to assess the homogeneity. The value of A for each set was plotted against the percentage increase in Far voltage and a linear fit performed to obtain the value where $A = 0$, as can be seen in Fig. 4.23. It can be seen that for the explored cases, the most homogenous response is found when the Far anodes have approximately 2% higher voltage applied to them.

Cross Talk

The capability to read-out the Near and Far anodes separately has been implemented experimentally. However, initial tests showed that when a signal was detected on either the Near

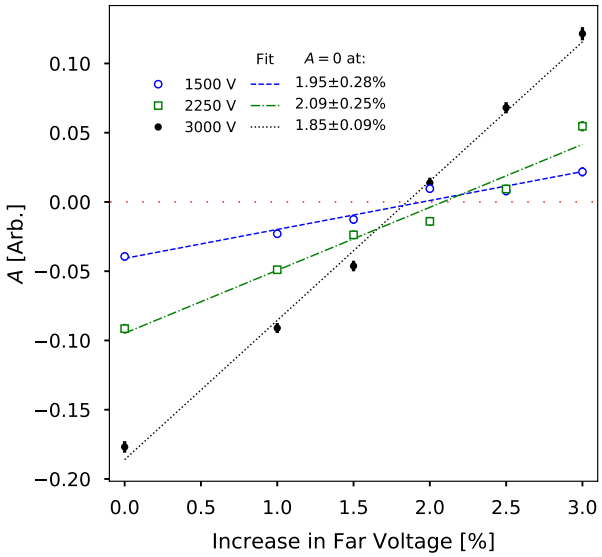

Figure 4.23: Amplitude A of sinusoidal function from fits in Fig. 4.22 as a function of the percentage increase in voltage applied to the Far anodes for three voltages applied to the Near anodes. A linear fit was applied to each data set and the increase in Far voltage required for $A = 0$ (red dotted line), which is considered to have the most homogeneous field, is given.

or the Far channel, it was often accompanied by a much smaller amplitude negative signal or a positive signal on the other channel. In order to understand this, weighting field were produced in ANSYS for the Near and Far anodes and were incorporated into the simulation framework. Examples of a signal exhibiting the same behaviour as observed in the experiment can be seen in Fig. 4.24. In the case where both channels have a positive signal, it was found that the electrons produced by the incident interaction, which is a 5.9 keV photon in the simulation, were being collected at both the Near and Far anodes.

In the case where a negative signal was observed, which corresponds to a positive current due to sign change introduced by the preamplifier, it was found that all of the electrons were collected to the side showing the positive signal. This is understood through the Shockly-Ramo theorem (Eq. 3.12). In Fig. 4.25 the electric field around the Far anodes is shown in both panels, with the weighting fields of the Far (Near) anodes overlaid in the left (right) panel. It can be seen that, while the weighting field of the Far and the electric field are

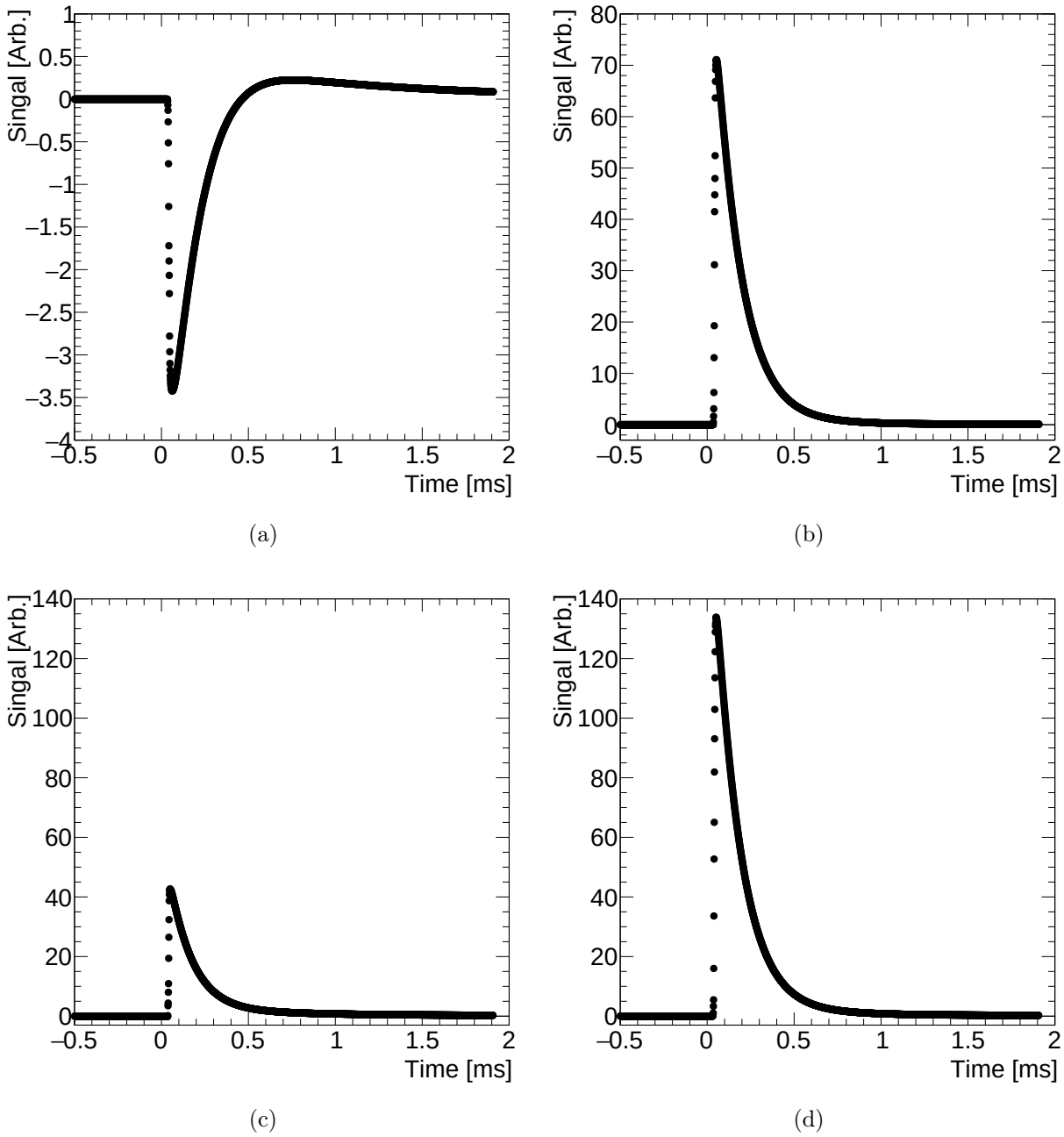

Figure 4.24: Signals induced by the interaction of a 5.9 keV photon in the gas on the Far ((a) and (c)) and Near ((b) and (d)) anodes. The pulses in each row correspond to the same event; in the top row all of the electrons generated by the interaction arrived to the Near anodes, while in the bottom row the 24% of the electrons arrived to the Far. The negative signal observed in (a) is explained by the Shockley-Ramo theorem (see text). Note the figures in the top row how different y-axis scales.

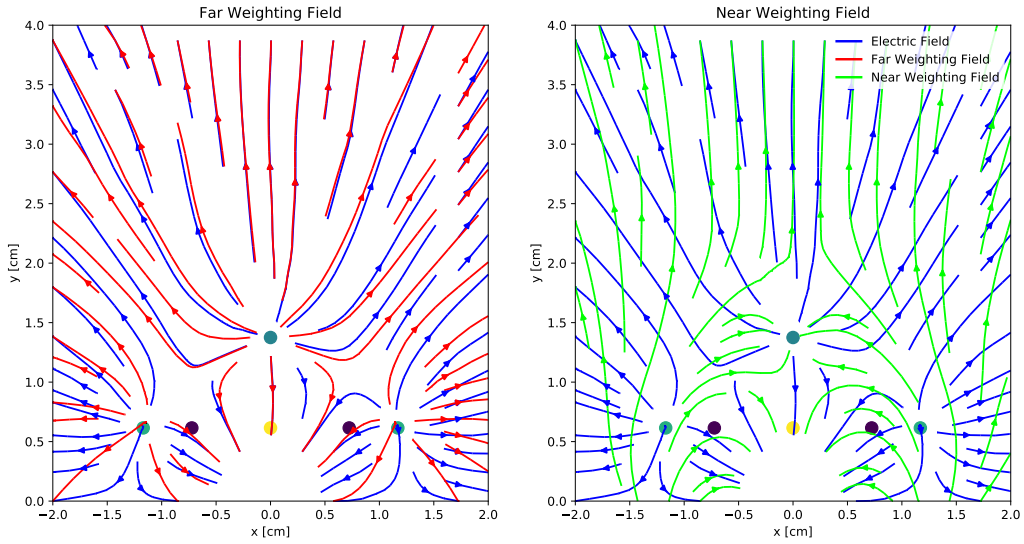

Figure 4.25: Electric field and weighting fields of the Near and Far anodes in the vicinity of the Far anodes.

mostly parallel, the Near weighting field is generally not aligned with the electric field at the surface of the anodes and is anti-parallel in places. Ions drifting away from the Far anodes will follow the electric field lines - neglecting diffusion - and so, by Shockly-Ramo theorem, the scalar product of the weighting field and velocity will be positive, resulting in a negative current and so a positive signal. However, for the signal generated at the Near anodes, the product of the field and velocity vectors will be negative, resulting in a negative signal.

Stability

The detector operated stably filled with 1000 mbar of Ar : CH4 (98% : 2%) and the anode voltage set to 2200 V. The amplitude of the ^{55}Fe peak was monitored and no significant gain variations were observed over approximately 15 hours, as shown in figure 4.26. The gradual decrease in gain over time is attributed to the introduction of contaminants coming from outgassing and leaks in the vacuum system, a behaviour that has been observed in earlier studies.

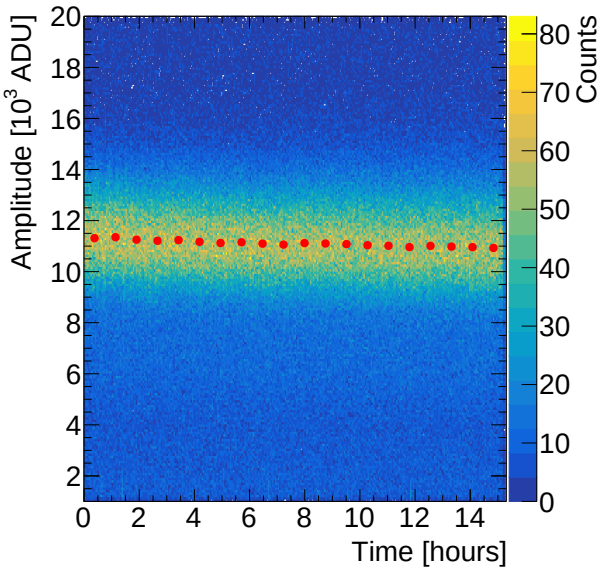

Figure 4.26: Amplitude versus time for a spherical proportional counter filled with 1000 mbar of Ar : CH4 (98% : 2%) and using an ACHINOS. The red points superimposed on the histogram show the mean amplitude in time slices. The slight decrease in amplitude with time is attributed to impurities leaking into the detector.

In further tests, the sensor was operated without issues for a period of 30 days despite an observed average of approximately one discharge per day. Furthermore, no damage was observed following intentionally induced discharges in a spark-test chamber.

4.3.5 Future developments

Improvements in the manufacturing provide a path to improve the ACHINOS construction, including the production of assembly tools for anode alignment and attachment of wires. As an example, an assembly tool constructed is shown in Fig. 4.27(a), along with the spacers used to align the anodes with during assembly, shown in Fig. 4.27(b).

To further improve the ACHINOS performance, the gain variation among different anodes needs to be reduced. A possible source of this variation arises from irregularities in the shape of the individual anodes. Methods to characterise and identify defective anodes before their

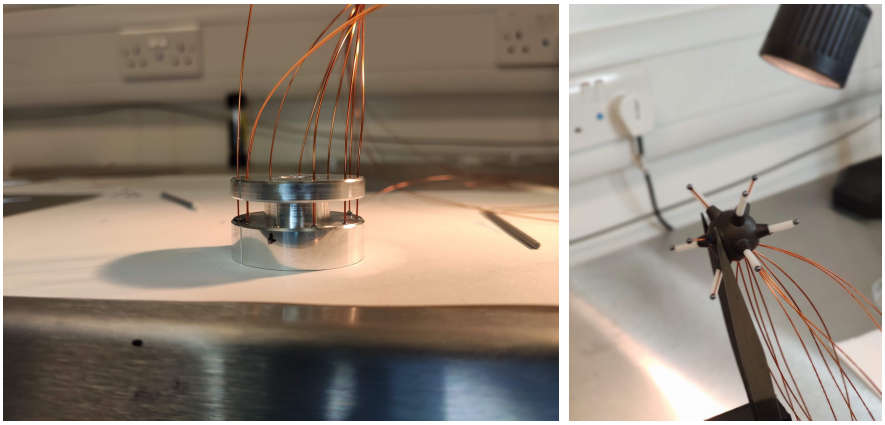

(a) (b)

Figure 4.27: (a) Assembly tool used for simultaneously bonding several wires and anodes. (b) An ACHINOS being constructed using custom-made spacers to position and align the anodes.

incorporation into a module, such as using a digital microscope to inspect the surface, would improve the construction.

To further increase the usefulness of ACHINOS as gas pressures are increased, anodes with smaller radii of order 100 µm, will be required. This would facilitate achievement of higher gain by increasing the electric field near the anode surface, without further increase of the anode voltage. An important challenge towards smaller anode radii is the bonding to the read-out wire, which needs to be performed in a manner that minimises exposed contacts which may lead to discharges. Several methods for achieving this are being explored. Firstly, the use of fast-setting conductive adhesives reduce the time that the wire and anode must be maintained in contact and well aligned. The use of precision tools for the construction can provide this alignment. A second alternative is the use of a wire-bonding technique to attach the wire.

Furthermore, the number and configuration of anodes in the ACHINOS may be optimised for each specific application, depending on the size and pressure of the vessel. These developments are being guided by FEM calculations and the dedicated simulation framework

previously discussed. In Fig. 4.28(a), the electric field magnitude as a function of radius is shown for a single-anode module, an 11-anode ACHINOS and an 'Infinite anodes ACHINOS' approximation, where the field is calculated analytically with Eq. 3.58 under the approximation that there is an infinite number of anodes all located at r_s, i.e. $r_a \rightarrow r_s$. This presents the highest electric field achievable at large radii with a given r_s. While the 11-anode ACHINOS provides an improvement in electric field magnitude over the single-anode module, it is significantly lower than the infinite anode limit and only provides a 0.04 V cm^{-1} electric field at the cathode surface. A prototype 60-anode ACHINOS has designed, shown in Fig. 4.28(b), with the anodes placed at the vertices of a truncated icosahedron, to increase the electric field at larger radii as shown in Fig. 4.28(a). This holds particular relevance for the proposed future spherical proportional counter for a direct DM search, DarkSPHERE, which will be discussed further in Chapter 7.

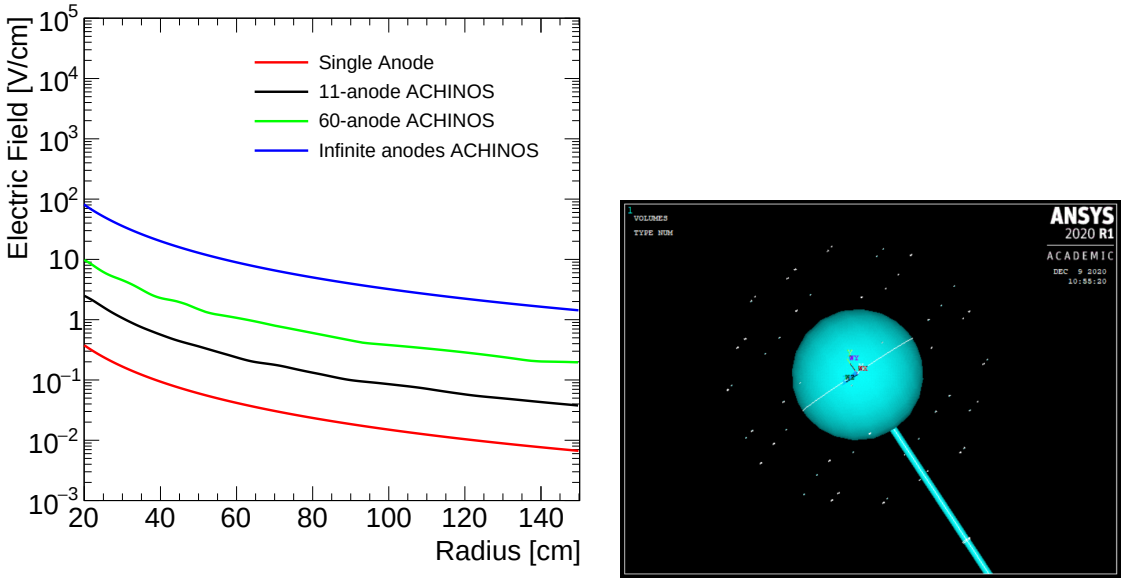

(a) (b)

Figure 4.28: (a) Electric field magnitude as a function of radius for a ⌀3 m spherical proportional counter for various read-out modules, each using ⌀1 mm anodes and an ACHINOS radius r_s (distance between each anode and the centre) of 10 cm. 'Infinite anodes ACHINOS' refers to the approximation where there are an infinite number of anodes all located at r_s. (a) The ANSYS model of the prototype 60-anode ACHINOS.

Another significant advancement would be the individual read-out and biasing of each anode. This would allow for the correction of differences in gain between individual anodes and anode-by-anode calibration. Additionally, reading out each anode individually would provide information about the part of the detector which an interaction took place in. In the case of tracks of ionisation, the sharing of ionisation electrons between different anodes would provide information about the particle's trajectory through the detector. Coupled with the interaction radius inferred from pulse rise-time [140], this information could allow the three-dimensional reconstruction of the ionisation track. The increased number of anodes of the 60-anode prototype may also provide increased position resolution. Investigation into the feasibility of this are already ongoing, and would be of particular importance to direct DM searches. As discussed in Chapter 2, the motion of the Sun about the galactic centre means that the DM-induced nuclear recoil spectrum is expected to be peaked in the direction of the Sun's motion. Observing directionality in a DM candidate signal provides a powerful signature for DM and also a strong background discrimination tool. Directionality also provides a tool for discriminating CEνNS interactions, which are primarily induced by solar neutrinos in the energy range of interest to NEWS-G. Selection against events with tracks originating from the Sun allows sensitivity to DM below the 'neutrino floor' - the DM-nucleon cross section at which the number of events in a given target medium is expected to be less than the number of CEνNS interactions, for a given DM candidate mass.

4.4 Segmented Rod Correction Electrodes

While the second correction electrode restores the homogeneity of the electric field near the anode and the ACHINOS address the challenge of the coupled drift and avalanche fields, the electric field homogeneity at larger radii remains distorted by the grounded rod, which can be seen in Fig. 4.30. This results in a larger drift time for electrons generated near the

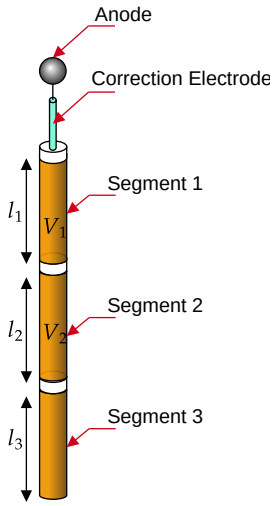

Figure 4.29: Schematic of the segmented rod correction electrode.

rod, thus more diffusion, and a commensurate increase in the pulse rise time. In the ideal detector, the electric potential difference V between a point at radius r and the grounded cathode can be derived by substituting Eq. 3.58 into the integral from of Eq. 3.56

$$V(r) - V(r_c) = V(r) = -\int_{r_c}^{r} \boldsymbol{E}(r) \cdot \mathrm{d}\boldsymbol{r}$$
$$V(r) = V_0 \frac{r_a}{r_c - r_a}\left(\frac{r_c}{r} - 1\right) . \tag{4.6}$$

In order to restore the ideal $1/r$ voltage dependence, a voltage could be applied to the grounded rod. A method to approximately achieve this, and can be practically implemented experimentally, is to divide the rod into several segments and apply a voltage to each. The tested configuration is shown schematically in Fig. 4.29. The rod is divided into three segments; the two nearest the anode have voltages V_1 and V_2, respectively, applied to them while the third is grounded by its contact with the cathode sphere.

This configuration was studied using FEM calculations for a single anode sensor module with an anode voltage of 2000 V. After accounting for the anode of 1.5 mm radius, a 4 mm separation between the anode and the second correction electrode, which itself is 10 mm

Table 4.1: Summary of configurations tested for segmented rod.

Segment Lengths l_1, l_2 [mm]	Central Segment Voltages V_1, V_2 [V]	Average Segment Voltages V_1, V_2 [V]
90, 26	21.60, 2.93	28.70, 3.01
26, 90	57.36, 12.82	57.36, 12.82
40.5, 40.5	43.25, 13.94	47.54, 14.55
58, 58	33.43, 6.15	39.06, 6.73

long, and the 2 mm plastic alignment piece used to hold it in place, the first segment starts at a radius of 17.5 mm. The segments are separated by 0.5 mm long plastic pieces, leaving 131.5 cm for total length of the segments. The lengths l_1, l_3, and l_3, respectively, of each segment and the voltages V_1 and V_2 were variables to be adjusted in the FEM calculation. Four configurations for the segment lengths and two voltage configurations for each were considered and are summarised in Tab 4.1. The 'central' voltage is the potential difference at the centre of the segment given by Eq. 4.6 and the 'average voltage' corresponds to the average voltage over the segment length which extends radially from r_2 to r_1 (i.e. $r_2 < r_1$),

$$\bar{V_{1,2}} = \frac{V_0}{r_2 - r_1} \frac{r_a}{r_b - r_a} \left(r_b \ln \left(\frac{r_2}{r_1} \right) + r_1 - r_2 \right) . \tag{4.7}$$

The influence of the segmented rod was first investigated near the anode and was found not to impair the homogeneity brought by the second correction electrode. The impact of each configuration on the homogeneity of the electric field at the outside of the detector is plotted in Fig. 4.30 for the central and average voltage schemes. All tested configurations offer a similar improvement in electric field magnitude and homogeneity. Experimental tests to verify this are planned for the future. Additionally, further improvements to homogeneity may be possible through the use of more segments, which could be achieved by applying a covering material to the rod with conductive strips on it. A resistive layer could then be applied to give a voltage gradient along the strips. The use of DLC-coated materials to achieve this are being explored.

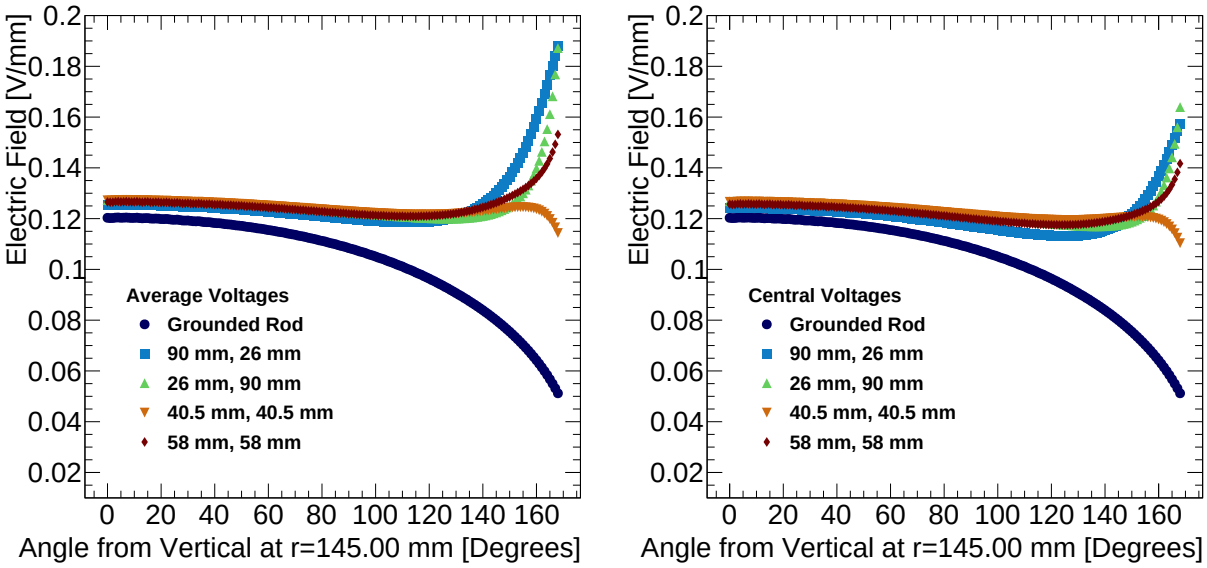

(a) (b)

Figure 4.30: Electric field magnitude as function of polar angle at a radius of 145 mm in a ⌀30 cm spherical proportional counter for different configurations of segments for the rod in the case where (a) average voltages are applied to the segments and (b) the central voltage is applied to the segment.

5

Ionisation by Nuclear Recoils

As mentioned in Chapter 3, recoiling nuclei induced by an elastic DM interaction can deposit their energy in a medium in a variety of ways. A detector typically is only sensitive to a part of this energy deposition, the rest being dissipated by 'invisible' means. For ionisation, this is quantified by the ionisation quenching factor, and it is a vital ingredient for NEWS-G DM searches. This chapter discusses the various definitions of the quenching factor, how it is calculated from theory and simulation packages, how it is measured in other media, and the few measurements in gases. A method for calculating it from previous, well-established measurements of the W-value is then presented for several gases down to keV and even sub-keV recoil energies. This work is presented in detail in Ref. [7], of which I am a main author and heavily contributed to the preparation of the manuscript. As a result, texts and figures from Ref. [7] are included here.

5.1 Ionisation Quenching Factor

Low energy nuclear recoils, such as those produced by a DM interaction, dissipate energy in a medium through electronic energy losses – inelastic Coulomb interactions with atomic electrons – and nuclear energy losses – elastic scattering in the screened electric field of the nuclei. While electronic energy losses dominate for fast ions, nuclear energy losses are increasingly important with decreasing ion kinetic energy E_R, and become dominant when the ion velocity is smaller than the electron orbital velocity [175]. The produced secondary recoil atoms and electrons may also undergo scattering, further transferring energy to other particles.

The partition of the total deposited energy is shared between different processes, which may be visible or not to a given detector, is parameterised by the quenching factor. In the literature, multiple definitions of the ionisation quenching factor may be found depending on the application:

q_{f_1}: the fraction of the ion kinetic energy that is dissipated in a medium in the form of ionisation electrons and excitation of atomic and quasi-molecular states – the definition of Lindhard et al. [176];

q_{f_2}: the ratio of the "visible" energy (i.e. charge) in an ionisation detector to recoil kinetic energy; and

q_{f_3}: the conversion factor between the kinetic energy of an electron and that of an ion that result to the same visible energy in the ionisation detector.

The "visible" refers to energy dissipated in a detectable form for the specific detection system, i.e. ionisation for detectors measuring charge. In each case, the ionisation quenching factor is a function of energy.

In order to measure the ionisation quenching factor in a material, the amount of ionisation induced by an ion species has to be measured as a function of its kinetic energy and compared to the corresponding ionisation by electrons of the same initial energy. This is the second definition and the ionisation quenching factor then takes the form,

$$q_{f_2} = E_d/E_R\,, \tag{5.1}$$

where E_d is the amount of electronic energy losses "visible" to a detector [177, 178]. Each of the definitions will be discussed in more detail in the following.

In direct DM searches, the quenching factor is used to infer the initial energy of a recoiling nucleus from the energy it deposited in the detector, and so is of critical importance. However, due to the fact that ions with precisely known kinetic energy are required, along with the capability to measure small energy deposits, measurements for low-energy recoils in gases are sparse. Methods for calculating the quenching factor will be discussed, followed by techniques used to measure it, by other DM experiments and also in gases, and finally how it may be calculated from W measurements in the literature.

5.2 Calculations of Quenching Factor

5.2.1 Lindhard Theory

Lindhard et al. pioneered the estimation of electronic and nuclear stopping powers for ions, and introduced the concept of ionisation quenching factor, q_f [176]. The energy deposited is considered to be portioned, independently, between atomic motion E_{k} and electronic excitation E_{ex}, and calculated each by integrating the electronic and nuclear stopping powers until the ion has dissipated all of its energy. The maximum available energy for ionisation

and scintillation is E_{ex}, with Lindhard et al. defining the quenching factor as the ratio of energy given to the electronic excitation over the ion's initial kinetic energy, E_{ex}/E_R. This is the first definition, q_{f_1}, given in Section 5.1.

A common parameterisation of the energy dependence of this model's quenching factor, for the case of a homogenous, monatomic target medium with the same atom being the incident one, is [54, 179, 180],

$$q_{f_1} = \frac{kg(\varepsilon)}{1 + kg(\varepsilon)}\,, \tag{5.2}$$

where $\epsilon = 11.5\frac{E_R}{1\,\text{keV}}Z^{-7/3}$ and $k = 0.133Z^{2/3}A^{-1/2}$, with Z and A the atomic number and atomic mass of the target medium's atoms. The function $g(\varepsilon)$ has been fit from the original graphical representation, yielding [54],

$$g(\varepsilon) = 3\varepsilon^{0.15} + 0.7\varepsilon^{0.6} + \varepsilon\,. \tag{5.3}$$

The quantity k is related to the electronic stopping power, and is usually left as a free parameter when the Lindhard model is used to fit experimental data.

Lindhard et al. caution that assumptions of the model may not be valid for energies below $\epsilon < 0.01$, corresponding to $\mathcal{O}(1 - 10\,\text{keV})$ for most ions [181]. The theory does not account for the interaction of secondary ions, which can induce further electronic energy losses [182]. Approximations to extend this parametrisation to different incident nuclei recoiling in a target or even a compound have been explored in the literature [182].

5.2.2 SRIM

SRIM [183] (Stopping and Range of Ions in Matter) is a computational tool primarily used for the estimation of ion ranges in matter. It is based on fits of experimental measurements of

the nuclear and electronic stopping powers. TRIM (TRansport of Ions in Matter), a module of SRIM, is a Monte Carlo tool often used to estimate the ionisation quenching factor in materials as it provides estimates for the portions of ion kinetic energy dissipated in electronic and nuclear energy losses, including contributions of secondary recoils. This aligns with the first definition of the quenching factor, q_{f_1}. In Fig. 5.1, TRIM simulations of the spatial profile of energy dissipation for light and heavy ions in a medium are shown. Heavier ions, like Ar^+ shown in Fig. 5.1(a), are subject to a higher rate of elastic scattering compared to lighter ions, such as protons shown in Fig. 5.1(b), of the same kinetic energy. TRIM estimates of the ionisation quenching factor of heavy ions in their own gas are presented in Fig. 5.2.

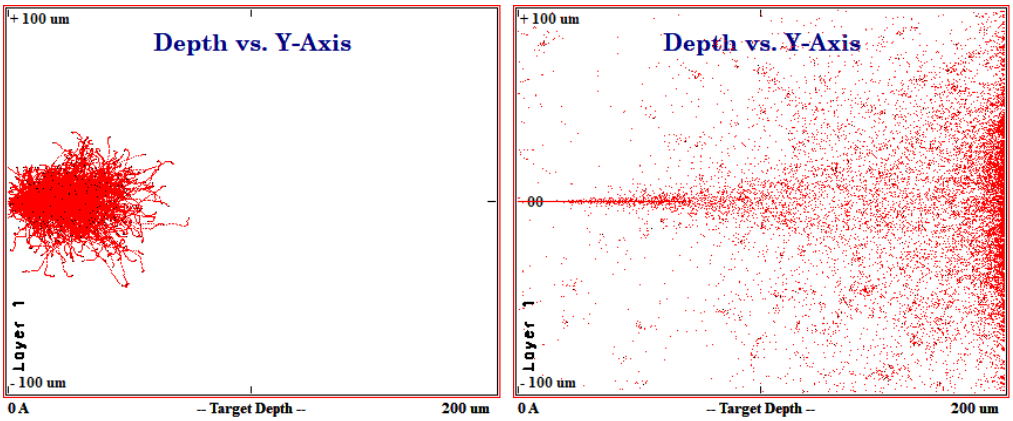

(a) (b)

Figure 5.1: Tracks of (a) 10 keV Ar^+ and (b) 10 keV protons in Ar gas simulated using SRIM. Figures reproduced from Ref. [7].

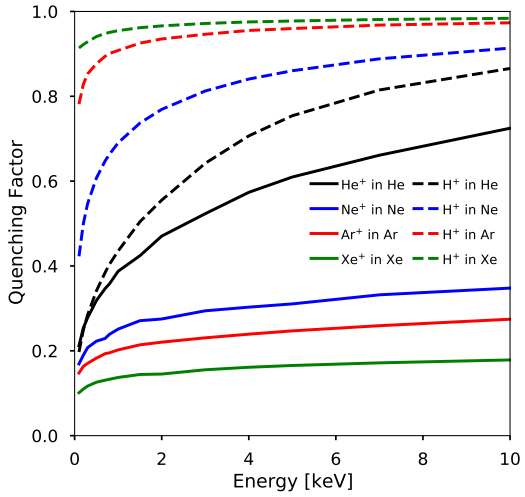

Figure 5.2: Quenching factor for ions in their own gas estimated using TRIM.

5.3 Measurements of Quenching Factor

5.3.1 Gas

To measure the quenching factor, recoil nuclei with precisely known kinetic energy are required, along with the capability to measure small energy deposits. As a result, although the ionisation quenching factor is critical for the modelling of the detector response to nuclear recoils — and, thus, for the sensitivity to discover DM — relevant measurements are scarce for low energy ions in gases.

Measurements have been performed by Santos et al. [184] and Tampon et al. [185], investigating the quenching of He^+ in He/C_4H_8 gas mixtures using an ion source and protons in C_4H_{10}/CHF_3 gas mixtures using a table-top low energy ion-electron accelerator, COMIMAC [186]. The measurements were performed with a Micromegas proportional counter [187]. The ionisation quenching factor was estimated as the ratio of the energy measured in the detector for ions to their initial total kinetic energy.

Measurements have also been performed with COMIMAC using a spherical proportional counter. The set-up for these measurements in presented in Fig. 5.3. The COMIMAC facility uses a COmpact MIcrowave Coaxial (COMIC) source, which is a compact Electron Cyclotron Resonance (ECR) source [188]. Low-pressure gas, $\mathcal{O}(10^{-2}$ mbar), inside the device is ionised to form a plasma. Electrons or ions are then extracted by an electric potential from a plasma in the accelerator and are passed through a $\varnothing$1 µm hole in a 13 µm plate which separates the low-pressure of the accelerator and the gas in the detector, which in this case was a 30 cm diameter spherical proportional counter. The electron beam extracted is pure, as they are the only negative ion species present in the plasma. However, the ion beam will contain any positive ion species in the plasma. A Wien filter [189] is used to select the desired species based on their mass, using orthogonal magnetic and electric field that are also orthogonal to the beam direction.

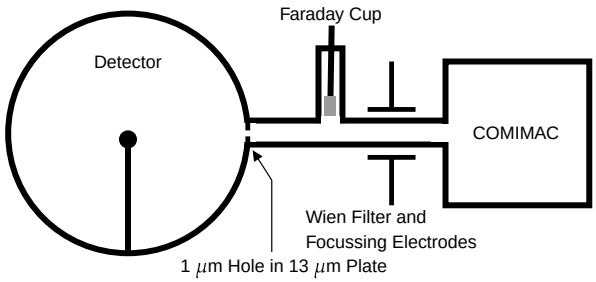

Figure 5.3: Set-up of the COMIMAC facility with a spherical proportional counter. The Faraday cup may be lowered into the path of the beam to monitor the beam current. The Wien filter uses orthogonal electric and magnetic fields to divert all but the desired ion species from the beam.

Several measurement campaigns were conducted, using He:CH_4 (95% : 5%), He:CH_4 (98% : 2%) and CH_4. The methodology in each campaign was similar, with just the gas under investigation and the read-out sensor changing between them, with the last campaign using an ACHINOS sensor.

In order to measure the quenching factor, the detector was first calibrated with electrons

of various energies. As an example, the rise time versus amplitude observed for a 6 keV electrons in He:CH_4 (95% : 5%) at 1 bar are shown in Fig. 5.4(a). Following a selection on the rise time and the pulse width to remove cosmic muons, the amplitude was fit with a Gaussian distribution to obtain the position of the peak, which is shown for the 6 keV electrons in Fig. 5.4(b).

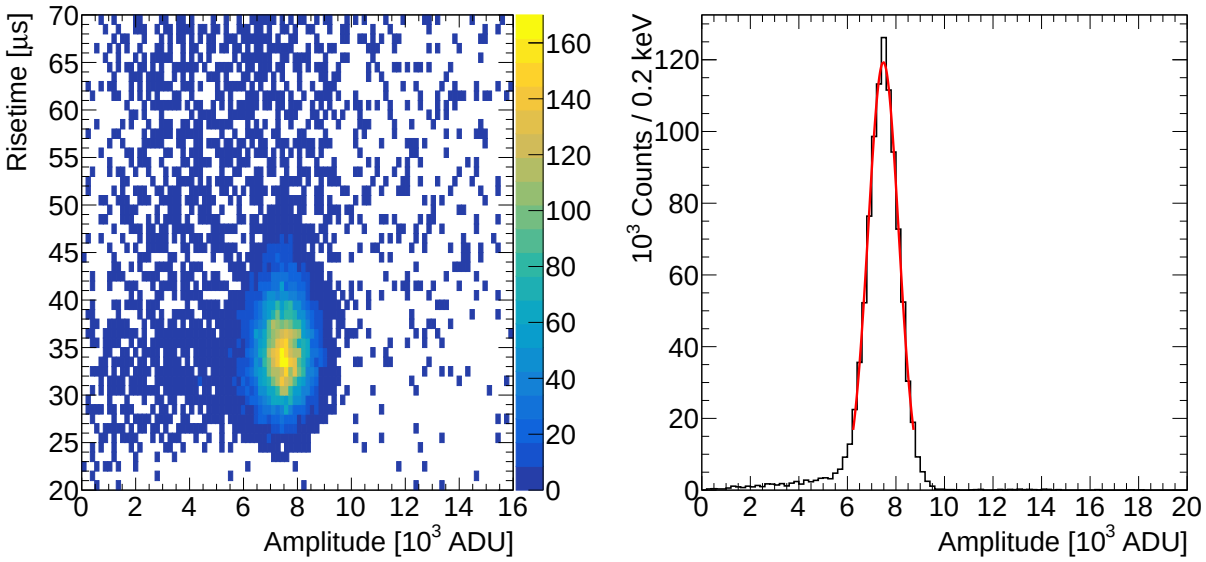

(a) (b)

Figure 5.4: (a) Pulse rise time versus amplitude and (b) amplitude distribution for a 6 keV electrons in He:CH_4 (95% : 5%) at 1 bar, after rise time and pulse width selections are applied. The mean of the electron peak is at $(7.48 \pm 0.01)10^3$ ADU.

The ions were treated in a similar way, with an example amplitude distribution for 6 keV ions in He:CH_4 (95% : 5%) at 1 bar shown in Fig. 5.5(a). Using the electron amplitudes at each energy, the detector could be calibrated, and the ion amplitudes compared to this to calculate the ionisation quenching factor, in line with definition q_{f_2}. A comparison of the electron and ion amplitudes recorded is shown in Fig. 5.5(b). The two points at 6 keV were obtained at the beginning and end the data taking.

Fig. 5.5(b) shows an unexpected non-linear trend in the electron calibration line.. The spherical proportional counter has previously been shown to exhibit a linear energy dependence

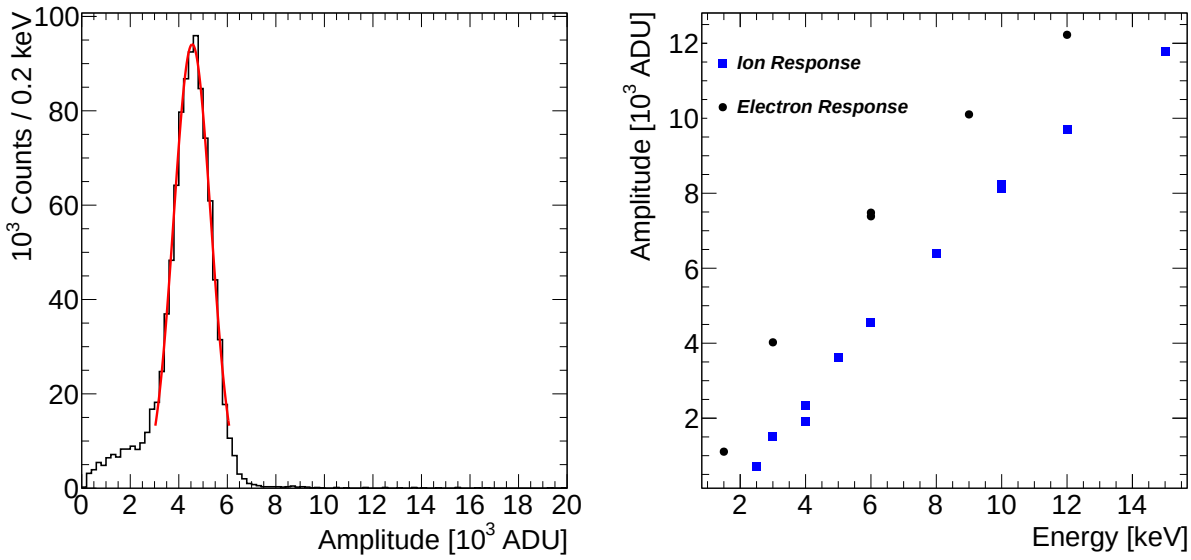

(a) (b)

Figure 5.5: (a) Amplitude distribution for 6 keV $^4He^+$ ions in He:CH_4 (95% : 5%) at 1 bar with selections applied on the rise time and width to remove cosmic muon background, and fit with a Gaussian distribution. The mean of the peak is at $(4.55 \pm 0.01)10^3$ ADU. (b) Comparison of the electron and ion amplitudes as a function of particle energy.

with amplitude in this energy region [141]. Potential sources of this discrepancy are energy loss from scattering in the detector-accelerator interface and incomplete charge collection of the ionisation electrons created by the incident electrons. The latter may be caused by ionisation electrons being produced close to the interface and generating enough charge density to cause significant recombination or electron loss to the cathode. This space-charge effect would be more pronounced for lower energy particles. A 10 keV electron will have a range of approximately 1.4 cm in 1 bar of helium, and will decrease significantly below this at lower energies [190]. However, ions of the same energy have a range of only 1.5 mm [183].

The space charge effect would also be greater with a higher rate of initial particles from the source resulting in a lower recorded pulse amplitude. To reduce this effect, an ACHINOS sensor was installed, which increases the electric field at larger radii and so reduces the buildup of electrons near the interface. To investigate if the rate has an effect on the amplitude, the

rate of 6 keV electrons from the source was varied during data taking. The detector was operated with 200 mbar of CH_4, and the recorded amplitude as a function of time is shown in Fig. 5.6(a). The data was divided into 24 equal time slices and the amplitude in each slice was fit with a Gaussian distribution to determine the mean. The mean amplitude and the rate in each time slice are presented in Fig. 5.6(b) and show a rate dependence of the amplitude. However, the change to the amplitude for an increase in rate from 100 Hz to 200 Hz is of the order of 1%, whereas most data was taken with a rate less than 100 Hz so other factors are likely contributing to the departure from linearity.

Analysis of data from the various measurement campaigns is ongoing to identify any potential systematic effect in order to assess the ionisation quenching factor.

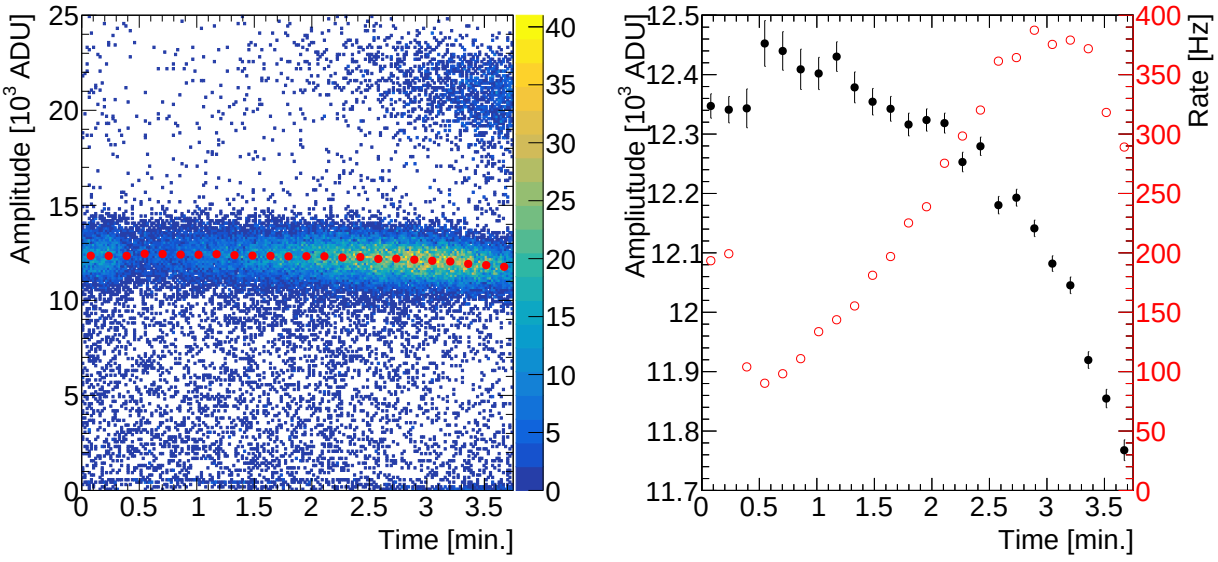

(a) (b)

Figure 5.6: (a) Amplitude recorded for 6 keV electrons versus time with 200 mbar of CH_4. Points indicate the mean of a Gaussian fit to the amplitude in time slices during the data taking. The second accumulation at higher amplitude which grows in population after around 2 minutes is pile-up caused by the increasing rate. (b) The mean of a Gaussian fit to the amplitude (solid black) and the rate (open red) in slices of time during the data taking. The decrease in recorded rate after 3 minutes is due to the increase in dead time.

5.3.2 Other Materials

The quenching factor is of great importance to all experiments observing from low-energy nuclear recoils. Typically, it is measured using a source of neutrons that interact in the material to induce nuclear recoils with an energy given by Eq. 2.29, with the DM mass and kinetic energy replaced by that of the neutron. Due to the angular dependence of the scattering, the neutron interactions induce a spectrum of recoil energies, complicating the quenching factor estimation. Several methods are employed to overcome this. In one method, beams of neutrons are directed onto the detector using the sample material of interest, where they may induce a nuclear recoil, emerge having scattered through some angle and be measured in a backing detector [180]. The coincident interaction in the sample material and known location of the backing detector allows the angle to be calculated, and so the recoil energy to be inferred. The signal induced by the recoil can then be compared to that produced by electrons and the quenching factor computed. A second method is to compare the measured nuclear recoil spectrums induced by a neutron beam and compare this to simulations of the unquenched recoil distribution [191, 179]. A model of the quenching factor is then applied to the simulated data and fit to the measured data. It is helpful to use neutron sources with distinct energy features or mono-energetic beams in order to minimise degeneracies when fitting to the simulated spectrum. Typical sources used for this are ^{241}Am-Be, ^{252}Cf and 'photoneutron' sources, such as ^{88}Y-Be or ^{124}Sb-Be, which provide near-monoenergetic neutrons with energies 152 keV and 23 keV, respectively, from (γ, n) reactions [192, 191, 193].

5.4 Quenching Factor from W-value Measurements

5.4.1 The W-value

The W-value, W, defined in Eq. 3.20, is the average energy required to produce an electron-ion pair and includes any ionisation produced by secondary particles e.g. δ-electrons, bremsstrahlung photons, or electron and nuclear recoils [194].

The W-value contains all the required information for converting the kinetic energy dissipated by ionising radiation in a medium to electric charge, and vice versa. The magnitude of the W-value is the outcome of the competition between ionising and non-ionising processes, such as excitation of atomic electrons and molecular degrees of freedom, dissociation processes (neutral fragmentation) in molecular gases, and production of neutral atomic recoils. As a result, the W-value also depends on the interacting particle species and, in general, tends to a constant value for increasing energy.

5.4.2 Energy dependence of W-value

Electrons

The W-value can be understood by examining how the energy deposited by an interacting particle is shared between different processes, such as that described in Ref. [195] for pure gases. The dissipated energy is apportioned between: 1. production of electron-ion pairs; and 2. production of discrete excited states or neutral dissociation fragments; 3. production of sub-excitation electrons, with kinetic energy below the lowest electronic excitation energy of the medium, namely, ionisation, excitation and heat. This can be summarised by the

relation,

$$E = N_T \bar{E}_T + N_{ex} \bar{E}_{ex} + N_T \epsilon \,, \tag{5.4}$$

where $\bar{E}_i$ is the mean energy transfer per electron-ion pair, N_{ex} is the mean number of excited states produced, $\bar{E}_{ex}$ is the mean energy transfer per excited state, and ϵ is the mean kinetic energy carried by sub-excitation electrons. From the definition of the W-value in Eq. 3.20, dividing Eq. 5.4 by N_T obtains the W-value,

$$W = \bar{E}_i + \frac{N_{ex}}{N_T} \bar{E}_{ex} + \epsilon \,. \tag{5.5}$$

It is conventional to express Eq. 5.5 in terms of the first ionisation energy I of the gas,

$$\frac{W}{I} = \frac{\bar{E}_i}{I} + \frac{N_{ex}}{N_i} \frac{\bar{E}_{ex}}{I} + \frac{\epsilon}{I} \,. \tag{5.6}$$

Since every term on the right-hand side of Eq. 5.6 depends on the energy of the ionising particle, the W-value also exhibits an energy dependence, which becomes weaker for $E \gg I$. Overall, high energy ionising particles have a W/I ratio of 1.7–1.8 in noble gases and 2.1–2.5 in molecular gases [195].

The energy dependence of the electron W-value as a function of kinetic energy is, typically, described as [196]

$$W(E) = \frac{W_a}{1 - U/E} \,, \tag{5.7}$$

where W_a is the asymptotic W-value for $E \gg I$ and U is a constant close to the average energy of sub-excitation electrons. This relation is in agreement with measurements in a number of gases including nitrogen, methane, and propane, down to low energies [197, 198, 199], although some measurements suggest a stronger dependence [200].

Ions

The energy dependence of the W-value for charged hadrons, such as protons, α-particles, mesons, and heavy ions is more complicated as it involves a larger number of reactions compared to electrons. In addition to secondary electron generation occurring during the energy loss process, electron capture and loss cycles are taking place. Moreover, collisions of ions with atoms and molecules result in energy transfers that can lead to further ionisation when ion velocities become comparable with electron orbital velocities. When ions carry electrons, as expected for slow ions, collisions with atoms and molecules give a number of products, including energetic ions and molecular fragments, that may result in further ionisation. No complete theoretical description of the energy dependence of the W-value is available, however, the cross sections for the individual process are being investigated [175].

The energy balance formulation for electrons can be extended for ions by adding the contribution of neutral recoils created during the cascade [176].

$$E = N_i \bar{E}_i + N_{ex} \bar{E}_{ex} + N_i \epsilon + N_{nr} \bar{E}_{nr} \,, \tag{5.8}$$

where N_{nr} is the number of neutral recoils produced and E_{nr} is their average kinetic energy. Dividing by N_i gives,

$$W_{ion} = \bar{E}_i + \frac{N_{ex}}{N_i} \bar{E}_{ex} + \epsilon + \frac{N_{nr}}{N_i} \bar{E}_{nr} \,. \tag{5.9}$$

The $N_i \bar{E}_i$ and $N_{ex} \bar{E}_{ex}$ terms include ionisation and excitation, respectively, induced by the secondary ions in addition to that induced by the secondary electrons.

It is worth noting that the ratio $\frac{N_{ex}}{N_i}$ is of particular importance to dual-phase liquid noble gas direct DM detectors, as it is found that this ratio differs for electron and nuclear recoils in the medium, and so is used for background discrimination.

5.4.3 Measurements of the W-Value

Measurements of W have been the topic of intense investigations for over a century [194, 201], with improved experimental methods and increased precision over time. The experimental set-up for these measurements is similar between different authors, and, generally, involves a particle gun with precisely known energy – for instance, defined by the extraction potential – fired into an ionisation chamber. In order to measure the W-value, the energy deposited by an incident particle and the amount of ionisation it induces must be measured. This was done in slightly different ways between the authors, however, two main methods were used. The first uses an electrode at the gun-detector interface to measure the beam current while collecting the ions generated in the gas with a proportional counter. During the measurement, the pressure in the detector is gradually increased. For low pressures, the incident particles can completely traverse the detector and so do not dissipate all of their energy in the detector, resulting in a gradually increasing ionisation current measurement as the pressure increases. At some pressure, the particle track is completely contained in the detector, however, the gas pressure at the gun-detector interface results in scattering of the incident particle into the interface and so not deposit its total energy in the gas. This latter effect is proportional to the gas pressure, and so an extrapolation of the ionisation current measurement as a function of pressure to that at zero pressure is used to remove these effects. The ionisation current and the beam current can then be compared to determine the average amount of ionisation produced per incident particle. A second method is to operate the detector with a fixed pressure ($\mathcal{O}$(10 mbar) in both ionisation and proportional modes for set periods of time. The operation in ionisation mode is used to measure the amount of ionisation in the given time, while the proportional mode is used to measure the total energy deposited in the time, which is the product of the number of particles entering the volume and their known energy. Comparing these two measurements, the average number of ionisations per particle can be calculated, and so the W-value. Other effects that may introduce uncertainties into the

measurement, such as particle energy uncertainties, gas contaminations etc., are particular to the exact experimental set-up used, and are discussed by the individual authors.

5.4.4 Relation of the W-value and the ionisation quenching factor

The W-values for different ionising radiations encapsulates all necessary information to estimate differences in the amount of induced ionisation. The quenching factor parametrises these differences. In Section 5.1, three definitions of the quenching factor were outlined. The first quenching factor definition is experimentally accessible only in the case where a detector is able to measure the total amount of energy deposited in electronic energy losses by an ion as a fraction of its total kinetic energy. The two other definitions can be measured with a detector relying on ionisation.

For a particle of energy E depositing all of its energy the detector will record a signal S proportional to the number of ionisation electrons generated N_T, related to W by Eq. 3.20. The constant of proportionality G includes the response of the read-out electronics and any electron multiplication. The detector can be calibrated with electrons of known kinetic energy in order to relate the signal recorded with the corresponding energy deposited in the detector, $S \rightarrow E$. In the case of incident electrons, where N_T^e ionisation electrons are generated, the corresponding signal for a given energy deposited will be $S_e = G \cdot N_T^e = G \cdot E/W_e(E)$. For incident ions of the same kinetic energy, N_T^i ionisation electrons will be generated, with corresponding signal $S_i = G \cdot N_T^i = G \cdot E/W_{ion}$. Through the calibration, the ion signal would be interpreted as an electron equivalent energy $E_{ee} = N_T^i \cdot W_e(E)$. E_{ee} is the energy visible to the detector, thus, from Eq. 5.1 the quenching factor can be written as:

$$q_f(E) = \frac{E_{ee}}{E} = \frac{N_i^i \cdot W_e(E)}{E} = \frac{W_e(E)}{W_i(E)} \tag{5.10}$$

When the kinetic energy is over a few keV, far away from the energy region where the W-value for electrons is energy dependent, the quenching factor can be derived from the ratio of the asymptotic W-value for electrons W_a over the W-value for ions W_i in the same medium. This is the case in the second definition, and is equivalent to Eq. 5.10 when $W_e \to W_a$.

The third definition of the quenching factor refers to the case where W_e remains energy dependent, and so accounts for the effective quenching of electrons at energies below a few keV.

From these definitions, the quenching factor can be inferred from precise, dedicated measurements of W in gases.

5.5 Quenching factor estimation

The estimation of the quenching factor, using Eq. 5.10, for different ions species relies on measurements of the W-values for ions and electrons; the latter being used to obtain W_a for electrons from Eq. 5.7. W-value measurements were selected based on two community reports produced by ICRU (1971) and IAEA (1995) international commissions, which surveyed multiple studies of W-values [194, 201]. The gases studied are H_2, CH_4, N_2, Ar, CO_2, C_3H_8 and W-values for electrons, protons, α-particles, and constituent ions are included. These gases are frequently used as counting gases and quenchers in proportional counters [113], and as components of tissue-equivalent gases, used to emulate energy deposition in the human body. Furthermore, some of these are of particular interest as targets for rare event searches with gaseous detectors, such as CH_4, N_2, and Ar.

5.5.1 Electron and ion W-value measurements

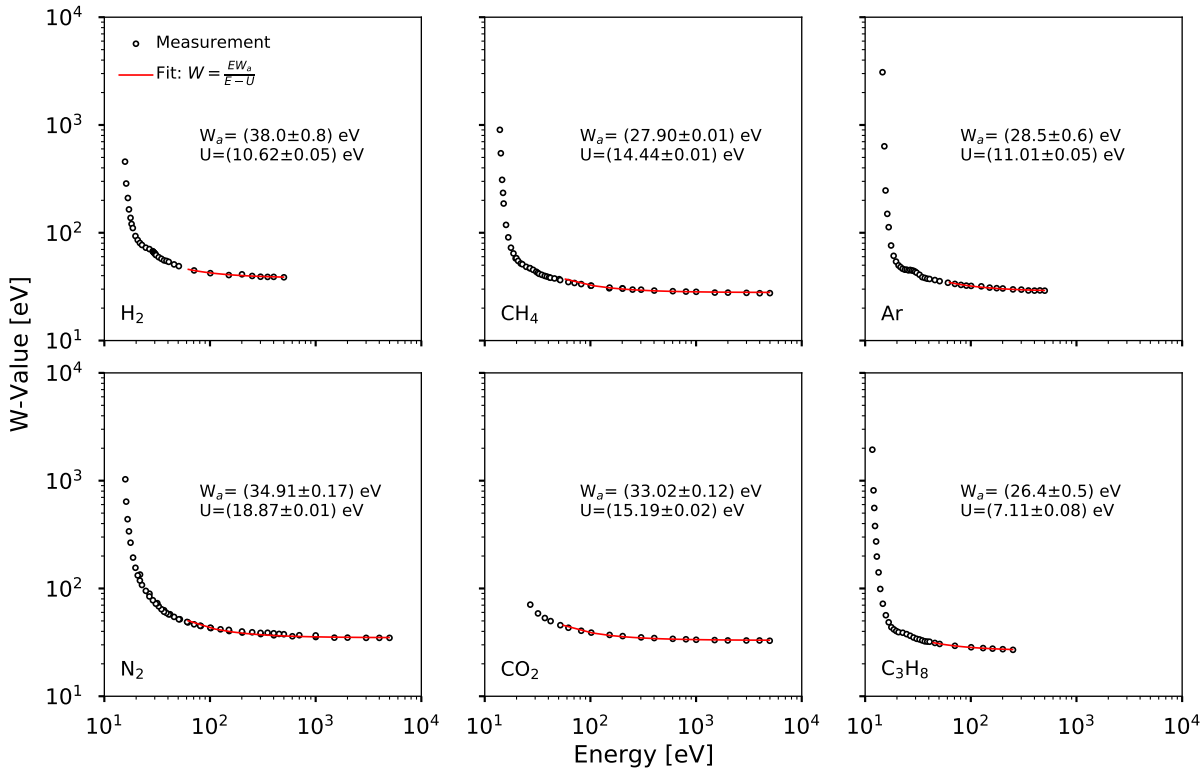

Figure 5.7: W-values versus electron kinetic energy for the gases studied. Data from Ref. [198] were used for H_2, Ar and C_3H_8. For CH_4, data from Refs [198] and [197] are combined. The data from Refs [198] and [202] were combined for N_2. Only the data from Ref. [203] was used for CO_2. The asymptotic W-value (W_a) for each gas was estimated from a fit of Eq. 5.7 to the data.

The electron measurements by Combecher et al. [198], Waibel and Grosswelt [197, 203, 202] are presented in Fig. 5.7, and demonstrate the discussed energy dependence of the W-value. CO_2 data from [198] were not used due to their discrepancy with other published measurements and calculations [201]. The data for each gas is fit with Eq. 5.7 using W_a and U as free parameters to estimate the asymptotic W-value for electrons in each gas. Only measurements for electron kinetic energies substantially larger than the first ionisation threshold are included in the fit. The measurement uncertainties are dominated by systematic effects, which are assumed to be fully correlated across the considered energy range. These results

Table 5.1: W-values for electrons in various gases. The asymptotic W-values are derived from the fits shown in Fig. 5.7.

Gas	W [eV]	
	ICRU	Asymptotic
H_2	36.5±0.7	38.0±0.8
CH_4	27.3±0.6	27.90±0.01
N_2	34.8±0.7	34.91±0.17
Ar	26.4±0.5	28.5±0.6
CO_2	33.0±0.7	33.02±0.12
C_3H_8	24.0±0.5	26.4±0.5

are summarised in Table 5.1. The resulting asymptotic W-values appear higher than those suggested by ICRU for high energy electrons [194], which are also shown in Table 5.1. The recommended ICRU values are an arithmetic average of measurements published by a number of authors before 1971, using different energies and methodologies, and the assigned uncertainties were chosen to embrace most of the available results. The results presented here are based on the later measurements recommended by the IAEA report [201]. The difference between the derived asymptotic W-value and the corresponding ICRU recommended value is assigned as a systematic uncertainty in the subsequent quenching factor estimate.

The W-values for protons and heavier ions were taken from various sources. Chemtob et al. [204] and Phipps et al. [205] were used for the W-values of protons, H_2^+, H_3^+, He^+ and Ar^+ in Ar gas; Huber et al [206], Boring et al. [207], Nguyen et al [208], Waibel et al. [209] for protons, H_3^+, He^+, N^+ and N_2^+ in N_2 gas; Huber et al. [206], Nguyen et al [208] and Waibel et al. [209] for protons, H_2^+, He^+, C^+ and O^+ in CO_2 gas; Huber et al. [206], Nguyen et al [208] and Waibel et al. [209] for protons, H_2^+, He^+, and C^+ in CH_4 gas; Willems et al. [210], and Posny et al [211] for protons, He^+ and C^+ in C_3H_8 gas; Grosswelt et al [212] for protons in H_2 gas. The W-value for electrons and ions in the gases studied are shown in Fig. 5.8. In the case of molecular ions, the energy is given per atom. In the case of proton and H_2 curves, it is observed that they practically coincide. This is explained by the molecules in the ion beam dissociating in the initial collisions with the gas constituents [206].

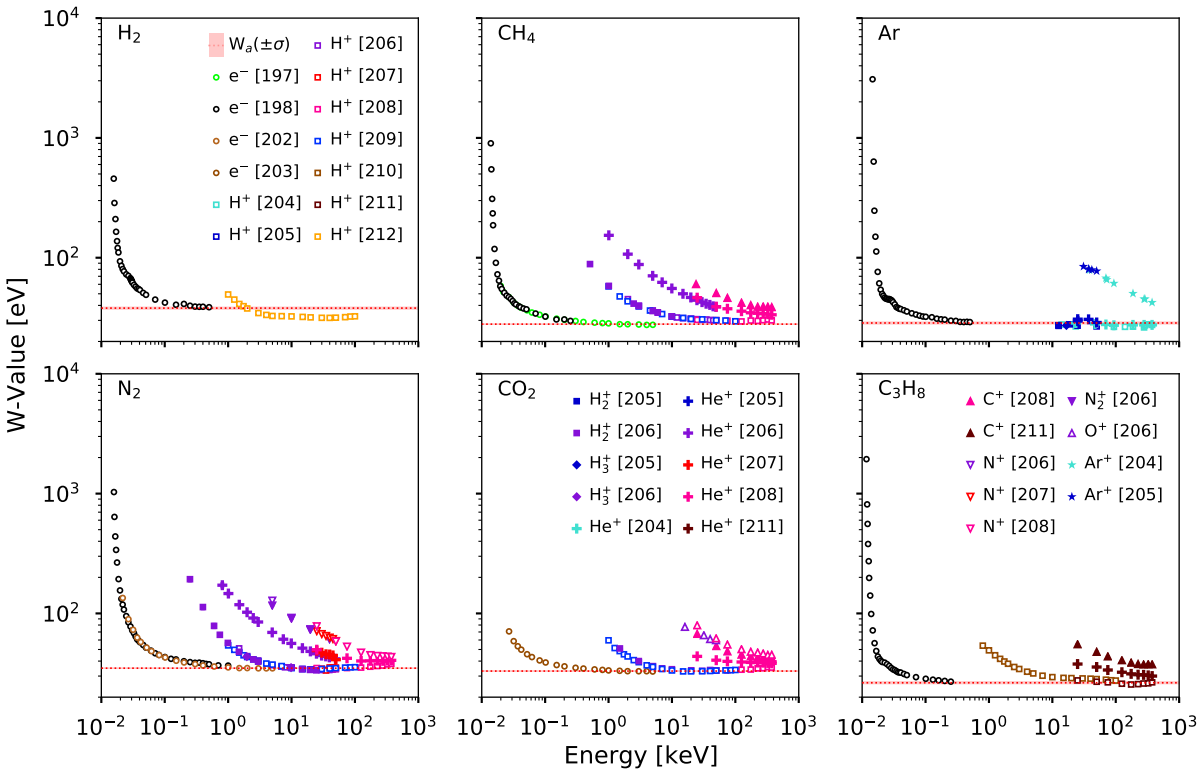

Figure 5.8: W-value versus the kinetic electrons and of ions for gases used in the studies. The asymptotic value estimated by the fit in Fig. 5.7 is displayed by the dashed line with its statistical uncertainty given as a band.

In Fig. 5.9 the fractional difference between the measured electron W-value and the corresponding asymptotic value is shown.

5.5.2 Results

The quenching factor (q_{f_2}) for each ion species in a gas was estimated using Eq. 5.10 with the asymptotic electron W-value, and are presented in Fig. 5.10. The uncertainty in the estimation of the W_a for electrons and the uncertainty for the W-values for ions provided in the respective publications were propagated to calculate the uncertainty in the quenching factor. The systematic uncertainty arising from the difference between the inferred W_a and

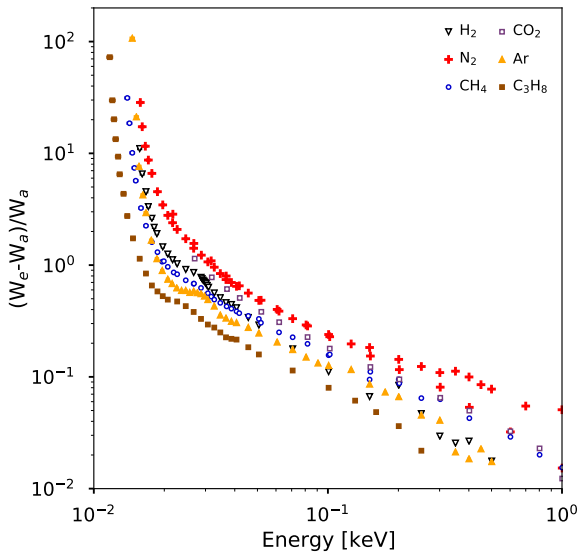

Figure 5.9: Relative difference of measured electron W-values to the asymptotic W-value in the gases under study.

that recommended by ICRU is indicated on each plot, but not included in the error bars. The estimated quenching factors provided by SRIM are also presented for reference [183].

The quenching factor displays an energy dependence, which is a consequence of the energy dependence of the W-value for ions. For electron kinetic energies lower than a few keV (Sec.5.4.2) the W-value for electrons becomes also energy dependent, as shown in Fig. 5.8, introducing an effective electron ionisation quenching. If the conversion between observed signal deposit and electron equivalent signal is to be calculated correctly, this additional reduction in ionisation has to be considered, which is definition q_{f_3}. The difference between W_a and the measured W-value for electrons in various gases is shown in Fig. 5.9. At an energy of 500 eV there is approximately a 3% difference between the two, which increases with decreasing energy.

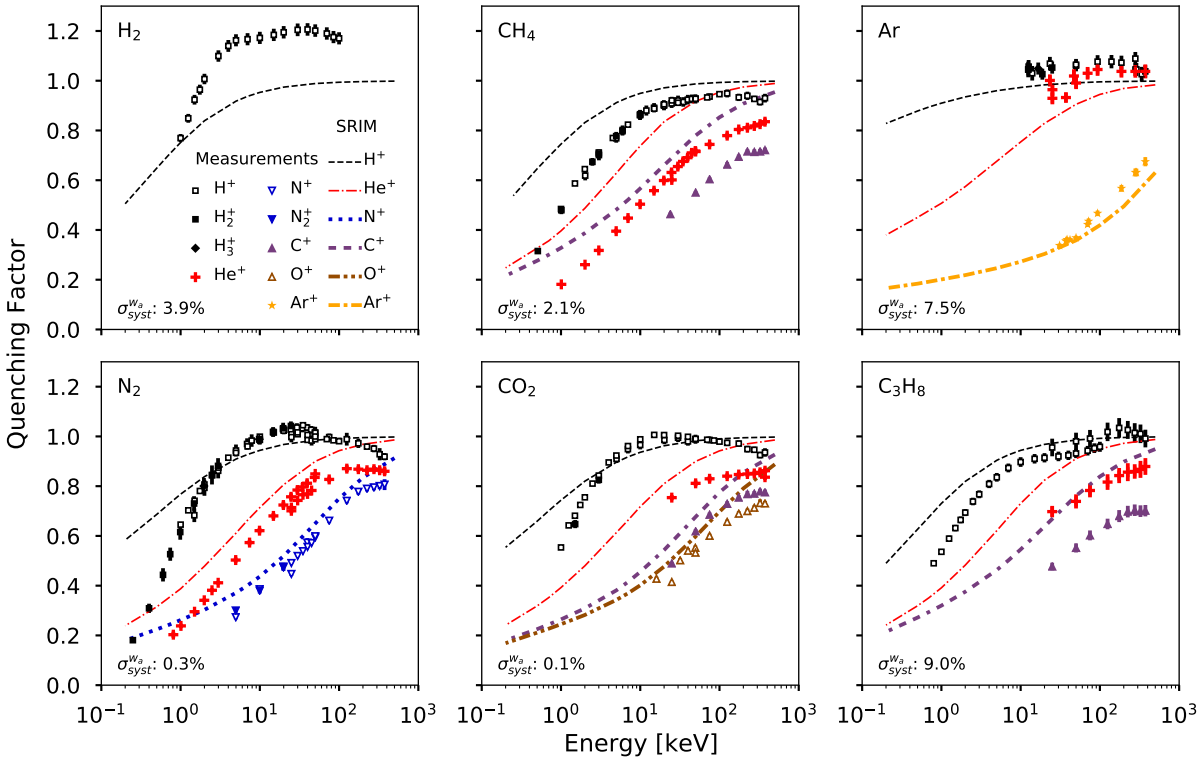

Figure 5.10: The ionisation quenching factor, inferred from measurements of the W-value, versus ion energy for several ion species in different gases. The quenching factors estimated by SRIM are also provided for comparison. $\sigma_{syst}^{W_a}$ is the systematic uncertainty on W_a, which is taken to be the difference between the fitted and ICRU recommended W_a.

5.5.3 Proton quenching factor greater than unity

The W-value for high energy protons, $\mathcal{O}$(MeV) kinetic energy, in any gas is in general larger than or equal to the one for electrons in the same gas [194]. However, in Fig. 5.10 the quenching factor for protons in H_2, Ar, N_2^+, and CO_2 is found to be greater than unity in some energies. This counter intuitive effect is a result of the minimum in the proton W-value curve which is observed in those gases, and can be seen in Fig. 5.8. This is attributed to charge exchange reactions involving H and the molecule (atom) of the gas [208, 213]. These reactions are dominant in the energy range around the minimum.

As an example, the case of N_2^+ is discussed, following the arguments found in Ref. [214]. The charge exchange cycle starts with the proton capturing an electron resulting in the production of neutral H and a N_2^+,

$$H^+ + N_2 \rightarrow H + N_2^+ \,. \tag{5.11}$$

The concluding stage of the cycle is the stripping of the electron from the neutral hydrogen by a collision with the N_2 molecule,

$$H + N_2 \rightarrow H^+ + e^- + N_2 \,. \tag{5.12}$$

However, before concluding the cycle, the H atom can further undergo the following reactions:

$$H + N_2 \rightarrow H + N_2^* \tag{5.13}$$

$$H + N_2 \rightarrow H + N_2 \,, \tag{5.14}$$

$$H + N_2 \rightarrow H + N_2^+ + e^- \,. \tag{5.15}$$

These possible interactions between the H atom and the N_2 are: Eq. 5.13, excitation; Eq. 5.14, elastic scattering; and Eq. 5.15, ionisation. This cycle converts an initially pure proton beam into a mixture of H^+ and H. Below 10 keV, the charge exchange and direct ionisation energy losses for the proton almost equally compete. This results in additional ionisation, due to charge cycle processes occurring, and so a lower W-value than would be anticipated from ionisation alone. Above approximately 100 keV, the charge exchange process shuts off, resulting in a rise in the W-value. Subsequent increases in the direct proton ionisation and δ-electrons around the MeV-scale result in a decrease in the W-value. While the latter effect is beyond the energy scale considered in the presented results, the ionisation enhancement due to the charge exchange cycle is visible in the W-value, and results in an increase in the

quenching factor to values greater than unity.

5.5.4 Comparison with predictions from SRIM

In Fig. 5.10, the estimated quenching factor curves are compared with quenching factor from SRIM calculations. The level of agreement with SRIM is variable, and depends on ion type, energy range and gas. SRIM predictions seem to be in reasonable agreement with results for N^+ in N_2^+, C^+ and O^+ in CO_2. SRIM predictions are also comparable to the results for He^+ in N_2, CO_2, Ar, as well as Ar^+ in Ar over 10 keV. SRIM predictions are consistently higher than the estimated quenching factors for energies below 10 keV. SRIM computes the total electronic stopping power, which includes effects such as excitation that could be invisible to a detector collecting charge. This could indicate that such effects become dominant for lower energies. This effect may also be accentuated by an overestimation of the electronic stopping power in low energies by SRIM, which has been highlighted in the literature [215].

Two further points of disagreement between SRIM and the experimental results are evident.

In the case of protons in H_2, Ar, N_2, and CO_2 there is a discrepancy that likely originates from the charge exchange cycle, resulting in additional ionisation with respect to the electronic stopping power estimated by SRIM. In carbon-containing molecules, the order of quenching factors is inverted with respect to what would be anticipated by molecular mass arguments, as shown in Fig. 5.11. For example, as predicted also by SRIM, ions in CO_2 would be expected to have a lower quenching factor than in CH_4 or C_3H_8. This behaviour has been also reported previously [216], but its source remains unclear.

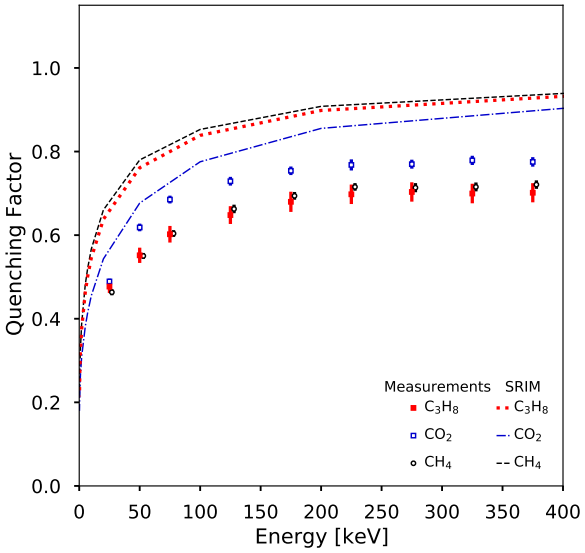

Figure 5.11: Quenching factor for C^+ ions in CO_2, CH_4 and C_3H_8. The energy in CH_4 data has been increased by 3 keV for visibility.

6

Background Suppression through Electroformation

Rare event searches have stringent limits on radioactive background in order to achieve their physics potential. The radiopurity of detector construction materials is of vital importance and has driven advancements in both radiopure material production and radioassay techniques. This chapter discusses the use of one such production technique, copper electroforming, to reduce the suppress radioactive backgrounds in SNOGLOBE. The process of producing highly-radiopure copper through electroforming is presented, along with its use to apply a copper layer to the inner surface of SNOGLOBE. Radioassays of the copper used for SNOGLOBE and of the electroplated layer are discussed. This work is presented in detail in Ref. [1], of which I am a main author and I prepared the manuscript. As a result, texts and figures from Ref. [1] are included here. The scale model presented in Section 6.4 was constructed and tested at PNNL. The measurements of the ^{210}Po contamination of C10100 copper used, presented in Section 6.2, were performed in collaboration by NEWS-G and XMASS. Both the scale model and ^{210}Po contamination are both included here for

completeness.

6.1 Copper as a Detector Construction Material

Copper is a common choice material for high-purity applications [217, 218, 219] because it is commercially available and there are no long-lived Cu radioisotopes; ^{67}Cu is the longest-lived with a half-life of 61.8 hours [145]. For this reason, the NEWS-G collaboration [144] chose C10100 (99.99% pure) copper, procured from Aurubis AG, to construct SNOGLOBE. C10100 refers to the Unified Numbering System (UNS) designation for Oxygen-Free Electronic (OFE) copper [220]. Even without long-lived Cu radioisotopes, a copper sample will have some (non-copper) radiogenic contamination resulting from cosmogenic activation and industrial production processes. For example, cosmic-ray neutrons interacting with copper through the $(n,\ \alpha)$ reaction can produce ^{60}Co. The half-life of the produced ^{60}Co is approximately 5.3 years, making it a long-lived background relative to the typical time scale of direct DM detection experiments. At the surface of the Earth, the added activity due to ^{60}Co is approximately 0.4 µBq/kg/day [221]. Other cosmogenic contaminants with shorter half-lives are also produced, e.g. ^{59}Fe. These contributions can be suppressed by minimising copper's exposure to cosmic rays. Other radiocontaminants primarily originate from the ^{238}U and ^{232}Th decay chains. The ^{238}U decay chain is shown in Fig. 6.1. This contamination is both inherent to the raw material and a result of the manufacturing and handling processes. An established technique to estimate this contamination is to directly measure the uranium and thorium levels with inductively coupled plasma mass spectrometry (ICP-MS), with a demonstrated sensitivity better than 30 fg/g to these contaminants [222, 223, 224]. The progeny activities can also be inferred and used to estimate background contributions to experiments, under the assumption of secular equilibrium. Some measurements of the uranium and thorium contaminations of commercial copper are shown in Table 6.1.

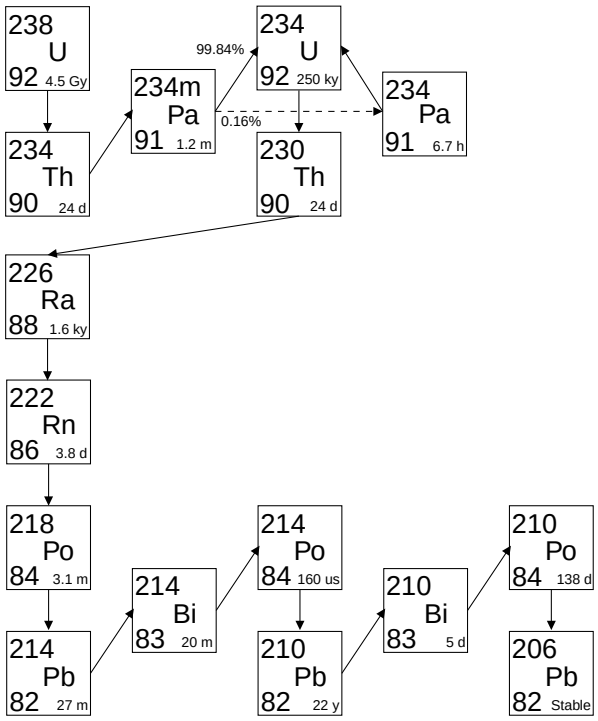

Figure 6.1: ^{238}U decay chain. All daughters are solid at room temperature and pressure except ^{222}Rn, which is a gas. Only decays with a branching fraction greater than 0.05% are shown. Data obtained from [145].

^{222}Rn, which is part of the ^{238}U decay chain, is a gas. As a result, ^{222}Rn may deposit its decay products on the copper surface or into the copper bulk at the raw ore stage or during manufacturing. This contribution adds to the contamination and may break the secular-equilibrium assumption. The longest-lived isotope in the ^{222}Rn decay chain is ^{210}Pb with a half-life of 22.2 years [225]. Accumulation of ^{210}Pb from ^{222}Rn deposits results in experiment backgrounds that cannot be inferred by ICP-MS measurements of the ^{238}U progenitor. One method to assess this contamination is by directly measuring the 5.3 MeV α particles from the ^{210}Po decays [226, 227, 228], using a high-sensitivity XIA UltraLo-1800 spectrometer [229], which has a sensitivity of 0.0001 α/cm^2/hour [229]. The XMASS collaboration established a method to estimate very low ^{210}Pb contamination in copper bulk, having demonstrated discrimination between bulk and surface contamination. in bulk from

Table 6.1: ICP-MS measurements of uranium and thorium contamination in C10100 copper samples [224].

Cu Type	U [μBq kg^{-1}]	Th [μBq kg^{-1}]
C10100 cake stock	0.21 ± 0.06	0.46 ± 0.06
C10100 saw cut	6.62 ± 0.66	10.2 ± 1.0
C10100 with machined surfaces	3.11 ± 0.39	1.88 ± 0.45
C10100 0.5" plate stock	0.009 ± 0.001	< 0.03

that on the surface [228]. For oxygen-free copper that was at least 99.96% pure by weight[1], the ^{210}Pb contamination in the bulk is estimated in the range 17–40 mBq kg^{-1} [228]. The corresponding measurement for the C10100 copper procured by the NEWS-G collaboration is 29^{+8+9}_{-8-3} mBq kg^{-1} as discussed in Section 6.2.

The measured level of ^{210}Pb in the C10100 copper bulk of the NEWS-G detector and the corresponding contamination of its progeny would represent approximately 82% of the experimental background below 1 keV [221], as estimated by means of a Geant4 [157] simulation, excluding possible contributions originating from activation of the copper induced by exposure to surface-level flux of cosmic muons. An approach to suppress the background from ^{210}Pb contamination is to grow a layer of ultra-radiopure copper onto the inner surface of the detector sphere [1]. This layer acts as an internal shield to suppress backgrounds, e.g. from β-decays of ^{210}Pb and accompanying X-rays and Auger electrons, and its progeny ^{210}Bi, originating from the bulk of the commercially sourced C10100 copper. It was estimated that a 500 μm-thick layer of ultra-radiopure copper will suppress this background contribution below 1 keV by a factor of 2.6 [221, 1].

An established method to deposit ultra-radiopure copper is potentiostatic electroforming [228, 230]. This method takes advantage of electrochemical properties to produce copper with reduced impurities. The process is described in Section 6.3. This method was previously used

[1] Japanese Industrial Standard, JIS:C1020.

to produce a variety of detector components, including those requiring extreme radiopurity. Internal fittings were fabricated for the Majorana Demonstrator [231] from electroformed copper with ^{238}U and ^{232}Th levels less than 0.099 and 0.119 µBq kg^{-1} at 68% confidence level, respectively[2] — limited by the ICP-MS assay precision [224]. The ^{210}Pb contamination of electroformed copper has previously been measured to be below the sensitivity of an XIA UltraLo-1800 spectrometer, with a 90% confidence level upper limit on its activity of <5.3 µBq kg^{-1} [228]. In order to apply this process to a hemispherical surface, a scale model was produced and used to determine the operating conditions.

6.2 ^{210}Pb Contamination in NEWS-G Copper

To assess the level of ^{210}Pb contamination in the C10100 copper used to construct the detector, samples were taken from the same batch of copper after casting. The α particles from ^{210}Po decays were measured using an XIA UltraLo-1800 ionisation chamber, which uses an active veto to obtain a second complementary signal arising from cases where the α particle does not originate from the sample under test. This is used to suppress background coming from the spectrometer's own construction materials. The sample is placed in the detector which is flushed with argon gas to minimise ^{222}Rn contamination. In this measurement, the ^{210}Po content of the bulk of the copper sample is of interest. The observable energy of 5.30 MeV α particles emerging from the bulk of the copper sample as a function of their original depth was estimated with a Geant4 simulation. An energy window of 2.5 MeV to 4.8 MeV was used to primarily select α particles originating from a depth of approximately 2 µm to 8 µm. This improves the signal-to-noise ratio for selecting bulk α particle events. The number of events detected in the accepted energy range must then be converted to a bulk activity. This was done by means of a Geant4 simulation which yielded

[2]For ^{238}U, 1 µBq kg^{-1} ≈ 0.081 pg/g. For ^{232}Th, 1 µBq kg^{-1} ≈ 0.244 pg/g.

2.7×10^2 (Bq/kg)/(α/cm^2/h) [228].

^{210}Po has a half-life of approximately 138 days, which is significant shorter than the approximately 22 years of the progenitor ^{210}Pb. As a result, the activities of ^{210}Po and ^{210}Pb may be different due to different contamination amounts at the production phase. Therefore, the activities of the two isotopes may be out of secular equilibrium; however, the ^{210}Po activity in a sample will evolve over time until it matches that of ^{210}Pb. Therefore, multiple measurements of the ^{210}Po activity over time are required to accurately infer the activity of ^{210}Pb in the copper. Four measurements of the α particles from the sample were made over the course of approximately one year, each lasting between 12 and 23 days. Table 6.2 shows the results of the four measurements.

Table 6.2: Measurements of the α particles in a 2.5 MeV to 4.8 MeV energy window originating from ^{210}Po decays in a C10100 copper sample. Table reproduced from Ref. [1].

Date	Measurement [10^{-4} α/cm^2/h]
Jul. 2–25, 2018	2.3 ± 0.4
Oct. 5–17, 2018	2.2 ± 0.4
Dec. 28, 2018–Jan. 9, 2019	1.4 ± 0.3
Apr. 19–May 7, 2019	1.4 ± 0.3

A likelihood fit of the measurements was performed and is shown in Fig. 6.2 along with the measurements. From this fit, it was estimated that the ^{210}Pb activity in the sample is 29^{+8+9}_{-8-3} mBq kg^{-1}, where the statistical and systematic uncertainties are given separately. This is consistent with other copper samples of similar purity [228].

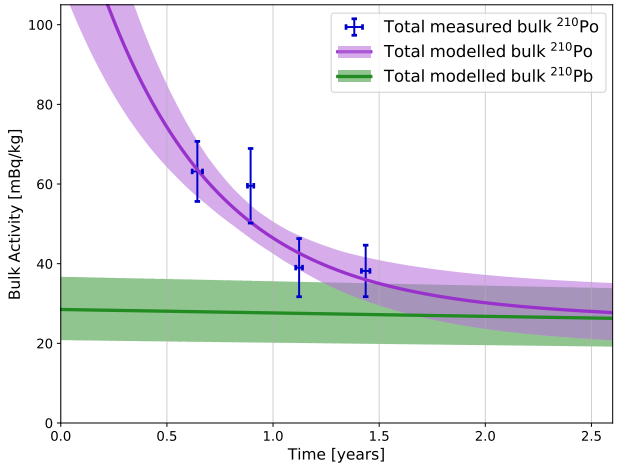

Figure 6.2: Measurements of the α particles from the decay of ^{210}Po in a sample of C10100 copper used in the production of the NEWS-G detector. Time is measured from the estimated production date of the copper. The purple (green) line shows the fitted ^{210}Po (^{210}Pb) activity over time, with the bands showing the $\pm 1\sigma$ region. Figure reproduced from Ref. [1].

6.3 Electroplating

6.3.1 The Electrolytic Cell

An electrolytic cell consists of a pair of electrodes, an anode and a cathode, separated by an electrolyte. A voltage difference is applied between the electrodes so that the anode is positively charged, as illustrated in Fig. 6.3. A current is used to supply electrons to the cathode where an ion undergoes a reduction reaction (gain of electrons), while oxidation reactions (loss of electrons) occur at the anode. The reactions occurring at each of the electrodes will be of the general form:

$$A^{(y+z)+} + ze^- \leftrightharpoons A^{y+}\,, \tag{6.1}$$

where A is the molecular species, y is its ionic charge and z is the number of electrons required for the reduction reaction (reading left-to-right) or the number of electrons released

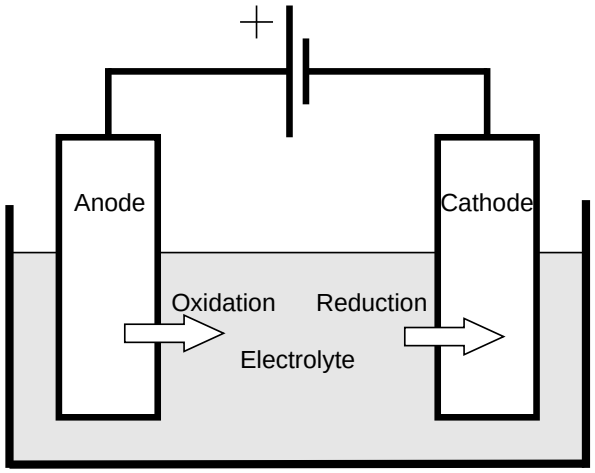

Figure 6.3: Schematic diagram of a simple electrolytic cell. Arrows indicate the motion of ions, which are released into the electrolyte by oxidation reactions at the anode and then deposited on the cathode in reduction reactions.

in the oxidation reaction (reading right-to-left). Reading this equation in one direction gives the "half-cell reaction", where the anode and cathode half-cell reactions are not necessarily the same; e.g., in the case where one species is oxidised at the cathode but a different species is reduced at the anode. Oxidation reactions each release z electrons to the anode, which flow through the circuit to the cathode where they may be used for reduction reactions. Conventionally, the amount of released charge is expressed in terms of the Faraday constant, F, defined as the electric charge per mole of electrons, eN_{A}, which is equivalent to approximately $9.65 \times 10^5\ \mathrm{C\,mol^{-1}}$.

6.3.2 Electroplating

The flow of electrons gives a current I through the circuit. As the reduction reactions require electrons, the number of reduced atoms during electroplating is proportional to the total supplied charge, $Q(t) = \int I \mathrm{d}t$. The number of moles n of ions reduced at the cathode

in time t is given by,

$$n(t) = \frac{Q(t)}{zF}\,, \tag{6.2}$$

The resulting deposited mass as a function of time is

$$M(t) = m_r n(t)\,, \tag{6.3}$$

where m_r is the molecular mass of the deposited species. This is the mathematical form of Faraday's laws of electrolysis [232]. When the current is reversed the process is called electropolishing, which is a technique used to remove material from a surface.

There will be several species of ions in the electrolyte available to electroplate to the cathode. The tendency of an ion species to be reduced is quantified by the reduction potential E^0. Examples are shown in Table 6.3 for copper and radioisotope contaminants. A greater value of E^0 indicates a species that is more easily reduced. Each half-cell reaction will have its own reduction potential. The standard cell potential E^0_{cell} of the electrolytic cell is defined as the difference between the reduction potentials of the half-cell reactions at the anode E_{A} and cathode E_{C},

$$E^0_{\text{cell}} = E^0_{\text{C}} - E^0_{\text{A}}\,. \tag{6.4}$$

The standard cell potential is related to the change in Gibbs free energy per mole $\Delta\mathcal{G}^0$ for the system by,

$$\Delta\mathcal{G}^0 = -zFE^0_{cell}\,. \tag{6.5}$$

For a system in equilibrium, the Gibbs free energy is minimised [233], so $\Delta\mathcal{G}^0 = 0$. $\Delta\mathcal{G}^0 < 0$, meaning $E^0 > 0$, is the case when the reaction is spontaneous, whereas, if $\Delta\mathcal{G}^0 > 0$, $E^0 < 0$, the process is not spontaneous and so cannot proceed unless driven by a voltage between the electrodes. For a given species being oxidised at the anode, the reaction will only proceed when the cathode half-cell reaction has a higher reduction potential, or a sufficiently high

Table 6.3: Reduction potential for copper and possible radiocontaminants.

Reductants		Oxidants	E^0 (V)	
$Cu^{2+} + 2e^-$	$\leftrightharpoons$	Cu	+0.34	[234]
$Pb^{2+} + 2e^-$	$\leftrightharpoons$	Pb	-0.13	[235]
$U^{3+} + 3e^-$	$\leftrightharpoons$	U	-1.80	[236]
$Th^{4+} + 4e^-$	$\leftrightharpoons$	Th	-1.90	[236]
$K^+ + e^-$	$\leftrightharpoons$	K	-2.93	[237]

voltage is applied between the electrodes. In the case of a copper anode being oxidised, only ion species in the electrolyte with a reduction potential greater than that of copper will reduce. The relatively high reduction potential of copper compared to many radioisotopes means that it is purified during electroplating.

However, other factors, such as mass transport of contaminant ions, can cause species with lower reduction potentials to be deposited with the copper in small amounts [230]. This is discussed further in the Section 6.3.3.

For electroplating the NEWS-G detector, a copper anode is used to provide Cu^{2+} ions to the electrolyte. For Cu^{2+} ions reducing at the cathode, the system will have $E^0_{\text{cell}} = 0$ V. Thus, to drive the reaction and overcome energy loss mechanisms in the system, the electrodes are kept at a potential difference of 0.3 V [238], which is low enough to prevent the plating of undesirable contaminant isotopes.

6.3.3 Nernst Equation

The previous discussion outlines the principle behind copper refinement in electroplating. However, there is currently no complete model for the electrochemical dynamics of the plating system, and so the advancements in the field are driven by empirical results. As an example, the Nernst equation describes how the standard cell potential is modified by the temperature

T and chemical activity a of reductants i and oxidants j, and is given by,

$$E_{\text{cell}} = E^0_{\text{cell}} - \frac{RT}{zF} \ln \left(\frac{\prod_i a_i^{s_i}}{\prod_j a_j^{s_j}} \right) , \tag{6.6}$$

where s_i (s_j) is the stoichiometric coefficient of the reductants (oxidants). Due to the difficulty in measuring chemical activity it is often approximated by the concentration. This can be used to compute the required concentration of a contaminant in order for it to electroplate, i.e., $E_{\text{cell}} > 0$. In the case of Th^{4+} ions reducing at the cathode and copper oxidising at the anode, a Th^{4+} concentration over 10×10^{150} mol L^{-1} would be required for it to electroplate. If the voltage between the electrodes was included, then the required concentration is still over 10×10^{125} mol L^{-1}. However, the Nernst equation assumes the electrolytic cell is in equilibrium, and the application of a voltage in electroplating creates a dynamic system. In previous studies of electroplating, the rejection rate of thorium was measured to be approximately 99.9% at a concentration of 4.31×10^{-9} mol L^{-1}, which is in disagreement with the simplified application of the Nernst equation – however, the authors note that this is a 'worst case scenario' because the measurement conditions were expected to produce significant mass transport of ions [230]. The observed plating of thorium was attributed to the influence of other factors, such as mass transport of contaminants to the cathode surface and co-deposition with the copper.

6.3.4 Reverse-Pulse Plating

It has been shown that applying a time-varying potential difference between the electrodes can have several benefits compared to a constant potential difference [239]. During electroplating, the region of the electrolyte at the surface of the cathode becomes depleted of Cu^{2+} relative to the bulk electrolyte. This slows down the rate of electroplating and affects the properties of the deposited copper [239]. The waveform of the time-varying potential differ-

ence allows this region to be replenished by allowing diffusion from the bulk electrolyte when no voltage is applied and by reintroducing more ions from the surface during the reverse-voltage part of the waveform. Also, differences in current density can arise due to differences in the distance between the anode and cathode surfaces (e.g. a surface rough point). High current density regions of the electrolyte are more depleted of Cu^{2+} than lower density regions. When no voltage is applied, ions can diffuse between two such regions and thus lead to a more uniform overall current density, while the reverse-voltage part of the waveform prevents a thick layer forming in the high current density regions [239]; both effects promote more uniform growth of the electroplated copper layer. The reversing of polarity also allows for release of contaminant ions that may have been entrapped during the high mass transport portion of the forward plating. The waveform used for the electroplating is shown in Fig. 6.4. Note that while the potential is applied it is potentiostatic at a level that favours the oxidation/reduction of copper.

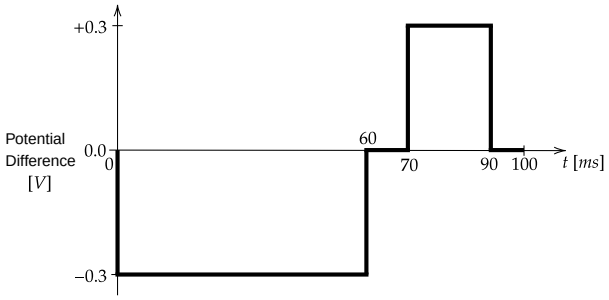

Figure 6.4: Waveform used in electroplating.

6.3.5 Transport of Ions in Electrolyte

During electroplating, the region of the electrolyte at the surface of the cathode becomes depleted of Cu^{2+} relative to the bulk electrolyte. The diffusion flux density of ions J_x in one dimension x, under the influence of a concentration gradient and a static electric potential

ϕ, may be modelled by an extension of Fick's law, the Nernst-Planck equation [240, 241],

$$J_x = -D\frac{\partial c}{\partial x} - \frac{zF}{RT}Dc\frac{\partial \phi}{\partial x} + uc\,, \tag{6.7}$$

where c is the concentration of the ion species, D is its diffusion coefficient and u is the fluid velocity. The three terms on the right-hand side of Eq. 6.7 describe movement of the ions under the influence of the concentration gradient (diffusion), electric potential gradient (migration) and due to hydrodynamic transport (convection), respectively. In the case of a weak electric potential, as is the case in potentiostatic electroforming, and assuming $u = 0$, J is dominated by diffusion, and so can be written as,

$$J_x \approx -D\frac{\partial c}{\partial x}\,. \tag{6.8}$$

During electroplating, ions in the electrolyte at the cathode surface are reduced first, resulting in a decreased concentration. Assuming a constant concentration in the bulk electrolyte, c_b, there will be some region between the cathode surface and bulk electrolyte where there is a concentration gradient, known as the diffusion layer. This is shown in Figure 6.5. A similar gradient is found at the anode surface, however, with a higher concentration than the bulk. If the diffusion layer is approximated to have a constant gradient over some distance δ_x, known as the Nernst diffusion layer [240], then J may be written as,

$$J_x \approx -\frac{D}{\delta_x}\left(c_b - c_0\right)\,, \tag{6.9}$$

where $\frac{D}{\delta_x}$ is defined as the mass transfer coefficient K_m.

The concentration and its gradient at the surface of the anode defines the maximum current at which plating can take place; qualitatively, operating with too high a current will cause the cathode-surface concentration to be lower, and the diffusion limits the ability for ions in the

bulk to replenish this. This affect can be reduced by agitating the solution (i.e. introducing a non-negligible u), which can bring ions from the bulk closer to the electrode surface. In the electroplating of the NEWS-G detector, this was achieved with the use of a pump that circulated the electrolyte, as mentioned in Section 6.5.

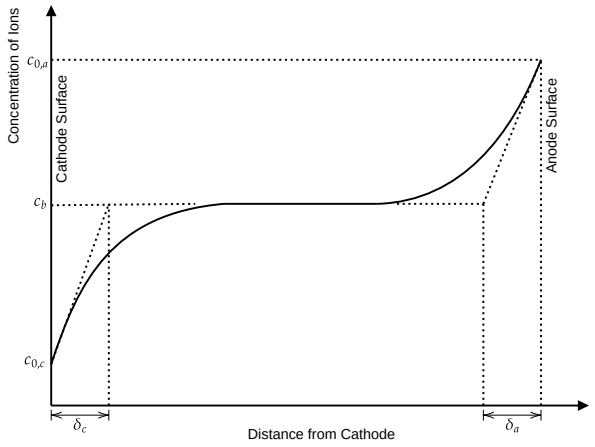

Figure 6.5: Pictorial figure of diffusion layer at electrode boundaries and the construction of the Nernst layer. The solid line represents the true concentration, where are the dashed lines show the constant gradient approximation concentration between the surface and bulk, and the distance between the intersection of these two lines and the electrode is the thickness of the Nernst layer. The subscript a, c are for the anode and cathode, respectively. Based on a figure in Ref. [240]

6.4 Scale Model

The copper electroplating procedure described in the previous section is a well-established method for over a decade [230]. However, fairly rigid operational conditions must be met to produce material with the required radiopurity and mechanical properties. Failure to meet these conditions may not only produce copper of poor radiopurity but often results in deposits with poor physical properties as well. For NEWS-G, the initial loading of copper into solution was generated from an initial electropolishing step, because commercially available copper sulphate is not sufficiently pure. However, for traditional electroforming, the amount

of copper required in the electrolyte is too great to achieve through electropolishing. As a result, the plating conditions for the NEWS-G hemispheres required a major deviation in the concentration of copper sulphate ($CuSO_4$) in the electrolyte.

Several parameters can have an effect on electrodeposition growth, such as ion concentration, temperature, current and the presence of other ion species. The exact effect of many of these is not well-understood, especially when multiple parameters are outside of their established optimal operating ranges. Prior experience has shown that electrolyte with a low copper-ion concentration can produce dendritic copper deposition. In the absence of accurate deposition models, it was necessary to run a scaled experiment prior to plating the full-sized ∅140 cm sphere underground in LSM. Key growth parameters were identified and an experiment was designed based on those that could be adjusted *in situ* at LSM and projected onto a scale model.

The key independent and adjustable variables were determined to be the concentration of copper and overall conductivity of the electrolyte, and the current based on the limiting set of voltage conditions. Control of the $CuSO_4$ concentration is limited by the amount of copper that can be dissolved during an initial electropolishing step, which serves two purposes: (a) expose the underlying bulk crystal structure to prepare the copper surface for electroplating; and (b) load the electrolyte with copper. During this step, the ∅140 cm hemisphere will act as the anode and careful control of the potential is not as important, whereas subsequently copper will be plated to the ∅140 cm hemisphere which will then be serving as the cathode. During the latter step, the voltage control and deposition rate are critical. As a result, establishing how the plating responds to small changes in $CuSO_4$ is crucial. As such, three variations of $CuSO_4$ concentration, three conductivities, and three voltage settings were identified for experimentation on the scale model.

A stainless-steel spherical float with a diameter of 30 cm was cut in half and used as a stand-

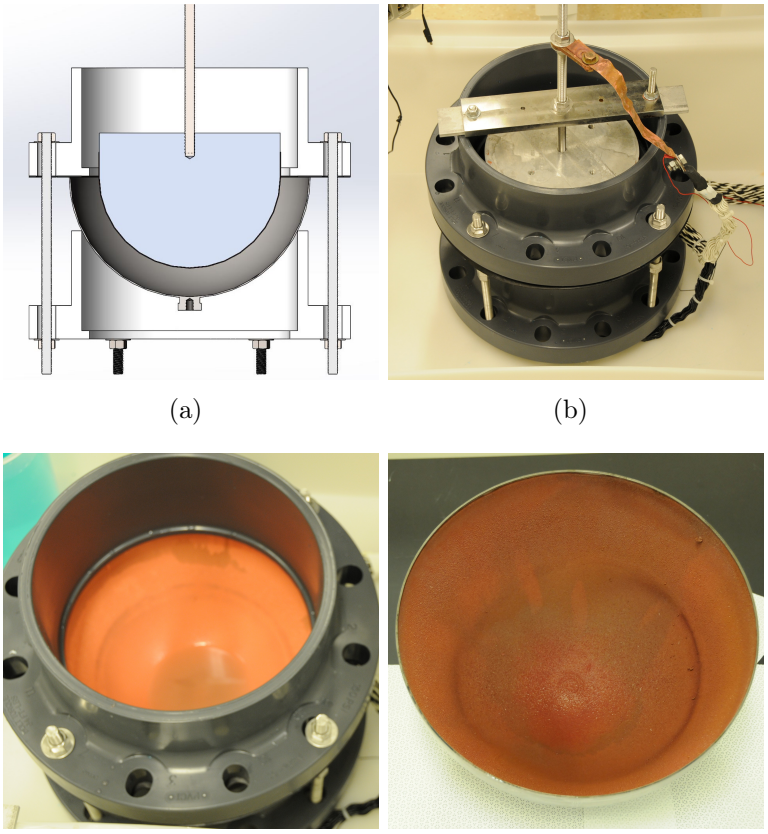

(a) (b)

(c) (d)

Figure 6.6: (a) CAD model of the small-scale setup; (b) the assembled scale-model experiment; (c) copper plated onto the scale model's stainless-steel hemisphere; and (d) the final scale-model growth of copper. Figure reproduced from Ref. [1].

in for the full-scale ∅140 cm copper hemisphere. A smaller hemisphere was machined from aluminium and plated with copper to serve as the anode after the initial electropolishing step. Fig. 6.6 shows the experimental setup of the scale model. Although the transport dynamics involved are not fully understood, previous experience has shown that the electrode gap (path length) has an effect on plating, regardless of $CuSO_4$ concentration and conductivity. As a result, while the spacing between the two electrodes was scaled, the impedance needed to be matched to that of the full-scale setup. This required the electrolyte conductivity to be reduced to compensate for the reduced electrode spacing in the model.

A bath, shown in Fig. 6.6(a) and 6.6(b), was designed to hold and stabilise the stainless-

steel hemisphere. Several iterations of plating were performed to cycle through the plating variations and determine the optimal electroplating conditions based primarily on the quality of grain uniformity and size observed in the deposit. Based on these trials, the parameters chosen for plating copper onto the full-scale hemispheres were a $CuSO_4$ concentration of 0.03 mol L^{-1}, a conductivity of 91.9 mS cm^{-1} (corresponding to a full-scale conductivity of 300 mS cm^{-1}), and a potential of 0.35 V. Using these parameters, the estimated time to electroplate each full-scale hemisphere was $\sim$ 8 days to attain a thickness of 500 µm. The resulting growth for the small-scale model is shown in Fig. 6.6(c) and Fig. 6.6(d).

6.5 Electroplating SNOGLOBE

The electroplating was conducted at LSM. The detector outer shell is comprised of two ⌀140 cm hemispheres, produced by a spinning technique using C10100 copper. The result after cleaning with commercial detergent is shown in Fig. 6.7(a). The hemispheres were then sanded with silicon carbide sandpaper to produce a smooth surface. During sanding, particulates of the abrasive substance can become embedded in the copper, which motivated the use of silicon carbide sandpaper as opposed to common alternatives, such as aluminium oxide, which are considered to be more radioactive. The subsequent preparation steps also help to remove these embedded particulates. Subsequently, the surface was chemically etched using an acidified hydrogen peroxide solution [226, 242]. The result of this preparation is shown in Fig. 6.7(b).

A smaller C10100 copper hemisphere was produced to act as the anode for electroplating and was cleaned in the same way as the detector hemispheres. It was suspended inside the detector, separated by an electrolyte comprised of deionised water (18 Mohm), Optima® grade sulphuric acid (Fisher Scientific), and copper sulphate produced by a previous electroplating. A pump provided mechanical mixing with a filter removing particulates greater than

(a) (b)

Figure 6.7: A detector hemisphere following (a) initial cleaning with detergent and (b) sanding and chemical etching with an acidified hydrogen peroxide solution. The discolouration observed in the latter is a result of oxidisation of the copper and it is removed when the hemisphere is put in contact with the electrolyte.

1 µm in size from the electrolyte. The anode and cathode were connected to a pulse-reverse power supply (Dynatronix, Amery, WI, USA), which could supply up to 80 A. The hemisphere was contained within a stainless-steel container to contain any leaks or spillages. The set-up was contained in a temporary purpose-constructed cleanroom to prevent particulates entering the electrolyte and subsequently providing nucleation sites for nodule-like copper

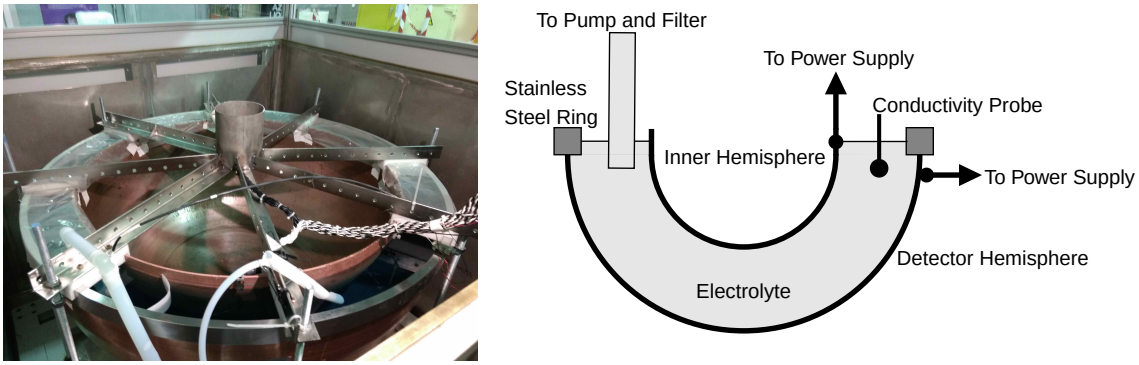

(a) (b)

Figure 6.8: (a) Electroplating setup showing the detector hemisphere, anode, support structures, and fixtures. (b) Schematic diagram of the setup.

growth [243]. The setup is shown in Fig. 6.8.

Prior to electroplating, each hemisphere was electropolished to remove a layer of material from the surface. This exposes the underlying crystalline structure and provides an ultra-clean surface prior to deposition. Furthermore, this process enhances the amount of Cu^{2+} in the electrolyte. A higher voltage was used for this process to extract all species from the surface. During electropolishing, (21.2 ± 0.1) µm and (28.2 ± 0.1) µm were removed from the first and second detector hemispheres, respectively. This was estimated from the integrated current and Eq. 6.3, assuming uniform polishing. Following this process, the electrolyte circulated through the filter for several days prior to electroplating to remove particulates released from the copper surface.

The electroplating procedure used the reverse-pulse plating waveform shown in Fig. 6.3. The current and voltage were monitored throughout, and the conductivity and temperature were recorded using a HACH inductive conductivity sensor. Electroplating continued for a total of 19.8 days and 21.0 days for the first and second hemispheres, respectively. The process took longer than estimated based on the small-scale experiments due to power supply current limitations, plating at slightly lower potential and a slightly lower electrolyte conductivity. This resulted in a slightly rougher surface than obtained in the model. The process was only interrupted for short periods to perform checks or due to power outages. The thickness of the deposited layer, which is shown as a function of time in Fig. 6.9, was estimated from the integrated current assuming a uniform deposition. Total copper thicknesses of (502.1 ± 0.2) µm and (539.5 ± 0.2) µm were plated onto the first and second detector hemispheres, respectively. The achieved plating rate corresponds to approximately 1.3 cm/year. A photograph of the final result is shown in Fig. 6.10 for each hemisphere. The surface of the first hemisphere displayed more nodular growths then the second, however, still below a level which would significantly affect the electric field in the detector. A possible explanation of the nodular growth is particulates released from the anode surface during the first electroplating can be

transported to the cathode by mass transport and be entrained into the electrodeposited layer, providing a nucleation site for further growth [243]. This was not observed during the electroplating of the second hemisphere.

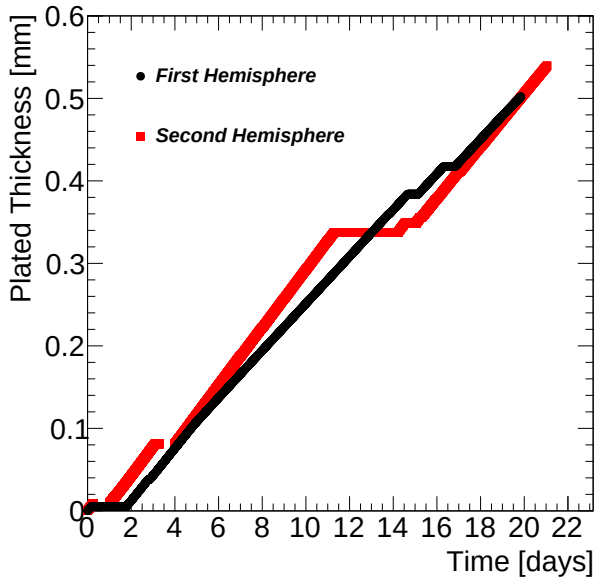

Figure 6.9: Estimated thickness of the electroplated copper for both detector hemispheres.

After removing the hemispheres from the setup, they were rinsed with deionised water and the surface passivated with a 1% citric-acid solution to prevent surface oxidation [242]. Following the welding of the hemispheres together, a final stage of surface etching using an acidified-peroxide solution will be undertaken in order to mitigate the surface contamination caused by contact with the air. This etching technique has been shown to reduce the surface contamination of ^{210}Pb on electroformed copper to the background level of the XIA UltraLo-1800, which is used in these assays [226]. This process is conducted under a nitrogen cover gas to mitigate possible surface recontamination following the etching. Following this stage, the inner detector surface will not be exposed to air again.

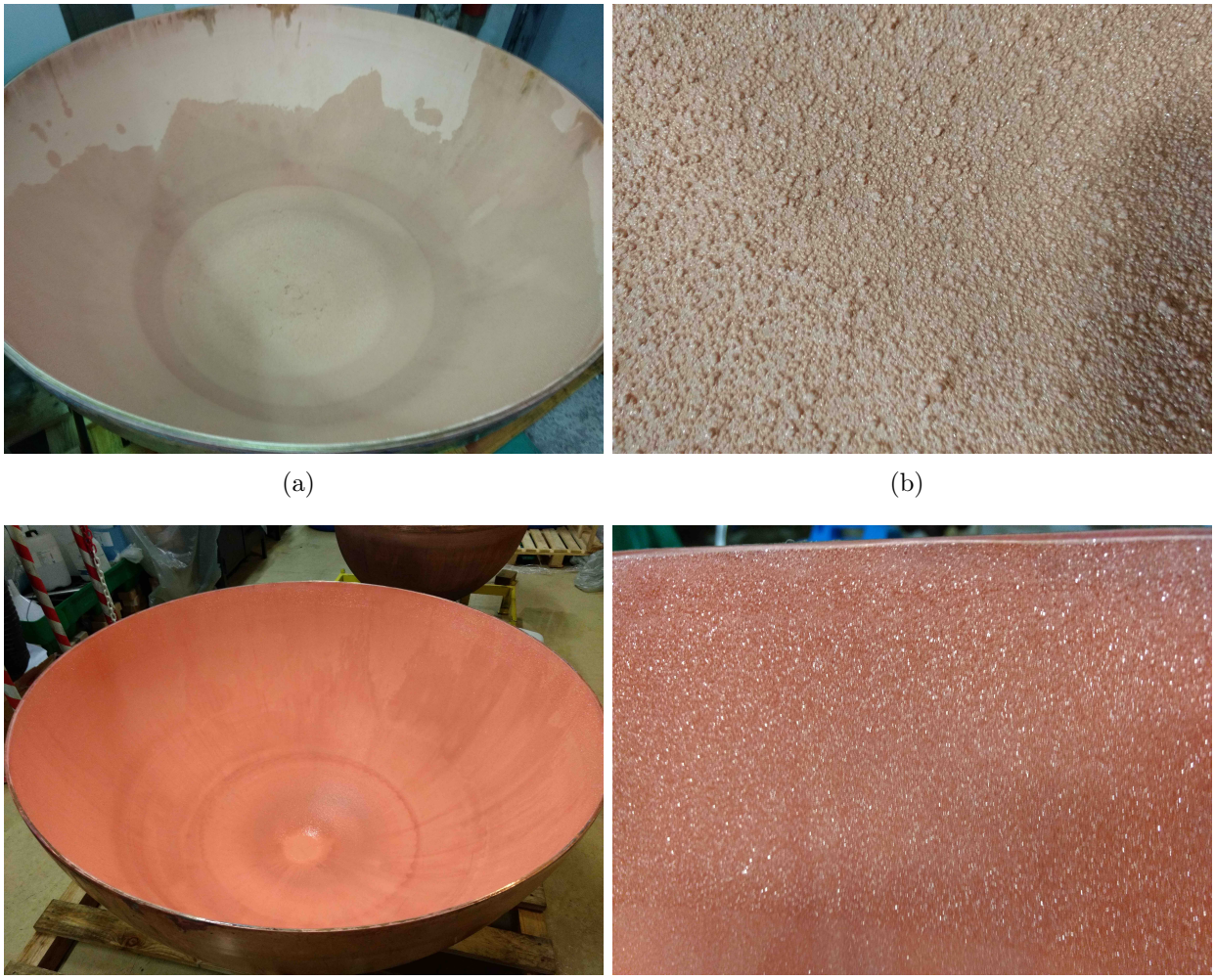

(a) (b)

(c) (d)

Figure 6.10: (a) ((c))The inner surface of the first (second) hemisphere after electroplating and (b) ((d))a close-up of the surface.

6.6 Radioisotope Assay Results

Samples of the electroplated copper were used to assess ^{238}U and ^{232}Th concentrations. Samples were taken from copper plated on the stainless-steel ring, shown in Fig. 6.8, to avoid damaging the detector cladding. These samples originate from near the electrolyte–air interface and from the stainless-steel surface; thus, they represent a contamination worst case scenario. The samples collected from each hemisphere are shown in Fig. 6.11.

Figure 6.11: Electroplated copper samples taken from the stainless-steel ring shown in Fig. 6.8.

Table 6.4: ICP-MS results for ^{238}U and ^{232}Th contamination in samples of the electroplated copper layer, along with representative examples of electroformed and commercially sourced copper [224]. These are quoted as 68% upper confidence limits, where the measurement sensitivity was limited by the available sample mass.

Sample	Weight [g]	^{232}Th [µBq kg^{-1}]	^{238}U [µBq kg^{-1}]
C10100 Cu (Machined)	-	8.7 ± 1.6	27.9 ± 1.9
Cu Electroformed	-	<0.119	<0.099
Hemisphere 1	0.256	<0.58	<0.26
Hemisphere 2	0.614	<0.24	<0.11

The samples were shipped to Pacific Northwest National Laboratory and analysed using ICP-MS following the methods described in Refs. [222, 223]. The results are summarised in Table 6.4, along with representative examples of electroformed and commercially sourced (machined) copper. A substantial improvement over the latter is observed, with radiopurity levels comparable to previously measured electroformed copper. The measurement sensitivity for the two hemispheres is limited by the mass of the available samples. Previous samples of electroformed copper have exhibited a bulk contamination of ^{210}Pb lower than the background of the XIA UltraLo-1800, and are often used for blank measurements or for the construction of the sample tray inside the device [226, 228].

7

Future Electroformed Spheres

In the previous chapter, the ability of electroformed copper to reduce the experimental background was demonstrated. This chapter discusses future application of electroforming to produce full spherical proportional counter cathodes. Two projects will undertake this; ECUME, which has secured funding and is undergoing planning, and DarkSPHERE, which is in the planning stage and physics assessment stage.

7.1 Fully Underground Electroformed Detectors

As discussed in Chapter 6, a 500 µm electroplated layer was used to reduce the background below 1 keV by a factor of 2.6 in SNOGLOBE. Despite this, as shown in Fig. 7.1, the ^{210}Pb contamination remains the dominant experimental background [221]. Cosmogenic activation is the second largest component, depending on the amount of exposure to sea-level cosmic muon fluxes and subsequent radioactive decay when installed in the underground laboratory.

The ^{210}Pb contribution can be suppressed by exclusively using electroformed copper for the

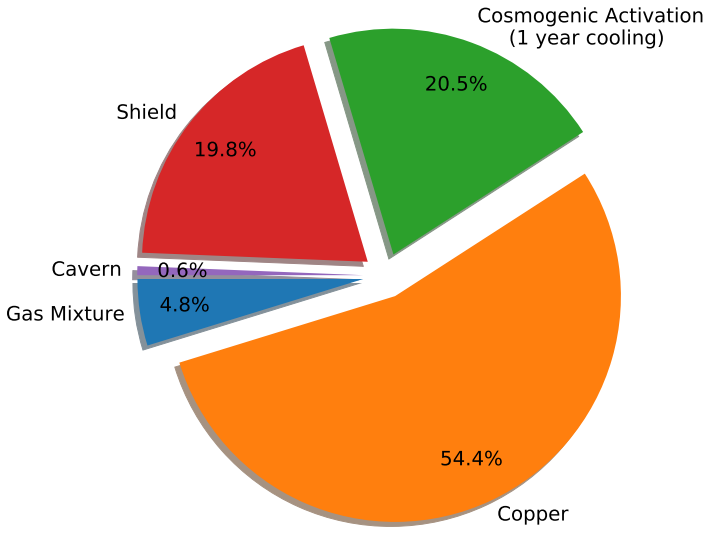

Figure 7.1: Fractional contribution of each background source to the total background of SNOGLOBE. Compiled from Ref. [221].

detector. As discussed in Chapter 6, the ^{210}Pb contamination of electroformed copper is below the sensitivity of an XIA UltraLo-1800 spectrometer, which is currently the most sensitive device for this measurement. If secular equilibrium in the ^{238}U decay chain holds in electroformed copper, then ICP-MS measurements can be used to infer the amount of ^{210}Pb. However, it has previously been shown that the process of machining electroformed copper can increase the uranium and thorium contamination [224]. For these reasons, a fully electroformed detector offers a method of producing a highly pure detector material. The presented electroplating of the NEWS-G inner detector surface achieved a plating rate of approximately 1.3 cm per year, which makes the production of a fully electroformed sphere feasible on the time scale of several months. The second largest contribution to the experimental background, arising from the cosmogenic activation of the copper, can be suppressed by directly electroforming the detector in the underground laboratory where it will be operated.

7.2 ECUME

The Electroformed CUprum Manufacturing Experiment (ECUME) will establish an underground electroforming facility in SNOLAB and as a first project will produce a ∅140 cm spherical cathode for the NEWS-G experiment. Electroforming will begin in autumn 2021 and is estimated to take approximately eight months to complete. The detector will then replace SNOGLOBE in its shielding and used in direct DM searches, following the exploitation phase of SNOGLOBE. The projected 90% confidence-level (CL) upper-limit on the DM-nucleon cross section as a function of DM candidate mass for ECUME operated with He:CH_4 (90%:10%) gas is shown in Fig. 7.2, calculated using the Optimal Interval Method (OIM) [244] assuming an exposure of 200 kg $\cdot$ days and a background of 0.3 dru. This background estimation was derived from the calculations for SNOGLOBE, but removing the background originating from copper [221]. Following the production of the NEWS-G detector, ECUME will be available as an underground electroforming facility for future experiments.

7.3 DarkSPHERE

Using a fully electroformed underground sphere, the background contribution from the copper becomes sub-dominant with the main remaining background contribution originating from the lead shielding [221]. Therefore, for future spherical proportional counter DM searches alternative shielding options need to be explored, including the use of a water shield. DarkSPHERE, a ∅300 cm spherical proportional counter fully electroformed underground, is proposed to be produced and subsequently operated in Boulby Underground Laboratory, UK. Boulby Underground Laboratory is located at a depth of 1.1km (2.8 m water equivalent) and contains a 1600 m^2 clean room, the Large Experimental Cavern, shared

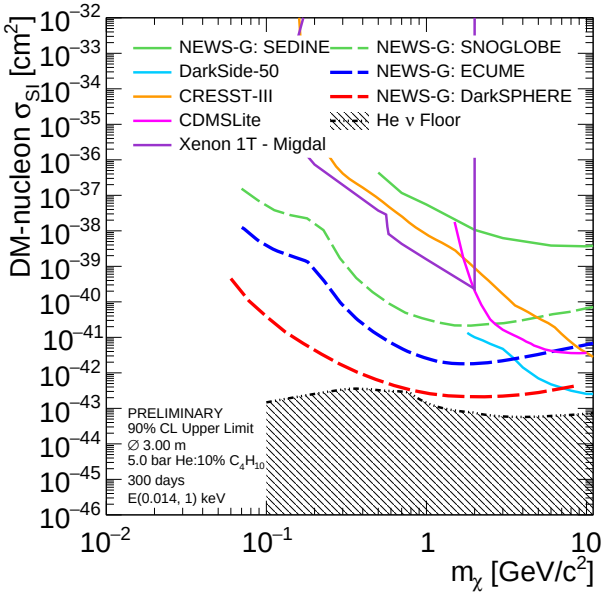

Figure 7.2: Projected 90% CL upper-limit on the DM-nucleon cross section as a function of DM candidate mass for SNOGLOBE and the future NEWS-G experiments ECUME and DarkSPHERE. Predicted 90% CL exclusion limits for SNOGLOBE and ECUME were calculated using an optimum interval method. The text describes the detector conditions for DarkSPHERE whose projection was calculated using a binned likelihood method. DarkSPHERE is projected to reach the neutrino floor, which is shown for helium [74]. Experimental exclusion limit measurements for SEDINE [144], and other direct DM experiments, DarkSide-50 [148], CRESST-III [149], CDMSlite [93] and Xenon-1T [104], are given for comparison.

between ISO 7 and ISO 6 standards. Thanks to the composition of the surrounding rock, the laboratory benefits from exceptionally low radon level in the air of below 3 Bq m^{-3}.

Studies of the shielding requirements to suppress environmental neutron and photon background contributions [245], originating in the walls of the laboratory, to levels comparable with that expected from the copper are ongoing. Current best estimates for the contamination of ^{210}Pb in electroformed copper come from assuming secular equilibrium in the uranium decay chain and taking current ICP-MS measurements of the uranium contamination of electroformed copper, corresponding to a background of 0.002 dru. It was found that a water shield, of 3.5 m thickness would achieve this goal. If the experiment was to be hosted in the Large Experimental Cavern then space requirements are more strict; however, a water-lead

shield, shown schematically in Fig. 7.3, comprising 130 cm water, 20 cm lead, and 30 cm water, can achieve comparable background suppression.

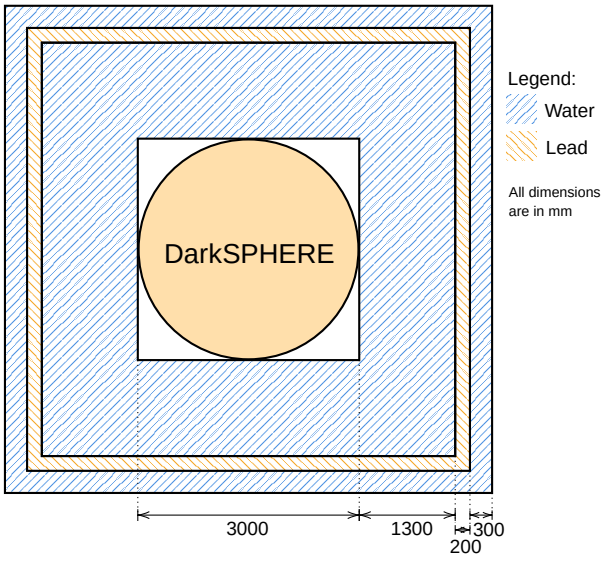

Figure 7.3: Proposed shielding for DarkSPHERE.

Additionally, gas mixtures with a higher abundance of light target atoms, such as the hydrogen-rich isobutane, C_4H_{10}, and helium are being explored, which provide increased sensitivity to light-DM. Furthermore, the advent of the DLC ACHINOS paves the way for future high-pressure operation, allowing the active mass of the detector to be increased. The 60-anode ACHINOS structure presented in Chapter 4 is a prototype read-out structure designed to achieve comparable electric field magnitudes at the outside of the detector as those obtained in SNOGLOBE. With this technological advancement, it is proposed that DarkSPHERE will operate with He:C_4H_{10} (90%:10%) at 5 bar, which gives a target mass of 27.3 kg.

In order to calculate the projected sensitivity of the experiment, the negative log-likelihood ratio was used as the test statistic comparing the signal plus background and the background

only hypotheses,

$$\lambda(\mu) = -2\ln\left(\frac{L(\mu|n)}{L(\hat{\mu}|n)}\right) = -2\ln\left(\frac{P(n;\mu s+b)}{P(n;\hat{\mu}s+b)}\right), \tag{7.1}$$

where the likelihood functions are Poisson distributions, $P(n;x) = x^n \mathrm{e}^{-x}/n!$, with s, b, being the expected signal and background event rates and n being the number of observed events. According to Wilk's therem [246], in the asymptotic limit λ, for one parameter of interest, follows a χ^2 distribution with one degree of freedom. From this, the 90% CL upper-limit on μ can be found when $\lambda = 2.706$. To estimate the 90% CL upper-limit that can be achieved, the Asimov data set with $\mu = 0$ is assumed [247]. The likelihood was binned in recoil energy, so that the negative log-likelihood ratio used was

$$\lambda(\mu) = -2\sum_i \ln\left(\frac{P(n_i;\mu s_i+b_i)}{P(n;b_i)}\right), \tag{7.2}$$

$$= 2\sum_i \left[n_i \ln\left(\frac{n_i}{s_i+n_i}\right) + s_i\right]. \tag{7.3}$$

The results that follow assume a flat background of 0.02 dru over 25 recoil energy bins. SRIM was used to provide quenching factors for the nuclear recoil energies. A COMPoisson distribution, with a Fano factor of 0.2, was sampled from to provide fluctuations in the primary ionisation [248] and a Polya distribution with a $\theta = 0.12$ was used to generate fluctuations in the avalanche [249]. Assuming an operating time of 300 days, the projected 90% CL upper-limit on the DM-nucleon cross section as a function of mass was calculated and is shown in Fig 7.2.

The contributions of each nuclei to the total excluded cross section are presented in Fig. 7.4(a), showing the relative importance of each for a given mass range. The sensitivity to sub-100 MeV DM masses is primarily though the interaction with hydrogen. In Fig. 7.4(b) the background-free exclusion limit is presented along with the exclusion limits that would be

obtained with 30, 150, and 600 days of data taking, compared to the nominal 300 days.

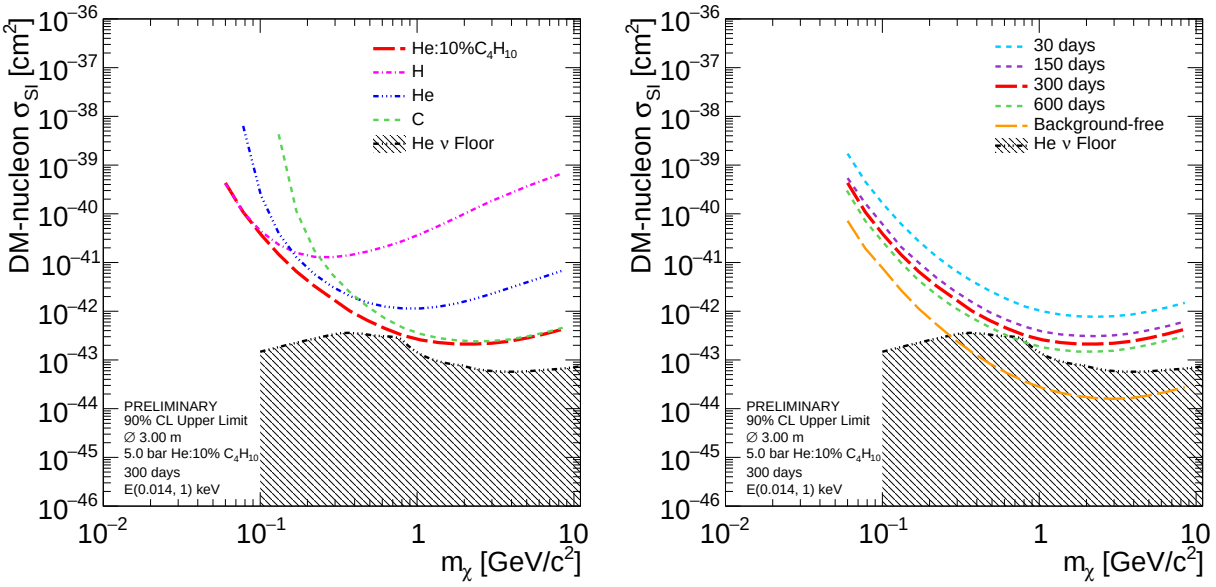

(a) (b)

Figure 7.4: Projected 90% CL upper limit on the DM-nucleon cross section as a function of DM candidate mass for DarkSPHERE (red dashed line), as shown in Fig. 7.2 with: (a) the contribution of each nucleus in the gas mixture; and (b) the expected sensitivity for different data taking periods, along with the back ground-free projection.

As highlighted in Chapter 2, there is some uncertainty in the parameters of the DM halo velocity distribution, such as the galactic escape velocity and velocity of the solar system relative to the galactic rest frame. These were considered as potential systematic uncertainties in the projection. They are of particular importance to light DM search experiments such as NEWS-G, where their influence on the highest energies in the recoil energy distribution can have a significant effect on the sensitivity. The spread in measurements is around 10%, and the result of applying this as a systematic change to the projection is presented in Table 7.1. Another potential source of uncertainty is the quenching factor. The discrepancy between SRIM and measured values varies between gases and has not been investigated for He:C_4H_{10} due to an absence of measurements. While this must be experimentally determined, either directly or through measurements of the W-value if these become available,

Table 7.1: Effect of systematic uncertainties on the expected sensitivity for different DM candidate masses, expressed as relative change of the 90% CL upper limit $((\sigma_{\text{nominal}}-\sigma)/\sigma_{\text{nominal}})$.

Parameter	m_χ [GeV]		
	0.06	0.2	1
$v_{\text{esc}} + 10\%$	9%	4%	2%
$v_{\text{esc}} - 10\%$	−21%	−7%	−2%
$v_{\text{ave}} + 10\%$	32%	20%	8%
$v_{\text{ave}} - 10\%$	−71%	−30%	−11%
$q_f + 30\%$	22%	18%	6%
$q_f - 30\%$	−45%	−33%	−13%

SRIM is currently the most appropriate source of this information. Therefore, potential differences between this and future measurements should be taken as a systematic uncertainty. In Table 7.1, the effect of a 30% systematic uncertainty in the quenching factor is shown.

8

Summary

The spherical proportional counter has previously demonstrated its potential in the direct search for light dark matter with its use by the NEWS-G collaboration. Building on this experience, the next generation detector, SNOGLOBE, has been constructed, and plans for experiments beyond this are underway. The presented work has enabled this, developing the understanding of the detector, the properties of gases, background suppression techniques and the physics potential of future experiments.

The understanding of the detector electric field is essential to detector operation. Finite element method calculations were used to guide the development of read-out sensors, as was a dedicated simulation framework for spherical proportional counters, based on Geant4 and Garfield++. The use of a high-resistivity secondary correction electrode improved detector operational stability and energy resolution by shaping the electric field. These sensors have been used by NEWS-G detectors and the R2D2 detector prototype.

The use of high-resistivity materials was extended to the multi-anode sensor, ACHINOS, which provides a means of operating with increasingly large and high-pressure detectors,

which is essential for the operation of SNOGLOBE and future spherical proportional counter rare-event searches. The use of a DLC coated, 3D-printed central electrode provided a breakthrough in detector stability and robustness. The simulation framework was used to understand Near-Far anode gain differences and the observed signal in each set of anodes. The future refinement of the construction techniques, the use of smaller anodes and more anodes will only improve the utility of ACHINOS. The addition of more anodes has been explored in the context of the proposed future spherical proportional counter for direct dark matter searches, DarkSPEHRE. The potential for directional sensitivity through the signal generated by multiple anodes is beginning to be explored through the simulation, and is a key future development.

The fraction of deposited energy dissipated as ionisation must be understood to infer the energy of a recoiling nucleus induced by dark matter elastic scattering. Measurements in gases are scarce and approximations intended for higher energies are often adopted. A method has been developed to compute this from precision measurements of the W-value in gases [7], which have been conducted for several decades. These provide experimental estimates of the ionisation quenching factor in several gases. The ionisation quenching factor in CH_4 is of particular importance to the NEWS-G collaboration, and is estimated to sub-keV recoil energies.

The construction of dark matter detectors places extremely rigorous constraints on the radiopurity of materials used. In the case of NEWS-G, despite using 99.99% pure copper, the ^{222}Rn introduced in the manufacturing leads to a ^{210}Pb contamination that brings the largest contribution to the experimental background. A method of suppressing this background is highly-pure copper electorforming, which has previously been used by experiments to produce detector components due to the significant enhancement in purity. The technique has been scaled up and applied to apply a highly-pure layer to the inner surface of SNOGLOBE, reducing the background below 1 keV by a factor of 2.6. This is the largest deep under-

ground electroforming ever performed, and has demonstrated the feasibility of the technique on large, spherical surfaces deep underground.

The impressive enhancement in radiopurity that can be achieved with this process has motivated the proposal of future spherical proportional counters, fully electroformed directly in the underground laboratory. The ECUME facility in SNOLAB will initially produce a 140 cm detector for NEWS-G, and is beginning operation this year. When installed in the shielding of SNOGLOBE, the fully electroformed detector will improve on SNOGLOBE's sensitivity to even lower dark matter nucleon cross sections in the sub-GeV DM candidate mass range. Beyond this, DarkSPHERE is proposed as the successor in the NEWS-G direct dark matter search. The 3 m fully underground electroformed detector, installed in an improved radiopurity shielding composed mainly of water, would have the potential to explore the DM candidate mass-cross section parameter space to the neutrino floor in the sub-GeV dark matter mass range. Advancements in ACHINOS in order to individually read out each anode could bring the potential to infer the direction of the recoil-inducing interaction, bringing the exciting possibility of distinguishing a DM signal from radioactive and even coherent elastic neutrino-nucleus scattering backgrounds.

Bibliography

[1] NEWS-G Collaboration, L. Balogh et al., *Copper electroplating for background suppression in the NEWS-G experiment*, Nucl. Instrum. Meth. A **988** (2021) 164844, arXiv:2008.03153 [physics.ins-det].

[2] I. Katsioulas et al., *Development of a simulation framework for spherical proportional counters*, J. Instrum. **15** (2020) no. 06, C06013, arXiv:2002.02718 [physics.ins-det].

[3] I. Katsioulas et al., *A sparkless resistive glass correction electrode for the spherical proportional counter*, JINST **13** (2018) no. 11, P11006, arXiv:1809.03270 [physics.ins-det].

[4] I. Giomataris et al., *A resistive ACHINOS multi-anode structure with DLC coating for spherical proportional counters*, J. Instrum. **15** (2020) no. 11, 11, arXiv:2003.01068 [physics.ins-det].

[5] R. Bouet et al., *R2D2 spherical TPC: first energy resolution results*, JINST **16** (2021) no. 03, P03012, arXiv:2007.02570 [physics.ins-det].

[6] I. Katsioulas et al., *Fast Neutron Spectroscopy with a Nitrogen-Based Gaseous Detector*, in *2019 IEEE Nuclear Science Symposium (NSS) and Medical Imaging Conference (MIC)*, pp. 1–3. 2019.

[7] I. Katsioulas, P. Knights, and K. Nikolopoulos, *Estimation of the ionisation quenching factor in gases from W-value measurements*, arXiv:2105.01414 [hep-ex].

[8] Planck Collaboration, N. Aghanim et al., *Planck 2018 results. VI. Cosmological parameters*, Astron. Astrophys. **641** (2020) A6, arXiv:1807.06209 [astro-ph.CO].

[9] M. W. Goodman and E. Witten, *Detectability of Certain Dark Matter Candidates*, Phys. Rev. D **31** (1985) 3059.

[10] A. Drukier and L. Stodolsky, *Principles and Applications of a Neutral Current Detector for Neutrino Physics and Astronomy*, Phys. Rev. D **30** (1984) 2295.

[11] S. P. Ahlen et al., *Limits on Cold Dark Matter Candidates from an Ultralow Background Germanium Spectrometer*, Phys. Lett. B **195** (1987) 603–608.

[12] M. Felcini, *Searches for Dark Matter Particles at the LHC*, in *53rd Rencontres de Moriond on Cosmology*. 9, 2018. arXiv:1809.06341 [hep-ex].

[13] E. Hubble and M. L. Humason, *The Velocity-Distance Relation among Extra-Galactic Nebulae*, Astrophys. J. **74** (1931) 43–80.

[14] F. Zwicky, *Die Rotverschiebung von extragalaktischen Nebeln*, Helv. Phys. Acta **6** (1933) 110–127. Republished in English.

[15] F. Zwicky, *On the Masses of Nebulae and of Clusters of Nebulae*, Astrophys. J. **86** (1937) 217–246.

[16] R. Gavazzi, C. Adami, F. Durret, J.-C. Cuillandre, O. Ilbert, A. Mazure, R. Pello, and M. P. Ulmer, *A weak lensing study of the Coma cluster*, Astron. Astrophys. **498** (2009) L33, arXiv:0904.0220 [astro-ph.CO].

[17] J. H. Oort, *Some Problems Concerning the Structure and Dynamics of the Galactic System and the Elliptical Nebulae NGC 3115 and 4494*, Astrophys. J **91** (1940) 273.

[18] L. M. J. S. Volders, *Neutral hydrogen in M 33 and M 101*, Bull. Astron. Inst. Netherlands **14** (1959) 323.

[19] M. S. Roberts and A. H. Rots, *Comparison of Rotation Curves of Different Galaxy Types*, Astron. Astrophys. **26** (1973) 483–485.

[20] A. Bosma, *The distribution and kinematics of neutral hydrogen in spiral galaxies of various morphological types*. PhD thesis, -, Jan., 1978.

[21] V. C. Rubin, W. K. Ford, Jr., and N. Thonnard, *Extended rotation curves of high-luminosity spiral galaxies. IV. Systematic dynamical properties, Sa through Sc*, Astrophys. J. Lett. **225** (1978) L107–L111.

[22] V. C. Rubin, N. Thonnard, and W. K. Ford, Jr., *Rotational properties of 21 SC galaxies with a large range of luminosities and radii, from NGC 4605 (R = 4kpc) to UGC 2885 (R = 122 kpc)*, Astrophys. J. **238** (1980) 471.

[23] T. S. V. Albada, R. Sancisi, M. Petrou, and R. J. Tayler, *Dark Matter in Spiral Galaxies [and Discussion]*, Phil. Trans. Roy. Soc. Lond. A **320** (1986) no. 1556, 447–464.

[24] SDSS Collaboration, D. J. Eisenstein et al., *Detection of the Baryon Acoustic Peak in the Large-Scale Correlation Function of SDSS Luminous Red Galaxies*, Astrophys. J. **633** (2005) 560–574, arXiv:astro-ph/0501171.

[25] 2dFGRS Collaboration, S. Cole et al., *The 2dF Galaxy Redshift Survey: Power-spectrum analysis of the final dataset and cosmological implications*, Mon. Not. Roy. Astron. Soc. **362** (2005) 505–534, arXiv:astro-ph/0501174.

[26] D. J. Fixsen, *The Temperature of the Cosmic Microwave Background*, Astrophys. J. **707** (2009) 916–920, arXiv:0911.1955 [astro-ph.CO].

[27] P. Particle Data Group, Zyla et al., *Review of Particle Physics*, PTEP **2020** (2020) no. 8, 083C01.

[28] S. W. Randall et al., *Constraints on the Self-Interaction Cross-Section of Dark Matter from Numerical Simulations of the Merging Galaxy Cluster 1E 0657-56*, Astrophys. J. **679** (2008) 1173–1180, arXiv:0704.0261 [astro-ph].

[29] D. Clowe et al., *A direct empirical proof of the existence of dark matter*, Astrophys. J. Lett. **648** (2006) L109–L113, arXiv:astro-ph/0608407.

[30] J. P. Dietrich et al., *Weak lensing evidence for a filament between the clusters A 222 and A 223 and its quantification*, Astron. Astrophys. **440** (2005) 453–471, arXiv:astro-ph/0406541.

[31] J. P. Dietrich et al., *A filament of dark matter between two clusters of galaxies*, Nature **487** (2012) 202, arXiv:1207.0809 [astro-ph.CO].

[32] S. D. McDermott, H.-B. Yu, and K. M. Zurek, *Turning off the Lights: How Dark is Dark Matter?*, Phys. Rev. D **83** (2011) 063509, arXiv:1011.2907 [hep-ph].

[33] SNO Collaboration, Q. R. Ahmad et al., *Measurement of the rate of $\nu_e + d \to p + p + e^-$ interactions produced by ^8B solar neutrinos at the Sudbury Neutrino Observatory*, Phys. Rev. Lett. **87** (2001) 071301, arXiv:nucl-ex/0106015.

[34] J. L. Feng, *Dark Matter Candidates from Particle Physics and Methods of Detection*, Ann. Rev. Astron. Astrophys. **48** (2010) 495–545, arXiv:1003.0904 [astro-ph.CO].

[35] J. L. Feng and J. Kumar, *The WIMPless Miracle: Dark-Matter Particles without Weak-Scale Masses or Weak Interactions*, Phys. Rev. Lett. **101** (2008) 231301, arXiv:0803.4196 [hep-ph].

[36] G. Jungman, M. Kamionkowski, and K. Griest, *Supersymmetric dark matter*, Phys. Rept. **267** (1996) 195–373, arXiv:hep-ph/9506380.

[37] G. Servant and T. M. P. Tait, *Is the lightest Kaluza-Klein particle a viable dark matter candidate?*, Nucl. Phys. B **650** (2003) 391–419, arXiv:hep-ph/0206071.

[38] H.-C. Cheng, J. L. Feng, and K. T. Matchev, *Kaluza-Klein dark matter*, Phys. Rev. Lett. **89** (2002) 211301, arXiv:hep-ph/0207125.

[39] N. Arkani-Hamed, A. G. Cohen, E. Katz, and A. E. Nelson, *The Littlest Higgs*, J. High Energy Phys. **07** (2002) 034, arXiv:hep-ph/0206021.

[40] A. Birkedal, A. Noble, M. Perelstein, and A. Spray, *Little Higgs dark matter*, Phys. Rev. D **74** (2006) 035002, arXiv:hep-ph/0603077.

[41] J. L. Feng, A. Rajaraman, and F. Takayama, *Superweakly interacting massive particles*, Phys. Rev. Lett. **91** (2003) 011302, arXiv:hep-ph/0302215.

[42] S. Dodelson and L. M. Widrow, *Sterile-neutrinos as dark matter*, Phys. Rev. Lett. **72** (1994) 17–20, arXiv:hep-ph/9303287.

[43] D. J. E. Marsh, *Axion Cosmology*, Phys. Rept. **643** (2016) 1–79, arXiv:1510.07633 [astro-ph.CO].

[44] E. A. Baltz, *Dark matter candidates*, eConf **C040802** (2004) L002, arXiv:astro-ph/0412170.

[45] M. Zumalacarregui and U. Seljak, *Limits on stellar-mass compact objects as dark matter from gravitational lensing of type Ia supernovae*, Phys. Rev. Lett. **121** (2018) no. 14, 141101, arXiv:1712.02240 [astro-ph.CO].

[46] M. Milgrom, *A Modification of the Newtonian dynamics as a possible alternative to the hidden mass hypothesis*, Astrophys. J. **270** (1983) 365–370.

[47] G. Bertone, ed., *Particle Dark Matter: Observations, Models and Searches*. Cambridge Univ. Press, Cambridge, 2010.

[48] M. Hindmarsh and O. Philipsen, *WIMP dark matter and the QCD equation of state*, Phys. Rev. D **71** (2005) 087302, arXiv:hep-ph/0501232.

[49] J. Zavala, M. Vogelsberger, and S. D. M. White, *Relic density and CMB constraints on dark matter annihilation with Sommerfeld enhancement*, Phys. Rev. D **81** (2010) 083502, arXiv:0910.5221 [astro-ph.CO].

[50] B. W. Lee and S. Weinberg, *Cosmological Lower Bound on Heavy Neutrino Masses*, Phys. Rev. Lett. **39** (1977) 165–168.

[51] C. Flynn, J. Sommer-Larsen, and P. R. Christensen, *Kinematics of the outer stellar halo*, Mon. Not. Roy. Astron. Soc. **281** (1996) 1027, arXiv:astro-ph/9603106.

[52] J. F. Navarro, C. S. Frenk, and S. D. M. White, *The Structure of cold dark matter halos*, Astrophys. J. **462** (1996) 563–575, arXiv:astro-ph/9508025.

[53] A. K. Drukier, K. Freese, and D. N. Spergel, *Detecting Cold Dark Matter Candidates*, Phys. Rev. D **33** (1986) 3495–3508.

[54] J. D. Lewin and P. F. Smith, *Review of mathematics, numerical factors, and corrections for dark matter experiments based on elastic nuclear recoil*, Astropart. Phys. **6** (1996) 87–112.

[55] T. Piffl et al., *The RAVE survey: the Galactic escape speed and the mass of the Milky Way*, Astron. Astrophys. **562** (2014) A91, arXiv:1309.4293 [astro-ph.GA].

[56] P. R. Kafle, S. Sharma, G. F. Lewis, and J. Bland-Hawthorn, *On the Shoulders of Giants: Properties of the Stellar Halo and the Milky Way Mass Distribution*, Astrophys. J. **794** (2014) no. 1, 59, arXiv:1408.1787 [astro-ph.GA].

[57] G. Monari et al., *The escape speed curve of the Galaxy obtained from Gaia DR2 implies a heavy Milky Way*, Astron. Astrophys. **616** (2018) L9, arXiv:1807.04565 [astro-ph.GA].

[58] I. D. Karachentsev and D. I. Makarov, *Orbital velocity of the Sun and the apex of the Galactic center*, Astron. Lett. **22** (1996) no. 4, 455–458.

[59] J. A. S. Hunt, J. Bovy, and R. G. Carlberg, *Detection of a dearth of stars with zero angular momentum in the solar heighbourhood*, Astrophys. J **832** (2016) no. 2, L25.

[60] M. C. Smith et al., *The RAVE Survey: Constraining the Local Galactic Escape Speed*, Mon. Not. Roy. Astron. Soc. **379** (2007) 755–772, arXiv:astro-ph/0611671.

[61] N. W. Evans, C. A. J. O'Hare, and C. McCabe, *Refinement of the standard halo model for dark matter searches in light of the Gaia Sausage*, Phys. Rev. D **99** (2019) no. 2, 023012, arXiv:1810.11468 [astro-ph.GA].

[62] C. McCabe, *The Earth's velocity for direct detection experiments*, JCAP **02** (2014) 027, arXiv:1312.1355 [astro-ph.CO].

[63] A. Helmi et al., *The merger that led to the formation of the Milky Way's inner stellar halo and thick disk*, Nature **563** (2018) no. 7729, 85–88, arXiv:1806.06038 [astro-ph.GA].

[64] C. A. J. O'Hare et al., *Velocity substructure from Gaia and direct searches for dark matter*, Phys. Rev. D **101** (2020) no. 2, 023006, arXiv:1909.04684 [astro-ph.GA].

[65] A. Kurylov and M. Kamionkowski, *Generalized analysis of weakly interacting massive particle searches*, Phys. Rev. D **69** (2004) 063503, arXiv:hep-ph/0307185.

[66] R. H. Helm, *Inelastic and Elastic Scattering of 187-Mev Electrons from Selected Even-Even Nuclei*, Phys. Rev. **104** (1956) 1466–1475.

[67] G. Duda, A. Kemper, and P. Gondolo, *Model Independent Form Factors for Spin Independent Neutralino-Nucleon Scattering from Elastic Electron Scattering Data*, JCAP **04** (2007) 012, arXiv:hep-ph/0608035.

[68] COHERENT Collaboration, D. Akimov et al., *Observation of Coherent Elastic Neutrino-Nucleus Scattering*, Science **357** (2017) no. 6356, 1123–1126, arXiv:1708.01294 [nucl-ex].

[69] W. C. Haxton, R. G. Hamish Robertson, and A. M. Serenelli, *Solar Neutrinos: Status and Prospects*, Ann. Rev. Astron. Astrophys. **51** (2013) 21–61, arXiv:1208.5723 [astro-ph.SR].

[70] F. Ruppin, J. Billard, E. Figueroa-Feliciano, and L. Strigari, *Complementarity of dark matter detectors in light of the neutrino background*, Phys. Rev. D **90** (2014) no. 8, 083510, arXiv:1408.3581 [hep-ph].

[71] D. Z. Freedman, *Coherent Neutrino Nucleus Scattering as a Probe of the Weak Neutral Current*, Phys. Rev. D **9** (1974) 1389–1392.

[72] J. Billard, L. Strigari, and E. Figueroa-Feliciano, *Implication of neutrino backgrounds on the reach of next generation dark matter direct detection experiments*, Phys. Rev. D **89** (2014) no. 2, 023524, arXiv:1307.5458 [hep-ph].

[73] J. B. Dent, B. Dutta, J. L. Newstead, and L. E. Strigari, *Effective field theory treatment of the neutrino background in direct dark matter detection experiments*, Phys. Rev. D **93** (2016) no. 7, 075018, arXiv:1602.05300 [hep-ph].

[74] C. Bœhm et al., *How high is the neutrino floor?*, JCAP **01** (2019) 043, arXiv:1809.06385 [hep-ph].

[75] T. Marrodán Undagoitia and L. Rauch, *Dark matter direct-detection experiments*, J. Phys. G **43** (2016) no. 1, 013001, arXiv:1509.08767 [physics.ins-det].

[76] M. Schumann, *Dual-Phase Liquid Xenon Detectors for Dark Matter Searches*, J. Instrum. **9** (2014) C08004, arXiv:1405.7600 [astro-ph.IM].

[77] XENON Collaboration, E. Aprile et al., *Dark Matter Search Results from a One Ton-Year Exposure of XENON1T*, Phys. Rev. Lett. **121** (2018) no. 11, 111302, arXiv:1805.12562 [astro-ph.CO].

[78] LUX Collaboration, D. S. Akerib et al., *Results from a search for dark matter in the complete LUX exposure*, Phys. Rev. Lett. **118** (2017) no. 2, 021303, arXiv:1608.07648 [astro-ph.CO].

[79] PandaX-II Collaboration, X. Cui et al., *Dark Matter Results From 54-Ton-Day Exposure of PandaX-II Experiment*, Phys. Rev. Lett. **119** (2017) no. 18, 181302, arXiv:1708.06917 [astro-ph.CO].

[80] DarkSide Collaboration, P. Agnes et al., *DarkSide-50 532-day Dark Matter Search with Low-Radioactivity Argon*, Phys. Rev. D **98** (2018) no. 10, 102006, arXiv:1802.07198 [astro-ph.CO].

[81] XENON Collaboration, E. Aprile et al., *Light Dark Matter Search with Ionization Signals in XENON1T*, Phys. Rev. Lett. **123** (2019) no. 25, 251801, arXiv:1907.11485 [hep-ex].

[82] XMASS Collaboration, K. Abe et al., *A direct dark matter search in XMASS-I*, Phys. Lett. B **789** (2019) 45–53, arXiv:1804.02180 [astro-ph.CO].

[83] DEAP Collaboration, R. Ajaj et al., *Search for dark matter with a 231-day exposure of liquid argon using DEAP-3600 at SNOLAB*, Phys. Rev. D **100** (2019) no. 2, 022004, arXiv:1902.04048 [astro-ph.CO].

[84] R. Bernabei et al., *Dark matter particles in the Galactic halo: Results and implications from DAMA/NaI*, Int. J. Mod. Phys. D **13** (2004) 2127–2160, arXiv:astro-ph/0501412.

[85] R. Bernabei et al., *First model independent results from DAMA/LIBRA-phase2*, Nucl. Phys. Atom. Energy **19** (2018) no. 4, 307–325, arXiv:1805.10486 [hep-ex].

[86] COSINE-100 Collaboration, G. Adhikari et al., *Search for a Dark Matter-Induced Annual Modulation Signal in NaI(Tl) with the COSINE-100 Experiment*, Phys. Rev. Lett. **123** (2019) no. 3, 031302, arXiv:1903.10098 [astro-ph.IM].

[87] J. Amaré et al., *First Results on Dark Matter Annual Modulation from the ANAIS-112 Experiment*, Phys. Rev. Lett. **123** (2019) no. 3, 031301, arXiv:1903.03973 [astro-ph.IM].

[88] SABRE Collaboration, M. Antonello et al., *The SABRE project and the SABRE Proof-of-Principle*, Eur. Phys. J. C **79** (2019) no. 4, 363, arXiv:1806.09340 [physics.ins-det].

[89] E. Behnke et al., *Final Results of the PICASSO Dark Matter Search Experiment*, Astropart. Phys. **90** (2017) 85–92, arXiv:1611.01499 [hep-ex].

[90] COUPP Collaboration, E. Behnke et al., *First Dark Matter Search Results from a 4-kg CF_3I Bubble Chamber Operated in a Deep Underground Site*, Phys. Rev. D **86** (2012) no. 5, 052001, arXiv:1204.3094 [astro-ph.CO]. [Erratum: Phys.Rev.D 90, 079902 (2014)].

[91] PICO Collaboration, C. Amole et al., *Dark Matter Search Results from the Complete Exposure of the PICO-60 C_3F_8 Bubble Chamber*, Phys. Rev. D **100** (2019) no. 2, 022001, arXiv:1902.04031 [astro-ph.CO].

[92] CRESST Collaboration, A. H. Abdelhameed et al., *First results from the CRESST-III low-mass dark matter program*, Phys. Rev. D **100** (2019) no. 10, 102002, arXiv:1904.00498 [astro-ph.CO].

[93] SuperCDMS Collaboration, R. Agnese et al., *Search for Low-Mass Dark Matter with CDMSlite Using a Profile Likelihood Fit*, Phys. Rev. D **99** (2019) no. 6, 062001, arXiv:1808.09098 [astro-ph.CO].

[94] SuperCDMS Collaboration, R. Agnese et al., *Results from the Super Cryogenic Dark Matter Search Experiment at Soudan*, Phys. Rev. Lett. **120** (2018) no. 6, 061802, arXiv:1708.08869 [hep-ex].

[95] EDELWEISS Collaboration, Q. Arnaud et al., *Optimizing EDELWEISS detectors for low-mass WIMP searches*, Phys. Rev. D **97** (2018) no. 2, 022003, arXiv:1707.04308 [physics.ins-det].

[96] C. E. Aalseth et al., *Maximum Likelihood Signal Extraction Method Applied to 3.4 years of CoGeNT Data*, arXiv:1401.6234 [astro-ph.CO].

[97] CDEX Collaboration, H. Jiang et al., *Limits on Light Weakly Interacting Massive Particles from the First 102.8 kg $\times$ day Data of the CDEX-10 Experiment*, Phys. Rev. Lett. **120** (2018) no. 24, 241301, arXiv:1802.09016 [hep-ex].

[98] DAMIC Collaboration, A. Aguilar-Arevalo et al., *Search for low-mass WIMPs in a 0.6 kg day exposure of the DAMIC experiment at SNOLAB*, Phys. Rev. D **94** (2016) no. 8, 082006, arXiv:1607.07410 [astro-ph.CO].

[99] DAMIC Collaboration, A. Aguilar-Arevalo et al., *Constraints on Light Dark Matter Particles Interacting with Electrons from DAMIC at SNOLAB*, Phys. Rev. Lett. **123** (2019) no. 18, 181802, arXiv:1907.12628 [astro-ph.CO].

[100] DRIFT Collaboration, J. B. R. Battat et al., *Low Threshold Results and Limits from the DRIFT Directional Dark Matter Detector*, Astropart. Phys. **91** (2017) 65–74, arXiv:1701.00171 [astro-ph.IM].

[101] Y. Tao et al., *Track length measurement of $^{19}F^{+}$ ions with the MIMAC directional Dark Matter detector prototype*, Nucl. Instrum. Meth. A **985** (2021) 164569, arXiv:1903.02159 [physics.ins-det].

[102] C. Kouvaris and J. Pradler, *Probing sub-GeV Dark Matter with conventional detectors*, Phys. Rev. Lett. **118** (2017) no. 3, 031803, arXiv:1607.01789 [hep-ph].

[103] M. Ibe, W. Nakano, Y. Shoji, and K. Suzuki, *Migdal Effect in Dark Matter Direct Detection Experiments*, J. High Energy Phys. **03** (2018) 194, arXiv:1707.07258 [hep-ph].

[104] XENON Collaboration, E. Aprile et al., *Search for Light Dark Matter Interactions Enhanced by the Migdal Effect or Bremsstrahlung in XENON1T*, Phys. Rev. Lett. **123** (2019) no. 24, 241803, arXiv:1907.12771 [hep-ex].

[105] LUX Collaboration, D. S. Akerib et al., *Results of a Search for Sub-GeV Dark Matter Using 2013 LUX Data*, Phys. Rev. Lett. **122** (2019) no. 13, 131301, arXiv:1811.11241 [astro-ph.CO].

[106] R. C. Fernow, *Introduction to Experimental Particle Physics*. Cambridge University Press, 1986.

[107] F. Sauli, *Principles of Operation of Multiwire Proportional and Drift Chambers*, CERN-77-09 (1977) .

[108] A. Crispin and G. Fowler, *Density effect in the ionization energy loss of fast charged particles in matter*, Rev. Mod. Phys. **42** (1970) 290–316.

[109] M. J. Berger et al., *Report 37*, Journal of the International Commission on Radiation Units and Measurements **os19** (2016) no. 2, NP–NP.

[110] J. F. Ziegler, *Stopping of energetic light ions in elemental matter*, Journal of Applied Physics **85** (1999) no. 3, 1249–1272.

[111] L. Landau, *On the energy loss of fast particles by ionization*, J. Phys. (USSR) **8** (1944) 201–205.

[112] P. V. Vavilov, *Ionization Losses of High-Energy Heavy Particles*, Sov. Phys. JETP **5** (1957) 749. [Zh. Eksp. Teor. Fiz.32,920(1957)].

[113] G. F. Knoll, *Radiation Detection and Measurement, 3rd ed.* John Wiley and Sons, New York, 3rd edition ed., 2000.

[114] H. Bethe and J. Ashkin, *Passage of radiation through matter*, in *Experimental Nuclear Physics Vol.1 Part 2*, E. Segre, ed. Wiley, New York, 1959.

[115] C. Grupen, *Particle Detectors.* Cambridge Monographs on Particle Physics, Nuclear Physics and Cosmology. Cambridge University Press, 1996.

[116] Y. Klein O., Nishina, *Über die Streuung von Strahlung durch freie Elektronen nach der neuen relativistischen Quantendynamik von Dirac*, Z. Physik **52** (1929) 853?868.

[117] W. Heitler, *The quantum theory of radiation.* International series of monographs on physics. Oxford Univ. Press, 2nd edition ed., 1944.

[118] O. Şahin, I. Tapan, E. N. Özmutlu, and R. Veenhof, *Penning transfer in argon-based gas mixtures*, J. Instrum. **5** (2010) no. 05, P05002.

[119] W. Blum and L. Rolandi, *Particle Detection with Drift Chambers.* Springer-Verlag Berlin Heidelberg, Berlin, 1 ed., 1993.

[120] D. Lide, *CRC Handbook of Chemistry and Physics, 84th Edition.* CRC HANDBOOK OF CHEMISTRY AND PHYSICS. Taylor & Francis, 2003.

[121] F. Sauli, *Gaseous Radiation Detectors: Fundamentals and Applications*, vol. 36. Cambridge University Press, 8, 2014.

[122] S. Biagi, *Magboltz*, https://magboltz.web.cern.ch/magboltz/. [accessed 13/01/2021].

[123] S. Biagi, *Monte Carlo simulation of electron drift and diffusion in counting gases under the influence of electric and magnetic fields*, Nucl. Instrum. Meth. A **421** (1999) no. 1-2, 234–240.

[124] T. Aoyama, *Generalized gas gain formula for proportional counters*, Nucl. Instrum. Meth. A **234** (1985) no. 1, 125 – 131.

[125] J. S. Townsend, *Electricity of gases.* Clarendon Press, Oxford, 1915.

[126] W. Bambynek, *On selected problems in the field of proportional counters*, Nucl. Instrum. Methods **112** (1973) no. 1, 103 – 110.

[127] A. Williams and R. Sara, *Parameters affecting the resolution of a proportional counter*, Int. J. Rad. Appl. Instr. **13** (1962) no. 5, 229 – 238.

[128] A. Zastawny, *Standardization of gas amplification description in proportional counters*, Nucl. Instrum. Meth. A **385** (1997) no. 2, 239 – 242.

[129] I. Giomataris et al., *A Novel large-volume Spherical Detector with Proportional Amplification read-out*, J. Instrum. **3** (2008) P09007, arXiv:0807.2802 [physics.ins-det].

[130] Y. Giomataris and J. Vergados, *Neutrino properties studied with a triton source using large TPC detectors*, Nucl. Instrum. Meth. A **530** (2004) 330–358, arXiv:hep-ex/0303045.

[131] Y. Giomataris, *Development and prospects of the new gaseous detector 'Micromegas'*, Nucl. Instrum. Meth. A **419** (1998) 239–250.

[132] Y. Giomataris, P. Rebourgeard, J. Robert, and G. Charpak, *MICROMEGAS: A High granularity position sensitive gaseous detector for high particle flux environments*, Nucl. Instrum. Meth. A **376** (1996) 29–35.

[133] ISEG, *Technical documentation: NHR series*. https://iseg-hv.com/files/media/iseg_manual_NHR_en_20201117140821.pdf. [accessed 10/01/2021].

[134] CREMAT, *CR-110-R2.1 charge sensitive preamplifier: application guide*. https://www.cremat.com/CR-110-R2.1.pdf. [accessed 03/06/2020].

[135] A. D. Fard, *Étude d'un détecteur sphérique gazeux pour la recherche d'événements rares á bas seuil en énergie*. PhD thesis, Université Paris Sud - Paris XI, 2014.

[136] Redpitaya, *Specifications*, https://www.redpitaya.com/f145/specifications. [accessed 03/06/2020].

[137] ORTEC/AMETEK, *Model 142AH Preamplifier: Operating and Service Manual*.

[138] Canberra, *Canberra 2006 Proportional Counter Preamp: User's Manual*.

[139] E. McDaniel and E. Mason, *The Mobility and Diffusion of Ions in Gases*. Wiley, New York, 1973.

[140] J. Derré, *Pulse shape in the SPC prototype*, Available: https://newsgorg.files.wordpress.com/2018/07/pulse-shape-in-the-spc-prototype.pdf [accessed 13/01/2021], Oct., 2007.

[141] E. Bougamont et al., *Ultra low energy results and their impact to dark matter and low energy neutrino physics*, J. Mod. Phys. **3** (2012) no. 1, 57–63, arXiv:1010.4132 [physics.ins-det].

[142] I. Savvidis et al., *Low energy recoil detection with a spherical proportional counter*, Nucl. Instrum. Meth. A **877** (2018) 220–226, arXiv:1606.02146 [physics.ins-det].

[143] A. Giganon et al., *A multiball read-out for the spherical proportional counter*, JINST **12** (2017) no. 12, P12031, arXiv:1707.09254 [physics.ins-det].

[144] NEWS-G Collaboration, NEWS-G Collaboration, *First results from the NEWS-G direct dark matter search experiment at the LSM*, Astropart. Phys. **97** (2018) 54–62, arXiv:1706.04934 [astro-ph.IM].

[145] *National Nuclear Data Center, information extracted from the Chart of Nuclides database*, 2021. Accessed: 05-01-2021.

[146] M. J. Berger et al., *XCOM: Photon Cross Section Database (version 1.5)*, 2010. http://physics.nist.gov/xcom. National Institute of Standards and Technology, Gaithersburg, MD.

[147] NEWS-G Collaboration, Q. Arnaud et al., *Spherical Proportional Counter: A review of recent developments*, J. Phys. Conf. Ser. **1029** (2018) no. 1, 012006.

[148] DarkSide Collaboration, P. Agnes et al., *Low-Mass Dark Matter Search with the DarkSide-50 Experiment*, Phys. Rev. Lett. **121** (2018) no. 8, 081307, arXiv:1802.06994 [astro-ph.HE].

[149] CRESST Collaboration, F. Petricca et al., *First results on low-mass dark matter from the CRESST-III experiment*, J. Phys. Conf. Ser. **1342** (2020) no. 1, 012076, arXiv:1711.07692 [astro-ph.CO].

[150] Y. Giomataris and J. Vergados, *A Network of neutral current spherical TPC's for dedicated supernova detection*, Phys. Lett. B **634** (2006) 23–29, arXiv:hep-ex/0503029.

[151] R. T. Kouzes et al., *Neutron detection alternatives to 3He for national security applications*, Nucl. Instrum. Meth. A **623** (2010) no. 3, 1035–1045.

[152] E. Bougamont et al., *Neutron spectroscopy with the Spherical Proportional Counter based on nitrogen gas*, Nucl. Instrum. Meth. A **847** (2017) 10–14, arXiv:1512.04346 [physics.ins-det].

[153] *Boulby Undergound Laboratory (https://www.boulby.stfc.ac.uk/Pages/Overview-of-the-Laboratory.aspx)*, https://www.boulby.stfc.ac.uk/Pages/Overview-of-the-Laboratory.aspx.

[154] A. Meregaglia et al., *Study of a spherical Xenon gas TPC for neutrinoless double beta detection*, J. Instrum. **13** (2018) no. 01, P01009, arXiv:1710.04536 [physics.ins-det].

[155] A. Meregaglia, *A new neutrinoless double beta decay experiment: R2D2*, J. Phys. Conf. Ser. **1312** (2019) no. 1, 012002.

[156] J. Allison et al., *Recent developments in Geant4*, Nucl. Instrum. Meth. A **835** (2016) 186–225.

[157] GEANT4 Collaboration, S. Agostinelli et al., *GEANT4: A Simulation toolkit*, Nucl. Instrum. Meth. A **506** (2003) 250–303.

[158] R. Veenhof, *GARFIELD, recent developments*, Nucl. Instrum. Meth. A **419** (1998) 726–730.

[159] H. Schindler, *Garfield++ user guide, (2020)*. https://garfieldpp.web.cern.ch/garfieldpp/documentation/UserGuide.pdf. [accessed 03/06/2020].

[160] I. Smirnov, *Modeling of ionization produced by fast charged particles in gases*, Nucl. Instrum. Meth. A **554** (2005) 474–493.

[161] D. Pfeiffer et al., *Interfacing Geant4, Garfield++ and Degrad for the Simulation of Gaseous Detectors*, Nucl. Instrum. Meth. A **935** (2019) 121–134, arXiv:1806.05880 [physics.ins-det].

[162] R. Ward et al., *Development of a Simulation Framework for Spherical Proportional Counters*, in *2019 IEEE Nuclear Science Symposium (NSS) and Medical Imaging Conference (MIC)*, pp. 1–3. 2019.

[163] T. Alexopoulos et al., *A spark-resistant bulk-micromegas chamber for high-rate applications*, Nucl. Instrum. Meth. A **640** (2011) 110–118.

[164] MAMMA Collaboration, J. Wotschack, *Development of micromegas muon chambers for the ATLAS upgrade*, J. Instrum. **7** (2012) C02021.

[165] ALICE ITS Collaboration, A. Yoshikawa et al., *Development of Resistive Electrode Gas Electron Multiplier (RE-GEM)*, J. Instrum. **7** (2012) C06006.

[166] W. Riegler and C. Lippmann, *The physics of resistive plate chambers*, Nucl. Instrum. Meth. A **518** (2004) 86–90.

[167] V. Datar et al., *Development of glass resistive plate chambers for INO experiment*, Nucl. Instrum. Meth. A **602** (2009) 744–748.

[168] M. Naimuddin et al., *Characterisation of Glass Electrodes and RPC Detectors for $INO-ICAL$ Experiment*, JINST **9** (2014) C10039, arXiv:1409.7184 [physics.ins-det].

[169] R. Kanishka, V. Bhatnagar, and D. Indumathi, *Optimisation and Characterisation of Glass RPC for India-based Neutrino Observatory Detectors*, arXiv:1605.09361 [physics.ins-det]. arXiv:1605.09361.

[170] J. A. Coles, J. L. Munoz, and F. Deyhimi, *Surface and Volume Resistivity of Pyrex Glass Used for Liquid Membrane Ion-Sensitive Microelectrodes*, in *Ion Measurements in Physiology and Medicine*, M. Kessler et al., eds., pp. 67–73. Springer Berlin Heidelberg, Berlin, Heidelberg, 1985.

[171] J. Busto, Y. Gonin, J. Vuilleumier, F. Hubert, and P. Hubert, *Radioactivity measurements of a large number of adhesives*, Nucl. Instrum. Meth. A **492** (2002) 35–42.

[172] Y. Lv, Y. Zhou, J. Liu, M. Shao, Z. Zhang, G. Song, and X. Wang, *Production and performance study of Diamond-Like Carbon resistive electrode in MPGD*, Nucl. Instrum. Meth. A **958** (2020) 162759.

[173] Y. Zhou, Y. Lv, L. Shang, D. Hong, G. Song, J. Liu, J. Feng, M. Shao, X. Wang, and Z. Zhang, *Fabrication and performance of a μ RWELL detector with Diamond-Like Carbon resistive electrode and two-dimensional readout*, Nucl. Instrum. Meth. A **927** (2019) 31–36.

[174] D. Attié et al., *Performances of a resistive Micromegas module for the Time Projection Chambers of the T2K Near Detector upgrade*, Nucl. Instrum. Meth. A **957** (2020) 163286, arXiv:1907.07060 [physics.ins-det].

[175] R. Evans, *The Atomic Nucleus*. Krieger Publishing Company, 2003.

[176] J. Lindhard, V. Nielsen, M. Scharff, and P. Thomsen, *Integral equations governing radiation effects (Notes on atomic collisions, III)*, Kong. Dan. Vid. Sel. Mat. Fys. Med. **33** (1963) .

[177] F. J. Iguaz et al., *Micromegas detector developments for Dark Matter directional detection with MIMAC*, J. Instrum. **6** (2011) no. 07, P07002–P07002.

[178] E. Daw et al., *Spin-dependent limits from the DRIFT-IId directional dark matter detector*, Astropart. Phys. **35** (2012) no. 7, 397 – 401.

[179] D. Barker, W. Z. Wei, D. M. Mei, and C. Zhang, *Ionization Efficiency Study for Low Energy Nuclear Recoils in Germanium*, Astropart. Phys. **48** (2013) 8, arXiv:1304.6773 [physics.ins-det].

[180] H. Chagani, P. Majewski, E. J. Daw, V. A. Kudryavtsev, and N. J. C. Spooner, *Measurement of the quenching factor of Na recoils in NaI(Tl)*, J. Instrum. **3** (2008) P06003, arXiv:0806.1916 [physics.ins-det].

[181] A. Mangiarotti, M. I. Lopes, M. L. Benabderrahmane, V. Chepel, A. Lindote, J. Pinto da Cunha, and P. Sona, *A Survey of energy loss calculations for heavy ions between 1-keV and 100-keV*, Nucl. Instrum. Meth. A **580** (2007) 114–117, arXiv:physics/0610286.

[182] A. Hitachi, *Bragg-like curve for dark matter searches: binary gases*, Radiat. Phys. Chem. **77** (2008) 1311–1317, arXiv:0804.1191 [astro-ph].

[183] J. Ziegler, J. Biersack, and M. Ziegler, *SRIM, the Stopping and Range of Ions in Matter*. 2008.

[184] D. Santos et al., *Ionization Quenching Factor Measurement of Helium 4*, 2008. arXiv:0810.1137 [astro-ph].

[185] B. Tampon et al., *Ionization Quenching Factor measurement of 1 keV to 25 keV protons in Isobutane gas mixture*, EPJ Web Conf. **153** (2017) 01014.

[186] J. Muraz et al., *A table-top ion and electron beam facility for ionization quenching measurement and gas detector calibration*, Nucl. Instrum. Meth. A **832** (2016) 214–218.

[187] I. Giomataris et al., *Micromegas in a bulk*, Nucl. Instrum. Meth. A **560** (2006) no. 2, 405 – 408.

[188] P. Sortais et al., *Ultracompact/ultralow power electron cyclotron resonance ion source for multipurpose applications*, Rev. Sci. Instrum. **81** (2010) no. 2, 02B314, https://doi.org/10.1063/1.3272878.

[189] H. Rose, *Geometrical Charged-Particle Optics*. Springer Series in Optical Sciences. Springer, 2009.

[190] M. Berger, J. Coursey, M. Zucker, and J. Chang, *ESTAR, PSTAR, and ASTAR: Computer Programs for Calculating Stopping-Power and Range Tables for Electrons, Protons, and Helium Ions*, Online, 2005. http://physics.nist.gov/Star.

[191] B. J. Scholz, A. E. Chavarria, J. I. Collar, P. Privitera, and A. E. Robinson, *Measurement of the low-energy quenching factor in germanium using an* $^{88}Y/Be$ *photoneutron source*, Phys. Rev. D **94** (2016) no. 12, 122003, arXiv:1608.03588 [physics.ins-det].

[192] L. Reichhart et al., *Quenching Factor for Low Energy Nuclear Recoils in a Plastic Scintillator*, Phys. Rev. C **85** (2012) 065801, arXiv:1111.2248 [nucl-ex].

[193] A. E. Chavarria et al., *Measurement of the ionization produced by sub-keV silicon nuclear recoils in a CCD dark matter detector*, Phys. Rev. D **94** (2016) no. 8, 082007, arXiv:1608.00957 [astro-ph.IM].

[194] ICRU, *Average energy required to produce an ion pair*, ICRU Report **31** (1979) .

[195] R. L. Platzman, *Total ionization in gases by high-energy particles: An appraisal of our understanding*, Int. J. App. Radit. Isotopes **10** (1961) no. 2-3, 116–127.

[196] M. Inokuti, *Ionization Yields in Gases under Electron Irradiation*, Radiat. Res. **64** (1975) no. 1, 6–22.

[197] E. Waibel and B. Grosswendt, *Spatial energy dissipation profiles, W values, backscatter coefficients, and ranges for low-energy electrons in methane*, Nucl. Instrum. Meth. **211** (jun, 1983) 487–498.

[198] D. Combecher, *Measurement of W Values of Low-Energy Electrons in Several Gases*, Radiat. Res. **84** (1980) no. 2, 189–218.

[199] E. Waibel and B. Grosswendt, *Determination of W Values and Backscatter Coefficients for Slow Electrons in Air*, Radiat. Res. **76** (1978) no. 2, 241–249.

[200] A. Cole, *Absorption of 20-eV to 50,000-eV Electron Beams in Air and Plastic*, Radiat. Res. **38** (1969) no. 1, 7–33.

[201] *"Atomic and Molecular Data for Radiotherapy and Radiation Research"*. No. 799 in TECDOC Series. International Atomic Energy Agency, Vienna, 1995.

[202] E. Waibel and B. Grosswendt, *Study of W-values, practical ranges, and energy dissipation profiles of low-energy electrons in N2*, in *Proc. Eigth Symposium Microdosimetry*, pp. 301–310. Commission of the European Communities, Luxembourg, EUR 8395, 1983.

[203] E. Waibel and B. Grosswendt, *Degradation of low-energy electrons in carbon dioxide: energy loss and ionization*, Nucl. Instrum. Meth. **B53** (1991) 239–250.

[204] M. Chemtob, N. Parmentier, and V. D. Nguyen, *Some experimental results on W-values for heavy particles*, Phys. Med. Biol. **23** (1978) no. 6, 1197–1199.

[205] J. A. Phipps, J. W. Boring, and R. A. Lowry, *Total Ionization in Argon by Heavy Ions of Energies 8 to 100 keV*, Phys. Rev. **135** (1964) A36–A39.

[206] R. Huber, D. Combecher, and G. Burger, *Measurement of Average Energy Required to Produce an Ion Pair (W Value) for Low-Energy Ions in Several Gases*, Radiat. Res. **101** (1985) no. 2, 237–251.

[207] J. W. Boring, G. E. Strohl, and F. R. Woods, *Total Ionization in Nitrogen by Heavy Ions of Energies 25 to 50 keV*, Phys. Rev. **140** (1965) A1065–A1069.

[208] V. Nguyen et al., *Recent experimental results on W-values for heavy particles*, Phys. Med. Biol. **25** (1980) no. 3, 509–518.

[209] E. Waibel and G. Willems, *W values for low-energy protons in methane-based tissue equivalent gas and its constituents*, Phys. Med. and Biol. **37** (1992) no. 1, 249–259.

[210] G. Willems and B. Grosswendt, *Experimental W values of low-energy protons in the alkane series from methane to pentane*, Phys. Med. Biol. **43** (1998) no. 2, 313–323.

[211] F. Posny, J. Chary, and V. D. Nguyen, *W values for heavy particles in propane and in TE gas*, Phys. Med. Biol. **32** (1987) no. 4, 509–515.

[212] B. Grosswendt, G. Willems, and W. Baek, *W Values of Protons Slowed Down in Molecular Hydrogen*, Radiat. Prot. Dosim. **70** (1997) no. 1-4, 37–46.

[213] E. Waibel and B. Grosswendt, *W values and other transport data on low energy electrons in tissue equivalent gas*, Phys. Med. Biol. **37** (1992) no. 5, 1127–1145.

[214] B. C. Edgar, W. T. Miles, and A. E. S. Green, *Energy deposition of protons in molecular nitrogen and applications to proton auroral phenomena*, J. Geophys. Res. **78** (1973) no. 28, 6595–6606.

[215] H. Paul, *Nuclear stopping power and its impact on the determination of electronic stopping power*, AIP Conf. Proc. **1525** (2013) no. 1, 309–313.

[216] A. Hitachi, *Bragg-like curve for dark matter searches: Binary gases*, Radiat. Phys. Chem. **77** (2008) no. 10, 1311 – 1317.

[217] C. Bucci et al., *First results from the Cuoricino experiment*, Nucl. Instrum. Meth. A **520** (2004) 132–134.

[218] E. Armengaud et al., *First results of the EDELWEISS-II WIMP search using Ge cryogenic detectors with interleaved electrodes*, Phys. Lett. B **687** (2010) 294–298, arXiv:0912.0805 [astro-ph.CO].

[219] DarkSide-20k Collaboration, C. Aalseth et al., *DarkSide-20k: A 20 tonne two-phase LAr TPC for direct dark matter detection at LNGS*, Eur. Phys. J. Plus **133** (2018) 131, arXiv:1707.08145 [physics.ins-det].

[220] S. of Automotive Engineers, A. S. for Testing, and Materials, *Metals & Alloys in the Unified Numbering System*. ASTM data series publication: American Society for Testing and Materials. Society of Automotive Engineers, 2001.

[221] A. Brossard, *Optimization of spherical proportional counter backgrounds and response for low mass dark matter search*. PhD thesis, Queen's University, Kingston, Ontario, Canada and Université Paris-Saclay, Saint-Aubin, France, 3, 2020. http://hdl.handle.net/1974/27649.

[222] B. LaFerriere, T. Maiti, I. Arnquist, and E. Hoppe, *A novel assay method for the trace determination of Th and U in copper and lead using inductively coupled plasma mass spectrometry*, Nucl. Instrum. Meth. A **775** (2015) 93–98.

[223] I. Arnquist, M. di Vacri, and E. Hoppe, *An automated ultraclean ion exchange separation method for the determinations of ^{232}Th and ^{238}U in copper using inductively coupled plasma mass spectrometry*, Nucl. Instrum. Meth. A **965** (2020) 163761.

[224] N. Abgrall et al., *The Majorana Demonstrator radioassay program*, Nucl. Instrum. Meth. A **828** (2016) 22–36, arXiv:1601.03779 [physics.ins-det].

[225] M. Shamsuzzoha Basunia, *Nuclear Data Sheets for $A = 210$*, Nuclear Data Sheets **121** (2014) 561–694.

[226] R. Bunker et al., *Evaluation and mitigation of trace ^{210}Pb contamination on copper surfaces*, Nucl. Instrum. Meth. A **967** (2020) 163870, arXiv:2003.06357 [physics.ins-det].

[227] G. Zuzel, K. Pelczar, and M. Wójcik, *Studies of surface and bulk ^{210}Po in metals using an ultra-low background large surface alpha spectrometer*, Appl. Radiat. Isot. **126** (2017) 165–167. Proceedings of the 7th International Conference on Radionuclide Metrology – Low-Level Radioactivity Measurement Techniques.

[228] K. Abe et al., *Identification of ^{210}Pb and ^{210}Po in the bulk of copper samples with a low-background alpha particle counter*, Nucl. Instrum. Meth. A **884** (2018) 157–161.

[229] *XIA Ultra-Lo1800*, 2020. https://www.xia.com/ultralo.html. Accessed: 02-03-2020.

[230] E. W. Hoppe et al., *Use of electrodeposition for sample preparation and rejection rate prediction for assay of electroformed ultra high purity copper for ^{232}Th and ^{238}U prior to inductively coupled plasma mass spectrometry (ICP/MS)*, J. Radioanal. Nucl. Chem. **277** (2008) no. 1, 103–110.

[231] Majorana Collaboration, N. Abgrall et al., *The Majorana Demonstrator neutrinoless double-beta decay experiment*, Adv. High Energy Phys. **2014** (2014) 365432.

[232] M. Faraday, *VI. Experimental researches in electricity.-Seventh Series*, Philos. Trans. R. Soc. **124** (1834) 77–122.

[233] W. Greiner, L. Neise, and H. Stöcker, *Thermodynamics and statistical mechanics*. Classical theoretical physics. Springer-Verlag, 1995.

[234] A. Bard, R. Parsons, and J. Jordan, *Standard Potentials in Aqueous Solution*. Monographs in Electroanalytical Chemistry and Electrochemistry. Taylor & Francis, 1985.

[235] P. Atkins, *Physical Chemistry, 6th edition*. W.H. Freeman and Company, New York, 1997.

[236] D. Lide, *CRC Handbook of Chemistry and Physics, 87th Edition*. Taylor & Francis, 2006.

[237] W. Haynes, *CRC Handbook of Chemistry and Physics, 92nd Edition*. CRC Press, 2011.

[238] E. W. Hoppe et al., *Microscopic evaluation of contaminants in ultra-high purity copper*, J. Radioanal. Nucl. Chem. **282** (2009) no. 1, 315.

[239] M. Chandrasekar and M. Pushpavanam, *Pulse and pulse reverse plating - Conceptual, advantages and applications*, Electrochim. Acta **53** (2008) no. 8, 3313–3322.

[240] N. Ibl, *Nomenclature for transport phenomena in electrolytic systems*, Electrochimica Acta **27** (1982) no. 5, 629–642.

[241] A. Szymczyk et al., *Contribution of convection, diffusion and migration to electrolyte transport through nanofiltration membranes*, Adv. Colloid Interface Sci. **103** (2003) no. 1, 77–94.

[242] E. Hoppe et al., *Cleaning and passivation of copper surfaces to remove surface radioactivity and prevent oxide formation*, Nucl. Instrum. Meth. A **579** (2007) no. 1, 486–489. Proceedings of the 11th Symposium on Radiation Measurements and Applications.

[243] N. Overman et al., *Majorana Electroformed Copper Mechanical Analysis*, Tech. Rep. PNNL-21315, Pacific Northwest National Laboratory, 01, 2012.

[244] S. Yellin, *Finding an upper limit in the presence of unknown background*, Phys. Rev. D **66** (2002) 032005, arXiv:physics/0203002.

[245] D. Malczewski, J. Kisiel, and J. Dorda, *Gamma background measurements in the Boulby Underground Laboratory*, J. Radioanal. Nucl. Chem. **298** (2013) no. 3, 1483–1489.

[246] S. S. Wilks, *The Large-Sample Distribution of the Likelihood Ratio for Testing Composite Hypotheses*, Annals Math. Statist. **9** (1938) no. 1, 60–62.

[247] G. Cowan, K. Cranmer, E. Gross, and O. Vitells, *Asymptotic formulae for likelihood-based tests of new physics*, Eur. Phys. J. C **71** (2011) 1554, arXiv:1007.1727 [physics.data-an]. [Erratum: Eur.Phys.J.C 73, 2501 (2013)].

[248] D. Durnford, Q. Arnaud, and G. Gerbier, *Novel approach to assess the impact of the Fano factor on the sensitivity of low-mass dark matter experiments*, Phys. Rev. D **98** (2018) no. 10, 103013, arXiv:1808.06967 [astro-ph.IM].

[249] NEWS-G Collaboration, *Precision laser-based measurements of the single electron response of spherical proportional counters for the NEWS-G light dark matter search experiment*, Phys. Rev. D **99** (2019) no. 10, 102003, arXiv:1902.08960 [physics.ins-det].

université PARIS-SACLAY

ÉCOLE DOCTORALE
Particules, hadrons, énergie et noyau: instrumentation, imagerie, cosmos et simulation (PHENIICS)

UNIVERSITY OF BIRMINGHAM

Titre: Recherche de Matière Noire Légère avec un Compteur Proportionnel Sphérique

Mots clés: Matière noire, Compteur proportionnel sphérique, Détecteur gazeux, Bruit de fond, Détecteurs de rayonnement,

Résumé: La collaboration NEWS-G mène des expériences qui recherchent des particules candidates pour la matière noire jusqu'à des masses en dessous du GeV avec un détecteur gazeux le compteur proportionnel sphérique. Le détecteur de nouvelle génération, SNOGLOBE, un compteur proportionnel sphérique de 140 cm de diamètre, a été construit et des plans pour des expériences futures sont en cours. Le travail présenté a permis de développer la compréhension du détecteur, les propriétés des gaz, les techniques de suppression de fond et le potentiel physique des futures expériences.

La compréhension du champ électrique du détecteur est essentielle au fonctionnement du détecteur. Les calculs de la méthode des éléments finis ont été utilisés pour guider le développement des capteurs de lecture, tout comme un programme de simulation, dédié aux compteurs proportionnels sphériques, basé sur Geant4 et Garfield ++. L'utilisation d'une électrode de correction secondaire à résistivité élevée avec le capteur à anode unique a amélioré la stabilité opérationnelle et la résolution d'énergie du détecteur en ajustant le champ électrique. L'utilisation d'une électrode centrale, imprimée en 3D pour le capteur multi-anode ACHINOS et enrobée d'une couche de le carbone adamantin (DLC) a permis une percée dans la stabilité et la robustesse du détecteur. ACHINOS offre un moyen de fonctionner avec des détecteurs de plus en plus grands et à haute pression, ce qui est essentiel pour le fonctionnement du SNOGLOBE et des futures recherches sphériques proportionnelles contre les événements rares.

La fraction d'énergie déposée en forme d'ionisation doit être bien comprise pour déduire l'énergie d'un noyau de recul induit par la diffusion élastique de la matière noire. Une méthode a été développée pour calculer cela à partir de mesures de précision de la valeur W dans les gaz, menées depuis plusieurs décennies. Ceux-ci fournissent des estimations expérimentales du facteur de 'quenching' d'ionisation dans plusieurs gaz. Le facteur de quenching d'ionisation dans CH_4 est d'une importance particulière pour la collaboration NEWS-G et est estimé à des énergies de recul en dessous du keV.

La construction de détecteurs de matière noire impose des contraintes extrêmement rigoureuses concernant la radio-pureté des matériaux utilisés. Dans le cas de NEWS-G, le ^{222}Rn incrusté dans le cuivre du détecteur, lors de sa fabrication, conduit à une contamination de ^{210}Pb, qui est la plus grande contribution au bruit de fond expérimental. Une méthode de suppression de ce fond dans le cuivre est l'électroformage, qui a été utilisé par des expériences pour produire des composants de détecteur suite à l'amélioration significative de la radio-pureté. La technique a été rééchelonnée et une couche de cuivre très pur a été déposée à la surface interne de SNOGLOBE, réduisant le fond en dessous de 1 keV par un facteur de 2,6. Il s'agit du plus grand électroformage souterrain jamais réalisé et a démontré la faisabilité de la technique sur de grandes surfaces sphériques profondément souterraines.

L'amélioration de la radio-pureté qui peut être obtenue avec l'électroformage a motivé le développement de futurs compteurs proportionnels sphériques entièrement électro-formés directement dans un laboratoire souterrain. L'installation ECUME de SNOLAB produira un détecteur de 140 cm pour NEWS-G et entrera en service cette année. Lorsqu'il est installé dans le blindage du SNOGLOBE, le détecteur entièrement électro-formé augmentera la sensibilité matière noire de NEWS-G. Au-delà, DarkSPHERE est proposé comme successeur dans la recherche directe de matière noire NEWS-G. Le détecteur électro-formé entièrement souterrain de 3 m, installé dans un blindage de radioprotection amélioré composé principalement d'eau, aurait le potentiel d'explorer l'espace de la section efficace pour la production de la matière noir proche au plancher des neutrinos solaires, dans la gamme de masse de matière noire inférieure à 1 GeV. Le potentiel physique d'un tel détecteur pour détecter la matière noire par recul nucléaire induit a été étudié.

université PARIS-SACLAY

ÉCOLE DOCTORALE
Particules, hadrons, énergie et noyau : instrumentation, imagerie, cosmos et simulation (PHENIICS)

UNIVERSITY OF BIRMINGHAM

Title: Searching for Light Dark Matter with a Spherical Proportional Counter

Keywords: Dark Matter, Spherical Proportional Counter, Gaseous Detectors, Background, Radiation Detectors

Abstract: The NEWS-G collaboration are conducting experiments that search for dark matter down to sub-GeV candidate masses with a gaseous detector, the spherical proportional counter. The next generation detector, SNOGLOBE, a 140 cm-diameter spherical proportional counter, has been constructed, and plans for experiments beyond this are underway. The presented work has enabled SNOGLOBE, developing the understanding of the detector, the properties of gases, background suppression techniques and the physics potential of future experiments.

The understanding of the detector electric field is essential to detector operation. Finite element method calculations were used to guide the development of read-out sensors, as was a dedicated simulation framework for spherical proportional counters, based on Geant4 and Garfield++. The use of a high-resistivity secondary correction electrode with the single-anode sensor improved detector operational stability and energy resolution by shaping the electric field. The use of a DLC coated, 3D-printed central electrode for the multi-anode sensor, ACHINOS, provided a breakthrough in detector stability and robustness. ACHINOS provides a means of operating with increasingly large and high-pressure detectors, which is essential for the operation of SNOGLOBE and future spherical proportional counter rare-event searches.

The fraction of deposited energy dissipated as ionisation must be understood to infer the energy of a recoiling nucleus induced by dark matter elastic scattering. A method has been developed to compute this from precision measurements of the W-value in gases, which have been conducted for several decades. These provide experimental estimates of the ionisation quenching factor (QF) in several gases. The QF in CH_4 is of particular importance to the NEWS-G collaboration, and is estimated to sub-keV recoil energies. The construction of dark matter detectors places extremely rigorous constraints on the radiopurity of materials used. In the case of NEWS-G, ^{222}Rn introduced into the detector copper during manufacturing leads to a ^{210}Pb contamination, which is the dominant experimental background. A method of suppressing this background in copper is electroforming, which has been used by experiments to produce detector components due to the significant improvement in radiopurity. The technique has been scaled up and applied to apply a highly-pure copper layer to the inner surface of SNOGLOBE, reducing the background below 1 keV by a factor of 2.6. This is the largest deep-underground electroforming ever performed, and has demonstrated the feasibility of the technique on large, spherical surfaces deep underground.

The enhancement in radiopurity that can be achieved with electroforming has motivated future fully electroformed spherical proportional counters directly in an underground laboratory. The ECUME facility in SNOLAB will produce a 140 cm detector for NEWS-G, and is beginning operation this year. When installed in the shielding of SNOGLOBE, the fully electroformed detector will increase NEWS-G's sensitivity. Beyond this, DarkSPHERE is proposed as the next generation detector. The 3 m fully underground electroformed detector, installed in an improved radiopurity shielding composed mainly of water, would have the potential to explore the dark matter candidate mass-cross section parameter space close to the solar neutrino floor in the subGeV dark matter mass range. The physics potential of such a detector has been explored.